

Investigations into the Formation of Carbonaceous Deposits via Autoxidation of Jet Fuels

Department of Mechanical Engineering



The
University
Of
Sheffield.

Charlie Adams

April 7, 2023

Abstract

Jet fuel is used as a coolant for lubricants and oils, and receives heat from the burner feed arm before combustion. The thermal stress received by the fuel, in combination with dissolved oxygen, results in reactions yielding carbonaceous deposits on fuel-wetted surfaces. These deposits can cause efficiency and safety issues as they grow on critical components. The initial stage of the deposition process involves a well understood autoxidation mechanism, leading to a series of well characterized oxidized molecules. However, it is less clear what chemical mechanisms lead to the agglomeration of these oxidized molecules producing deposits. The aim of this thesis is to gain a more fundamental understanding of the agglomeration and deposition process. Density functional theory (DFT) and experimental techniques including gas/liquid chromatography mass spectroscopy (GC/LC-MS) were used to investigate these processes. Additionally, kinetic analysis using pseudo-detailed mechanisms were performed throughout to explore competing pathways.

The Soluble Macromolecular Oxidatively Reactive Species (SMORS) mechanism has previously been proposed as a universal mechanism for deposition, but has received little mechanistic scrutiny. Our DFT calculations performed here showed that the originally proposed SMORS mechanism involving electrophilic aromatic substitution (EAS) was kinetically and thermodynamically prohibited. Instead, it was found a homolytic aromatic substitution (HAS) mechanism could allow C-C bonds to form to lead to agglomerated species. Additionally, the SMORS mechanism neglects to elucidate the role of indigenous fuel sulfur compounds, which have a major influence on deposit formation. Using surrogate fuels and deposit characterization with GC/LC-MS, it was shown that the addition of sulfur containing compounds to 5-membered fuel nitrogen heterocycles led to oligomers containing nitrogen-nitrogen compounds. This implied sulfur compounds were able to catalyze the coupling. Indigenous fuel sulfurs were also shown to play a crucial role in the early stage of deposition. DFT calculations showed that compared to other fuel oxygenated com-

pounds, sulfur acids formed from autoxidation of indigenous sulfurs have the highest adsorption energy on stainless steel surface oxides. Exploring the heterogeneity of stainless steel surface oxides, sulfur acids had a higher adsorption energy on Cr_2O_3 and carboxylic acids had a higher adsorption energy on Fe_2O_3 . Other oxygenated and indigenous fuel components were found to physisorb at lower adsorption energies.

Finally, using the mechanistic findings from this thesis, 6 pseudo-detailed kinetic mechanisms were built using DFT calculate barriers, each representing a fuel containing a common antioxidant/heteroatom. The calculated mass of deposit dimer from our mechanisms correlated well with the measured mass of deposit formed from 6 equivalent surrogate fuels. The results here show how DFT can be used to build deposition mechanisms from first principles. The chemical mechanistic findings throughout this whole thesis will help guide future researchers to build new predictive models for deposition from first-principles.

Acknowledgements

This thesis would not have been possible without the support and guidance of so many people. Firstly, thanks to Kevin Hughes as my first supervisor for his invaluable knowledge of chemical kinetics, and his guidance throughout my PhD. Thank you Simon Blakey for his wisdom in approaching the thesis as a series of research questions. Your kindness and guidance towards the end of my PhD is much appreciated. Anthony Meijer, the precision of your mind and hard work in guiding me to be a greater chemist and scientific writer will not be forgotten. I have a newly discovered love of computational chemistry thanks to your supervision. I'd like to thank Marco Conte, despite not being an official supervisor, for your kindness adopting me into your group. Your support academically and mentally helped me through some of the toughest period of my PhD, I am forever grateful. Ehsan Alborzi, I would like to thank you for your good humour and deep-knowledge of fuels. You are a great scientist, politician, poet, and friend.

In the office, I'd like to thank Yousef Sadat for all the PhD memes and excellent conversation. I hope we have been able to support each other with success throughout this journey. Rahima, although I knew you only briefly, your humour helped me in the toughest periods of my write-up. Good luck for the rest of your PhD.

This journey would not have been possible without my friends and family too. Nabhan Ahmed, our paths took similar twists and turns, and you were there throughout the whole thing. Your intelligence and hilarity is always in inspiration. Innes, thanks for being a fantastic housemate and friend for most of my PhD. I can't think of anyone as easy-going and as good-natured as you. Soph, thanks for always being there from day one, you always make me smile. Dom, thank you for the puns and the theme-tunes, you added colour to my weekends. Will, you have always been a source of endless laughter, and continue to be. I'd like to thank my parents, Chris and Judith, and my brother for their continued love and support throughout this journey.

Finally, thank you to Ella, the love of my life and best-friend. You were so many things to me at every step of the way, and I am forever grateful. I hope that we can continue our adventures through life many years into the future.

Decleration

I hereby declare all the work in this thesis is my own except where explicitly stated.

Contents

1	Introduction	1
1.1	Jet Fuels and Energy	1
1.2	Jet Fuels and Aviation	2
1.3	Origins and Composition of Jet Fuel	4
1.3.1	Composition of Fuels	6
1.4	Jet Fuels and Thermal Oxidative Stability	9
1.5	Generalized Deposition Process	11
1.6	Thesis Outline	16
2	Literature Review	18
2.1	Methods used to Investigate Thermal Stability	18
2.1.1	Experimental Methods for Investigating Autoxidation and Deposit Formation	18
2.1.2	Computational Methods for Investigating Autoxidation and Deposit Formation	23
2.1.3	Concluding Remarks on Experimental and Computational Methods used to Investigate Thermal Stability	25
2.2	Factors Affecting Autoxidation and Deposit Formation	26
2.2.1	Oxygen	26
2.2.2	Bulk Hydrocarbon Composition	28
2.2.3	Physical Conditions	30
2.2.4	Heteroatomics	34
2.2.5	Wall Effects	63
2.2.6	Metals in Situ	66
2.2.7	Concluding Remarks of Factors Affecting Autoxidation and Deposit Formation	68
2.3	Generalized Deposition Models	70

2.3.1	Soluble Macromolecular Oxidative Reactive Species (SMORS) Mechanism	71
2.3.2	Pseudo-Detailed Predictive Mechanisms	75
2.4	Concluding Remarks of Generalized Deposition Models	80
2.5	Conclusion to Literature Review and Key Research Themes of the Thesis	81
3	Theoretical Background	83
3.1	Transition State Theory and Thermochemistry of Chemical Reactions	84
3.2	Potential Energy Surface	86
3.3	Born-Oppenheimer Approximation	89
3.4	Geometry Optimization	89
3.5	Quantum Mechanics	90
3.6	Schrödinger Equation	92
3.7	The Hamiltonian Operator	95
3.8	The Variational Principle	97
3.9	Hartree-Fock Self-Consistent Field Method	99
3.9.1	The Slater Determinant	99
3.9.2	Formation of the Hartree-Fock Energy Expression	101
3.9.3	Formation of the Hartree Fock Equations	105
3.9.4	Roothaan-Hall Equations	108
3.9.5	Deficiencies With the HF Method	109
3.10	Recovering Correlation Energy	111
3.10.1	Restricted Open-Shell Hartree-Fock and Unrestricted Hartree- Fock	111
3.10.2	Post-Hartree Fock Methods	113
3.11	Density Functional Theory	115
3.11.1	The Hohenberg-Kohn Theorems	115
3.11.2	Kohn-Sham Equations	116
3.11.3	Approximations to the Exchange Correlation Functional . . .	119
3.12	Basis Sets	124
3.12.1	Slater-Type Orbitals	124
3.12.2	Pople Basis Stets	125
3.12.3	Dunning's Correlation Consistent Basis Set	126
3.12.4	Plane Wave Basis Sets and Projector Augmented Wave Method	126

4	Investigations into the SMORS Mechanism	130
4.1	Introduction	130
4.2	Materials and Methods	132
4.2.1	Computational Details	132
4.2.2	Surrogate Fuels	132
4.3	Results and Discussion	132
4.3.1	Formation of the Keto-Peroxyl Radical	133
4.3.2	Formation of Quinones	136
4.3.3	Quinone Heteroatom Coupling Step	140
4.3.4	Flask Tests	148
4.3.5	Discussion and Implication for Fuels	151
4.4	Conclusions and Next Steps	153
5	The Interaction of Nitrogen Heteroatomics with Sulfur	154
5.1	Introduction	154
5.2	Materials and Methods	156
5.2.1	Surrogate Fuels	156
5.2.2	Method of Thermal Stressing	157
5.2.3	Characterization	158
5.2.4	Computational Details	159
5.2.5	Hansen Solubility Analysis	159
5.3	Results and Discussion	160
5.3.1	Pure Indole Deposition	160
5.3.2	Effect of Sulfur with Indole	160
5.4	Reaction of Sulfur with Other Nitrogen Heterocycles and Compounds	168
5.5	Mechanism Discussion and Implication for Jet Fuels	173
5.6	Conclusions and Next Steps	176
6	Understanding the Wall Deposition Mechanism	178
6.1	Introduction	179
6.2	Methods	182
6.2.1	Surface Model	182
6.2.2	Computational Details	184
6.2.3	Justification for using the OptPBE	185
6.3	Results and Discussion	187
6.3.1	Results from the Aviation Fuel Thermal Stability (AFSTU) Rig	187

6.3.2	Computational Results	188
6.3.3	Conclusions	192
7	Predicting Thermal Stability Behavior with Quantum Chemistry	194
7.1	Introduction	194
7.2	Methods and Materials	196
7.2.1	Surrogate Fuels for this Study	196
7.2.2	Method of Thermal Stressing and Deposit Measurement	197
7.2.3	Hansen Solubility Parameters and Computational Details	197
7.2.4	Pseudo-Detailed Mechanism in Fuels	198
7.3	Results and Discussion	198
7.3.1	Homolytic Aromatic Substitution Mechanism	198
7.3.2	Comparison of Antioxidant Oligomer Solubility and Pathway to Deposit	200
7.3.3	Predicting Deposition formation using DFT	203
7.4	Implication for Fuels	215
7.5	Conclusions	216
8	Discussion, Future Work and Conclusions	217
8.1	Key Research Questions	217
8.2	Summary of Each Chapter and Critical Evaluation of the Work	218
8.3	Limitations and Future Work Directions	221
8.4	Conclusion	223
9	Published Work from this Thesis	225
	Bibliography	263
10	Appendix	264
10.1	Investigations into the SMORS Mechanism	264
10.1.1	Thermochemical and Kinetic Data	264
10.1.2	Intrinsic Reaction Coordinate Calculations	268
10.1.3	DLNO-CCSD(T) Electronic Energy Corrected Gibbs Energy for Phenol Oxidation	268
10.1.4	Flask Test	272
10.2	The Interaction of Nitrogen Heteroatomics with Sulfur	282
10.2.1	Hansen Solubility Sphere and Table of Sphere Calibration Data	282
10.2.2	Analysis of Clean Solutions	285

10.2.3	GCMS Analysis of Stressed <i>n</i> -Dodecane	286
10.2.4	Sediment Masses and Appearance of Flasks from Indole Runs	289
10.2.5	Indole Analysis	290
10.2.6	GCMS Chromatograms of Liquid-Liquid Extract from the Stress Heteroatom Solutions	296
10.2.7	LCMS areas associated with Each Species Class	305
10.2.8	Compounds Detected in LCMS Chromatograms	306
10.3	Appearance of Pyrrole and Quinoline Flasks	312
10.4	Sulfonation Barriers of Various Common Fuel Nitrogen Heterocycles .	314
10.4.1	Electrostatic Potential of Various Nitrogen Heterocycles	315
10.5	Understanding the Wall Deposition Mechanism	316
10.5.1	Relaxed Surface Terminations	316
10.5.2	Adsorption Energies	317
10.5.3	Alkane Adsorption Charge Density Difference Plots	319
10.5.4	Effect of Tail Length	321
10.5.5	Detailed Geometries Surface Structures	321
10.6	DFT Calculated Routes to Jet Fuel Deposits	328
10.6.1	IRC Calculation of the Re-aromatization	328
10.6.2	Thermochemical and Kinetic Parameters Calculated for Each Step	329
10.6.3	Comparison of Different Sites for Pyrrole and Indole	331
10.6.4	HAS Reaction Between Propanal Doublet and Various N- heterocycles	332
10.6.5	Effect of Temperature on Each Mechanism	333

List of Figures

1.1	Feedstock to fuel production pathway	5
1.2	Bulk species found in conventional distillate fuel	7
1.3	Heteroatomics found in fuel	8
1.4	Organometallic Salt in Fuel- Copper Naphthanate	8
1.5	Examples of Additives in Fuel	9
1.6	An example of a fuel driven heat exchange system within a jet engine	10
1.7	Effect of Deposits on Fuel Sprazy Nozzle Patters	11
1.8	GeneralizedAutoxidation	13
1.9	GeneralizedDeposition	14
1.10	Formation of Gum and Depletion of Oxygen in a Jet-A	15
2.1	Generic Flask Oxidizer	20
2.2	Generic Flow System Diagram	21
2.3	Alkyl Peroxyl Radical Formation Process	27
2.4	Multistep Oxidation Stages	29
2.5	Antioxidant Stabilizing Effect	30
2.6	Effect of Flow Velocity on Deposit Forming Process	31
2.7	Effect of Temperature on Oxygen in Fuels	33
2.8	Total Sulfur and Mass of Deposit in a QCM	35
2.9	Generic Thiol Structure	35
2.10	Proposed Autoxidation Pathways for Thiols	38
2.11	Generic Sulfide Structure	41
2.12	Oxidation of Sulfides	43
2.13	Generic Disulfide Structure	44
2.14	Generic Disulfide Thiophene	46
2.15	Correlation Between Total Deposits and Net Hydrogen Concentration from Acid	51
2.16	Resonance Stabilization of Phenoxy Radicals	52

2.17	Effect of Various Phenolic Constituents on the peroxy Stability . . .	53
2.18	Silylation of Phenols and its Effect on Jet-A Deposition in a QCM at 140°C	54
2.19	Products From 2,6-dimethylphenol Stressing Produced An Autoclave Autoxidizer Detected By ESI-MS	57
2.20	LIF Spectra of Jet-A Deposits and a Phenolic Resin	58
2.21	Common Nitrogen Compounds in Fuel	59
2.22	QCM Test on Exxsol D80 Solvent Doped with Various Nitrogen, Sul- fur and Phenolic Compounds	60
2.23	Proposed Reaction Pathways Between Nitrogen Species and Sulfur Species	62
2.24	Indole Coupling Products Detected by ESI-MS from an Autoclave Oxidizer	63
2.25	Wall Material Effect on Deposition in a JFTOT	65
2.26	Effect of Dissolved Copper on Oxygen and Hydroperoxide Concen- tration	68
2.27	Soluble Macromolecular Oxidatively Reactive Species (SMORS) Method of Analysis	72
2.28	SMORS Mechanism Step 1	72
2.29	SMORS Mechanism Step 2	73
2.30	Final Steps of the SMORS Mechanism	74
2.31	Predicted and Measured Oxygenated Products from a DFT Con- structed Pseudo-Detailed Mechanism	80
3.1	Potential Energy Surface	87
3.2	Example Reaction Coordinate Diagram	88
3.3	Example Potential Energy Curve Including Vibrational Levels	89
3.4	Black Body Ultraviolet Catastrophe	91
3.5	Restricted Hartree-Fock, Restricted open-shell Hartree-Fock and Un- restricted Hartree-Fock	112
3.6	Jacob's Ladder of Functionals	120
3.7	Comparison of a Slater with STO-1G,3G functions	125
3.8	A Simplified Periodic System	128
3.9	Projector Augmented Wave Method	129
4.1	Formation of the Keto-Peroxyl Radical	135
4.2	Reactions of Keto-Peroxyl Radical on the Singlet Surface	138

4.3	Reactions of Keto-Peroxy Radical Yielding non-quinone Products . . .	140
4.4	Proposed SMORS EAS Step	141
4.6	Acid Catalyzed EAS Step Calculated at the B3LYP//cc-pVTZ <i>n</i> - dodecane PCM Level of Theory.	144
4.7	Generalized Homolytic Aromatic Substitution Mechanism	145
4.8	Homolytic Aromatic Substitution Mechanism Applied to the SMORS Indole + Quinone Substitution Step	146
4.9	HAS Step Calculated at the B3LYP//cc-pVTZ <i>n</i> -dodecane PCM Level of Theory	148
4.10	150
4.11	Modified SMORS Mechanism: Quinone Production Pathway	152
4.12	Modified SMORS Mechanism: Coupling Mechanisms Between Indole and Quinone	152
5.1	Relative Peak Areas of The Deposit Species Classes for the Indole Sulfur Surrogates	162
5.2	Examples of Compounds Detected in the Indole Oligmer Compound Class	163
5.3	Examples of Compounds Found in the Indole-Sulfur Oligmer Class . .	165
5.4	Examples of Compounds Found in the Oxidized Sulfur Class	166
5.5	Mechanism of SO ₃ Production in Fuels	166
5.6	Examples Of Compounds Found In The Alkylated Indoles Compound Class	167
5.7	GCMS Chromatogram of the Solutions of Pyrrole, Pyrrole + Dode- canethiol, Quinoline, and Quinoline + Dodecanethiol After 8h Stress- ing at 140 °C	169
5.8	Selected Putative Structures From The Compounds Detected By Lcms Detected In The Pyrrole And Pyrrole+Dodecanethiol Deposit	171
5.9	Selected Putative Structures From The Compounds Detected By Lcms Detected In The Quinoline Deposit	172
5.10	Proposed Mechanism Of Acid Catalyzed For 5-membered Nitrogen Heterocycles In Fuel	175
6.1	Stainless Steel Surfaces Used in Study	183
6.2	Map Of Constituent Elements Detected via EDX analysis of Deposit Corresponding to an Arbitrary Point in an AFTSU Burner Feed Arm	187

6.3	Adsorption Energies Calculated Using Optpbe For The High Coverage Metal-terminated and Oxygen-terminated Stainless-Steel Surfaces.	189
6.4	Chemisorbed geometries in our tests including charge density difference plots,	190
7.1	HAS Reactions Considered for Fuel Coupling Reactions.	199
7.2	Comparison of Different HAS Pathways at the B3LYP-D3//cc-pVTZ Level of Theory	200
7.3	Effect of Oligomer Unit Size on Solubility Calculated Using the HSPiP Software	202
7.4	H-abstraction Sites and Dimers Selected for the Pseudo-Detailed Mechanisms	204
7.6	O ₂ Depletion Behavior of our Surrogate- Comparison Between Model and Experiment	208
7.7	Insoluble Formation Behavior of Our Surrogate Fuels- Comparison Between Model and Experiment	211
7.8	Blending Effect of HAS Model	212
7.9	Sensitivity Analysis of the Bespoke Insoluble Pseudo-Detailed Mechanisms	213
7.10	Change in the Concentration of Insolubles and ROOH Over the Course of the 24h Psuedo-Detailed Models	214
10.7	HSPiP Sphere	283
10.8	HSPiP Sphere Parameter Fits	283
10.9	Clean Indole GCMS Analysis	285
10.10	Clean Indole + Hexyl- <i>n</i> -Sulfide GCMS Analysis	285
10.11	Clean Indole Hexyl- <i>n</i> -Disulfide GCMS Analysis	286
10.12	Clean Indole Dodecanethiol GCMS Analysis	286
10.13	Clean <i>n</i> -dodecane GC Chromatogram	287
10.14	Stressed <i>n</i> -dodecane GC Chromatogram Run 1	287
10.15	Stressed <i>n</i> -dodecane GC Chromatogram Run 2	288
10.16	GC Relative Peak Intensities of Oxygenated Species Detected By MS in <i>n</i> -dodecane Stressed for 24 h at 140 °C	288
10.17	Visual Comparison of the Indole, Indole+Hexyl Sulfide, Indole+Hexyl Disulfide and Indole+Dodecanethiol Flasks	289
10.18(+)	LCMS Chromatogram for Indole 0.1 mol L ⁻¹ Deposit Dissolved in Trisolvent	292

10.19	Selective Putative Structures Found in (+)LCMS from the 8h Indole	293
10.20	(-)LCMS Chromatogram for Indole 0.1 mol l ⁻¹ Deposit Dissolved in Trisolvent	293
10.21	Selective Putative Structures Analyzed Found un (-)LCMS from the 8h Indole Run	294
10.22	LLE Enhanced GCNS Chromatogram from yhe 8h Indole 0.1mol L-1 Solution Analysis.	295
10.23	GCMS Analysis of the Solution from the of LLE Concentration Enhanced Indole And Sulfur + Indole Test	296
10.24	GCMS Analysis of the Solution from the of LLE Concentration Enhanced Indole and di- <i>n</i> -hexylsulfide 8 h Test	302
10.25	GCMS Analysis of the Solution from the of LLE Concentration Enhanced Indole and di- <i>n</i> -hexyldisulfide 8 h Test	303
10.26	GCMS Analysis of the Solution from the of LLE Concentration Enhanced Indole and Dodecanethiol 8 h Test	304
10.27	(+)LCMS Chromatograms of the Deposit from the of Indole and Sulfur + Indole Surrogates	305
10.28	(-)LCMS Chromatograms of the Deposit from the Indole and Sulfur + Indole Surrogates	306
10.29	LCMS(+) Chromatograms of the Dissolved Pyrrole and Pyrrole + Dodecanethiol Deposit	309
10.30	LCMS(-) Chromatograms of the Dissolved Pyrrole and Pyrrole + Dodecanethiol Deposit	310
10.31	LCMS(+) Chromatograms of the Dissolved Quinoline And Quinoline + Dodecanethiol Deposit	310
10.32	LCMS(-) Chromatograms of the Dissolved Quinoline And Quinoline + Dodecanethiol Deposit	311
10.33	Visual comparison of the Pyrrole + Dodecanethiol, Pyrrole, Quinoline + Dodecanethiol, and Quinoline flasks	312
10.34	ESP of Various Protonated Nitrogen Compounds	316
10.35	Relaxed metal-terminated Fe ₂ O ₃ (brown atoms), metal-terminated Cr ₂ O ₃ (blue atoms), oxygen-terminated Fe ₂ O ₃ and oxygen-terminated Cr ₂ O ₃ from left to right	317
10.36	Charge Density Difference Plots Showing Ethane Ethane Adsorbed Onto Transition Metal-Terminated Stainless Steel	319

10.37	Charge Density Difference Plots Showing Ethane Adsorbed Onto Transition Oxygen-terminated Stainless Steel	320
10.38	Effect Of Tail Length on the Adsorption Energy of Sulfonic Acid Adsorbed onto Metal Terminated Fe ₂ O ₃	321
10.39	Charge Density Plots of Oxygenated Species Adsorbed on Metal Ter- minated Stainless Steel	322
10.40	Charge Density Plots of Oxygenated Species Adsorbed on Oxygen Terminated Stainless Steel	323
10.41	Charge Density Plots of Indigenous Sulfur Species Adsorbed on Metal Terminated Stainless Steel	324
10.42	Charge Density Plots of Indigenous Sulfur Species Adsorbed on Oxy- gen Terminated Stainless Steel	325
10.43	Charge Density Plots of Sulfur Acids Adsorbed on Metal Terminated Stainless Steel	326
10.44	Charge Density Plots of Sulfur Acids Adsorbed on Oxygen Termi- nated Stainless Steel	327
10.45	ROOH re-aromatization of the Σ -intermediate	328
10.46	ROH re-aromatization of the σ -intermediate	329
10.47	Potential Energy Surface for the Pyrrole Coupling at the C2 Position, Comparing H-abstraction at the N1 or C2 Position	331
10.48	Potential Energy Surface for the Indole Coupling at the C3 Position, Comparing H-abstraction at the N1 or C3 Position	332
10.49	Propanal Doublet Has Attack Step Pathway Calculated at the B3LYP- D3//cc-pVTZ Level of Theory	333
10.50	Effect of temperature on the Concentration of Deposits in the Indole Deposition Mechanism	334
10.51	Effect of temperature on the Concentration of Deposits in the Pyrrole Deposition Mechanism	335
10.52	Effect of temperature on the Concentration of Deposits in the Quino- line Deposition Mechanism	336
10.53	Effect of temperature on the Concentration of Deposits in the Naphth- alene Deposition Mechanism	337
10.54	Effect of temperature on the Concentration of Deposits in the Phenol Deposition Mechanism	338
10.55	Effect of temperature on the Concentration of Deposits in the Toluene Deposition Mechanism	339

Nomenclature

Abbreviations

AFTS	Aviation Fuel Thermal Stability
AO	Atomic Orbital
ASTM	American Society for Testing and Materials
CAN 3.23	Canadian Jet Fuel Specification
CFD	Computational Fluid Dynamics
DEF STAN	UK Defence Standardisation
DFT	Density Functional Theory
EAS	Electrophilic Aromatic Substitution
EIP	Extraction Induced Precipitation
ESI	Electrospray Ionisation
ESP	Electrostatic Potential
FT	Fischer-Tropsch
GC-MS	Gas Chromatography Mass Spectroscopy
HAS	Homolytic Aromatic Substitution
HF	Hartree-Fock
IPA	Independent Particle Approximation
LC-MS	Liquid Chromatography Mass Spectroscopy
LIF	Laser Induced Fluorescence

LLE	Liquid-Liquid Extraction
MO	Molecular Orbital
MS	Mass Spectroscopy
PAW	Projector-Augmented Wave
PCM	Polarizable Continuum Model
QCM	Quartz Crystal Microbalance
SAM	Self-Assembled Monolayer
SEM	Scanning Electron Microscope
SMORS	Soluble Macromolecular Reactive Species
SPE	Solid Phase Extraction
SS	Stainless Steel

Roman Letters

MB/D	Millions of Barrels Per Day
-------------	-----------------------------

Chapter 1

Introduction

1.1 Jet Fuels and Energy

Energy generation and supply is an essential component of our modern industrial lives. As of 2017, burning of oil represented 31.7% of the worlds energy production with air transportation using 7.5% of that consumption. Oil demand for aviation reached 6 MB/d in 2016 and is expected to rise to 8.9 MB/day by 2040 [1]. As the world begins to face the problems of climate change driven by anthropogenic CO₂ generation and depletion of fossil fuel reserves, the array of sources from which we derive energy has expanded out of necessity. Since 1973, reliance on natural hydrocarbon reserves has fallen from making up almost 100% our energy supply to $\approx 75\%$ of the total in 2015, with increasing energy sources being derived from nuclear and bio-fuels.[2] There is also increasing intergovernmental pressure on industry itself to move towards carbon neutrality [3].

In general, emissions can be defined as being from:

1. Point sources, where the emissions are localized, e.g. a coal power plant stack.
2. Mobile sources, where the emissions are produced from a moving source e.g. a car exhaust.[4]

Decarbonization of point sources has already gained significant momentum with viable alternatives like nuclear power being well established and renewable generation increasingly cost effective.[5] With regards to mobile sources, trains have undergone electrification across many countries and commercial electric cars are becoming increasingly common. However, the prospect of CO₂-free generation for aircraft is still

beyond the horizon due to the limitations of technological alternatives to traditional kerosene-powered gas turbines. These alternatives include:

- Hydrogen-powered aircraft, which have faced issues of safety as well as volume of storage required for fuel. Although hydrogen is almost 3 times as energy dense than kerosene it requires 4 times the volume of storage [6].
- Electrified aircraft, which if powered by batteries or solar power, face serious energy density issues, even with extrapolated projected improvements within the next 50 years.[7]

It is clear that for the foreseeable future conventional jet fuels will remain as the main energy source for air travel. Mitigation of the environmental and supply issues instead focuses on the production of the fuel itself, which will be discussed in the next section.

1.2 Jet Fuels and Aviation

During the first few years after the development of the jet engine, the fuel of choice was a mixture of kerosene and gasoline known as a 'wide cut'. This was discarded in the 1970s for a purer kerosene fraction due to the unfavorable vaporization of gasoline at higher altitudes. This led to the development from the JP-4 wide cut to the JP-8 kerosene cut. Within the commercial sector, wide cuts (Jet-B) are still used in certain areas where gasoline blends offer favorable performance in colder climates (Jet-A-1) but again kerosene majority blends (Jet-A) dominate.[8]

Now the industry is fully established across the globe, aviation is an important sector in the world economy. In 2018 \$871 billion was spent on air travel, an increase of 5.3% from the previous year; further consistent growth is expected into the future. Aviation represents roughly 1% of global GDP, up from 0.9% in 2016. From a logistical point of view, the aircraft industry transports 4,358 million passengers per year. Kerosene, its operation within jet engines and its production is an integral part of this industry, with 356 billion liters of kerosene burnt in 2018.[9]

Kerosene itself refers to a specific fraction of distilled crude oil between the boiling range of 205 °C-260 °C.[10] Depending on its source it can have a wide variety of chemical compositions. Jet fuel originating from crude typically has a composi-

tion of 20% n-alkanes, 40% iso-alkanes, 20% cycloalkanes, and 20% aromatics.[11] Synthetic jet fuels, like Fischer-Tropsch derived fuels, are generally composed of a greater number of straight chain alkanes and fewer aromatics. Moreover, biofuels are highly dependent on their feedstocks.[12] The composition of jet fuels will be discussed in detail in section 1.3.1.

Fuel composition allowances are tightly controlled by a series of governmental bodies, and require an extensive approval process by the American Society for Testing (ASTM) International Committee, which has historically taken up 10 years for a new fuel pathways of production to be approved.[13] This is done to ensure the new jet fuel has the desirable physical and chemical properties to operate safely and economically within existing jet engine designs. Currently, there are a number of alternative fuels approved for usage within jet engines, including a 50/50 mix of conventional Jet A-1 fuel with Fischer-Tropsch produced fuel.[14]

Commercially, jet fuel is available in a number of grades which broadly fall into civil or military usage. Their categorization can be defined based on the demands of their local climate, engine specifications, or particular fuel chemistry or even a combination of these categories. Table 1.2 summarizes some of the most common grades with their specifying bodies shown alongside.

In order to meet the different requirements the properties can be modified by changing the bulk hydrocarbon concentration, as seen with Jet-B where a wider cut allows for a lower vapor pressure and a lower freeze point. Alternatively, as is seen with JP-8+100, additives can be added to the fuel to help improve thermal oxidative stability.

Fuel	Specifying Bodies	Remarks
Jet A-1	UK Specification DEF STAN 91-91 and ASTM specification D 1655	Common outside of the USA, commercial jet fuel. Flash point of 38 °C. Freeze point minimum -47°C
Jet A	ASTM D 1655	Only available in the USA. Higher freeze point of -40°C . Commercial.
Jet B	ASTM D 1655 and CAN 3.23	Wider cut, with a lower vapor pressure, which improves cold starts. Commercial. Freezing point at -50°C .
JP-8	NATO Code F-34	Dominant military jet fuel for NATO forces. Equivalent to Jet A-1 with addition of corrosion inhibitor and anti-icing component.
JP-8+100	NATO Code F-37	JP-8 with additional antioxidants
TS-1	Russian Jet A-1 specification GOST 52050-2006	Russian grade with lower freeze point of -57°C and low flash point of 28°C

Table 1.2: Key Jet Fuel Grades Available Worldwide [15]

1.3 Origins and Composition of Jet Fuel

Jet fuel can be classed as being derived from renewable and non-renewable feedstocks.[10] Non-renewable feedstocks refer to fossil fuels, most typically crude oil, which undergoes distillation and refining processes. Renewable feedstocks refer to sources that are replenishable in the short term (see Figure 1.1). Consequently, fuel derived from these feedstocks are termed Sustainable Aviation Fuels (SAFs).

Distillation refers to the boiling of crude oil under atmospheric or vacuum conditions, where different 'fractions' condense at different temperatures. The most common fraction within jet fuel, kerosene, falls in the $145-300^{\circ}\text{C}$ condensation range. It typically has a carbon chain length ranging from $\text{C}_9\text{-C}_{16}$. [18] Fuel produced directly from distillation is known as "straight run" fuel.[19]. Heavier fractions, longer chains, can be 'cracked' to shorter hydrocarbons using high temperatures and/or a catalyst.

Natural gas and coal feedstocks also fall under the definition of non-renewable sources. They can be converted to jet fuel using the Fischer-Tropsch (FT) pro-

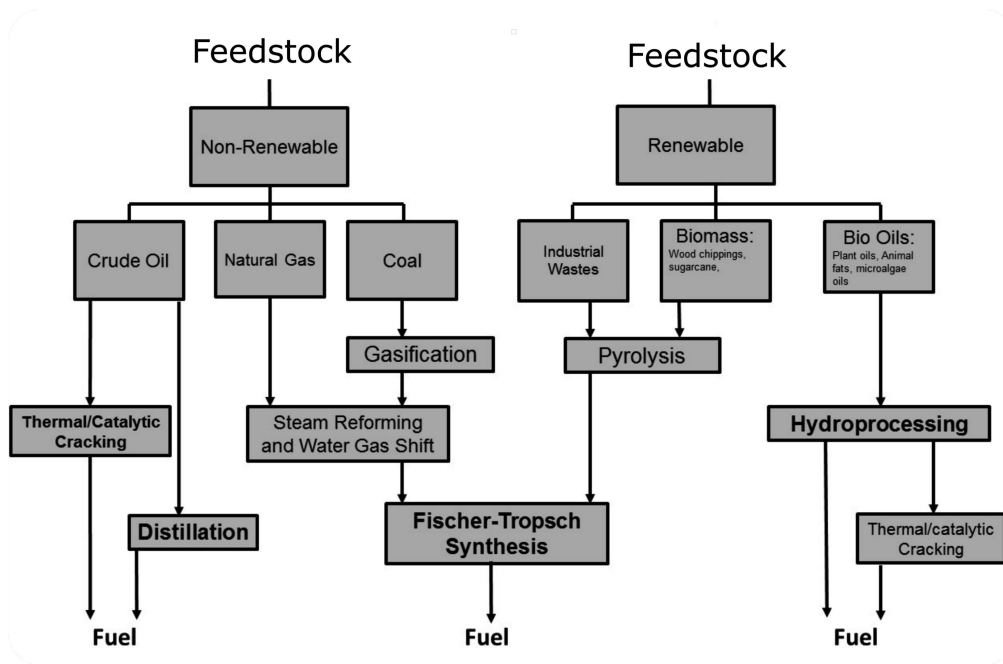
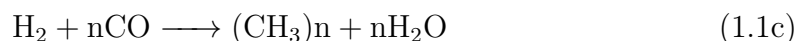


Figure 1.1: A simplified overview of the various feedstocks and production pathways [16, 17]

cess in a series of sequential steps:



Adjusting processing conditions in the FT process gives excellent control in reproducing the kerosene fractions as well as the degree of branching and presence of impurities. In contrast, fuel from natural crude oil produced via distillation tend to be more heterogeneous in their composition and hydrocarbon mix.[16] This will be elucidated in the next section.

Renewable feedstocks are commonly derived from three main sources: industrial/municipal wastes, biomass and bio oils (Figure 1.1). Since many renewable fuels originate from biological matter, they allow for a carbon recycle loop appreciable in a human lifetime. As a consequence, they are often described as being carbon neutral.[20] However, this is frequently disputed since the production of such fuels is often more

carbon-intensive than the carbon offset which it provides.[14] Renewables have the distinct advantage in that their production is not limited to any particular location, so many security-of-supply issues can be overcome. [21]

Solid wastes undergo a conversion process known as pyrolysis whereby they are heated under high temperature (500°C) and pressure. This process breaks down longer chain hydrocarbons in the wastes to shorter chains to form oils or gases. These can be sent to FT conversion processes to form jet fuels.[22] Bio-oils, from animal and plant sources, have also received attention as a renewable source of fuel. Waste grease, animal fats, vegetable oils, and algal oil have all been used to produce jet fuel. The main production route, known as hydroprocessing, involves removing oxygen from the fatty acids and esters in these oils to produce shorter chain hydrocarbons via reaction with hydrogen gas. Water is produced as a by-product. These can be cracked and broken down further to produce carbon chains of optimum length for jet fuel.[23]

1.3.1 Composition of Fuels

1.3.1.1 Conventional Distillate Fuels

Due to the heterogeneous nature of crude oil, fuel produced via distillation contains thousands of species.[8] Naming each one would become intractable, as a consequence it is better to group them into categories based on similar chemical properties.

First, the bulk component in fuel comprises alkanes, alkenes, and aromatic compounds. Their composition is summarized in Figure 1.2. *N*-alkanes refer to straight-chain alkenes whereas iso-alkanes are branched, cyclo-alkanes refer to non-aromatic saturated compounds.[24] The average alkane chain length is C12.[25] *N*-alkanes have higher freeze points due to greater Van der Waals forces between the molecules as they are able to pack more tightly than iso-alkanes. However, the high lubricity of *n*-alkanes makes pumping more difficult, therefore most fuels also contain iso-alkanes. The aromatics present are of a wide variety, and can include polycyclic aromatic rings, such as naphthalenes.[26] Aromatics are known to improve lubricity as well as improve seal swelling.[27]

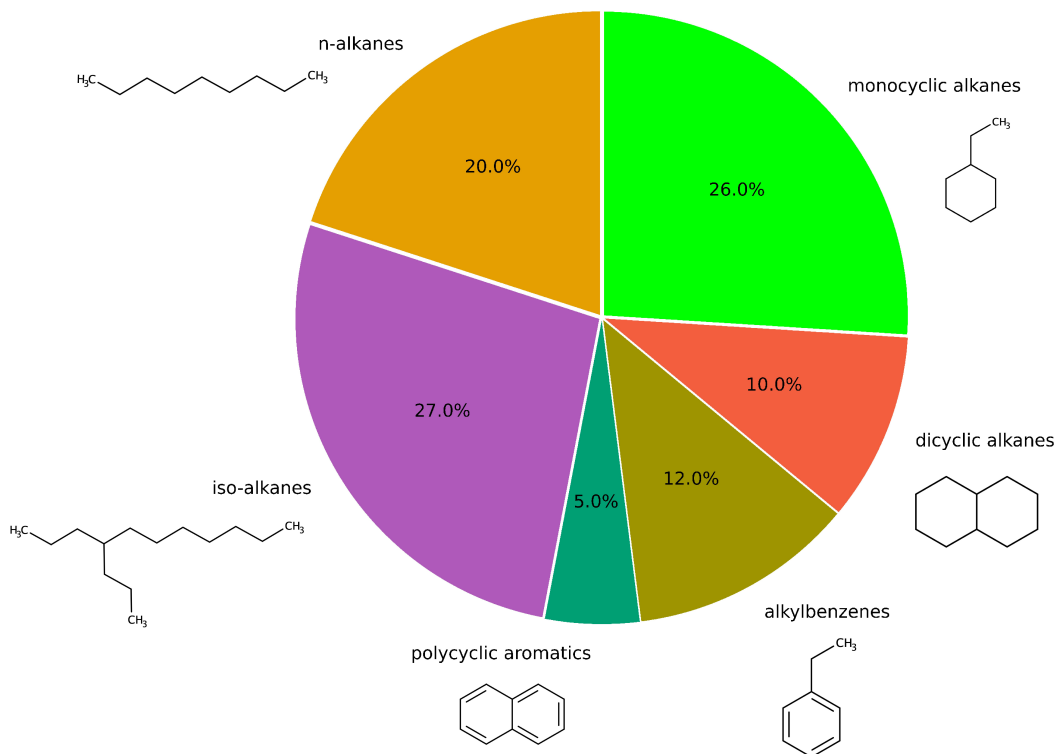


Figure 1.2: Bulk species found in conventional distillate fuel, average of 48 locations across the world, adapted from [28]

The minor components consist of heteroatomic impurities and additives. Heteroatomics represent a wide variety of compounds. They have a large effect on thermal-oxidative stability, even though they represent less than 1% of fuel composition.[29] They can be split into polar species, sulphur species, nitrogen containing species, and metals. Polar species include phenols and hydroperoxides. They get their polarity from oxygen containing functional groups like carbonyl and hydroxyl groups. Nitrogen species include aromatics like indoles and carbazoles. Sulphur can be present in both elemental form and within organic molecules like thiols and sulfides.[24, 29]

A number of metals are known to be present in conventional distillate fuels. These include copper, manganese, magnesium, iron and zinc, present in the ppb-ppm range.[30] It has been noted that where the copper concentration is high the

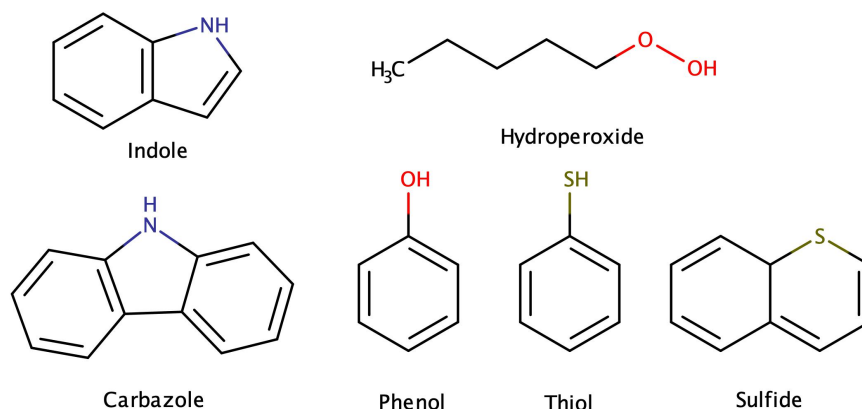


Figure 1.3: Examples of heteroatomics found in fuel

manganese concentration tends to be lower.[24]

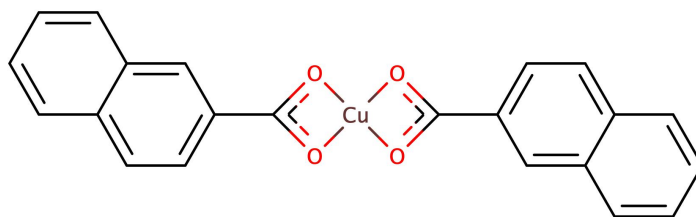


Figure 1.4: Organometallic Salt in Fuel, Copper Naphthanate

Along with the components naturally found in fuel, a number of additives are seen in military grade fuels. Dispersants, icing inhibitors, metal deactivators and antioxidants are all present in the JP-8+100 package, and can all be classified as thermal stability enhancers.[31, 15, 32].

1.3.1.2 Hydroprocessed and Fischer-Tropsch Produced Fuels

In contrast to conventional distillate fuels, the production methods of hydroprocessed and FT fuels results in simpler mixtures, with fewer constituent compounds.[33] FT and hydroprocessed fuels tend to be formed of mainly iso and normal alkanes. However, the composition is heavily dependent on the production pathway. Cycloalkanes also feature in small quantities in certain FT blends, such as Sasol IPK.[14] A jet fuel arising from hydroprocessed cellulose matter can contain aromatics.[34] Hydroprocessed and FT fuels in general contain almost no heteroatomics.[33]

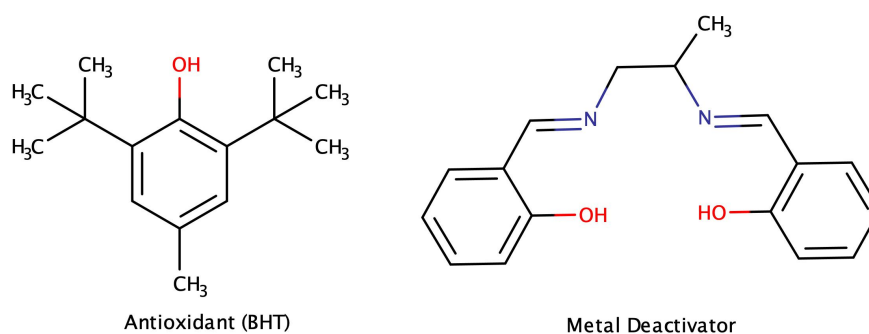


Figure 1.5: Examples of Additives Within Fuel

1.4 Jet Fuels and Thermal Oxidative Stability

Jet engines produce heat during their operation. To cool the engines a combination of airflow and unburnt fuel is used.[33] In supersonic aircraft where air friction presents another heat source and the use of air cooling systems are limited, fuels are put under even greater thermal stress.[35] Cooling is essential to prevent thermal expansion of components, which is detrimental to the safe operation of the engine. However, not only components need to be cooled, oil within the jet engine system also undergoes extensive temperature increases due to heat of friction generated by moving parts. Fuel cooling systems play a direct role by cooling the oil with heat exchangers to deal with excess heat (Figure 1.6).

In the future there will be an increasing need to boost the thermal efficiency of jet engines, allowing aircraft to consume less fuel per km as well as boosting power outputs. However, this will increase the heat load on components and lead to greater thermal stressing of the fuel.[36] Greater heat loads can lead to a series of chain reactions initiated by oxygen, known as autoxidation. The outcome of these reactions is that fuel-insoluble deposits within the engine will begin to form.[32] The ability for a fuel to resist oxidative deposition is known as thermal oxidative stability. Thermal oxidative deposition occurs between the temperature ranges of 150–425 °C. At higher temperatures pyrolytic thermal decomposition occurs which can also lead to deposits.[37] However, this thesis is primarily concerned with the oxidative region of deposition.

Since 2000 deposits formed from autoxidation reactions have been known to block

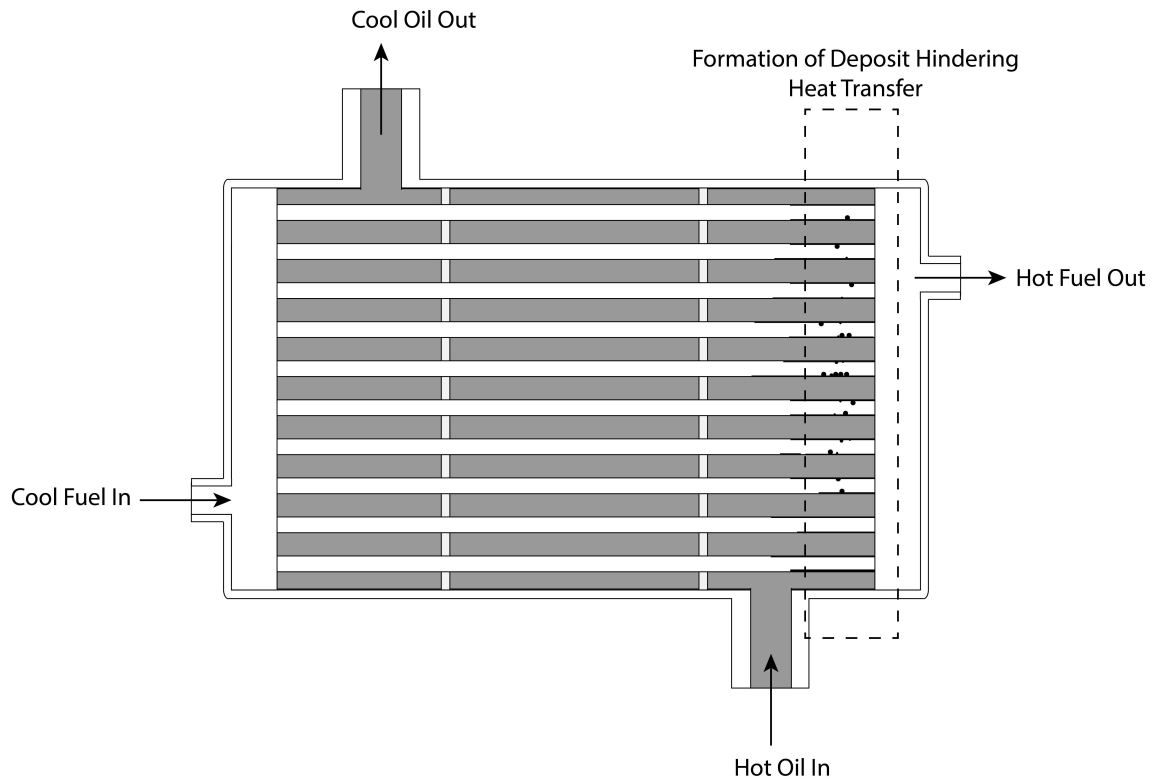


Figure 1.6: An oil cooling system where unburnt fuel acts as the heat sink.[13]

filters at an increasing rate.[38] These blockages are often caused by insoluble solids originating from thermal oxidative instability, which deposit on the mesh fuel filters. Thus, it is possible for contaminants to shut down the engine, if abnormal engine performance is noticed by the pilot after the bypass has been opened.[39].

Deposits can also decrease heat exchanger efficiency in parts of the aircraft where fuel is used as a coolant. Deposits can begin to foul the walls of the matrix assembly, shown in Figure 1.6. Even a small carbonaceous layer forming on the walls of heat exchangers can have a dramatic effect. For example, at 500°C the conductivity of thermal coke is around 3000 times lower than that of copper.[33] In other parts of the aircraft, insolubles can create irregular fuel injector nozzle spray patterns by blocking small apertures or distorting the shapes of the exit channels.[40] This results in fuel not correctly reaching optimum mixing zones as shown in Figure 1.7. This can result in asymmetric temperature zones in the engine. Irregular temperature zones lead to in poor engine efficiency, as well as compromising safe engine operation. Furthermore, deposits have the potential to block up pipes within the engine architecture leading to system failure.[41] Deposition throughout pipes and injector nozzles increases the rate of servicing required to clean the engine. Finally,

autoxidation products have been suggested to increase particulate emissions.[42]

To understand these issues in more detail, it is necessary to build up a detailed chem-

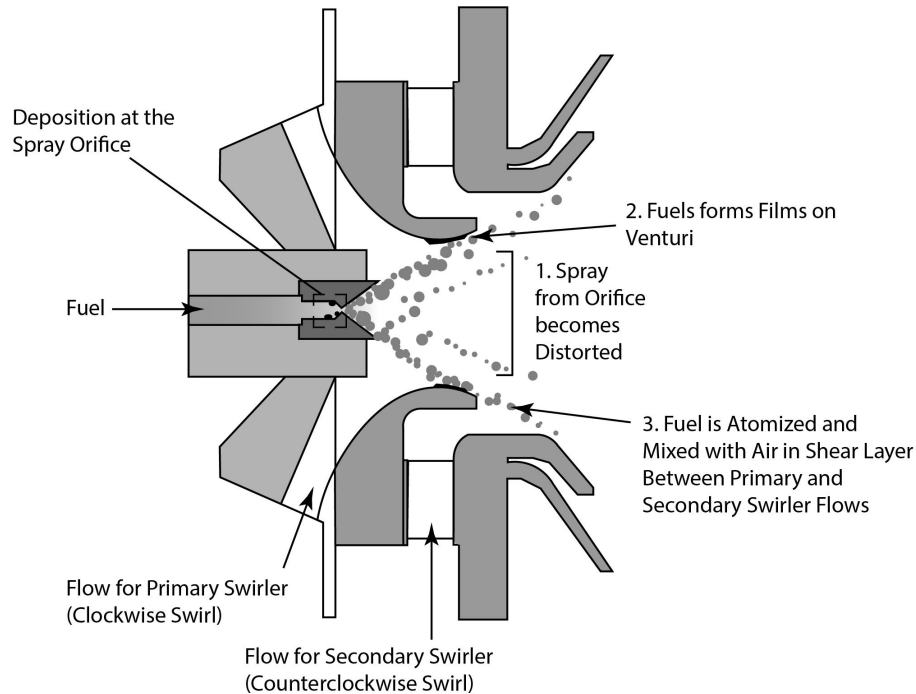


Figure 1.7: The Effect of Deposits on Fuel Spray Nozzle Patterns [40]

ical mechanism of the deposit formation. Detailed chemical mechanisms will allow researchers to devise ways to minimize their formation and impact. Furthermore, the importance of understanding the mechanisms behind deposition will increase since conventional fuel stocks are becoming increasingly heterogeneous in their chemical composition with lower thermal stability.[43] By contrast, the increasing uptake of low-heteroatom SAF will likely be blended with conventional aviation fuel, which often leads to non-linear deposition behavior.[44] Deeper chemical understanding of deposition will enhance understanding of these blends. Finally, a detailed chemical mechanism will be able to be integrated into computational fluid dynamic (CFD) simulations to predict deposit formation over time within complex geometries.

1.5 Generalized Deposition Process

The formation of autoxidative deposits in/on critical fuel components has received considerable attention since the 1950s. A greater understanding of the deposition process leads to greater predictive and preventative capabilities. Engine designers

are able to integrate mechanisms into computational fluid dynamics (CFD) software and locate the magnitudes and location of deposits,[45] depending on the accuracy of the chemical kinetic model supplied. The accuracy of deposition models are a function of a number of crucial points: understanding of what chemical reactions are responsible for deposition, accurate thermochemical rate parameters and appropriate sensitivity to starting conditions. Of course, the accuracy of the mechanism can also be limited by the size of the mechanism, which is limited by the computational resources available. In order to simplify models without compromising predictability, appropriate mechanism reduction techniques can be applied such as lumping [46] and grouping species into classes.[24] However, this thesis is primarily concerned with elucidating the chemical reactions leading up to deposition, with emphasis on the agglomeration of reactants leading to deposits.

The deposition process has been described as a multi-step mechanism.[47] Recent work [38, 48] has added increasing evidence to this postulation, with the deposition process being characterized by an initial rapid autoxidation stage forming a number of oxidatively-reactive products followed by the agglomeration of these products into larger molecular weight species.

The generalized autoxidation mechanism is presented in Figure 1.8. Step **1** shows the formation of an alkyl radical ($R\cdot$) from the bulk fuel. This happens via a poorly-understood initiation step, which is believed to be related to the catalytic characteristics of the fuel wetted surface.[49] This alkyl radical subsequently reacts with dissolved oxygen (O_2), leading to the formation of a peroxy radical ($ROO\cdot$). In step **2** the peroxy radical ($ROO\cdot$) will abstract hydrogen from indigenous bulk fuel compounds (RH), leading to an alkyl radical ($R\cdot$) and a hydroperoxide molecule ($ROOH$). Chain-breaking phenolic antioxidants (AH) can also undergo hydrogen abstraction, forming stable radical species ($A\cdot$), which are thought to participate in the formation of insoluble species in the later stages of fuel thermal degradation.[24] In step **3** heteroatomic species (such as nitrogen and sulfur-containing species) are oxidized *via* reactions with hydroperoxides ($ROOH$). Of these heteroatoms species, indigenous sulfur compounds are shown to be strongly deleterious to fuel thermal stability. In particular, thiols [50, 51, 52], successively react with hydroperoxides to form sulfenic ($RSOH$), sulfinic ($RS(=O)OH$) and sulfonic ($RS(=O)_2H$) acids.[53, 54] At step **4** unreacted hydroperoxides will readily undergo homolytic fission in the presence of dissolved metals and/or heat, forming hydroxyl ($RO\cdot$) and alkoxy ($HO\cdot$)

radicals.[55] At step 5 alkoxy ($\text{RO}\cdot$) and hydroxy ($\text{HO}\cdot$) radicals individually react with bulk fuel (RH), resulting in water and oxygenated compounds including ketones/aldehydes (RHO), alcohols (ROH) and carboxylic acids (RCOOH).[24]

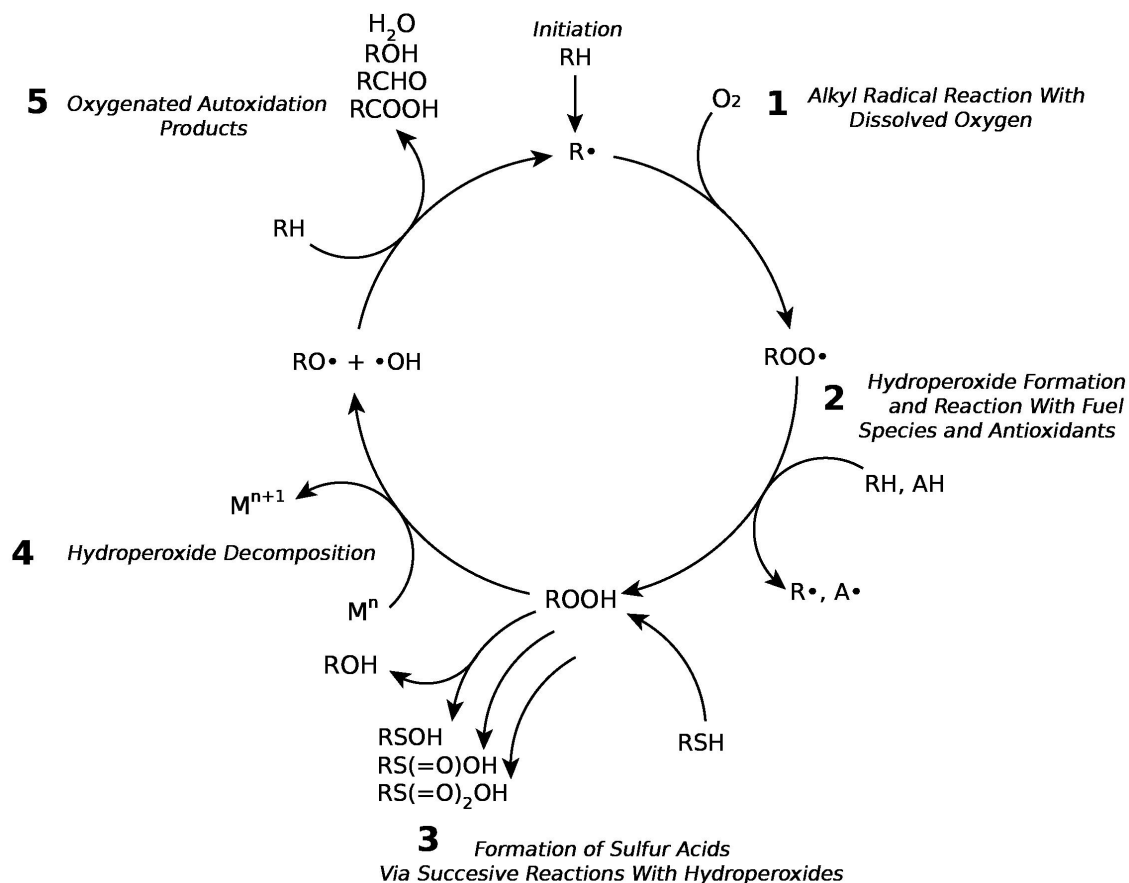


Figure 1.8: Generalized Autoxidation Mechanism

From a macro-molecular perspective deposition/fouling reactions occur at the wall and within the bulk, demonstrated in Figure 1.9. It is thought that soluble (**A**) and insoluble (**B**) oxidized species formed in the bulk diffuse the the wall layer and adhere to the wall. There is also the growth of deposits directly on the wall from surface reactions, these reactions are exacerbated by the fact that the fuel at the wall experiences much greater residence times.[45] The formation of insoluble species **B** in the bulk and at the wall eventually adhere to the wall forming deposit species **C**.

The initial stage of autoxidation has been well studied [57, 58] and the prod-

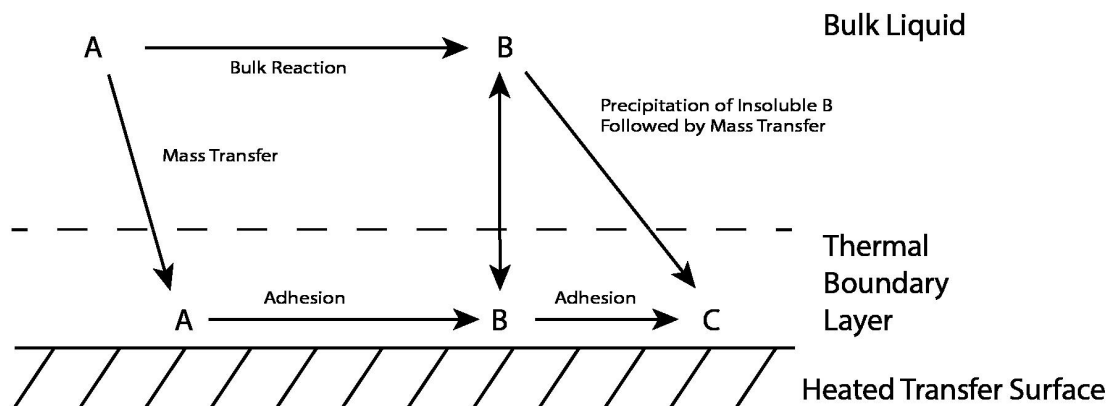


Figure 1.9: Generalized scheme for chemical fouling presented in [56]

ucts arising from the autoxidation from many species found in jet fuel have been measured.[59, 20, 60] The second stage, the agglomeration of autoxidation products, has received considerably less attention. This is reflected in the existing chemical mechanisms [24, 38] which are mainly composed of autoxidation reaction steps compared to a small number of highly-generalized one step reactions leading to deposits in both the bulk and on the wall. Only the most recent mechanism [61] presented in the literature begins to add more details to the agglomerations steps, with a number of pseudo-species detailing a multi-step pathway to deposits. In order to build more robust models a greater understanding of the reactions leading to deposits is required, with an understanding of the final deposit structure forming a key part of this task.

The existing dominant theory [24] for the formation of deposits states that antioxidants, namely heteroatomic species, are involved in the agglomeration reactions responsible for deposits. The involvement of antioxidants in deposition highlights the importance in understanding the distinction between autoxidation and deposition. Antioxidants have been shown to increase deposition but slow down the autoxidation process, and this has been highlighted in the inverse relationship between oxygen consumption (rapid oxygen consumption meaning rapid autoxidation) and total deposits for various fuels.[62] This inverse relationship is demonstrated by Fig-

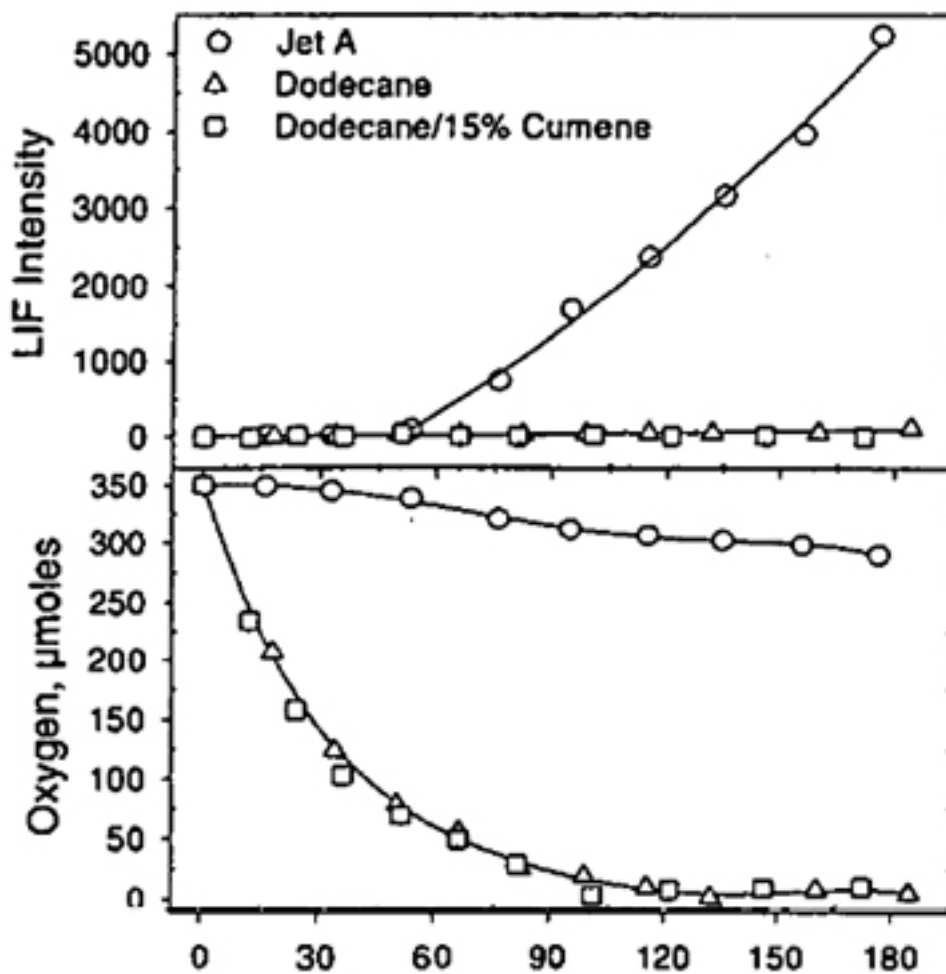


Figure 1.10: Formation of gum, depletion of oxygen and formation of hydroperoxides in a Jet-A, Dodecane and Dodecane/15% Cumene [52]. Laser induced Fluorescence (LIF) intensity corresponds to the formation of deposits.

ure 1.10. Here, a pure *n*-dodecane (average alkane chain length of jet fuel) oxidizes far more rapidly than a conventional jet-A and yet produces no deposits (deposits correspond to LIF intensity), and vice versa. Nevertheless, there are exceptions to this rule. For example, nitrogen containing species often have little/no effect on the rate of deposition, and yet have consistently been shown to increase deposition.[63] Adding complexity to the picture is the synergistic deposition enhancement between species, particularly seen between nitrogen and sulfur-containing species.[64]

Particular emphasis has been placed on phenol as an antioxidant responsible for deposition.[65] As to what form these reactions take place, only the SMORS mech-

anism provides a theory.[32] The SMORS mechanism was formulated on characterization work based on diesel deposits. Later characterization work has attempted to add credence to this mechanism.[38, 66] However, the SMORS theory has received little mechanistic scrutiny.

In recent years quantum chemistry has emerged as a powerful tool to understand fundamental molecular interactions. As a consequence, it has enabled researchers to explore complex reaction mechanisms which would be difficult to achieve in an experimental setting. Nevertheless, the role that experiments play is still important. Real and surrogate fuels can be thermally stressed in controlled settings, allowing deposits to be characterized. Retrosynthetic techniques can then be used to propose mechanisms based on the structures characterized. It is the aim of this thesis to use these tools to gain a more fundamental understanding of the agglomeration and deposition process. Emerging from these findings will be a deeper knowledge of how the chemical composition of current and future fuels affect the deposition process.

1.6 Thesis Outline

- Chapter 9 will present published work from this thesis.
- Chapter 2 will present a detailed literature survey, where the research questions of this thesis will emerge.
- Chapter 3 will present the quantum chemistry theory relevant to the calculations performed in this thesis.
- Chapter 4 will present modelling and experimental work on the SMORS mechanism.
- Chapter 5 will present experimental work on the synergistic effects of nitrogen and sulfur compounds in fuel.
- Chapter 6 will present modelling work on fuel-surface interactions.
- Chapter 7 will present work using DFT methods to predict the formation of insolubles from thermal oxidative reactions.
- Chapter 8 will present a general discussion on the work performed, future work and conclusions.

- Chapter 10 is the appendix, where extra information for each chapter is presented in sections.

Chapter 2

Literature Review

This literature review is split into three sections. Firstly, the experimental and computational methods used to investigate thermal oxidative stability will be explored. An understanding of the advantages and disadvantages of experimental rigs is essential to critically evaluate studies attempting to understand thermal stability. Additionally, an understanding of the existing methods helped to inform the design studies in this thesis. The second section will review papers trying to understand the variables, both chemical and physical, affecting deposition. In addition, proposed chemical and physical pathways to deposit will be reviewed. The third section will then review the existing attempts to generalize the deposition process for predictive purposes. Additionally, the third section will explore limitations of existing generalized mechanisms, in the context of the existing understanding of fuel deposition factors explored in section 2. These limitations, will allow the key research questions of this thesis to emerge.

2.1 Methods used to Investigate Thermal Stability

2.1.1 Experimental Methods for Investigating Autoxidation and Deposit Formation

To understand the processes behind jet fuel thermal degradation, rigorous testing procedures and apparatus have been designed. It would be impractical, costly, and dangerous to rely on in-flight tests to generate conditions for deposit formation. Additionally, there would be little control of variables like temperature and pressure. As a consequence, rigs of varying size and complexity have been designed; from small-scale static rigs, to medium-scale flowing rigs and finally large scale rigs. This

section will elucidate the experimental test methods that have been employed to study jet fuel.

2.1.1.1 Static Rigs

The term static tests refers to tests where small volumes of fuel are heated for short amounts of time. They tend to be bench scale tests with a temperature ranging from 140–250 °C. Static rigs are easy to set up and are useful for examining the purely chemical contributions to autoxidation because flow regime variables are removed. In all the static rigs, post-test analysis of the fuel mixture can be achieved with techniques like Liquid-Chromatography Mass Spectroscopy and/or Gas-Chromatography Mass Spectroscopy (LC-MS/GC-MS) depending on the species of interest.[67]

Flask oxidation tests involve heating the fuel in a container, and are cheap and easy to set up. Flask oxidation tests can either be open to the air [38] or under a controlled atmosphere.[68] Examples in previous studies have used glass [38, 69, 70] in order to the limit metal surface catalytic effects.[38] Aliquots can be taken from the vessels throughout each run to study kinetics. The solution can also be filtered at the end of the experiment and subject to gravimetric analysis to determine the total deposits. Lack of precise control of oxygen availability is the main disadvantage of this equipment, since the diffusion of oxygen from the head space into the fuel was identified as a potential rate limiting step in autoxidation.[71]

Quartz Crystal Microbalance Tests (QCM), sometimes referred to as Parr Bomb systems, are sealed containers which allow greater control and monitoring than flask oxidation tests. Firstly, with the container being sealed, the rate of reaction can be monitored precisely by saturating the fuel with oxygen at the start and measuring the decrease in concentration over time.[40] Furthermore, the rate of deposit production can be determined through time with accuracy less than $1 \mu\text{g cm}^{-2}$ by using the change in the oscillation frequency of the microbalance to measure the mass variance per unit area.[72] Several other parameters like pressure and temperature can be measured with excellent precision. Nevertheless, QCM devices are costly, with only limited production worldwide.

PetroOxy the petroOxy device is a special type of flask oxidizer designed to

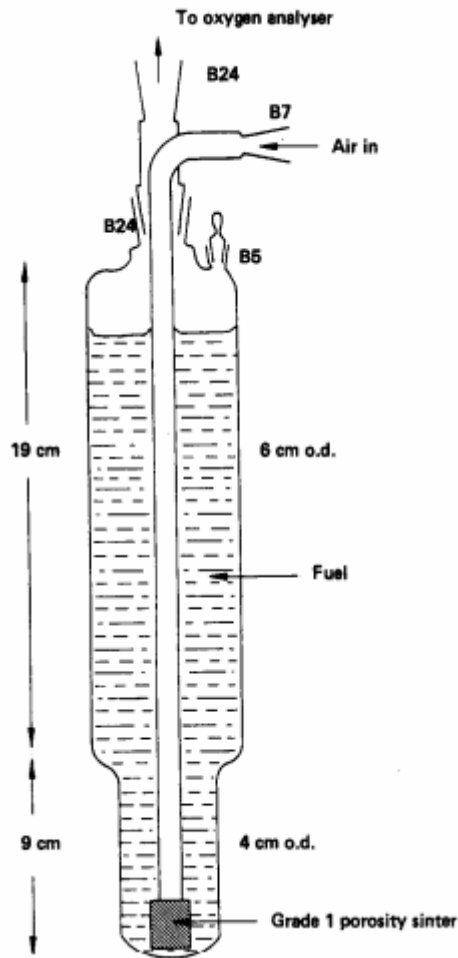


Figure 2.1: An example of a flask oxidizer, produced from [70]

monitor the rate of autoxidation of a given fuel sample. A petroOxy device heats a small volume of fuel (typically 5 mL) and monitors the oxygen partial pressure in a headspace above the fuel volume. As oxygen is consumed in the fuel volume, oxygen in the headspace diffuses into the liquid. It is assumed that the rate of oxygen partial pressure depletion in the headspace is related to the rate of autoxidation.[73] Gold walls are often employed in petroOxy devices, ensuring an inert container. Several studies have deployed the petroOxy device to investigate the oxidation rate of real fuels,[74][75] pure hydrocarbon solvents,[76] and surrogate fuels.[77]

2.1.1.2 Flowing Rigs

A wide variety of flowing rigs exist to investigate the formation of deposit in conditions more realistic to fuel in aircraft compared to static rigs. Nevertheless, flowing rigs tend to have higher levels of complexity, introduce physical variables, and make

chemical effects harder to study in isolation. Fluid dynamic effects can be varied in flowing rigs, where the flow can be adjusted between laminar, transition and turbulent regimes. Furthermore, fuel within jet engines receives heat from fuel-oil heat exchangers and before burner feed arms in pipes,[13] so these can be simulated easily within these rigs along with the same wall materials to investigate any surface effects. The generalized design of all these rigs includes a heated section of pipe where fuel is passed through. The fuel is often saturated with air or an inert gas dependent on the conditions required (Figure 2.2).

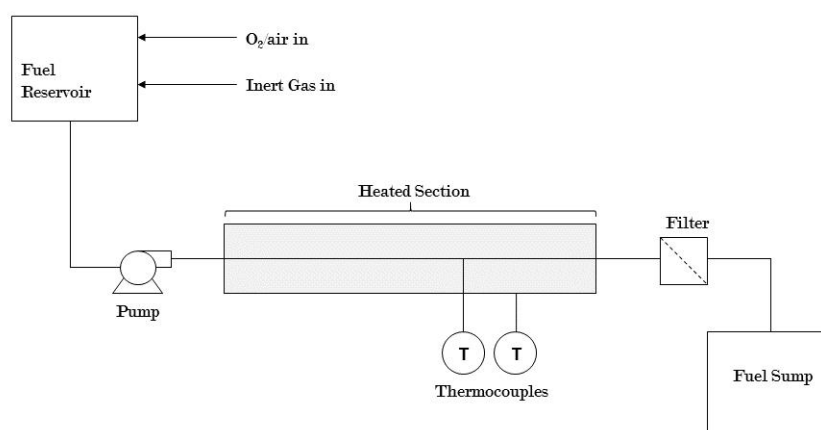


Figure 2.2: Generic flow system diagram

There are several design considerations which must be taken into account, when designing flowing rigs. Firstly, the phases of the heated region must be considered, i.e. whether a fuel is entirely internal flow or two phase annular flow is used. This choice is based on what section of the fuel system is being modelled, with sections with headspace (e.g. fuel tanks) more suitable to annular flow and internal flow being reserved for single phase sections (e.g. burner feed arm).[33]

The material of choice for the pipe must reflect that of the internal flowing systems of the aircraft, since metal surfaces are known to influence autoxidation chemistry.[78] If the chemistry of the bulk reactions is the sole point of investigation, an inert layer, like silicon steel, can be added to the internal walls to passivize any surface effects.[79]

There are a number of different in-line and post-experiment measurements that can be done to study the reactions. Quantification of the surface deposits is usually done by carbon burn-off analysis or a surface carbon analyzer (which also relies on carbon burn-off, but at higher temperatures).[61] Deposits can be characterized macromolecularly using scanning electron microscope (SEM) images, which can give useful information about the growth of deposits on walls.[80] Since deposits form in the bulk too, filters can be added at the outlet of the heated zone where they can be quantified by pressure drop or carbon burn-off.[81] Oxygen consumption due to autoxidation reactions, can be measured in-line in a continuous gas-chromatography system. This system is also able to measure other gases like methane and hydrogen.[82][61] For other species, aliquots can be taken throughout the run and analyzed after. Hydroperoxides, for instance, can be quantified by the addition of triphenylphosphine.[83] Once again, post-test chemical analysis using GC-MS/LC-MS/GC×GC can be performed. Due to the low concentrations of heteroatomics in real fuels, pre-concentration methods such as liquid-liquid extraction (LLE) [84] or solid-phase extraction (SPE) [85] can be used to improve analysis. Pre-concentration methods are more successful in flowing rigs than static rigs due to the larger fuel to extractant ratio, a result of the larger volume of fuel used.

2.1.1.3 Large Scale Rigs

Larger scale rigs aim to offer an even-closer simulation of the real life situation faced with fuel, where complex geometries are utilized, often closely replicating a real internal flow system of a jet engine. Longer test durations are another advantage of large scale rigs. However, as a result of the lengthy duration (days or weeks) the fuel consumption is higher.[40] Moreover, due to the complexity of these tests, where temperature varies in different sections, there is limited scope for production of chemical kinetic data as seen in flowing rigs. Instead, large scale rigs have focused on developing empirical models.[86, 87] A few examples of large scale rigs are presented below. Much like flowing tests, carbon burn off and visual inspection is used for quantification.

Aviation Fuel Thermal Stability Test Unit (AFTSTU) test rig closely models the zones seen in a real jet engine, with careful choice of materials and components. This rig has the capability for single flow, spill flow and full re-circulation.

The system is split into low (0-96.85 °C) and high temperature (0-226.85 °C) areas and a sparging system is employed to oxygenate the fuel.[88] Methods of analysis include carbon-burnoff, giving the total mass of deposit.[89, 90]

Extended Duration Thermal Stability Test (EDTST) is simpler in geometry, similar to those seen in flowing rigs. The key difference is the time duration of test. It can run for long periods, greater than 96 hours. The system is able to run up to 218 °C and could be automated.[91]

2.1.2 Computational Methods for Investigating Autoxidation and Deposit Formation

A key disadvantage associated with all experimental rigs is the difficulty controlling independent variables. Even in static rigs, low ppb concentrations of metal can affect the final result, without the researcher even being aware of the contaminant.[33] In addition, construction of chemical mechanisms from flowing/static rigs can lead to the production of thermochemical and kinetic data with non-chemical contributions from physical effects (flow velocity, turbulence etc.) idiosyncratic to the rig.

To overcome these challenges, computational methods have become an increasingly popular tool to understand chemical reactions at the molecular scale. Isolation of particular reacting species allows thermochemical and kinetic data to be produced from *ab-initio* (or semi-empirical in some cases) calculations. Moreover, computational techniques allow extremely rapid free-radical chemical mechanisms to be studied in a step-wise manner. Nevertheless, computational methods have their drawbacks. As elucidated in Chapter 3, different quantum chemical techniques have to be weighed up in terms of cost and accuracy of the calculation. In relation to jet fuel, quantum chemistry is an emerging tool, where experimental techniques are still dominant. Nonetheless, a combination of computational and experimental techniques will become increasingly common in the future.

2.1.2.1 Density Functional Methods

Density functional theory has been used extensively to study the autoxidation phase of fuel thermal oxidative degradation.[48][76][29] Throughout a majority of the work, this widely popular B3LYP functional was employed. However, differing basis set

sizes and inclusion of solvent effects has become the standard for recent work. Specifically, the PCM solvent model has been used, with *n*-hexane being chosen as the representative solvent.[76][48]

Early work by Zabarnick *et al.* used B3LYP//6-31G(d) to relate bond dissociation energies (BDEs) to the hydrogen abstraction barriers. In general increasing the size of the basis set from 6-31G(d) successively up to 6-311G(3df,2p) moved the calculated phenol and BHT O-H bond strengths towards the experimentally calculated values.[29] Building on these findings, Dwyer employed the larger cc-pVTZ basis set.[26] As elucidated in Chapter 3, the Dunning basis sets are correlation consistent, and are designed to converge to the basis set limit for post-HF methods. In general, the Dunning basis sets converge smoother to the basis set limit than Pople basis sets employed in Zabarnick *et al.*'s study, albeit at a higher computational cost.[92] Furthermore, Dwyer employed broken symmetry basis sets which was included to recover correlation energy in open shell radical systems.[26]

Aside from the basis sets, to further improve on accuracy, Dwyer used a PCM solvent model and added corrections to the enthalpy using the goodvibes script.[93] Inclusion of the PCM solvent model allowed effects of the fuel bulk to be approximated. Additionally, the correction applied using the goodvibes script helps overcome inaccuracies arising from the rigid-rotor harmonic oscillator treatment, which is standard in electronic structure programmes. Dwyer's work added thermochemical and kinetic data to a new chemical kinetic mechanism. The new mechanism was able to accurately predict the oxygen depletion in a simple solvent.[48]

Recent work by Parks *et al.* also employed the popular B3LYP functional with a mixed deployment of the cc-pVTZ and SDD basis set to explore the reactivity of metals towards hydroperoxides in fuel. In Parks *et al.*'s study, the SDD basis set, which adds a core potential to the non-valence shell of the copper atoms studied, saving computational cost. The newer M06 functional was used as a comparison to the B3LYP functional to compare the calculated energetic pathways.[94] Although M06 produced different thermochemical and kinetic values, the general reactivity trends were found to be the same. In related work by Mielczarek *et al.*, usage of more modern M06-2X functionals was shown to be preferable for the generation of accurate thermochemical and kinetic mechanisms.[95] On the other hand, for the investigation of reactivity, and comparing competing deposit pathways, the

B3LYP//cc-pVTZ method has shown to be a well proven method. Nonetheless, Mielczarek *et al.* correctly asserts that dispersion should be applied to B3LYP to correct for its poor treatment of long-range interactions.[95]

2.1.2.2 Post-HF methods

A key disadvantage of DFT methods is the single reference nature of the calculation. Because radical chemistry, and thus open-shell systems, dominate the autoxidation process, treatment of the system as single reference leads to inaccuracies. As explained in the previous section, broken symmetry DFT can recover some correlation energy. Multi-reference methods, particularly MCSCF, are specifically designed to recover static correlation from open-shell systems (see Chapter 3 Section 3.10). MCSCF//def2-SVP was employed by Dwyer to study the homolytic fission of methyl hydroperoxides. Pure MCSCF was found to be good at recovering static correlation, but dynamic correlation, arising from the movement of electrons as the O-O bond is broken was handled poorly. As a consequence, Rayleigh-Schrödinger perturbation corrections were applied allowing the methyl hydroperoxide homolytic fission barrier to be calculated within 2 kcal mol^{-1} of the literature value.[48] However, key disadvantage of the MCSCF method is the computational cost required. Systems larger than methyl hydroperoxides become too costly for most post-HF methods, meaning studying the formation of larger deposit structures precludes the use of many post-HF methods.

2.1.3 Concluding Remarks on Experimental and Computational Methods used to Investigate Thermal Stability

A variety of computational and experimental tools now exists to study the thermal oxidative stability of jet fuel. Each method has advantages and disadvantages, and is useful for studying thermal stability at different scales. Static rigs are the most useful tool for studying the chemistry of deposition experimentally. The removal of fluid flow effects in static rigs allows focus solely on the chemical effects. Flowing and large scale rigs increases in size and complexity, which allow fluid effects to be studied in conjunction with chemical effects.

Computational techniques to study deposition have become more popular in recent years because of larger computational resources available. Density functional theory has proven to be a particularly useful tool to explore reaction mechanisms

and isolate thermochemical and kinetic parameters from fluid effects. Nonetheless, both computational and experimental techniques should be employed to complement each other. Computational chemistry techniques are often limited by the accuracies of the method, and require an understanding from real experiments to have a basis for the perform calculations. On the other hand, experimental techniques can be limited in their ability to completely control all independent variables, particularly in the case of complex free-radical chemistry. The complexity of the deposition and autoxidation process will be highlighted in the next section, which will explore these physical and chemical factors in detail.

2.2 Factors Affecting Autoxidation and Deposit Formation

Since the 1950s work has been conducted using previously described methods and equipment to understand the mechanisms behind autoxidation and deposit formation. This has mainly been done by correlating the starting species with the rate of deposit formation, characterization of deposit and oxygen consumption experiments in variety of rigs. Computational techniques have assisted in testing the validity of mechanisms. Since deposit formation is governed by both chemical and physical process; factors like flow, temperature and pressure will also be discussed.[33]

2.2.1 Oxygen

Dissolved oxygen tends to be at a concentration 50-60 ppm in jet fuel at room temperature and pressure.[96] An early investigation demonstrated that dissolved oxygen was a crucial species in deposit formation in fuels. Conventional fuel sparged with nitrogen before being sent through a flowing kinetic unit yielded no deposits, conversely fuel saturated with oxygen formed deposits readily.[35] Dissolved oxygen versus deposit deposition profiles show that there is often a lag before deposits are observed.[81] This suggests that rather than there being a single step from oxygen + fuel \longrightarrow deposits, there is a series of chain reactions leading to deposits.

The effect of oxygen concentration on deposit formation seems to attract conflicting findings. Some studies indicate that lower oxygen concentrations leads to fewer deposits,[72] whereas other research indicates that deposition is zeroth order with

respect to oxygen concentration moving to first order at limiting concentrations,[97] with one paper even demonstrating that a decreased oxygen concentration resulted in higher deposits.[98] The conclusion of later studies is that merely assigning zeroth order dependence on deposit formation was a simplification of the chain reactions occurring. Lower oxygen concentration broadly decreases deposit formation, but there are some cases where this effect is not observed as strongly which is attributed to the specific fuel chemistry.[71, 99, 24]

The latest work indicates that decreasing oxygen concentration in fuel leads to a first-order relationship in the reduction of deposits.[63] The consensus that emerged is that oxygen is involved with a crucial first step in the autoxidation process by forming alkyl peroxy radicals, which go on to form peroxides by abstracting hydrogens from the hydrocarbon mixture in fuel (Figure 2.3).[26, 29, 24]

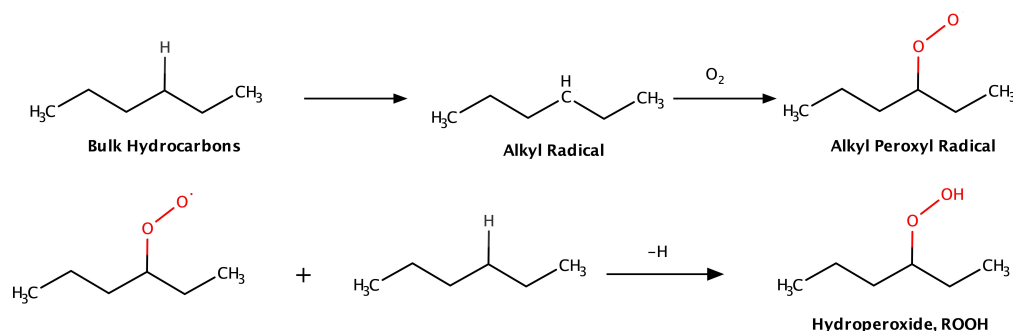


Figure 2.3: Alkyl Peroxyl Radical Formation Process [100]

The uncatalyzed homolytic fission of hydroperoxide, owing to the comparatively weak O-O bond (bond dissociation energy $30 - 40 \text{ kcal mol}^{-1}$), can produce two free radicals.[101]



Hydroperoxide has been shown to be the initiation step for a series of further radical reactions leading to deposits in jet fuel,[102] such that even small ppb concentrations have severe deleterious effects on the fuel oxidative stability.[24] Hydroperoxide has also shown to be initiators in other oxidative chain reactions in other fields including wine aging[103] and within the body as a mechanism for DNA

damage.[104]

2.2.2 Bulk Hydrocarbon Composition

When considering the fuel chemistry (details in Section 1.3.1.1), let us first consider the main bulk compounds, alkanes. These consist of iso-, *n*- and cyclo-alkanes. A study using QCMs to compare alternative fuels composed only of iso- and *n*- alkanes showed that the degree of branching had a negligible effect on thermal stability.[12] Nonetheless, a fuel containing highly-branched species would be expected to oxidize slower due to the higher stability of tertiary carbons.[20] In related research, three distinct stages of oxidation of alkanes in fuels have been identified: a first stage where only oxygen contributes to the main oxidation reactions, a second stage where the oxidation of fuel by alkyl-peroxy radicals form polyfunctional alkyl-peroxy radicals and a third stage where polyfunctional alkyl-peroxy radicals form larger molecular weight products.[105]

The chain length of the bulk fuel alkane had little effect on the type of autoxidation products. These included oxygenated hydrocarbons like ketones, alcohols, and acids as well as alkenes and alkanes from the first stage of autoxidation. Products from subsequent stages included lactones and furanones.[105][106] These findings are supported by earlier work [107] and by GC×GC analysis of oxidized fuel mediums as shown in Figure.2.4 Nevertheless, increasing chain length showed improved thermal stability for alkanes until 12 carbons, where any further improvement was found to be negligible.[108] Cyclic alkanes have been shown to have little effect on thermal stability compared to straight chain compounds. However, they increase fuel density compared to iso-alkanes so can be seen as a favorable addition to fuel chemistry.[26] Recent work focusing on the deposition mechanisms of a decalin (cyclic alkane) jet fuel under oxygenated stress proposed a number of deposition mechanisms for bulk hydrocarbons. After thermal stressing a pure decalin flask oxidizer, LC-ESI-MS analysis of the deposits suggested that condensation reactions and/or polymerization reactions were responsible for the formation of deposit.[74]

Aromatics are also present in fuels (Figure 1.2). They have been implicated in increasing the total amount of deposits, but in also decreasing the rate of deposit formation.[109, 110] Alkyl peroxy ($\text{ROO}\cdot$) and alkyl hydroxyl ($\text{RO}\cdot$) (Equation 2.1) radicals both abstract hydrogens from the fuel hydrocarbons. DFT work has

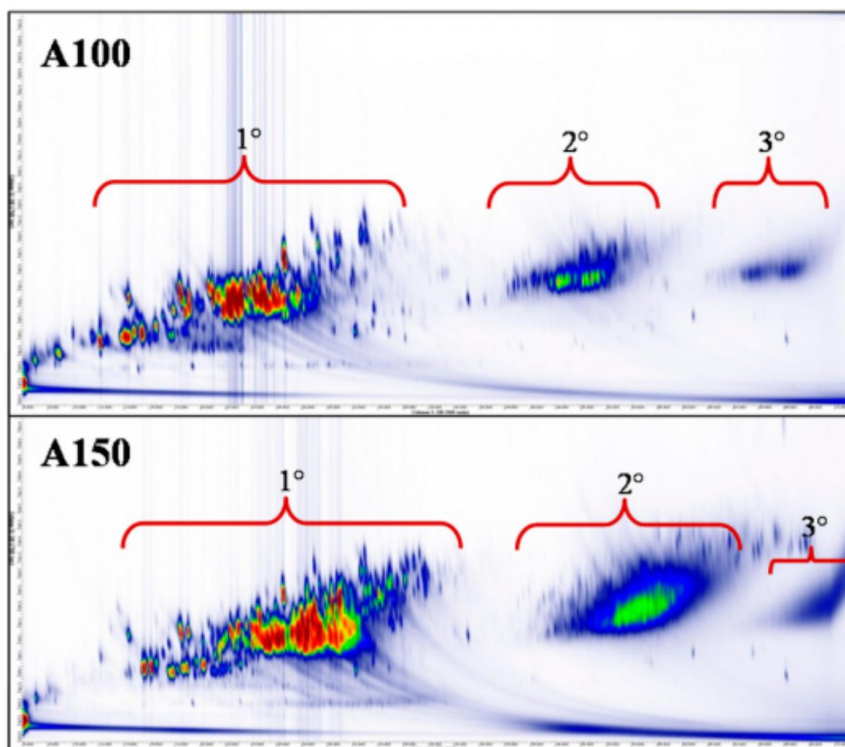


Figure 2.4: GC×GC analysis of stressed Jet-A fuels. Multistep oxidation stages shown, where three distinct regions of oxidation products are identified [27]

shown weaker C–H bonds in benzylic species compared to alkyl C–H bonds.[29] In fact, a DFT study employing B3LYP//6-31G(d) noted that the higher calculated barrier to abstract a hydrogen from *n*-butane compared to aromatic ethylbenzene meant the aromatic molecule was 65 more times likely to react with radical species. This means that they are more susceptible to oxidation than straight chain species [30], as exemplified in Figure 2.5. The stabilizing delocalization effects of aromatic rings make the subsequent radical species more stable than alkyl radicals, creating a 'chain-breaking' effect. As a consequence, the resultant aromatic radical species are less likely to react leading to a slower rate of oxidation of the rest of the fuel.[100] A similar effect is seen with the antioxidant BHT (see Figure 1.5). Here, the methyl group adds extra stability to the already stable ring system, when the hydrogen atom on the phenol group is abstracted.[111]

The increased deposit formation overall can be explained by the propensity of aromatic radicals to form larger molecules (oligomers). These oligomers are, in general, less soluble in solution. Moreover, they can undergo further oligomerization reactions to form even larger macromolecules.[42] Thus, diaromatics form more de-

posits than single aromatic ringed species, given that for the former there are fewer successive steps to insoluble deposits.[27] However, further elucidation of the chemical mechanisms to deposit is needed, since some aromatics have shown to decrease both the total amount of deposit formed as well as the rate of deposit formation.[111]

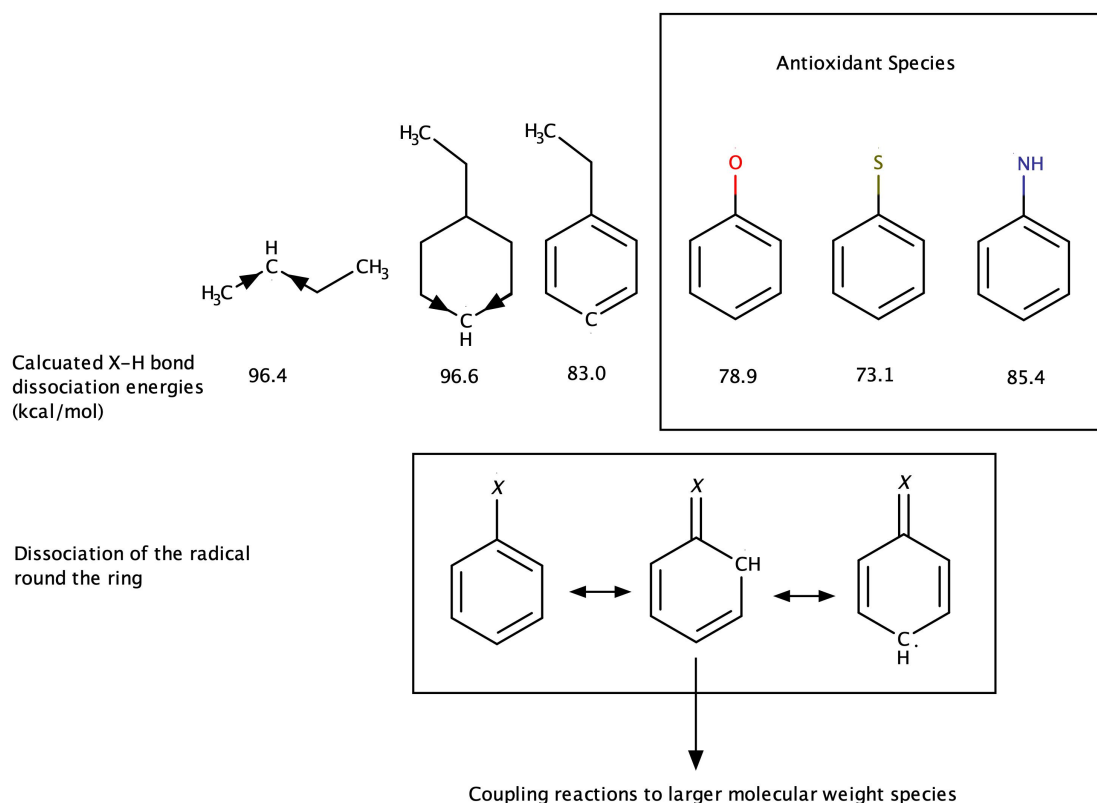


Figure 2.5: Stabilizing effect of antioxidants and aromatics, the bond dissociation energies are calculated using DFT with a B3LYP functional [29]

2.2.3 Physical Conditions

2.2.3.1 Flow Conditions

Flow conditions, namely shear stress and velocity, have been shown to have an impact on the formation of deposits.[112, 113, 114, 115] Shear stress can be said to be a function of velocity, pipe geometries, wall roughness, and flow viscosity.[116] Flow velocity is treated separately here, since it not only influences shear stress but has an effect on residence time and heat transfer coefficient. Experiments in flowing rigs

have shown that an increase in velocity increases the amount of deposits,[117, 113] which can be explained by increased mixing at higher velocities which leads to better mixing of reactants and increased heat transfer. A secondary effect of increased velocity is a higher shear stress on the walls, which could lead to 'scrubbing off' of the deposits. Moreover, increases in velocity lead to a reduced residence time, possibly reducing the total deposits formed. However, both these secondary effects do not have as strong an influence as the enhanced heat and mass transfer (see Figure 2.6). One paper found that at very low laminar velocity flows, the peak deposition rate occurs at a lower temperature, due to the increased residence time, but higher flow rates still resulted in greater overall deposits.[112]

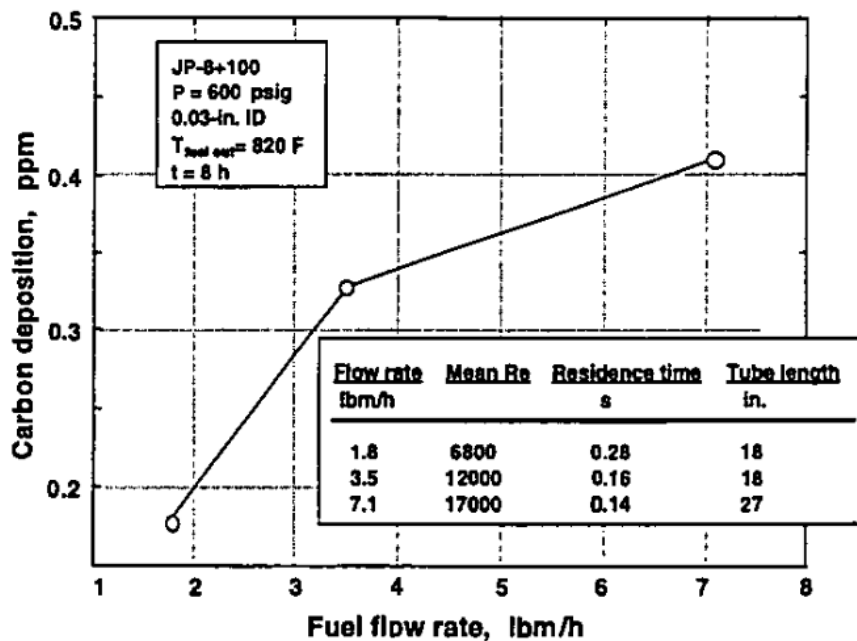


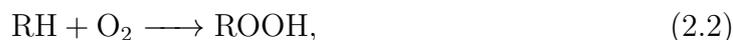
Figure 2.6: Effect of Flow Velocity on Deposit Forming Process [117]

With regard to the effects of shear stress, since the viscosity of jet fuel is roughly kept constant, surface roughness and pipe geometries are the key avenues of investigation. Decreasing the pipe diameter increases the shear stress on the walls if all other variables are kept constant, and has been shown to increase the amount of deposits.[117] Once again, despite the increase in shear stress, the higher Reynolds flows produced by small diameters leads to greater mass and heat transfer conditions, increasing deposit formation. The effect of increased surface roughness, increasing shear stress, results in greater deposit formation in the turbulent region only. This is due to roughness projecting roughness elements into the bulk flow and increas-

ing mass and heat transfer. So once again, the effect of shear stress is negligible here.[118]

2.2.3.2 Temperature

Temperature is one of the most important factors affecting thermal oxidative stability. Although fuels are known to degrade over time in ambient conditions,[119] ambient fuel degradation is a slow process requiring months of testing time to produce deposit.[120] By contrast, the temperatures experienced by fuel in aircraft are in excess of 100 °C, with temperatures at around 160 °C at the fuel injector.[38] The increase in temperature leads to the build up of deposit measured in hours. To begin with, research by Zabarnick *et al.* has shown that the autoxidation of fuel accelerates above ambient temperatures (Figure 2.7).[121] Increased autoxidation rate is due to the rate increase for several reactions. However, crucially, hydroperoxides undergo homolytic fission (Figure 2.3) at much greater rates at higher temperatures. Additionally, higher temperatures allow for the increased hydroperoxide formation from the reaction:



due to the high energies required to break the C–H bond. In turn, the higher levels of hydroperoxides produces will then further decompose to more radical species.[100][60][122]

Although it is clear deposit formation is greatly accelerated above ambient conditions,[113] the rate of deposition has been found not to increase with temperature indefinitely. Early work by Taylor and Wallace indicated a linear relationship between temperature and the rate of deposition in a flowing rig for both conventional fuels [35] and pure hydrocarbons.[110] Nonetheless, the researchers noted that, at a certain temperature unique to each fuel, the rate of deposition suddenly leveled off or even decreased.[35] A similar observation was found by Balster *et al.*, where the mass of deposit generated by several conventional fuels in a near-isothermal flowing reactor was lower at 225 °C compared to 185 °C. It is important to note at 225 °C the rate of deposition dropped was lower than in Taylor and Wallace’s study, which found temperatures in excess of 450 °C were required to observe a drop in deposition rate, potentially due to a different starting chemistry of the fuel. Nevertheless, in order to explain these effects, the Balster *et al.* study noted two possible effects. The first effect is a chemical one. The authors propose that the direct reaction of

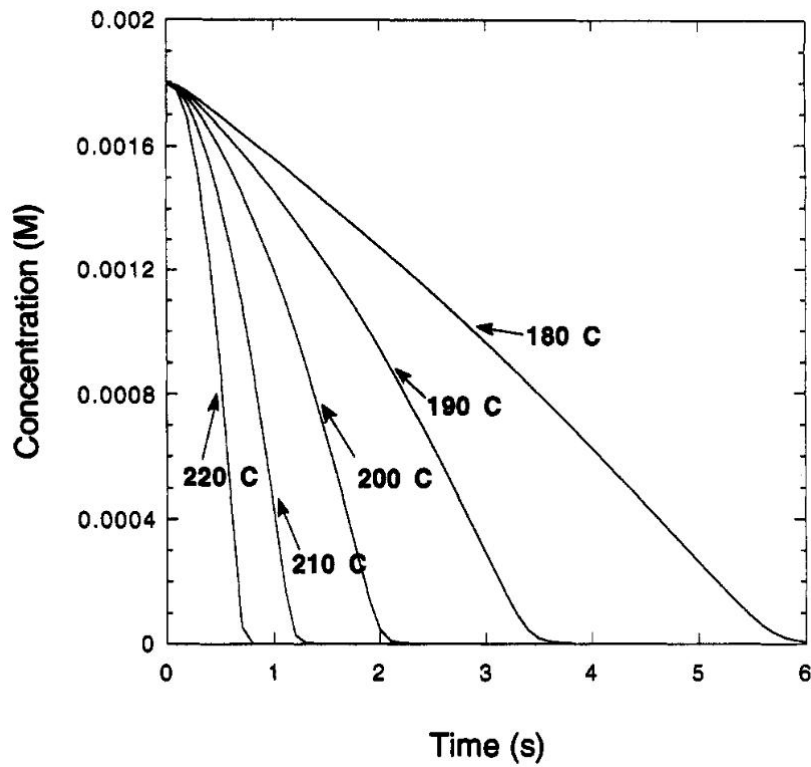


Figure 2.7: Effect of Temperature on Oxygen in Fuel [121]

hydroperoxides with antioxidants is the key step to deposition, but at higher temperatures, the decomposition of hydroperoxides is accelerated reducing their availability to directly form deposits. The second effect proposed is physical, where the increase from 180 °C to 225 °C leads to a higher solubility potential.[123]

2.2.3.3 Pressure

Because an aircraft experiences varied pressure as it moves through various altitudes during its operation, the effect of pressure on deposition and autoxidation has been studied. Since the dissolved oxygen concentration in fuel is related to Henry's law, and thus related to the total pressure and partial pressure of oxygen, the rate of autoxidation and deposition will decrease at higher altitudes.[124][35]

In relation to the pressure of the *fuel*, work has shown that higher pressures have a negligible influence on deposition.[125][112][79] Ervin *et al.* found that thermal oxidative deposits from a conventional fuel did not change significantly as the system pressure was increased from 3.89 MPa to 6.31 MPa. Interestingly, the effect of

pressure of the *fuel* had a much more pronounced effect on pyrolytic deposition.[79] Similarly, Marteney and Spadaccini found no strong relationship between deposition and pressure with a JP-5 fuel in a flowing rig. The authors highlight that fuels should only exhibit significant changes in deposition regimes below the critical point.[112] As Hazlett indicates, fuels below the critical point will produce abnormal deposition regimes due to the emergence of a vapor phase.[33] Nonetheless, the typical operating pressures of fuel systems means that it is unlikely fuels will ever drop below their critical pressure.[126]

2.2.4 Heteroatomics

The heteroatom component of fuel is typically less than $>0.1\%$ of the fuel body, and therefore make up a minor component of the fuel mixture.[33] The main heteroatoms present in fuel can be split into sulphur, nitrogen, dissolved metals, and, oxygen-containing species. Despite their low concentrations within the fuel, they are known to have a significant impact on deposit formation. This is why synthetic fuels containing almost no heteroatoms are known to yield almost no deposits, despite their vulnerability to quick autoxidation. The inverse effect is again highlighted in Figure 1.10 where a single component dodecane oxidizes quickly but yields no deposit. This section will explore the effects of the heteroatoms in fuel, and attempt to separate their role in the autoxidation process and subsequent agglomeration steps.

2.2.4.1 Sulfur Species

Early investigations found sulfur levels at a higher concentration in deposits, suggesting that they play a role in deposit formation.[35] Other authors postulate that acid-forming sulfur species are a catalyst for condensation reactions observed in fuels.[127] The total sulfur is limited in a number of standards.[128] [129] However, a comparison by Rawson *et al.* in Figure 2.8 clearly demonstrates that the total sulfur content is a poor predictor for amount of deposits. In order to fully understand the role that sulfur plays in jet fuel deposition the sulfur class must be split into its constituent species, each with their own influence on the autoxidation and deposition chemistry on fuel.

The main classes of sulfur species are: mercaptans/thiols, sulfides, disulfides, and thiophenes. Each compound has a varying effect on the amount of deposit and rate of autoxidation, even within specific classes. Moreover, there are often contradictory

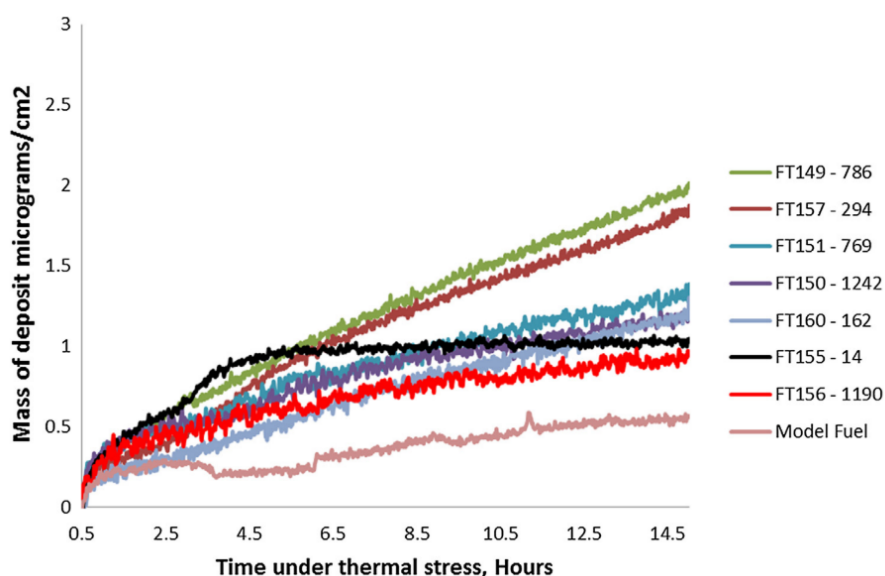


Figure 2.8: Total Sulfur and Mass of Deposit in a QCM, the total sulfur is given to the right of the fuel names in ppm. Taken from [51]

results between the same compounds, reflecting the sensitivity between the test conditions and thermal oxidative stability. This section will explore the studies investigating the sulfur species classes has on thermal oxidative stability, and then compare each of the classes with one another.

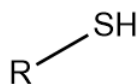


Figure 2.9: Generic Thiol Structure

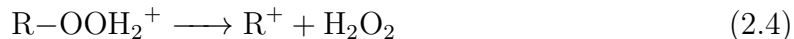
Thiols/Mercaptans Thiols/Mercaptans are end-chain sulfur species. They are the only class of sulfur species to have limits placed on their maximum concentrations by jet fuel standards. where they are limited to a maximum concentration of 0.003 w/w% in Jet-A-1 in the DEFSTAN standard.[129] This is because they are thought to reduce the thermal oxidative stability in fuel even at low concentrations.[33] Therefore, a process to convert thiols to disulfides known as 'sweetening' is employed at the refinery stage to reduce the concentration of thiols below maximum specification levels.[8]

First, the effect thiols have on autoxidation will be examined along with their subsequent products. Naegeli *et al.* found that 50 ppm of thiophenol added to dodecane at 433 K for 4 h in a static aluminum vessels slowed down the rate of autoxidation. A straight-chain thiol was then tested, which had a smaller effect on slowing autoxidation. 50 ppm of hexanethiol at the same conditions had little effect on the autoxidation rate, but 200 ppm slowed the rate to a similar extent as 50 ppm of thiophenol.[52] By contrast, Rawson and colleges found that a straight chain thiol reduced the autoxidation rate to a greater degree than thiophenol. In their study, 20 mmol L⁻¹ of decanethiol and 39 mmol L⁻¹ of thiophenol was added to a model 80% dodecane- 20% toluene fuel for 15 h at 413 K in a stainless steel static vessel. The pure model fuel reached 0% oxygen concentration in the headspace after 4 h but decanethiol slowed the rate of autoxidation significantly more, with a drop from 45% to 38% oxygen in the headspace after 15 h stressing. On the other hand, unlike Naegeli's study, the aromatic thiophenol slowed the rate of autoxidation to a lesser degree, with a drop of 43% to 17% oxygen in the headspace after 15h stressing.[51] The contradictory results here could be initially attributed to the time length of tests, since it has been shown that aromatic thiols behave differently under longer stressing conditions compared to straight chain thiols.[130] However, since Naegeli *et al.*'s experiments run to complete oxygen depletion, this can be ruled out as a possibility. Alternatively, there is the possibility that Rawson *et al.*'s model fuel is not representative enough of the Jet-A fuel employed in Naegeli *et al.*'s study, or the different vessel wall materials have an influence. Nevertheless, both studies show the retarding effect thiols have on autoxidation.

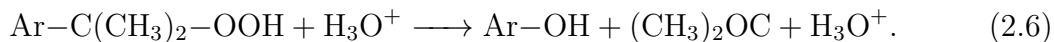
Direct measurement of hydroperoxides, a key initiating species in the autoxidation radical chain reaction, provides another method of measuring the antioxidant effects of species. Watkins *et al.* found that concentrations of thiophenol in the range 0.03-0.1% in a Jet-A fuel at 65°C inhibited hydroperoxide formation for a number of weeks, until all thiophenol was depleted. The tests were carried out in glass vessels.[131] In another study, 1000 ppm of hexadecyl thiol was added to Jet-A-1 at 160°C for 30 minutes in a glass flask. Hexadecyl thiol reduced peroxide formation by two orders of magnitude compared to Jet-A-1.[69] From these studies, it is clear thiols can act as antioxidants by decomposing hydroperoxides.

Several mechanisms are proposed to explain the thiol antioxidant properties. Chien *et al.* propose that sulfonic acids, arising from the oxidation of thiols, decom-

pose hydroperoxides via the following mechanism:



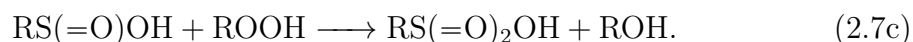
[132] However, the role that these acids play in decomposing hydroperoxides attracts contrasting results. On the one hand, Rawson *et al.* demonstrate, that the direct addition of sulfonic acid to a fuel seemed to have little effect on the rate of autoxidation of fuel.[51] Moreover, the termination product from the above reactions will still be unstable due to the peroxide linkage, leading to the scission of the O-O bond and production of hydroxy ($\text{RO}\cdot$) radicals.[133] On the other hand, the addition of an acid inhibitor additive by Naegeli *et al.* into Jet-A led to an increased rate of autoxidation.[52] However, there could be several mechanisms whereby the inhibitor itself could be displaying antioxidant characteristics here. Other studies outside the area of fuels demonstrate the power of strong sulfuric acids to decompose cumene hydroperoxides to phenols and acetone via the following reaction:



[134]

However, these reactions were carried out in an aqueous solvent, and could explain the lack of autoxidation inhibition when sulfonic acid was added to the non-aqueous fuel phase, as observed by Rawson *et al.*[51]

Another way that thiols can act as antioxidants in fuels is as hydroperoxide sinks. In a step-wise manner, they are able to react to form sulfinic (2.7a), sulfenic (2.7b) and eventually sulfonic acids (2.7c):



[70, 135] It also proposed that hydroperoxides decompose via the following mechanism, forming disulfides:



[136, 137, 138] With regards to the formation of disulfides from thiol, Mushrush *et al.* demonstrated that a *n*-nonanethiol added to a JP-5 fuel oxidized through this (equations 2.8) pathway preferentially over the acid forming pathway (equations 2.7).[139, 140] Mushrush *et al.* were also able to demonstrate that alcohols were the major product when hydroperoxides react with sulfides, with acetone as a minor product.[140] They propose the following scheme for the oxidation of thiols:

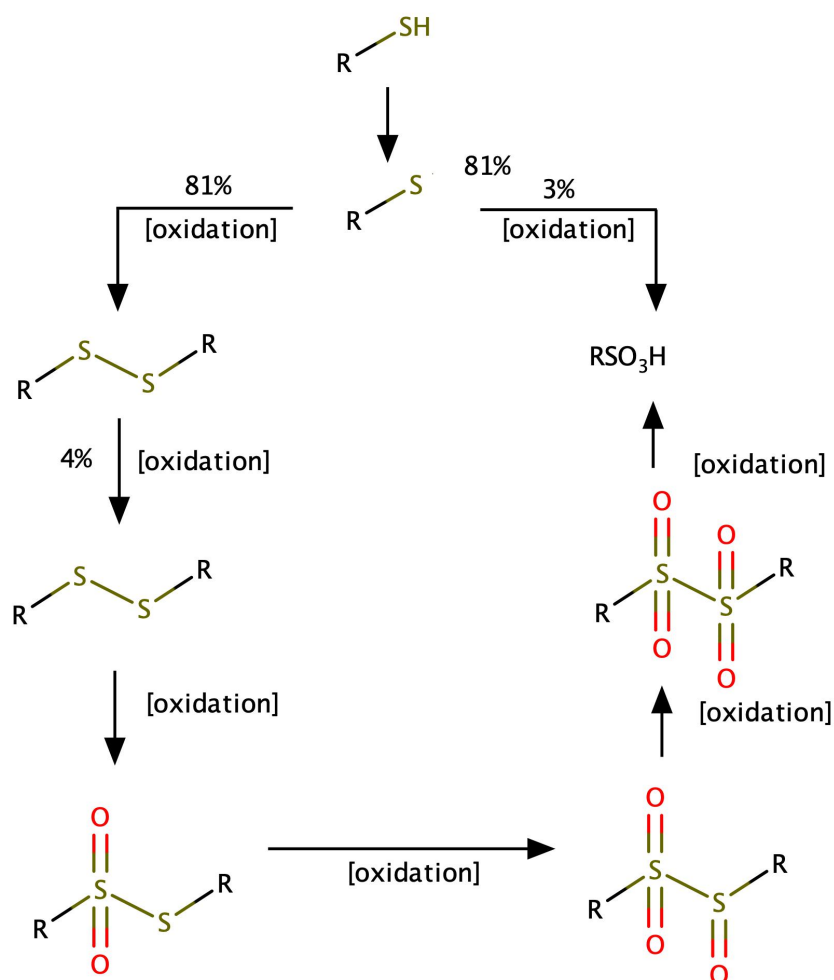


Figure 2.10: Proposed autoxidation pathways for thiols, presented in [139]

Sulfonic acids, and other sulfur organic acids, are known to greatly increase deposition, and are regarded as a key species whereby thiols influence the formation deposits by a number of authors.[127, 141] An early study looking at the influence of thiols by Taylor and Wallace, demonstrated that 1000 ppm of hexadecanethiol and dodecanethiol added to Jet-A fuel increased the deposition rate, and that this rate increased exponentially from 456 to 500 K.[142] Another study showed the removal

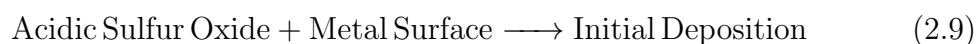
of thiophenol, shown in Naegali *et al.*'s study [52] to have a strong inhibiting effect on autoxidation, to below 10 ppm significantly reduced the formation of deposits.[143] Further evidence of the deleterious impact of thiols on oxidative stability is provided by a study by Daniel and Heneghan, where the addition of $10 \mu\text{g L}^{-1}$ of butane, pentane and benzene thiol to Jet-A in a glass walked container at 408 K all increased deposits above the pure fuel control.[62] Daniel and Heneghan's work also suggests that straight-chain thiols are the most problematic species for thermal oxidative stability. Straight chain thiols were also found to be more problematic in Naegeli *et al.*'s study, where 50 ppm of hexane thiol increased the formation of gums to a greater extent than 50 ppm of benzene thiol under same conditions.[52] This is interesting since in the same study showed that benzene thiol had the greatest retarding effect on autoxidation, suggesting that it would have formed a larger amount of sulfonic acid via reactions 2.7. This could add further support for the non-acid forming antioxidant mechanism like that presented in equation 2.8 competing for the formation of sulfonic acid pathways.

Not all studies point to thiols as being problematic for the fuel. In recent work, Rawson and colleagues added 20 mmol L^{-1} of decanethiol and 39 mmol L^{-1} of thiophenol to a model 80% dodecane- 20% toluene fuel for 15 h at 413 K. These produced similar amounts of deposits to the un-doped model fuel. However, when sulfonic acid was directly added to the model fuel, the amount of deposit was greatly increased. Like Naegeli *et al.*'s work, this could suggest that thiols either form small quantities of acid (Figure 2.10) or an alternate pathway. Interestingly, Rawson *et al.* found when investigating several real Jet-A fuels characterized by their total thiol content, that the fuels with the highest thiol content were not significant depositors.[51] This highlights the divide in literature and the sensitivity to the individual testing conditions. Additionally, as will be discussed in Section 2.2.4.3, sulfur compounds may require nitrogen species to produce deposits.

The mechanism whereby sulfonic acids, arising from thiol oxidation, form deposits on the wall and the bulk has been explored by a number of authors. Firstly, within the bulk fuel, early studies suggest that sulfonic acid catalyze esterification reactions in the heating fuels.[144] There is evidence for the presence of esterification products in bulk fuels,[105] where strong sulfonic acids could catalyze their production. Acid-base reactions between sulfur and basic nitrogen compounds within hydrocarbon fuels are also proposed in later work.[145][63] However, a study correlating

the basicity of nitrogen compounds and total deposits found that it was the non-basic compounds that caused the formation of the highest amount of insolubles.[146] The role that nitrogen species will be discussed in further detail in Section 2.2.4.3. It has also been suggested that acids catalyzing the formation of phenols play a role in forming phenols (see equations 2.6),[69, 147] which have been shown to be extremely deleterious to thermal oxidative stability by multiple studies (Section 2.2.4.2).

Sulfonic acids from thiols are also implicated in playing a role in the adhesion to the wall. Kauffman *et al.* hypothesized that sulfonic acids are crucial to first stage of deposition:



[69]The authors demonstrated that the treatment of steel wires with various acid neutralizing compounds reduced deposits. Increasing levels of ferric oxide (12, 25, 50 ppm) and calcium oxide (50, 100 ppm) were able to successively reduce deposit thickness on the steel wires down from 1800 nm untreated to a minimum of 80nm treated. By contrast, powders known to be unreactive towards acid like silicon dioxide and aluminum oxide had little on the thickness of the deposit. These result highlight the importance of a judicious selection of wall material for testing deposition. Overall, it is clear there is a large body of work implicating sulfur based acids in the formation of deposits.

Not all authors believe acids, arising from autoxidation of thiols, play a significant role in the formation of fuels. Hardy and Wechter,[148] discovered that measuring the total acidity alone was not a predictor for the formation of bulk deposits in diesel. Moreover, the addition of an organic base (trialkylamine) to neutralize these acids increased deposits. In a different study, the addition of tridodecylamine, another organic base, also increased the formation of deposits, but in this case the authors pose that the suppression of hydroperoxide decomposing acids (see equations 2.5 and equations 2.6) as to the reason why deposits increase.[52] By contrast, Hazlett *et al.* showed the addition of piperidine, an organic base, was able to decrease the amount of deposition.[127] With such contrasting results, and acids possibly affecting autoxidation and later agglomeration stages in different ways, it becomes difficult to conclude the mechanism of acid catalyzed deposition from just the addition of basic nitrogen compounds. Especially since nitrogen heteroatoms have been implicated

in the formation of deposits themselves (see Section 2.2.4.3).

One study which is particularly critical of the acid theory of deposition used a solvent extraction gravimetric technique to examine the effect of acids on fuel. In this work, Hardy and Wechter were able to show that addition of dodecylbenzene sulfonic acid (DBSA) to a diesel fuel had no significant effect on deposition. In their study, acids had no influence on deposits whether polars were kept in or removed from the diesel fuel, suggesting that sulfonic acids do not catalyze reactions between polar constituents in fuel. Moreover, unlike many other studies, upon addition of the acid the fuel was immediately filtered to remove any immediate acid-induced precipitate. The workers deemed precipitates produced instantaneously upon addition of acids were not reflective of real deposit masses, but rather solvency effects from adding a strong acid to the non-polar fuel. It was shown that the precipitate immediately generated was of a similar mass to the added DBSA. Nevertheless, one of the fuels stressed for 90°C from fuel filtered immediately after the addition of acids, was shown to increase deposits by two fold.[149] In summary, it is not clear still as to what role acids play in bulk deposition, and whether acid-catalyzed pathways contribute to a large portion to the formation of bulk deposits. But this is most likely reflective of the fact that bulk deposition occurs through multiple mechanisms as highlighted by Hazlett in an extensive review into jet fuel thermal oxidative stability.[33]

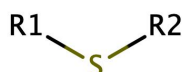


Figure 2.11: Generic structure of a sulfide

Sulfides Sulfides as a species class are not limited by their composition in fuel, apart from being encompassed in the total sulfur specification for Jet-A.[128] [129] Sulfides are characterized by singular sulfur atoms taking the place of a carbon atom, analogous to an ether when compared to oxygen.

First, looking at the effect of sulfides have on autoxidation. Naegeli *et al.* found that the addition of 50 ppm of thioanisole to a dodecane-15%cumene model fuel had no effect on autoxidation.[52] Another study by Rawson and workers found similar

results, where butyl sulfide (23 mmol L^{-1}) and phenyl sulfide (24 mmol L^{-1}) had no effect on autoxidation in an 80% dodecane- 20% toluene. The tests were performed in a steel vessel 15 h at 413 K.[51] By contrast, another study by Mielczarek *et al.* found that when dibutyl sulfide was added to dodecane in a petrOxy, the rate of autoxidation was significantly slowed. Dibutyl sulfide and dodecane were combined in a 1:500 volume ratio in a PetroOxy device at 423 K, in this study the PetroOxy device automatically switches off after a 10% pressure drop, giving the total residence time. The addition of dibutyl sulfide increased the residence time by +43% compared to neat dodecane, slowing autoxidation. [115] Kauffman *et al.* were able to show that the addition of 1000 ppm benzyl phenyl sulfide to Jet-A was able to reduce the amount of hydroperoxides.[69] The variation in results here highlights the sensitivity to the specific structure of the sulfide compound, as was also highlighted in a study exploring sulfur constituents in gasoline fuels.[130]

In order to examine the autoxidation behaviors of sulfide containing fuels, their oxidation mechanism can be explored. When sulfides are oxidized they form sulfoxides and then sulfones in successive steps shown in Figure 2.12.

Mushrush *et al.* were able to demonstrate that sulfoxides were the major product of sulfide oxidation,[139] whereas sulfones were the minor components. The authors also showed that alcohols were the main product when hydroperoxides reacted with sulfides with acetone as a minor product.[140] Epping *et al.* showed that sulfones and sulfoxides, formed from sulfide oxidation, were shown to have no effect on deposition in fuels. When 0.1 mol L^{-1} of pentamethylene sulfide was added to a model fuel sample in a steel autoclave at 4.5 bar of air for 24 h at 120°C , the amount of deposit decreased by almost half compared to the un-doped fuel.[68] In another study, $10 \mu\text{g L}^{-1}$ of dibutyl and dipentyl sulfide was added to Jet-A in a glass walked container at 408 K both reduced deposits after 168h thermal stressing.[150]

Not all studies indicate sulfides as effective deposit reducers. Naegeli *et al.* found that 50 ppm of thioanisole added to Jet-A fuel for 180 min at 433 K had no effect on the amount of deposit. These were tested in an aluminum static vessel.[52] Additionally, recent work by Zabarnick *et al.* showed that 100 mg L^{-1} di-*n*-hexyl sulfide had no effect on deposition when added to a simple commercial solvent in a steel walled QCM.[63] By contrast, Taylor and Wallace found that 1000 ppm of thioanisole and phenyl propyl sulfide doped in Jet-A for 4 h at 436 K increased deposition in a tita-

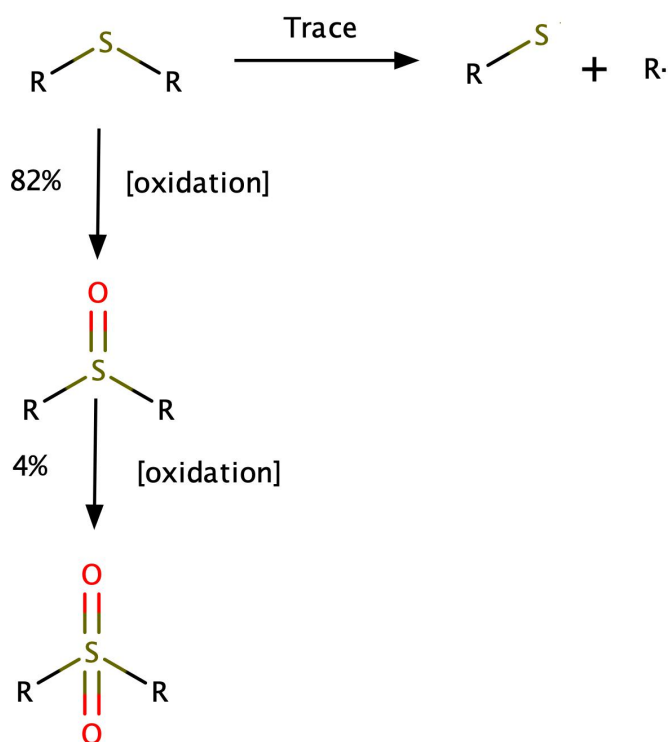


Figure 2.12: Oxidation of sulfides in a Benzene solvent containing 3×10^{-4} M of t-butylhydroperoxide and 9×10^{-4} M hexyl sulfide.[139]

nium alloy (Ti-8Al-1Mo-1V) walled flowing rig.[142] The difference in concentration here as well as longer testing time and wall effects may have played a role in the difference from Naegeli's study. Taylor and Wallace's study also demonstrate the effect structure has on the sulfide deposition characteristic, with 1000 ppm of dibenzyl disulfide and benzyl phenyl disulfide had no effect on deposition. Here, there is a clear difference between the diaryl and single ringed sulfide. The increased inductive effects, adding to the strength of the C-S bond, could be a key explanation for the difference in deposition characteristics between the di-aryl and single-ringed system. Taylor and Wallace propose that the scission of C-S bonds in the deposit leading to sulfides being part of the mechanism of deposition:



[142] However, little is presented in the literature as to how these species then form insoluble products. One pathway could be the direct reaction of $\text{RS}\cdot$ with other fuel species, or even lead to the formation of acids via the formation of thiols which can then be oxidized. Moreover, Mushrush *et al.* [139] point to the resistance of

sulfoxides and sulfones to form acids, which could explain why some studies discussed previously found they had a minimal effect on deposition.



Figure 2.13: Generic structure of a disulfide

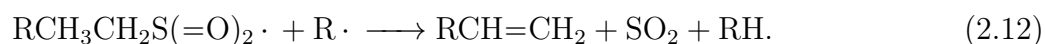
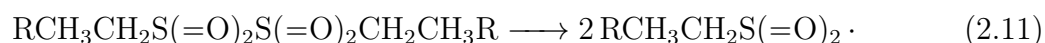
Disulfides Like sulfides, disulfides are not specifically limited as a class by standards, but are encompassed in the total sulfurs class.[128] Disulfides are naturally found in fuels, but also arise out of the sweetening process, where sulfides are converted to disulfides.[33]

Most studies indicate that disulfides slow the rate of autoxidation. Naegeli *et al.* investigated the addition of *t*-butyl disulfide to dodecane with 15% cumene for 180 minutes at 433 K in an aluminum vessel. Increasing concentration of 8, 20, 50 and 300 ppm of *t*-butyl disulfide led to successively lower oxygen consumption, slowing autoxidation.[52] In another study dibutyl disulfide was added to dodecane in a volume ratio 1:500 in a PetroOxy device with gold plated walls, the temperature was 423 K. The addition of dibutyl disulfide increased the residence time by +320% compared to neat dodecane, slowing autoxidation.[115]

The oxidation products arising from disulfides in decane, a simple jet fuel surrogate solution, were analyzed by Rawson *et al.*[51] In their study 400 μL of diphenyl disulfide and 200 μL *t*-butyl hydroperoxide (at a concentration of 5-6 mol dm^{-3}) was added to decane and stressed for 2 h at 413 K. The products were characterized using GC-MS and GC-AED. The dominant product was thioanisole, a sulfide, suggesting the scission of the S-S disulfide bond. No evidence of thiosulfonate or thiosulfinate products was found, as were suggested in Figure 2.10. However, in earlier work, Mushrush *et al.* identified thiosulfonates and thiosulfonates at 338 K when 0.03% of diphenyl disulfide was added to JP-5.[139] The different products between Rawson's and Mushrush's study highlights the sensitivity to the testing conditions, and the potential role of sulfonate and sulfinates as intermediate species to further oxidized products. The addition of *t*-butyl hydroperoxide in Rawson *et al.*'s study could have led to exaggerated oxidation conditions, compared to the Mushrush *et al.*'s study

which relied on the formation of peroxides *in-situ* from dissolved oxygen.

The mechanisms whereby disulfides slow autoxidation are explored by Naegeli *et al.*, who proposed that disulfones produced from the autoxidation of disulfides were responsible for slowing the rate of autoxidation via:



[52] Here, SO_2 produced is proposed to react with also produced alkenes, leading to polysulfone deposits. Moreover, SO_2 could react with trace water in fuels and form sulfuric acids. The formation of sulfuric acids via the oxidation of the disulfones, as shown in Figure 2.10, will also decompose hydroperoxides (see equation 2.6). Decomposition of hydroperoxides from disulfides can be seen in the results of Kauffman *et al.*'s study in which 1000 ppm of diphenyl disulfide was able to reduce peroxides from 5.5 mmol L^{-1} in un-doped fuel to 1.5 mmol L^{-1} . Interestingly, the addition of disulfides also lead to increased levels of phenols, which have been shown to greatly increase deposition.[69] Counter to this hypothesis, once again Wechter *et al.*'s work can be cited,[149] which argues against acids in fuel due to solvency effects.

Looking at the effect of disulfides on deposit formation. An early study by Taylor and Wallace explored the deposition characteristics of dibenzyl disulfide and dibutyl disulfide in 1000 ppm in a conventional jet fuel. They found that both compounds increased the deposition formation rate, with dibenzyl disulfide having the greatest effect.[35] In one study, *n*-butyl disulfide and diphenyl disulfide was added to a Jet-A fuel and a dodecane solvent for 180 min at 433K in an aluminum vessel. Both the sulfur compounds increased deposition.[52]. When Rawson *et al.* doped 2.1 mmol L^{-1} of diphenyl disulfide in Jet-A-1 fuel deposit were greatly increased compared to the un-doped fuel at $12\,000 \mu\text{g mol}^{-1}$ at the end of 15 h stressed. This is even in comparison to a fuel with 1.6 mmol L^{-1} of sulfonic acid which produced around $6000 \mu\text{mol}^{-1}$ after 15h.[51] Overall, it is clear that disulfides have a deleterious impact on fuel deposition.

The mechanism for disulfide deposit formation can be presumed to be similar to deposition from the thiol class since disulfides eventually form sulfonic acids, see Figure 2.6. Rawson *et al.* also studied the role that disulfides had on deposition.

Although no acid production was directly measured, there was evidence of sulfonic acids by the presence of sulfonic acid esters.[51]



Figure 2.14: Generic structure of a Thiophene

Thiophenes Thiophenes are thought to be a relatively benign sulfur species by some authors,[151, 152, 153] but like many of the previous sulfur compounds other studies disagree.[150, 130] There are no limits placed on thiophenes specifically in jet fuel standards,[128] but are limited through the wider sulfur fuel limit. Thiophenes are often identified as the most abundant sulfur compound class in jet fuel.[154]

Let's first consider the autoxidation behavior of fuels containing thiophenes. Rawson *et al.* found that 58 mmol L^{-1} of tetrahydrothiophene doped in Jet-A-1 for 14 h at 433 K slowed down the rate of autoxidation.[51] Thiophene autoxidation products were studied by Epping and colleagues in model fuels containing aromatics and straight chain compounds, thiosulfoxides and thiosulfones were the only two products detected by ESI-MS.[68] Here, thiophenes slow the rate of autoxidation by acting as a radical sink, a preferential site for oxidation rather than direct reduction of hydroperoxides compared to the other sulfur species. This was demonstrated by Kauffman *et al.* who showed that sulfones and sulfoxides in fact increase the concentration of hydroperoxides.[69] Mushrush *et al.* also highlights the phenomena of thiophenes increasing hydroperoxide concentration, but it is unclear as to how this occurs.[139]

The deposition characteristics of fuels containing thiophenes has been investigated by several authors, where there seems to be disagreements on their effect on the formation of deposits. In an early study, Taylor and Wallace found that 1000 ppm of dibenzothiophene added to a conventional jet fuel had no discernible effect on the deposition rate over the temperatures 456-500 K.[35] Mushrush *et al.* point to thiophenes being low-deposit promoters due to their low reactivity towards hydroperoxides, where they found that less than 1% of thiophenes react in a 2-fold molar excess of *t*-butyl hydroperoxide. However, since it has been shown that thiophenes have a retarding effect on autoxidation, this is unlikely to be direct evidence

for low deposition characteristics.[141] Nevertheless, in a later study comparing the deposition tendencies of two Jet-As, one containing 0 ppm of sulfur and one containing 4200 ppm of dibenzo and benziothiophenes showed that both fuels had almost identical deposit concentrations after heating for 363 K in a glass container for 16 h.[154] Despite evidence presented here suggests that thiophenes are innocuous to fuels, a few studies find the opposite is the case.

Looking at studies showing thiophenes increasing deposition, Daniel and Heneghan found that adding $10 \mu\text{g L}^{-1}$ of dibenzothiophene to Jet-A in a glass walled container at 408 K increased average deposition over an un-doped fuel.[150]. A later study by Epping *et al.* doped 0.1 mol L^{-1} of dibenzothiophene in fuel showed that deposition increased by 60% compared to the clean fuel.[68] Outside the jet fuel area, one study demonstrates that a number of different thiophene compounds increase deposits in gasoline, with dibenzothiophene being especially deleterious.[130]

Exploring a possible mechanism that thiophenes may lead to deposits may help explain the conflicting results between the above studies. As was highlighted evidence from Epping *et al.*, thiophenes tend to form non-acid products like sulfones and sulfoxides.[68] Moreover, elemental analysis from deposits produced in fuel doped with thiophenes show no increase in sulfur compared to deposits from an thiophene-free fuel, suggesting thiophenes themselves do not take part in directly in deposit forming reactions. However, the ability of thiophenes to increase the concentration of hydroperoxides as shown by Kauffman *et al.* and Mushrush *et al.*,[69, 139] could mean that fuels with other components known to produce deposits in the presence of increased hydroperoxides are responsible for the increased deposition. Because even conventional fuels are hugely varied in composition, trace compounds other than the thiophene component could explain the observation that some studies show no effect on deposition whereas others show an increase.

2.2.4.2 Oxygenated Species

Various oxygen-containing species are present in jet fuel, the key classes are: ketones, aldehydes, alcohols, carboxylic acids and phenolic species.[33] Many of these species are formed in storage by low temperature autoxidation or are found as indigenous species.[155] When the fuel undergoes autoxidation and dissolved oxygen forms hydroperoxides, oxygenated species are formed at various proportions depending on

the physical and chemical properties of the bulk medium.[27] Several papers have attempted to correlate the presence of these species to the formation of deposits in order to better understand their role in deposition mechanisms.

Ketones, Aldehydes and Carboxylic Acids The oxygenated species- ketones, aldehydes and carboxylic acids - arise from the majority of autoxidation reactions from hydrocarbons, albeit in different proportions, so studying their specific effect on deposits has been difficult.[101] Nonetheless, several authors have studied their effect on deposition- either by correlating their initial concentrations to their influence on the fuel or by doping fuels with them.

An investigation by Taylor and Frankenfield looked into the effect of oxygenated compounds in low oxygen conditions. Removal of oxygen from the fuel simulates the depletion stage experienced by fuel in a closed system (Figure 1.10). In this way the ability of autoxidation products to oligomerize/polymerize into larger species can be studied in isolation from their effect on autoxidation. Nonetheless, removal of oxygen also precludes any free-radical deposition effects, which may be required for agglomeration of oxygenated species. The base fuel chosen was a JP-5, a US military grade fuel, with less than 1ppm thiol sulfur, 234 ppm total sulfur and 1 ppm total nitrogen. In each case, the compounds were added to deoxygenated JP-5 bring the total oxygen heteroatom level to 100 ppm. A flowing 316 steel walled rig at 69 atm was employed with 4 zones at 371 °C, 427 °C, 482 °C and 538 °C respectively. Several classes of oxygenated compounds were investigated as shown in Table 2.1. The hydroperoxides tested increased deposit compared to the base fuel as they act as initiators to the radical chain mechanism in the absence of oxygen. Presumably these radical products would begin to form products with the impurities in the JP-5 fuel. *N*-dodecanoic acid also showed increased deposit in relation to the base fuel, the other acids tested also slightly increase deposition with the exception of 2-ethylbutyric acid.[156] Within the context of sulfurs, acids have been suggested to take part in condensation reactions in the bulk phase and/or play a role in the adhesion of deposits to metal walls (see Section 2.2.4.1). Carboxylic acids have been suggested to take part in similar mechanisms.[74]

Antonio *et al.* found that carboxylic acids tend to chemisorb to iron in model diesel fuels in.[49] In another study, Hazlett *et al.* found carboxylic acids- dode-

canoic, furoic and chloroacetic- all increased the amount of bulk deposits in straight run distillate fuel. The fuels were aged over 2 weeks at 80°C in a glass walled vessel. Interestingly, the H⁺ concentration in aqueous solution for each acid was able to predict the total amount of deposits produced (Figure 2.15). However, this correlation broke down when comparing strong (sulfonic) and weak acids (carboxylic). Nonetheless, authors note that it is surprising that such an analytical approach would be successful due to the extent of acid dissociation in non-polar media. The authors state that fact that such a correlation was able to be produced is suggestive of some limited dissociation in organic media. Furthermore, since no chlorine was found in the final deposits when chloroacetic acid was added, the authors indicate that the acids are acting as catalysts in deposit formation.[127]

The other compounds demonstrating significant deposit enhancement in Taylor and Frankenfield's study were methyl benzoate and 5-nonanone, whereas phenols and aliphatic alcohols demonstrated a moderate increase (Table 2.1). By contrast, aromatic esters and other naphthenic compounds were mostly inert or low depositors. The authors note that the naphthenic compounds, which tend to produce lower levels of deposits, are known to have a lower resistance to pyrolysis. Therefore, they explain the low deposition characteristics through the enhanced solubility of the naphthenic compounds towards polar agglomeration products compared to their aliphatic counterparts.[156] In another study, Tseregounis also proposes that oxidative species formed from autoxidation, are inhibiting deposit formation due to solvency effects. Tseregounis proposed that oxygenated compounds may increase the solubility of deposit precursors in fuels, therefore delay deposit formation.[130] It has been shown in other papers that jet fuel deposits are soluble in alcohols and mixtures of alcohols and ketones, albeit at much higher concentrations that would be formed from the autoxidation of fuel.[157, 158]

Phenols Phenolic compounds have long been known as autoxidation inhibitors in fuel, but inversely are known to increase deposition.[159] Phenols are present in fuel as indigenous components,[24] as antioxidants in fuel,[78] and are even thought to form from thermal autoxidative stressing of fuel.[24] The antioxidant capabilities of phenols in fuels are due to two main factors: the bond strength of the O–H moiety and the ability of phenoxy radicals to stabilize themselves. Firstly, the bond disso-

Total Deposits				
Class of Oxygen compound	Added Compound	Oxygen Content, ppm of O ₂	μg of carbon	As ppm based on fuel
Peroxide	Di- <i>tert</i> -butylperoxide	0.2	2878	1.49
	Cumene hydroperoxide	0.1	7219	3.73
	<i>tert</i> -Butylhydroperoxide	0.2	8934	4.62
	Cyclohexanecarboxylic acid	0.1	1563	0.82
Carboxylic acid	<i>n</i> -Decanoic acid	0.1	2997	1.54
	Cyclohexanebutyric acid	0.2	1730	1.54
	2-Ethylbutyric acid	0.2	1291	0.67
	2,4-Dimethylbenzoic acid	0.3	1801	0.93
Phenol	2-Methylphenol	0.2	1561	0.81
	2,6-Dimethylphenol	0.1	2048	1.06
	2,4,6-Trimethylphenol	0.1	1451	0.75
Furan	Benzo(b)furan	0.2	1505	0.78
	Dibenzofuran	0.2	1410	0.73
Alcohol	<i>n</i> -Dodecyl alcohol	0.9	2046	1.06
	4-Methylcyclohexanol	0.3	1356	0.70
Ketone	5-Nonanone	0.7	2422	1.26
	4-Methylcyclohexanone	0.3	1244	0.64
	Methylcyclohexanone	0.2	1318	0.68
Ester	Methyl benzoate	0.7	2488	1.29
	Pentyl formate	0.8	1894	0.98
	Base fuel	0.4	1485	0.77

Table 2.1: Effect of various oxygenated compounds of jet fuel deposition, recreated from [156]

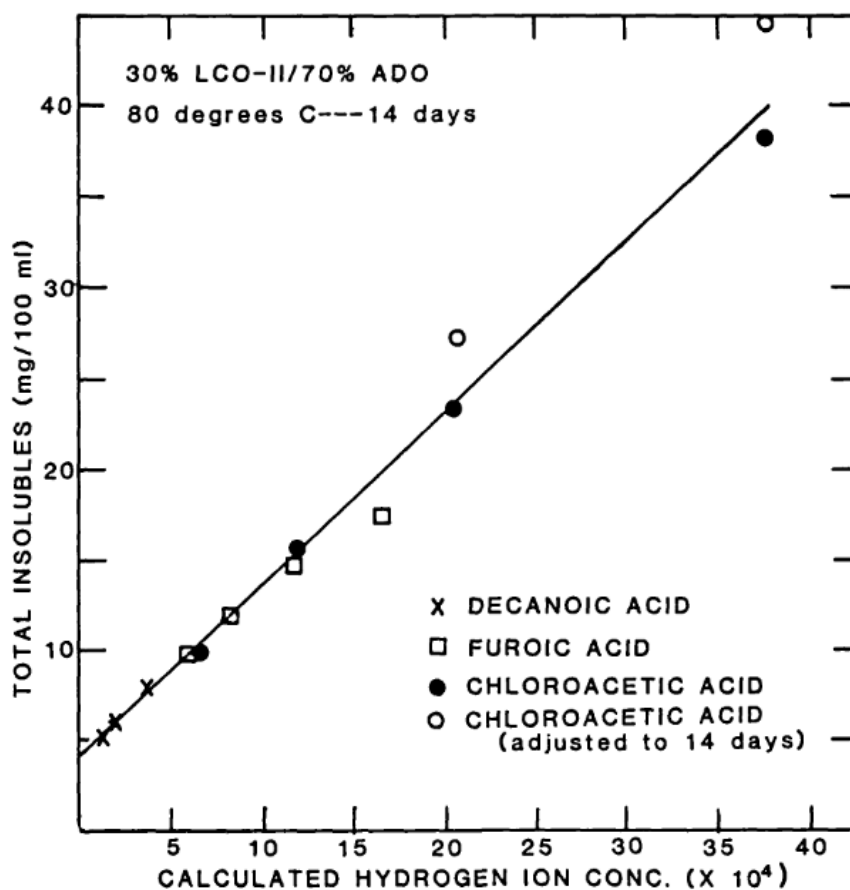


Figure 2.15: Correlation between total deposits and net hydrogen concentration, taken from [33]

ciation energy (BDE) of the O-H bond compared to the aliphatic C-H bond shown to be 79 kcal mol^{-1} and $96\text{-}83 \text{ kcal mol}^{-1}$ respectively from DFT calculations.[29] The difference in O-H and C-H BDE means the phenolic hydrogen preferentially abstracted compared to the bulk fuel. In addition, alkyl-substituted phenols have enhanced stability due to inductive effects adding electron density to the ring as shown in Figure 2.16. The enhanced stability of phenoxy radicals allows them to act as a thermodynamic sink, slowing the free-radical chain reaction ('chain breaking').

First the effect that phenols have on autoxidation will be explored. Zabarnick *et al.* were able to show that the addition of BHT to Jet-A fuel slowed the rate of autoxidation significantly. The doped run led to a far slower drop in headspace pressure, indicative of slower oxygen consumption.[159] A later study by Kerkering *et al.* showed that various substituted phenols were able to slow the rate of autox-

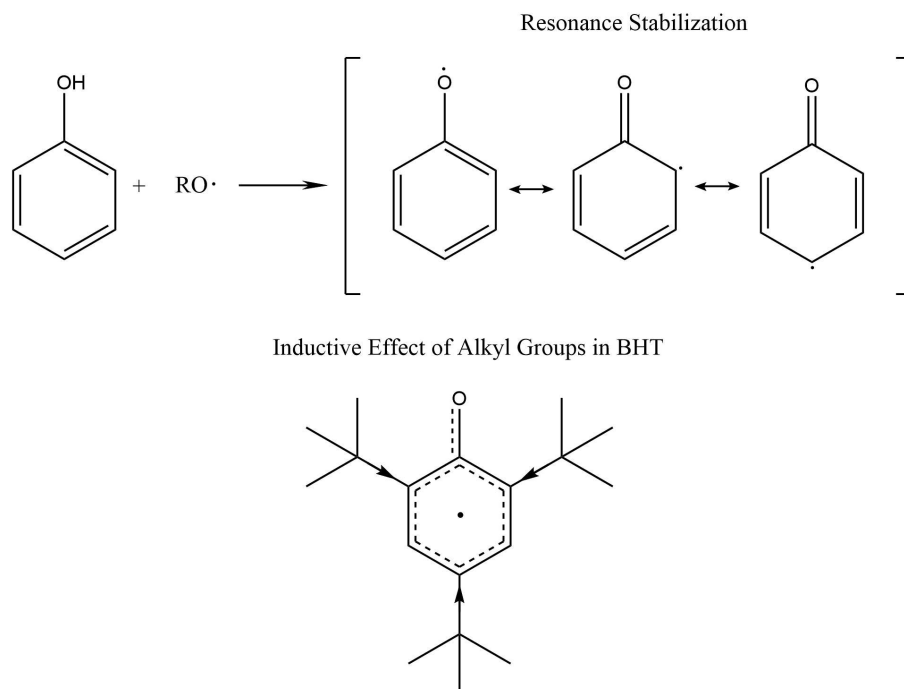
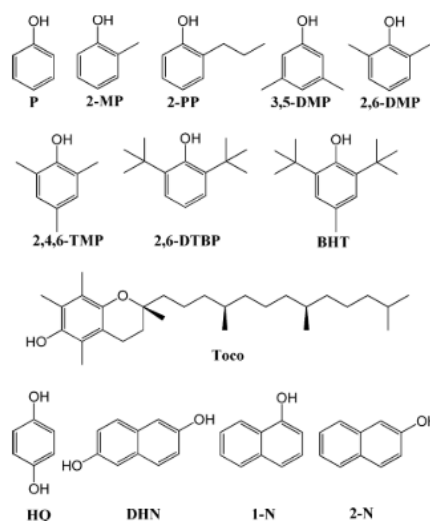


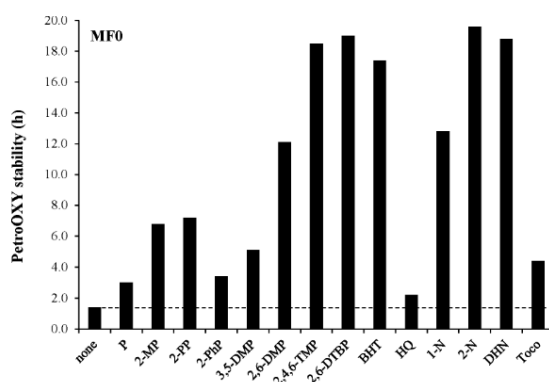
Figure 2.16: Resonance stabilization of the phenoxy radical and BHT

idation significantly in several model fuels. The results show that all the phenolic compounds employed slowed down the rate of autoxidation as shown in Figure 2.17. Moreover, the greater degree of methyl substitution the greater the stability, due to inductive effect described in Figure 2.16. The opposite effect is seen in the case of 2-phenylphenol (2-PhP on Figure 2.17b), where the electron withdrawing capabilities of the phenyl group lead to a lower retarding effect on autoxidation compared to methyl groups.[160] Overall, it is clear both indigenous and additive phenols have an influence on slowing the rate of autoxidation.

In contrast to their retarding effect on autoxidation, phenols have consistently been shown to enhance deposition. Studies correlating constituent and doped phenols with final deposits are numerous. Early work by Hazlett *et al.* employed caustic extraction techniques to isolate natural phenol components from real fuels, and demonstrated that the addition of these phenol-rich caustic extracts to stable fuels increased deposition. In their study, several Bass Strait fuels were aged at 80°C for 42 days in a glass-walled reactor and total insolubles were measured after. A fuel (LCO-II) with known high phenolic content was selected for caustic extraction- the light brown extract representing 0.9 g L⁻¹ of the total fuel contained almost no organic acids and high concentrations of substituted and non-substituted phenols. The



(a) Phenols Tested



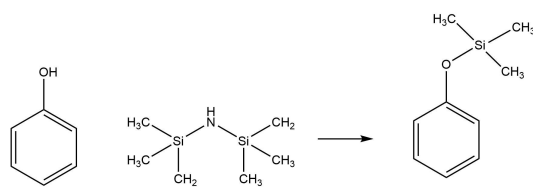
(b) Effect of Phenols on petroOxy Stability

Figure 2.17: Effect of various phenolic Constituents on the petroOxy stability- time to reach 10% pressure drop [160]

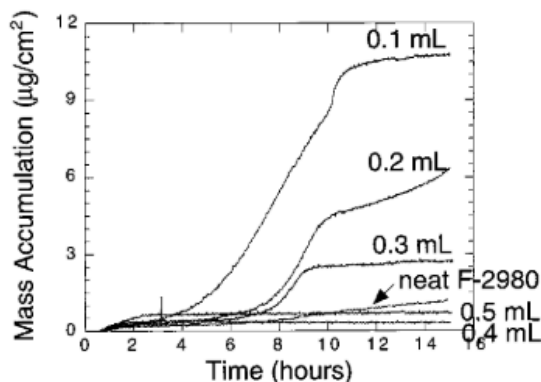
authors highlighted that absence of indigenous acids meant that any acid catalyzed formation of deposits could be discounted. However as highlighted previously, acids could still form from autoxidation reactions during aging.[123] When LCO-II extract was added to a low depositing fuel (ACO), the total insolubles at the end of testing increased from 20 mg L^{-1} to almost 50 mg L^{-1} . When the neat LCO-II was compared with the LCO-II after caustic extraction, the total insolubles were also reduced.[161]

Further exploring phenolic deposition effects, Zabarnick *et al.* found that passivation of the reactive portion of the phenol molecule by silylation agents (Figure 2.18) were able to significantly reduce deposits. Several Jet-A fuels were doped with hexamethyldisilazane (HMDS) in the range of $0.1 - 0.5 \text{ mL}/60 \text{ mL}$ fuel and stressed

in a QCM device. Interestingly, for some of the fuels, before a variable threshold concentration of HMDS, deposition was higher. However, above the HMDS concentration thresholds lower insolubles were produced for all the fuels tested, attributed to blocking activity of the phenolic $-OH$ group. Nevertheless, a solid phase extraction technique, similar to the caustic extraction technique as described in Hazlett *et al.*'s study above, showed that removing phenols was more effective at reducing deposition.[162] Both Hazlett *et al.*'s [161] and Zabarnick *et al.*'s [162] extraction/passivization studies demonstrate that phenols contribute significantly to deposition. Correlations between initial phenol concentration and final deposit also indicate phenol's role in deposition.



(a) Silylation of Phenols



(b) Effect of Varying Concentrations of Hexamethyldisilazane on Deposition

Figure 2.18: Silylation of phenols and its effect on Jet-A deposition in a QCM at 140°C [162]

In the 2000s, two studies testing a large suite of fuels with varying heteroatomic components showed initial phenol concentrations were a strong predictor for deposition. The first study by Balster *et al.* quantified the total polar concentrations of 20 fuels and the distributions of the polars. Quantification and classification was achieved via solid phase extraction followed by HPLC then GC-MS (SPE-HPLC-GC-MS). Each fuel was stressed and total deposits were measured in a QCM at 140

°C for 15 h. For the 20 fuels tested, total phenols gave the strongest correlation with total deposits, but only an extinction coefficient (R^2) of 0.21. However, when several outlier fuels were excluded (defined by strong deviations between total polars and deposit amount) in this class, this increased to 0.60. The other polar classes quantified in Balster *et al.*'s study were the nitrogen compounds indoles, carbazoles, pyridines, anilines, and other oxygenates. All these gave poor correlations before 'unusual' fuels were excluded.[65] Poor correlations could be due to the fact that other heteroatoms known to cause deposition were excluded in the analysis. The unusual fuels could also have contained high amounts of reactive sulfur and/or dissolved metals skewing the data.

The second study, by Sobkowiak *et al.*, quantified the polar content in 4 Jet-A fuels and 1 Fischer-Tropsch (FT) fuel and correlated the composition against total deposits produced in a flowing reactor. The 4 Jet-A fuels were used in the previous study by Balster *et al.*, but the FT fuel was used to create fuel blends in order to adjust the total polars. When the 4 neat fuels were tested alongside 4 1/1 FT blends in the flowing reactor at 550°C, an R^2 of 0.8354 coefficient of determination was produced between total concentration of phenols and mass of deposit. FT fuels tend to be completely free of heteroatoms, so when blended with conventional fuels they will act as a diluent for fuel heteroatoms. When one outlier fuel was removed, a coefficient of determination of 0.9777 was given. The authors compare this to the R^2 of 0.5855 of the total polars to deposits in Balster *et al.*'s study. However, since their selection of fuels is itself a subset of Balster *et al.*'s study, the comparison is invalid. The inclusion of 4 1/1 FT blends of the original study helps to artificially increase the data set size for the phenol deposits correlation. The inclusion of the blends highlights a linear relationship between phenol concentration and total deposits within specific fuels- rather than specifically showing a stronger correlation between indigenous phenols and total deposits.[163] The linear relationship between FT blend and thermal oxidative instability was not observed in a previous study where blending gave a complex non-linear relationship.[44] Despite the deficiencies of the second study, both demonstrate that indigenous phenol concentration gives reasonable prediction for oxidative deposits. However, since thermal oxidative decomposition is a complex multi-component process, outlier fuels had to be excluded in order to produce significant correlations in both studies. Outlier fuels may contain other components like sulfurs or dissolved metals which were not quantified prior to stressing.

Table 2.2: Studies correlating phenols with mass of deposit

Reference	Coefficient of Determination (R^2)	Coefficient of Determination Excluding Unusual Fuels (R^2)
[65]	0.21	0.60
[163]	0.8353	0.9777

Not all studies indicate that phenols exhibits large amounts of deposit . A study by Clark and Smith quantifying deposits generated from doped fuels using a JFTOT and carbon burn-off technique showed phenols only very slightly elevated deposit formation. A clean conventional Jet-A-1 fuel yielded 10 μg of deposit at 623 K. The same fuel and conditions doped with 100 mg L^{-1} of 3,5-dimethylphenol and 2,6-dimethylphenol produced 14 and 15 μg deposit respectively. The levels of deposit generated by phenols are low in contrast to the other compounds tested such as ethane sulphonic acid, which generated 225 μg of deposit. Furthermore, the phenol deposit levels are lower than all the nitrogen and sulfur species tested.[164] The results here are not explicitly contradictory with the work highlighted previous work showing phenols as depositors. However, the work here shows that the influence phenols have on deposition may be lower than for other species. Moreover, the flowing configuration in the JFTOT device may not provide enough residence time for phenols to form deposits, despite being a closer representation of a real fuel system. As highlighted in Figure 2.22, some phenols only exhibit deposits after a long stressing time. Interestingly, Clark and Smith found that phenols combined with strong and weak acids lead to a synergistic effect of deposit formation. The synergistic effect manifests in higher levels of deposits than the sum of individual total deposits forming from phenols and acid separately.

The studies demonstrating phenols as high depositors in Table 2.2 neglected to test for the presence of sulfur components. Naegeli *et al.* suggests the ability of phenols to form deposits could be reliant on the presence of acids. Naegeli *et al.* compared the LIF spectra of a phenolic resin and deposits generated from a stressed Jet-A fuel (Figure 2.20). Phenolic resin was formed by acid-catalyzed

cross-coupling reactions between and aldehydes.[147] Nonetheless, a recent study by Zabarnick *et al.* showed that sulfide suppresses phenol deposit interactions (Figure 2.22). However, the identity of the sulfur compounds could have a varying effect on the interaction. Further characterization work needs to be done to understand phenol-sulfur interactions.

Work characterizing the structure of deposits from a surrogate fuel [68] and a low-heteroatom phenol-containing middle-distillate [155] has indicated phenols oxidatively couple. In each study, deposits were generated with a flask oxidizer, and the resultant deposit was analyzed using soft-ionization mass spectroscopy techniques. The compounds detected match generic phenolic oxidative-coupling products presented in Figure 2.19. In the case of the middle distillate fuel tested, the authors suggest copper and pyridine could catalyze the oxidative-coupling reactions, enhancing the amount of deposit.[155] Oxidative coupling occurs in the presence of free-radicals, and are known to occur for a large number of compounds, particularly aromatic compounds.[165]

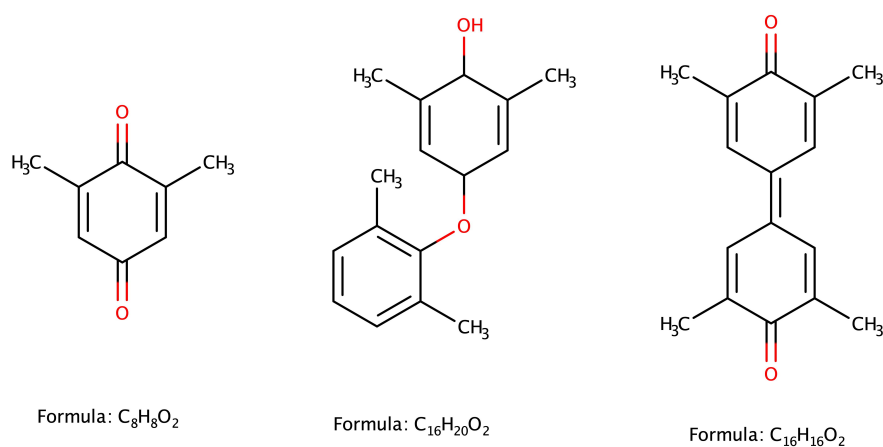


Figure 2.19: Products from 2,6-dimethylphenol stressing produced an autoclave autoxidizer detected by ESI-MS [68]

Despite the relationship between indigenous phenols and deposits, the phenolic antioxidant BHT is added to military grade fuels as a way of reducing thermal oxidative deposits. Its widespread usage as a deposit reducer highlights the importance understanding the link between the structure of the phenolic species and its tendency to form deposits. In a series of flowing tube tests Ervin *et al.* clearly showed that BHT has a strong influence in reducing deposition.[167] Since BHT is a sub-

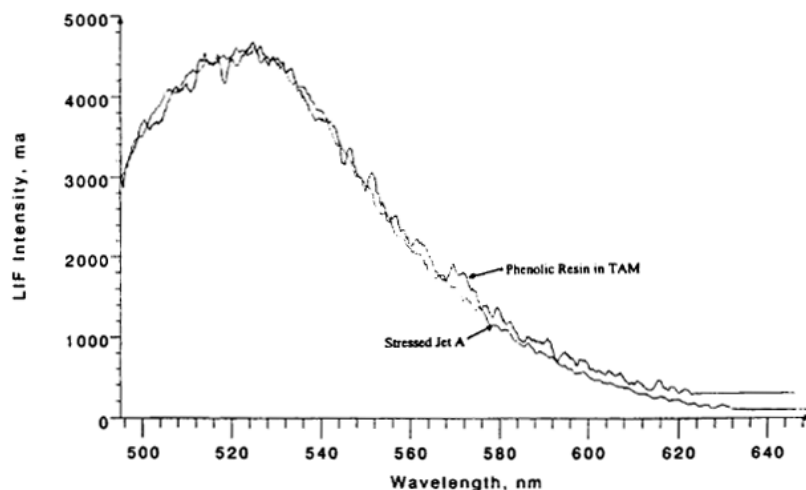


Figure 2.20: LIF spectra of Jet-A deposits and a Phenolic Resin [166]

stituted on the ortho- and para- positions on the ring structure as shown in Figure 2.16, there is a large steric penalty for any oxidative coupling on these sites. The effect that substituted methyl groups have on the binding sites of oxidative coupling can be seen in the production of polyphenylene ethers (PPEs). Here PPEs are made with the 2,6-dimethyl phenol monomer as the methyl groups prevent binding on the ortho- and meth- sites of the phenol, yielding polymer chains bonded only on the para- sites.[165] However, Zabarnick *et al.* showed that BHT will eventually form oxidative deposits greater than a neat fuel via coupling reactions if the residence time is long enough. In Zabarnick *et al.*'s study, a neat Jet-A was tested and with 25 mg L^{-1} BHT in a QCM device at $140 \text{ }^\circ\text{C}$ for 15 h. Initially the BHT doped fuel gave a lower rate of deposition but after around 8h the BHT-doped fuel gave greater amounts of deposit.[159] Comparing it to Ervin *et al.*'s study where BHT-doped fuels gave significantly lower deposition in a flowing rig, it is likely fuels in a flowing rig, and in a real fuel system, will have far lower residence times than the 15 h static test undertaken in Zabarnick *et al.*'s study.

2.2.4.3 Nitrogen Species

Nitrogen species tend to be at a lower concentration in fuels than oxygenated and sulfur-containing species. Nonetheless, nitrogen has often been found at higher levels in deposits than in the parent fuel.[168] The most commonly found nitrogen species in jet fuels are: indoles, carbazoles, anilines, pyridines, and amines.[28, 24] In general, the majority of literature has demonstrated that nitrogen-containing compounds exhibit varying antioxidant capabilities, and has adverse effect on ther-

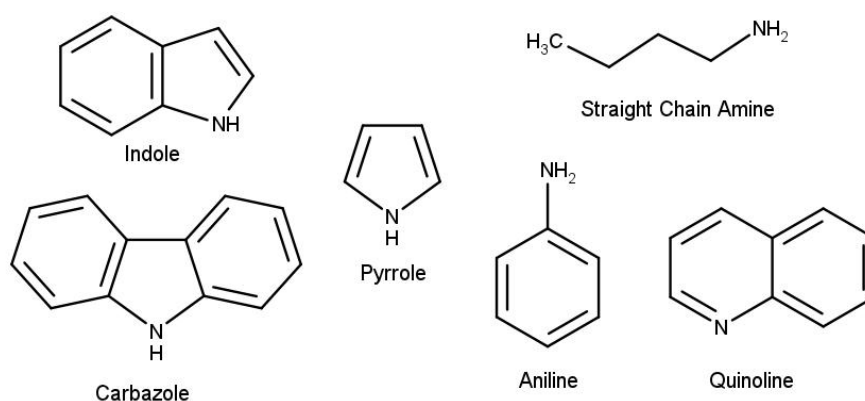


Figure 2.21: Common nitrogen compounds in fuel

mal oxidative stability. The effect that nitrogen species have on the autoxidation of fuels has received little attention, but they have been extensively investigated in relation to their effects on deposition.

Despite limited studies on the effect of nitrogen species on autoxidation, work by Smith and Clark provides some insight into differing antioxidant properties of nitrogen compounds in fuels.[169] In Smith and Clark's study, 2,5-dimethyl pyrrole demonstrated mild antioxidant properties whereas several quinolines promoted oxidation. Interestingly, indole displayed neither antioxidant or pro-oxidant characteristics. All compounds were added as 40 ppm of nitrogen to conventional Jet-A-1 and were tested in the flask oxidizer pictured in Figure 2.1 at 433 K.[170] A later study by Zabarnick and workers reinforced the findings that indoles have a neutral effect on the rate of oxidation. In their study a QCM device was employed with measurable headspace oxygen. The QCM test demonstrated that the oxygen consumption did not change when 100 mg L⁻¹ of indole was added to a jet fuel-like solvent (Exxsol D80), compared to the clean solvent. In the same study, several other nitrogen compounds were investigated for their effect on oxidation rate. None of the nitrogen compounds- carbazoles, anilines, quinolines and pyridines -demonstrated significant antioxidant or pro-oxidant characteristics.[63] It is clear that more work needs to be done on elucidating the role that nitrogen compounds play in the autoxidation stage.

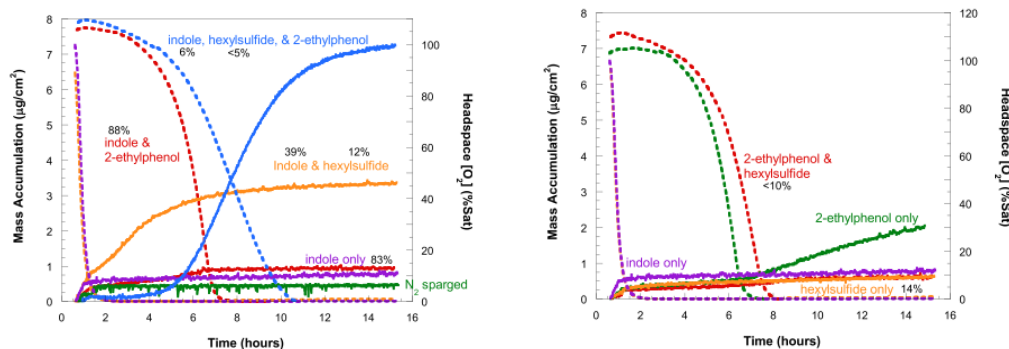


Figure 2.22: QCM test on Exxsol D80 solvent doped with various nitrogen, sulfur and phenolic compounds. The numbers adjacent to the species names are the percentage of remaining reactant at the end of the run [63].

An early investigation by Thompson *et al.* on distillate fuels demonstrated that pyrroles promoted the greatest amount of deposit compared to an array of common nitrogen compounds. Thompson and workers selected two distillate fuels: fuel 1 with poor storage stability and high sulfur content, and fuel 2 with better storage stability and low pyrrole and sulfur content. The fuels were stored in a glass flask at 311 K for periods of up to 315 days, and doped with pyrroles, quinolines and pyridines. Both fuels exhibited greater levels of deposit when doped with all classes of nitrogen compounds. In fuel 1, pyrroles produced 0.105 mg L^{-1} of insoluble gum compared 0.070 mg L^{-1} when an equivalent amount of isoquinoline was added. The same test was not performed for fuel 2. Nonetheless, when fuel 2 was tested with indole (a substituted pyrrole) and aminopyrrolidine (a 6-membered nitrogen heterocycle similar to quinoline) the indole produced around twice the amount of insoluble material. The authors investigated whether the increased acidity the 5-membered heterocycles was responsible for enhanced deposition, but a caustic wash had no effect on deposition. Elemental analysis of all the deposits indicated that the deposit was not entirely composed of the nitrogen species coupling with each other, but the main fuel was involved in deposits too.[171] A possible explanation for these results, not indicated by the authors, is that 5-membered rings have a greater propensity for coupling with electrophilic species than 6-membered rings due to the stability of the pyrrole intermediate.

The deleterious effect of nitrogen compounds on fuel oxidative stability was reinforced by Antoine. Antoine found that nitrogen compounds universally decrease break-point temperatures in a JFTOT.[172] Jet-A doped with indole and pyrrole

(5-membered heterocycles) exhibited the most extreme drop in break-point temperature. By contrast, pyridine, quinoline and 4-ethyl-pyridine (6-membered heterocycles) solutions only lowered the break-point temperature slightly.[172] In another study, a survey of twenty conventional fuels correlating the mass of deposit with measured heteroatom species found that indole and carbazole were correlated with the mass of deposit, but pyridines, anilines, and quinolines had no correlation. In the survey, total polars were detected via a SPE-HPLC-GC-MS system, and the fuels were stressed in a QCM. When outlier fuels were excluded, indole and carbazole gave correlation coefficients of 0.38 and 0.37 respectively. On the other hand, pyridine, aniline and quinoline gave no correlation, with coefficients of 0.04, 0.00 and 0.02 respectively.[65] The work here further demonstrates the higher propensity of 5-membered nitrogen heterocycles to form deposits compared to 6-membered rings.

Expanding on the work on 5-membered rings by Thompson *et al.*, Oswald and Alexis studied the effect 5-membered pyrroles had on bulk deposition in fuels. Pyrrole alone added at 0.3 mol L^{-1} did not generate when doped into solutions of tetrahydronaphthenate, hexadecane and xylene in glass containers at 316 K. However, when thiols were added, the combination of thiol and pyrrole lead to deposition. The deposition observed with thiols and pyrrole was the highest for the aromatic solvents xylene and tetrahydronaphthenate. Investigating the reactions between pyrroles and thiols further, the authors reacted two methyl-substituted pyrroles with a thiol with a hydroperoxide initiator, and analyzed the the insoluble product. The product contained OH/NH, CO, and sulfone groups. In addition, elemental analysis suggested the insoluble product contained 3 nitrogens for every 1 sulfur, indicating the thiol is directly coupling with the nitrogen species. The work here also ruled out the action of acids in the formation of deposits, since no acidity increase was found in any of the test solutions after the stress periods. In fact, Oswald and Alexis suggest the agglomeration mechanism between the pyrroles and thiols tested were free radically polymeric. In addition, the authors indicate acid-free condensation reactions between pyrroles and oxygenated species could also lead to deposit (summarized Figure 2.23).[64] However, since the characterization of the deposits was limited to elemental analysis and IR spectroscopy, the mechanism leading to insolubles is still unclear.

The synergistic effect between nitrogen species and sulfur species was further highlighted by Zabarnick *et al.*. In this study, the addition of hexyl sulfide to a fuel

surrogate (Exxsol D80) containing various 5- and 6-ring nitrogen heterocycles universally increased deposition tendency, with the exception of carbazole, whereby hexyl sulfide in fact decreased deposition. This synergistic deposition effect between nitrogen and sulfide compounds is highlighted in Figure 2.22, where the combination of indole and hexylsulfide led to a large increase compared to the mono-component indole run. Nevertheless, in Zabarnick *et al.*'s study, there seems to be no clear trend between the deposition tendency of 5- or 6-membered nitrogen compounds. Contrary to Oswald and Alexis, Zabarnick *et al.* propose an acid-base condensation reaction as the origin of the N+S interaction.[63] Bolstering the acid-base theory, the 5-membered nitrogen compounds have been shown to have lower basicity than the less problematic 6-membered nitrogen compounds.[173] Nevertheless, basicity was found to correlate with deposition tendency within each nitrogen class, but this trend broke down when comparing between classes.[174] What is clear is that further characterization work needs to be completed in order to understand the mechanism of nitrogen-sulfur interactions.

In fact, limited work has focused on the mechanisms of the deposit formation mech-

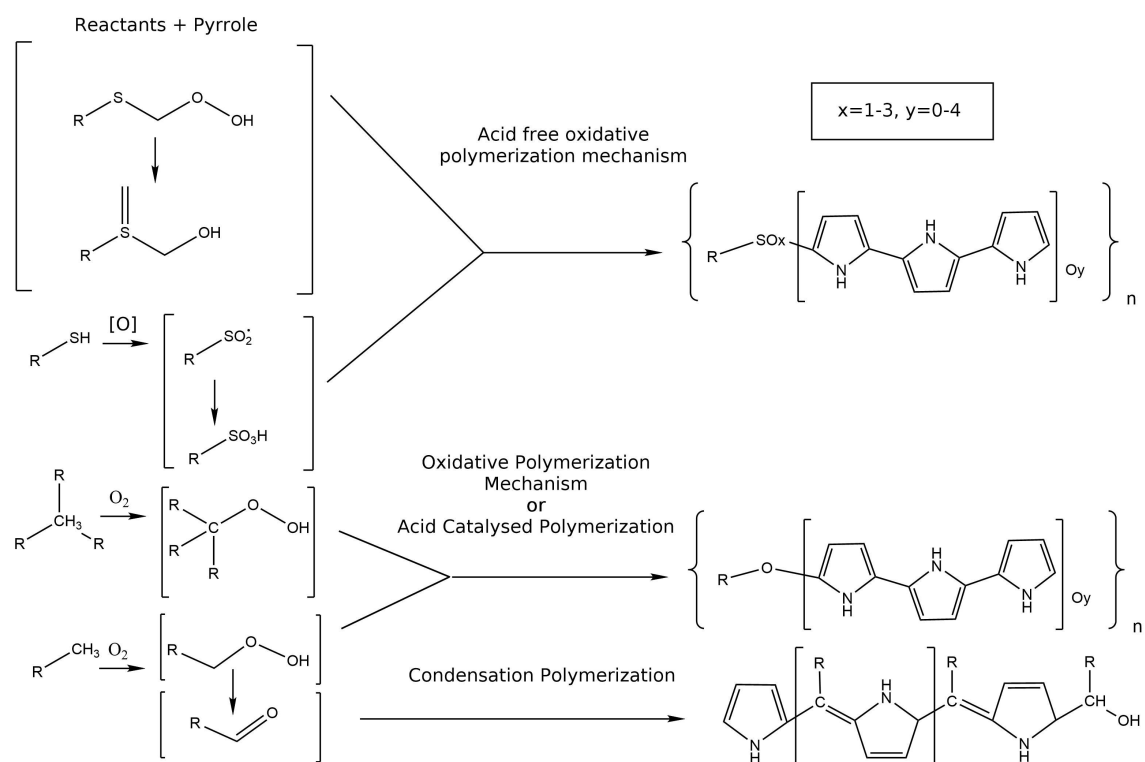


Figure 2.23: Proposed reaction pathways between nitrogen species and sulfur species and proposed mechanisms [64]

anisms of nitrogen species as a whole. Nevertheless, recent characterization work on a surrogate fuel containing indole species by Epping *et al.* indicated oxidative coupling products, analogous to phenol coupling (Figure 2.19). In Epping *et al.*'s study, a model fuel was employed where 0.1 mol L^{-1} of 1-methylindole was added to a fuel surrogate in a flask oxidizer. Soft-ionization mass spectroscopy was employed and was able to identify the probable chemical formula of the products. Due to exact knowledge of the starting components in the surrogate, the authors were able to offer likely chemical structures as shown in Figure 2.24. Oxidative coupling between nitrogen species has also been observed outside the fuels literature in non-polar media under oxidizing conditions, for pyrrole [175] and quinone.[176] Thus, this appears to be a plausible route to deposit formation for nitrogen species. Nevertheless, further characterization work is needed to confirm this.

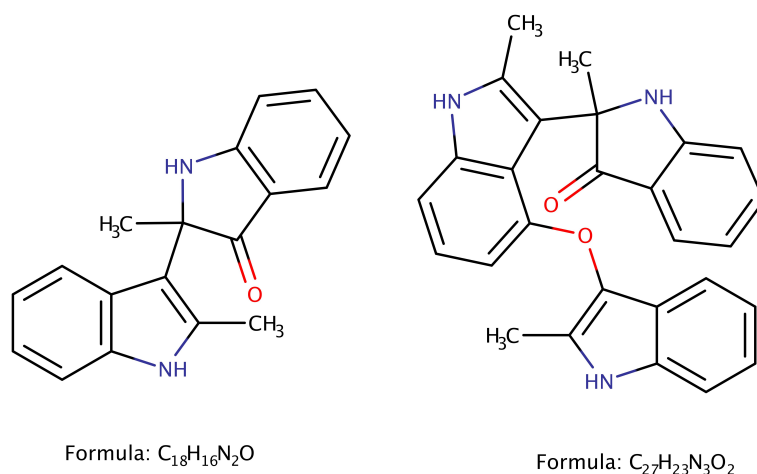


Figure 2.24: Indole coupling products produced in autoclave oxidizer detected by ESI-MS [68]

2.2.5 Wall Effects

The problem of jet fuel deposition ultimately concerns deposit growth on metal surfaces. A variety of metals come into contact with the heated fuel throughout the engine architecture, including 316 stainless steel, aluminum, and brass.[13] Deposits on the heated surfaces on jet fuel components have consistently been observed as being varnish like and difficult to remove.[33, 115, 35] Moreover, studies employing thermal gravimetric analysis (TGA) of the deposits found that deposit layers on steel surfaces only begin to be removed at $350 \text{ }^\circ\text{C}$, with the entire layer being removed 750

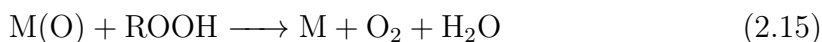
°C. Results from TGA analysis and the strong adhesion to metal surfaces implies strong chemisorption of oxidized fuel constituents to the surfaces as the predominant means of adsorption.[177] The metallurgy of the surface has been shown to influence the magnitude and nature of deposits greatly, and thus the degree of adsorption.[178] The metal surfaces have also been thought to influence autoxidation at the initiation stage:



where M represents the metal wall.[33] In the propagation stage the decomposition of hydroperoxides has been shown to be catalyzed on metal surfaces:



with the resultant metal oxide also able to decompose hydroperoxides:



thus completing the catalytic cycle.[123, 179] Various studies have attempted to understand the deposition mechanisms by correlating specific metal surfaces with deposit magnitudes and autoxidation.

Starting with the effects on autoxidation, Jones and Balster found that fuel exposed to steel tubes led to faster rate of autoxidation compared to 304 stainless steel treated with an inert siloxane polymer mono layer. In their investigation a flowing rig at 185 °C was used to test 16 fuels of varying sulfur and dissolved metal content. Autoxidation for most fuels was slowed down by the presence of the inert mono-layer. The authors posit that the dissociation of hydroperoxides is catalyzed on the metal surfaces, leading to an accelerated rate of autoxidation. It is also highlighted that a small amount of uniform deposit on the surfaces passivates further autoxidation enhancement.[123] Ervin and workers also found that silica-based layers 10,000 Å thick led to the reduction of autoxidation rate. Here, two fuels were employed in a flowing rig, a neat Jet-A fuel and the same Jet-A with BHT and MDA additives. Autoxidation was studied by measuring the fraction of dissolved oxygen remaining at the end of the tube at temperature points in the 373-513 K range. With the neat Jet-A test, the silica-treated tubes allowed a higher maximum bulk temperature of 10 K before full oxygen consumption. The Jet-A fuel, with thermal stability additives had a 20 K higher bulk temperature before full oxygen consumption.[167]

An early investigation by Kendall and Mills showed that a greater weight of deposits formed on stainless steel surfaces compared to aluminum surfaces. seven fuels with varying sulfur content were tested in a JFTOT device with aluminum tubes and stainless steel tubes at 623 K.[178] Both aluminum and stainless steel form passivation layers in air, so it is these layers where initial deposit growth will occur. For aluminum, layers are composed of Al_2O_3 , whereas with 316 steel these layers are composed of mainly ferric oxides, ferric hydroxides and Cr_2O_3 [180]. A later study by Kauffman *et al.* initially appears to contradict the Kendall and Mills study since they showed that ferric oxide powders had a far lower depositing propensity than aluminum oxide powders layered onto stainless steel.[69] However, as highlighted in an earlier paper, the lower deposition propensity of aluminum is most likely due to the migration of magnesium (present in many magnesium alloys) when the tube undergoes thermal stressing.[181] Nonetheless, oxide layers tend to reduce deposition regardless of the species involved. Antonio *et al.* highlights this in a recent study comparing the rate of deposition on polished (no oxide layers), annealed (partial oxide layer) and fully oxidized layers. The polished surface yielded the greatest amount of deposits in a hexadecane solution at 473 K after 72 h of testing.[49] Overall, it is clear that the reactivity of the oxidized surface plays a key role in determining the rate of deposition.

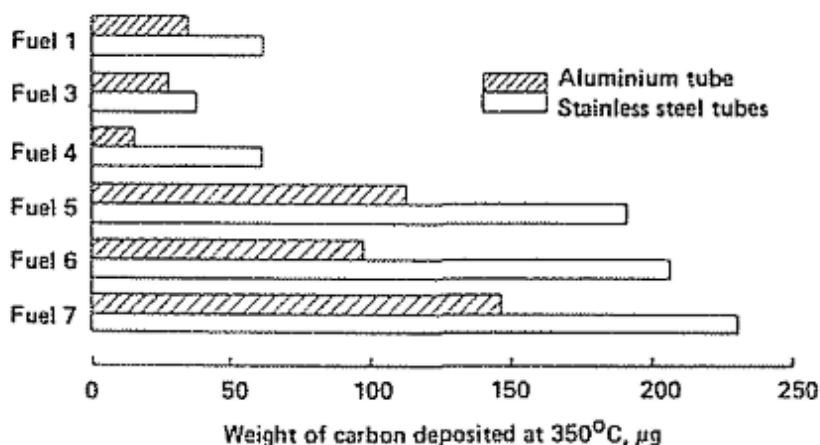


Figure 2.25: Wall material effect on deposition in a JFTOT [178]

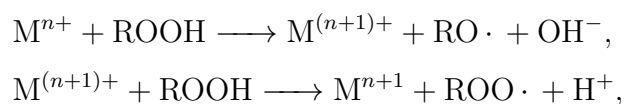
An understanding of the chemical mechanisms of adhesion of deposits to fuel system surfaces remains limited. As highlighted in section 2.2.4.1, Kauffman *et al.* have proposed that sulfur acids, formed from the oxidation of indigenous sulfur

compounds, could play a role in the deposition process. This seems plausible, particularly as sulfur acids have been used for self-assembled monolayers (SAM) outside the fuel literature.[182] Nevertheless, other indigenous and oxygenated fuel species may also attach to the wall.[182] In particular, carboxylic acids formed from autoxidation (section 2.2.4.2) could attach to the wall, particularly as they have been used as SAMs on stainless steel.[183] Further mechanistic investigations need to be undertaken to understand deposit-wall interactions.

2.2.6 Metals in Situ

Dissolved metals, or metals present as small particles in fuel, represent an acute problem for thermal stability. Dissolved metals have been suggested to slowly dissolve in the fuel via organic acids. Organic acids themselves form in the fuel due to oxidative reactions and are proposed to react with metals in the system.[184] Ppb levels of transition metals like copper, iron and molybdenum have been shown to more than double total oxidative-deposits.[125] Metals have also been shown to increase the rate of oxidation of fuel, mainly as a result of their ability to catalytically decompose hydroperoxides.

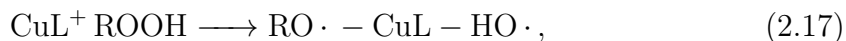
Work on the influence of copper on the oxidation of conventional fuel showed that copper ions accelerated oxidation. In Morris *et al.*'s work, copper was added to a conventional fuel and tested in a JFTOT device. The total oxygen and hydroperoxide concentration was measured over time (Figure 2.26). The rapid consumption of oxygen, and removal of hydroperoxides suggested that copper was catalytically decomposing the hydroperoxides formed. Interestingly, the authors found that copper entrained in deposit as a heterogenous phase had a low/negligible impact on oxidation, suggesting copper needs to be present in solution to have catalytic effects. The catalytic role that copper plays has led to the development of metal deactivator additives (Figure 1.5), which have been shown to reduce the oxidation of jet fuel somewhat.[185] A DFT investigation by Zabarnick *et al.* employed the B3LYP//6-31G(d) method to explore the mechanism responsible hydroperoxide decomposition by copper. The commonly cited hydroperoxide decomposition reaction:



was found to have excessively high thermodynamic barriers. The authors indicate that the existence of charged species in their non-aqueous gas phase model the used would lead to high calculated barriers. Instead, they proposed the following alternate mechanism:



where M was represented by iron, cobalt and copper in their study. Although the thermodynamic barriers were reduced, the entire reaction scheme was found to be endothermic, and hence could not be considered catalytic.[29] Building on this work, Parks *et al.* employed the *cc-pvTZ/SDD/B3LYP* method to further explore the mechanisms behind hydroperoxide decomposition. A copper naphthenate was chosen as a representative dissolved copper species due to the prominence of naphthenic acids in fuel stocks. Parks *et al.* found that although the copper naphthenate decomposed hydroperoxide readily:



the resultant $RO \cdot - CuL - HO \cdot$ did not favorably liberate the resultant radicals. Nevertheless, $RO \cdot - CuL - HO \cdot$ could readily react with fuel hydrocarbons:



potentially offering a catalytic route for hydroperoxide decomposition and thermal oxidative degradation by metals.[94]

Metals also have been shown to increase deposition rates. In an early study by Taylor, iron, copper, nickel and cobalt acetate were all added at 50ppm to a conventional Jet-A fuel. For each metal, the deposit rates increased, with all the dissolved metals exerting a similar influence. To explain these results, Taylor referred to the ability of metals to initiate the free-radical chain reaction via equation 2.13. A later study by Jones *et al.*, employing a conventional fuel containing ppb levels of copper and iron, looked at the effect of adding a metal deactivator on deposition. Deposition was reduced at short stress times in a flowing rig, but at longer times deposition reached the level of fuels containing no metal deactivator.[31] Like Taylor, Jones *et al.* point to the role of metals in initiating the free radical decomposition process. In addition, since nitrogen and phenol species have been shown to oxidative couple (figures 2.19 and 2.24), there is the possibility of transition metals catalyzing this

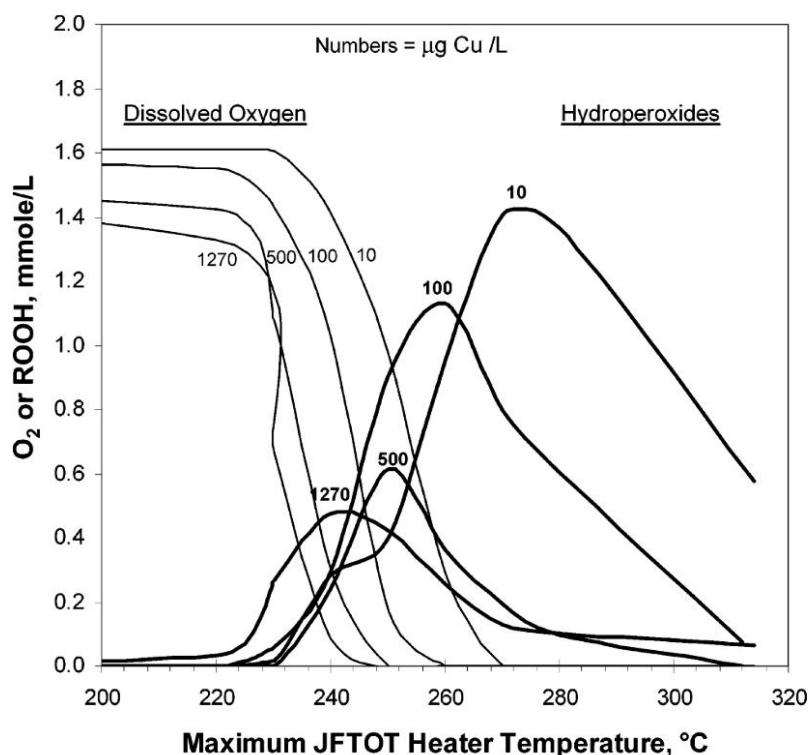


Figure 2.26: Effect of dissolved copper on oxygen and hydroperoxide concentration [186]

coupling process too.[187] The possibility of copper accelerating oxidative coupling was suggested by Jones *et al.*,[155] but this has not received further mechanistic investigation. Overall, it is clear more work needs to be done to understand the mechanisms that metals catalyze in the deposition process.

2.2.7 Concluding Remarks of Factors Affecting Autoxidation and Deposit Formation

The autoxidation and deposition process is a complex chemical and physical phenomenon with competing chemical and physical effects. Researchers have utilized static, flowing and large scale rigs to understand which factors influence thermal stability. Additionally, characterization work on the deposit formed has allowed mechanisms to be proposed.

The entire autoxidation and deposition process is initiated by dissolved oxygen,

with the formation and decomposition of hydroperoxides leading to the initiation of a free-radical chain reaction. Physical effects like temperature influence the rate of formation and decomposition of these hydroperoxide species. Once the radical chain mechanism begins, the resultant free-radicals react with different fuel components producing a variety of species. Bulk hydrocarbons form various oxygenated compounds, and have been suggested to couple via free-radical and/or condensation reactions. Nevertheless, aromatics appear to be far more reactive than aliphatic species in fuel, owing to their ability to stabilize free-radicals and lower C-H bond strengths.

The minor heteroatomic components of fuels appear to have a large influence on deposit formation. Sulfur species are the only heteroatom specifically limited in fuel standards, owing to their deleterious effect on thermal stability. Nonetheless, not all sulfur species contribute to deposition equally. Mercaptans/thiols have consistently been shown to contribute to deposits, and are specifically limited in fuel standards. Disulfides also are found to contribute to deposition, but are not limited in standards. Sulfides and thiophenes are not limited by standards, and are found to reduce autoxidation and have a limited effect on deposition. The suggested mechanisms whereby sulfur compounds form deposit are particularly focused on their ability to form sulfur acids. It is unclear how these sulfur acids influence the formation of deposits however. Acid-base reactions between nitrogen fuel species and sulfur acids are proposed, but not all authors are in agreement. A particular weakness of the acid-base theory is the lack of suitable solvent in fuel, and the fact that the basicity of nitrogen class did not appear to correlate well with total deposits. Further work needs to be done to understand this interaction between nitrogen and sulfur compounds to gain a greater mechanistic understanding of the interaction.

Within the nitrogen class, many authors indicate that 5-membered heterocycles like indole and carbazole had a greater influence on deposit than 6-membered compounds like pyridine and quinolines. Analysis of the indole containing surrogates revealed that oxidative coupling was the most likely reaction between nitrogen containing fuels. Similarly, analysis of phenolic deposit has suggested an oxidative coupling mechanism. It is clear that dissolved metals have a large influence on deposition and autoxidation too. Computational work has revealed that metals can decompose hydroperoxides and then react with bulk fuel species, accelerating autoxidation. However, the role that metals play in deposition is less clear. The

wall material of the fuel system has also been shown to play a role, but the suggestion of sulfur acids attaching to the wall has received little mechanistic investigation.

Emerging from this review is a complex picture, with different chemical classes synergistically interacting with one another. Much work has focused on correlating initial species concentrations with the rates of autoxidation and deposition. Less work has been performed on the characterization of the fuel deposits, namely due to the complexity of the deposit structure. Mechanisms that have been proposed are difficult to scrutinize under experimental conditions. Nevertheless, recent studies, particularly on the reactions of metals with hydroperoxides, have successfully scrutinized existing pathways and proposed new ones based on calculated energetic barriers.

The review of existing chemical and physical processes will lead us to critically examine the proposed mechanisms in the next section. In particular, the next section will explore attempts to generalize the autoxidation and deposition processes based on the chemical trends observed in this section.

2.3 Generalized Deposition Models

One obvious motivation for researchers attempting to understand thermal oxidative stability mechanisms is to identify methods of enhancing thermal oxidative stability, via equipment design or addition of additives. Nonetheless, formation of deposit is an inevitable process, even for highly stable fuels.[74] As a consequence, generalized models have been proposed to help predict the deposition and autoxidation process. Generalized models attempt to encapsulate the important aspects of the chemical and physical processes of deposition. We will focus on chemical and pseudo-detailed computational mechanisms

With respect to generalized chemical mechanisms of deposition, only the soluble macromolecular oxidatively reactive species mechanism (SMORS) is found in the literature. The SMORS mechanism attempts to generalize the role of nucleophilic nitrogen species and phenols into an overarching deposition mechanism.

Numerous pseudo-detailed computational mechanisms exist, which are intended to be integrated into computational fluid dynamics (CFD) prediction of deposition in

fuel systems. Pseudo-detailed mechanisms are limited by computational resources. Consequently, they need to be able to capture the most important chemical and physical contributions to deposit formation.

The limitations of the generalized mechanisms will be discussed in relation to the chemical and physical contributions to deposit explored in the previous section. As a result, the key research questions of this thesis will emerge.

2.3.1 Soluble Macromolecular Oxidative Reactive Species (SMORS) Mechanism

The origins of the SMORS mechanism can be found in a paper by Hardy and Wechter on diesel deposits. The paper proposed a method of isolating and identifying storage deposit precursors using methanol extraction.[84] The authors reasonably assumed that the precursors would be more polar than the bulk fuel, and thus would be amenable to extraction using a polar solvent like methanol. Their extraction process is shown in Figure 2.27. In fact, the insoluble nature of deposits, attributed to the presence of oxygen and nitrogen groups, are a result of the higher polarity compared to bulk fuel.[168] The researchers termed the methanol extracted deposit precursors soluble macromolecular oxidatively reactive species (SMORS). The methanol extract was then treated with hexane yielding a precipitate. The precipitate was termed extraction induced precipitate (EIP). This isolates agglomerated polars from indigenous polars. The resultant precipitate was then separated from the liquid phase by filtration. After redissolution in THF, the EIP was analyzed using size-exclusion chromatography, yielding a mass range of 600-900 Da. Elemental analysis from combustion gases of compounds this range revealed an average empirical formula of $C_{21}H_{20}O_2N$. However, no elemental analysis was conducted on sulphur, with no explanation provided. This has implications for later work based on this study. Sulphur compounds have been shown to form an equal, if not greater component, of deposits.[69, 35].

Based on the precursors identified in middle distillates being in the range of 600-900 Da with both N and O groups, a chemical mechanism leading directly to deposits in jet fuel was proposed.[32] Termed the SMORS mechanism, the mechanism incorporates the fact that antioxidants, which form stable radical species, are known to increase deposits.[33] The first step, shown in Figure 2.28, involves the

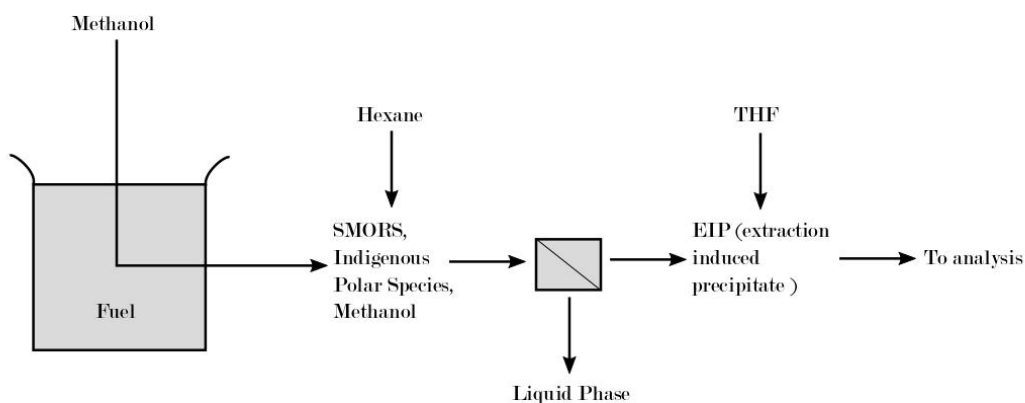


Figure 2.27: SMORS method of analysis

abstraction of a hydrogen from an phenolic species (**1**) via a hydroperoxy radical (**2**) (equation 2.1). The stable radical species generated, species (**3**), is proposed to react with dissolved oxygen in the fuel. Oxygen is naturally found in the triplet state. This yields compound (**5**), a ketoperoxy radical.

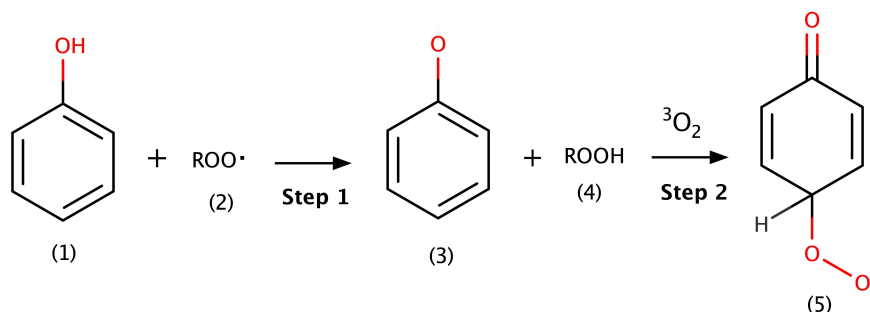


Figure 2.28: SMORS mechanism step 1

The ketoperoxy radical (**5**) then undergoes a termination step, producing a tetraepoxide intermediate compound (**6**) (Figure 2.29). This compound is then proposed to rapidly decompose through the Russell mechanism [188] producing a hydroquinone (**7**), quinone (**8**) and a singlet oxygen species (**9**). In the mechanism presented in reference [32], triplet oxygen is produced. However, in order to adhere to the conservation of spin angular momentum, this reaction should yield singlet oxygen, which is highly reactive towards electron-rich molecules.[189]

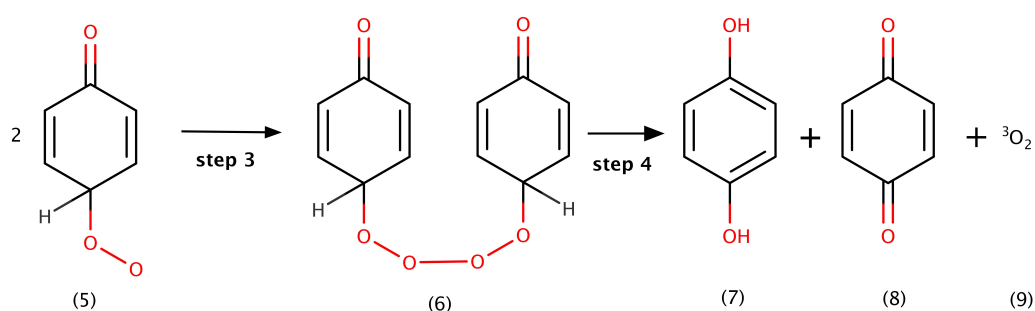


Figure 2.29: The proposed SMORS mechanism step 2, ketoperoxy radical self reaction- yielding a hydroquinone (7), quinone (8) and singlet oxygen (9). The original mechanism proposes the formation of triplet oxygen [32].

Production of electron-deficient quinone-like species is essential for this mechanism. Quinone is a strong electrophile.[163] As a result, the researchers propose that it goes on to react with indigenous carbazoles (species (10)) via electrophilic aromatic substitution (EAS) reactions in Figure 2.30 to form (12). Compound (12) has an empirical formula similar to one of the SMORS precursors detected in the original diesel study.[84] Once again, because this is a generalized mechanism quinones can also react with other electron-rich heteroatoms and aromatic species.[38] Compound (13) is then oxidized in step 6. The oxidized compound (13) can then react with another compound (12), to form compound (14). Compound (12) has the empirical formula and weight similar to that of the SMORS detected by the initial SMORS study into diesel fuel,[84] and is a precursor species to further EAS additions to larger insoluble compounds. In an attempt to include sulfur in the SMORS mechanism, the authors also suggest that aryl thiols would directly react with the metal surface. The resultant metal sulfide is then attacked by a SMORS quinone species, then following the described SMORS steps 1-7.

Alongside the non-conservation of spin angular momentum in step (4) mechanism, there are other issues with both of these proposed mechanisms. The original work by Hardy and Wechter neglected to analyze for sulfur.[84] Consequently, the empirical formula presented may bear little relation to the actual fuel precursor. Additionally, the empirical formula presented in the original SMORS paper is an average of several different fuel precursors. Therefore, assigning a precise structure information on an average empirical formula, and building a subsequent mechanism

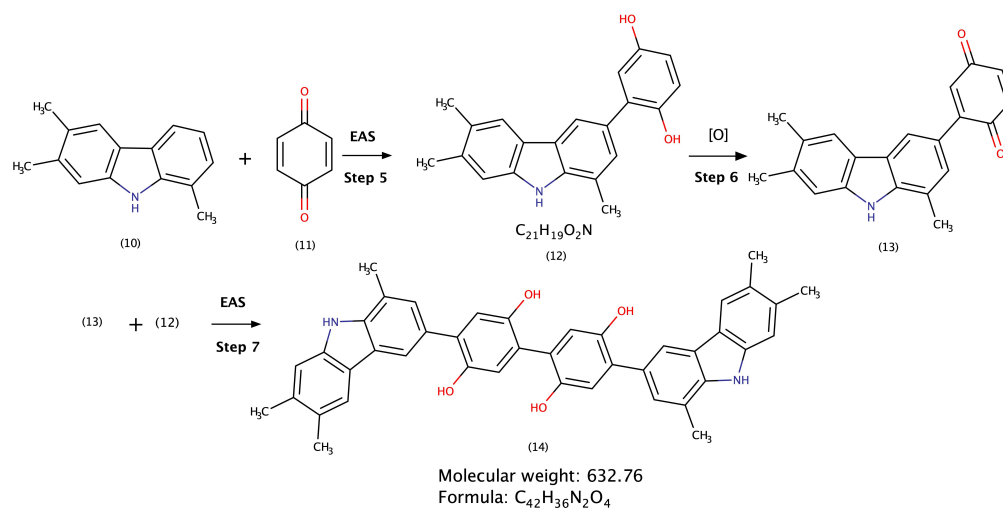


Figure 2.30: Final Steps of the SMORS Mechanism

on this structure is not without its weaknesses. Moreover, the reactions proposed here are presented with little experimental justification. In the original SMORS mechanism paper by Beaver *et al.*, the researchers were unable to produce any of their proposed compounds in jet fuel.[32] As a final point of weakness, the mechanism proposes that aryl thiols are a key species for deposition. By contrast, alkyl thiols are consistently shown to be more problematic for thermal stability [52][62].

Despite these weaknesses, several papers have further explored this mechanism. One study by Sobkowiak *et al.* showed increasing phenol, indole, and carbazole concentrations correlated with increased thermal oxidative deposit formation.[163] Sobkowiak *et al.* do implicate phenols, indoles and carbazole species as deposit forming, but there is little evidence elucidating the mechanism by which they form deposits. Later work by Kabana *et al.* managed to produce compound **12** in Figure 2.30 by coupling a quinone and indole species in an aqueous medium. However, an aqueous medium is a poor representation of the real fuel environment. Nevertheless, Kabana *et al.* were able to detect quinone species from fuels.[38] Quinone species have also been detected in work with surrogate fuels.[68, 155]

Another study in 2011 focused on the use of electrospray ionization mass spectroscopy (ESI-MS) to explore the generation of deposit precursors prior to stressing.[47] ESI-MS is particularly amenable for analysis for deposit precursors due to its high selectivity of polar species and its ability to volatilize compounds up to 200 MDa.

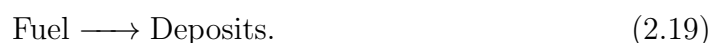
The researchers found an increase in polar compounds in the 200-400 Da range was found after stressing the fuel. The presence of odd-numbered ion peaks corresponding to an even mass compound implies the presence of compounds containing an even number of nitrogen atoms. There was little indication of odd containing nitrogen compounds. This suggests that compound [12] in Figure 2.30 (molecular weight of 317) is not appearing in a stressed Jet A-1.

Recent work employing two surrogates did detect empirical formulae which could be indicative of a SMORS species. Two surrogate fuels containing 2-naphthol + 2-methylindole and 2-naphthol + 2,5-dimethylpyrrole were stressed. ESI-MS analysis found two molecular formulas consistent of hydroquinone-like products bonded to the respective nitrogen-species.[68] As a result, the SMORS mechanism as a mechanistic pathway to deposits cannot be ruled out. Quinone-like species have been detected in fuels, but whether they react with nitrogen heterocycles via the original SMORS scheme is unclear.

2.3.2 Pseudo-Detailed Predictive Mechanisms

Since the 1980s, predictive pseudo-detailed mechanisms have grown in complexity and accuracy. An increasing availability of computational power, as well as an enhanced understanding of the chemistry of thermal oxidative stability has permitted this development. Kinetic mechanisms offer researchers a way to predict oxygen depletion, as well as the location, and magnitude of deposition. The term 'pseudo-detailed' refers to the fact that mechanisms cannot realistically model of every single fuel reaction, and therefore need to group and lump various reactions and species. Before these models can be built, chemical kinetic parameters, specifically activation energies and the pre-exponential factor A, must be obtained. Work has been done to obtain these parameters for specific reactions within the fuel [102, 110] as well as more general lumped parameters for the general fuel-to-deposit mechanisms.[113] Models can then be implemented into computational fluid dynamic (CFD) simulations to predict deposits in a variety of geometries.

Early work by Chin *et al.* attempted to create a generalized one step model for deposits formed on the wall based of off:

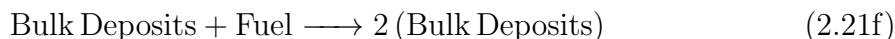


This was then represented by:

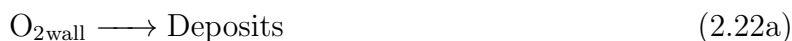
$$\frac{dD}{dt} = \alpha A \exp\left\{\frac{-E_{2a}}{RT}\right\}, \quad (2.20)$$

where D is the amount of deposit formed. A and E_{2a} are dependent on the fuel type and correlated from experimental data and α is a flow parameter. The simplification of the deposit forming process was shown to be useful for predicting deposit formation in simple conditions. But the omission of oxygen limited the ability of the model to predict the change in deposit formation at different sections of a flowing test rig.[113] Inclusion of oxygen in a subsequent one-step model wall model gave more accurate results in lower oxygen environments.[190] Nevertheless, the simplification of the deposition to process into one step neglected reactions in the bulk in Figure 1.9.

Models adding reactions in the bulk began by focusing on the generation and destruction of deposit precursors. Deshpande *et al.* attempted to take into account these general processes by conceiving a precursor creation, precursor destruction and precursor to deposit term. The precursor to deposit term involves the rate term R_m , which is the mass transfer rate onto the wall. The rate terms are calibrated from experiments with particular fuel, making them empirical terms. Deshpande *et al.*'s three step model allows for deposit generation in the bulk, which then diffuses to the wall.[191] This creates a lag between oxygen levels and deposit location, which is observed in tests.[33] This is an important development from previous models described which only allowed for deposit generation at a wall. However, validation experiments performed by Katta *et al.* showed that Deshpande *et al.*'s model fails to predict the peak deposition rate, location, and the oxygen consumption profile accurately.[44] The simplification of the model into 3 steps, and the exclusion of fuel species classes, was identified as the key reason for prediction failure. As a result, Katta *et al.* developed an expanded 9 step model with 6 bulk generation terms:



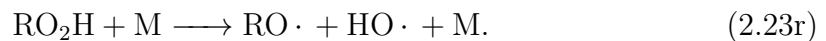
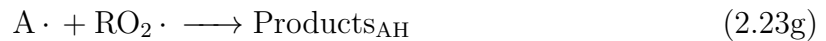
This also included wall generation terms too:



This had a greater accuracy of prediction than the 3-step model. This was due to the inclusion of specific reactants, and the multiple routes of deposit generation on the wall. However, this model still omitted species like antioxidants and metals. Moreover, the kinetic equations associated with these still relied on empirical calibrations from flowing rigs for the rate parameters, rather than rate parameters from chemical kinetic first principles. As a result, fuel blending with a FT and conventional distillate fuel produced poor predictions. Inclusion of indigenous antioxidants (phenols, fuel polars etc.) appeared to be another crucial improvement in closer reflecting the varying chemistry of different fuel.

To improve upon the sensitivity of pseudo-detailed mechanisms to different fuel species, a more complex mechanism reflecting the autoxidation of the fuel was conceived by Zabarnick *et al.* in 1993. Inclusion of an antioxidant term **AH** allowed for the effect of different antioxidant concentrations in fuels to be studied. Zabarnick *et al.*'s model showed that at low **AH** concentrations O_2 depletion was inhibited. Whereas, at high **AH** concentrations, the rate of oxidation would increase. The model also underlined the importance of including **ROOH** decomposition as crucial step in the autoxidation process.[41] Improvements on the original 1993 model involved the addition of **SH** thiol sulfur species, adding further sensitivity to different fuel species to the model.[192] Kuprowicz *et al.* added additional peroxy radical

reaction steps to the mechanism, and tuned the kinetic parameters. These improvements led to the accurate prediction of oxygen depletion in a simple hydrocarbon solvent at different oxygen concentrations and temperatures.[193] Finally, in the most recent iteration of the mechanism, the inclusion of metals led to the following scheme:



The pseudo-detailed mechanism was then tested with two potential global deposition terms, such that each one could be compared. The concentrations of the heteroatom terms (**AH**, **ROOH**, **M**, **SH**) were calibrated against several real fuels. The mechanism was able to predict the change of hydroperoxide concentration along a near isothermal tube reactor (NIFTR) with accuracy. Moreover, the 3-step global deposition term was able to predict the peak deposit accurately for most fuels tested. Nevertheless, for some fuels, the peak deposition was not predicted accurately.[24] Additionally, when the model was applied to a non-isothermal simulation, kinetic

parameters were calibrated with deposition experiments. In this sense, the reactions are implicit, and the complex chemical contributions to the deposition state are heavily simplified. Additional deposition steps were added to the up-to-date mechanism in a recent paper by Liu *et al.*, reflecting the differing deposition rates of hindered and non-hindered phenols.[61] Nevertheless, even this recent paper suffers from the issue of empirical rate parameters calibrated to specific fuels.

In the future, jet fuel chemistry will become more varied and complex as alternative fuels are used alongside conventional fuels. As a consequence, mechanisms relying solely on fitted chemical kinetic parameters will struggle to remain sensitive to varying chemical compositions. In response to this challenge, several researchers have attempted to build mechanisms from 'first-principles', using chemical kinetic parameters calculated from semi-empirical/*ab-initio* methods. Dwyer, in his PhD thesis, built a pseudo-detailed autoxidation mechanism for bulk fuel with the cc-pVTZ//B3LYP method. In order to simplify the complexity of the bulk, calculations were performed on *n*-dodecane (straight chain), decalin (cyclic) and toluene (aromatic). Each species represented a distinct class of the bulk fuel. A mechanism for each class was constructed, taking into account the formation of aldehydes, alcohols and ketones. Additionally, the pathway to the formation of alkenes was calculated. Although the mechanism was not tested, it proved DFT as a method for building and constructing pseudo-detailed mechanisms.[48]

A further development in building a pseudo-detailed mechanism from semi-empirical/*ab-initio* techniques was inclusion of the peroxy radical self-reaction. Alborzi *et al.* integrated peroxy self-reaction into a pseudo-detailed autoxidation mechanism. Rate parameters were calculated with the cc-pVTZ//B3LYP method. Additional oxidation reactions were included to model the production of aldehydes and ketones. A simple solvent composed of jet fuel range *n*-paraffins was used to test the predictive capabilities of the pseudo-detailed autoxidation mechanism. The mechanism gave accurate predictions of oxygen depletion at differing hydroperoxide concentrations and temperatures. Furthermore, the predicted oxygenated fuel concentrations (Figure 2.31) followed the change of measured oxygenated fuel components. Nevertheless, the model tended to under-predict the true concentrations of fuel autoxidation products. The under-prediction potentially arising from the high initiation barrier ($\text{RH} \longrightarrow \text{R}\cdot + \text{H}$), where the direct reaction of O_2 with RH could provide a lower barrier (equation 2.2).[76]

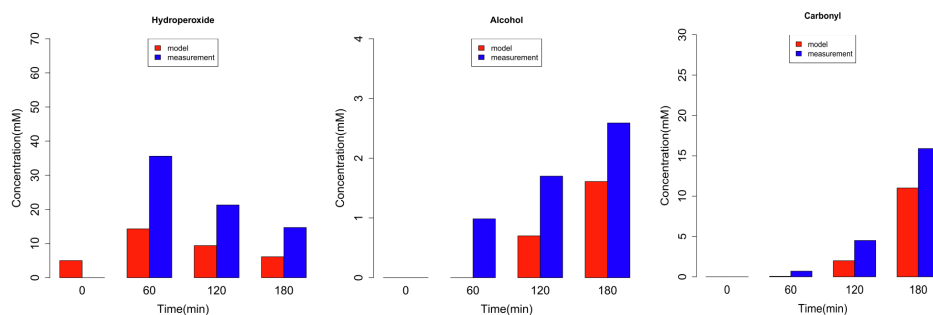


Figure 2.31: Predicted and measured oxygenated products from a DFT constructed pseudo-detailed mechanism found in [76]

Inclusion of heteroatom species into pseudo-detailed mechanisms using DFT was explored by Parks *et al.*. Firstly, the modeling of copper hydroperoxide decomposition led to the addition of 5 other reaction steps, expanding on equation 2.23r.[94] In a second paper, the reaction of indigenous sulfur with hydroperoxides was modeled, leading to formation of sulfonic acids and other sulfur species. The DFT calculations on a variety of sulfur classes allowed for structural variations within species classes to be taken into account, and chemical kinetic parameters proposed.[54] For both studies, the cc-pVTZ//B3LYP method was used.

2.4 Concluding Remarks of Generalized Deposition Models

The pseudo-detailed and the SMORS chemical mechanism arise from the desire to encapsulate the autoxidation and deposition in a series of human readable reactions. Consequently, the deposition and autoxidation of jet fuel can be predicted based on a set of known starting conditions (temperature, species concentrations etc.).

The SMORS mechanism attempts to generalize the deposition process into a reaction between electrophilic quinones and nucleophilic fuel heteroatomics. Additionally, the SMORS mechanism proposed that aryl thiols act as 'anchors' to the internal metal fuel surfaces. A significant body of research subsequently used the SMORS mechanism to explain certain fuel behaviors, particularly the apparent synergistic interaction between nitrogen and phenolic species. Nevertheless, despite the

fact that SMORS compounds have been detected in fuel surrogates, the pathways proposed have not received extensive mechanistic scrutiny.

Pseudo-detailed predictive mechanisms have been developed in recent years to be integrated into computer codes for predictive purposes. Nascent mechanisms were simplistic (reflecting availability of computational power at the time), mostly focusing on the deposition process, with low sensitivity to fuel starting chemistry. Later mechanisms included new species classes as input parameters, and added complex autoxidation chemistries. The higher complexity of autoxidation chemistry, and fitted deposition steps led to oxygen depletion and deposition being predicted with accuracy. Nevertheless, the deposition steps remained simplistic, and tied to the existing fuels they were calibrated for.

To build pseudo-detailed mechanisms from a more 'first-principles' approach, DFT has become an increasingly popular tool. Several pseudo-detailed mechanisms have been constructed recently using DFT methods, with a sole focus on producing chemical kinetic parameters for autoxidation steps. A key advantage of a DFT constructed pseudo-detailed mechanism is the ability to capture a wider range of fuel chemistries. Nevertheless, a first principles approach to the deposition steps presents a greater challenge than the autoxidation steps. Since the formation of large macromolecules characterizes the deposition process, the ability to model the process in terms of even one fuel heteroatom becomes intractable due to the number of possible reactions. A method of approaching this problem with DFT methods and available computational power still eludes researchers.

2.5 Conclusion to Literature Review and Key Research Themes of the Thesis

This literature review has highlighted the key issues regarding the mechanistic understanding of deposition. Previous research has highlighted which species affect thermal stability in positive and negative ways is well established. In addition, previous work has allowed us to split thermal oxidative stability into broadly two phases. First, there is the autoxidation stage, where indigenous fuel components are oxidized. Then the second stage involves the deposition stage, which encapsulates the agglomeration of oxidized fuel components which eventually forms insolubles.

The chemical pathways, regarding the first autoxidation step are well characterized. As a consequence, existing predictive models have detailed oxidation steps, but are generally empirical and simplistic at the deposition step. DFT has emerged as an important tool to study the different fuel reaction pathways, and offers a potential way of studying the agglomeration process. Additionally, DFT can be used to help build predictive mechanisms from 'first principles'. DFT calculations can obtain thermochemical and kinetic data which can be used in predictive mechanisms. However, it is unclear how DFT can be used to help build the mechanisms for the deposition stage. Arising from these issues is a clear set of themes for this thesis to follow. Firstly, the thesis will attempt to enhance our understanding of the poorly defined deposition process using experimental and computational techniques. Then, DFT as a tool to build predictive methods will be assessed. Emerging out of these themes, a discrete set of questions arise:

- **Can DFT successfully model the SMORS pathway?** Due to the deficiencies of the SMORS highlighted in the third section of the literature, is it possible to model the pathway using DFT methods? If the proposed pathway is unfeasible, what other routes to SMORS species can be conceived?
- **How do nitrogen and sulfur species interact synergistically in jet fuel?** There is still considerable debate as to how nitrogen and sulfur species in fuels. Can experimental and DFT techniques be used to help understand the mechanisms behind nitrogen and sulfur interactions in fuels?
- **How do oxidized fuel species interact with the heated walls to form the initial deposit layer?** Investigations into the early stages of deposition have been a challenge experimentally, can we use DFT methods to elucidate which species are likely involved with the early stages of deposition?
- **How can researchers approach constructing predictive deposition mechanisms with DFT methods?** The autoxidation stage of deposition has been modeled with DFT and integrated into pseudo-detailed mechanisms with success. By contrast, the deposition process presents a significant challenge due to the complexity of reactions. Using simplistic surrogate fuels, how can DFT be related to the deposition process?

Chapter 3

Theoretical Background

Quantum chemical methods allows mechanistic and thermochemical data to be obtained from chemical reactions. Quantum chemistry has gained popularity in recent years, driven by an ever-expanding availability of computational resources at lower cost. Within the area of fuel autoxidation, quantum chemistry allows complex reactions to be studied in isolation of one another, leading it to be a popular choice mechanistic investigations [29, 194, 195]. By comparison, experiments attempting to study fuel autoxidation have to contend with thousands of side-reactions and multi-step processes that are difficult to isolate from one another. However, the accuracy of data produced from computational methods is sensitive to the choice of the specific method and the representative system. Moreover, bar very small cases of little interest within fuels, no system can be modeled with 100% accuracy. However, if the errors are consistent, general mechanistic trends can be observed. Furthermore, the thermochemical data generated can be employed in chemical kinetic mechanisms. These mechanisms often have greater sensitivity to different initial concentrations that previous ones correlated from empirical data of specific fuels.

The following chapter will detail the theory behind the quantum chemical methods that will be discussed and used in this thesis. Thermochemical parameters are produced from the differences between local minima, for reactants and products, and maxima, for transition states on a potential energy surface. The potential energy surface is a concept that relates the geometric structure of a atom/molecule to energy. Geometric structure in the potential energy surface in this instance is defined by positions of the *nuclear* coordinates. This thesis aims to use quantum chemical methods to relate the structure and position of atoms/molecules at local minima and maxima to gain greater insights in jet fuel thermal oxidative stability. This

theory section will start with the background behind these techniques, including quantum mechanics and the Schrödinger equation. Then we will explore methods of approximating solutions to the Schrödinger equation starting with Hartree-Fock (HF) theory. Although pure HF will not be used in this thesis, the self-consistent field procedure used to solve the HF equations is used throughout quantum chemistry. Post-HF methods will be briefly outlined, but with the caveat that many are too expensive to study the size of systems required for jet fuel agglomeration. Density Functional Theory (DFT) will then be introduced as a method of achieving high accuracy calculations for lower computational cost compared to post-HF methods. The background theory, key equations, and functionals associated with DFT will be explored in detail.

3.1 Transition State Theory and Thermochemistry of Chemical Reactions

One of the main goals of this thesis is to extract thermochemical, entropic and kinetic data from deposition forming reactions using quantum chemical methods. Transition state theory provides a means of interpreting the data in the context of deposit forming reactions, and can provide a quantitative measure of the rate of reaction. On the other hand, thermochemical interpretations of chemical reactions gives information about the stability of reactions and the degree of spontaneity. Since these concepts will be referred to throughout this thesis, transition state theory and the thermodynamics of chemical reactions will be discussed briefly in this section.

A reaction between two reactants A and B producing C, which can be represented with the following symbolic equation:



The rate of the forward reaction can be represented with the equation:

$$r = k_f[A][B] \quad (3.2)$$

where r represents the rate of reaction and k_f is the forward rate constant. In order to relate the temperature to the rate of reaction, Arrhenius proposed the following relation in 1910 [196]:

$$k_f = Ae^{\frac{E_a}{RT}}, \quad (3.3)$$

where E_a is the activation energy, A is the pre-exponential factor, R is the gas constant and T is the temperature of reaction. At its conception the pre-exponential factor did not have an explicit physical interpretation, reflecting the empirical nature of the equation. Furthermore, the activation energy was not defined in terms of what we now understand as the difference between an activated complex and the reactants. Several authors attempted to build on the Arrhenius equation (equation 3.3) from a thermodynamics, kinetic or statistical mechanics angle [197]. However, it was Eyring who united the three approaches in his transition state theory. This produced the following expression for the forward rate constant:

$$k_f = \frac{k_B T}{h} e^{-\Delta_f^\ddagger G/RT}. \quad (3.4)$$

Here, the Gibbs energy can be expanded giving a physical expression for the pre-exponential factor A :

$$k_f = \overbrace{\frac{k_B T}{h} e^{\Delta_f^\ddagger S/R}}^A e^{-\Delta_f^\ddagger H/RT} \quad (3.5)$$

Here k_B refers to the Boltzmann constant, h to Plank's constant, T to temperature, S to entropy, H to enthalpy, R to the universal gas constant and G to Gibbs energy [198]. Compared to the Arrhenius equation, Eyring's equation gave an explicit interpretation of the transition state, where the symbols Δ_f^\ddagger refer to the difference between the reactants and the transition state complex. Furthermore, unlike the Arrhenius equation, which was primarily conceived for gas phases systems, the Eyring expression can be applied to any reaction, regardless of phase. From the above expression, once entropy and enthalpy are known for a particular reaction, a value of the forward rate constant can be derived [197]. Eyring's expression will be used in the work here to generate forward rate constants from entropy and enthalpic values generated in quantum chemical calculations.

Thermochemistry has its origins in work by Van't Hoff who expressed the concentration equilibrium of a reversible reaction in terms of the difference in standard internal energy U between the reactants and products [199]. In chemical systems, particularly condensed systems at constant phase temperature and pressure, the Gibbs energy expression is more often used:

$$K_{eq} = e^{-\Delta_r G/RT}. \quad (3.6)$$

Here $\Delta_r G$ is the difference in Gibbs energy between the reactants and products. The equation 3.6 can also be expressed as a ratio of forward and reverse reactions:

$$K_{eq} = \frac{k_f}{k_r}, \quad (3.7)$$

where k_f and k_r are the forward and reverse reactions respectively. A physical interpretation arises from the relationship between equations 3.6 and 3.7. A reaction in which the products are at a higher Gibbs energy than the reactants, leading to a high positive value of $\Delta_r G$, a small K_{eq} will be formed and thus $k_f \ll k_r$, meaning the equilibrium will be shifted towards the reactants. In the case where $k_f \ll k_r$ a reaction is described as endergonic. In the opposite case where the products are at a lower Gibbs energy compared to the reactants, $k_f \gg k_r$ leading to equilibrium shifted towards the products. A reaction where $k_f \gg k_r$ is described as exergonic. In a deeper sense, $\Delta_r G$ governs the degree of *spontaneity* of reactions. In this thesis, the vast majority of reactions will be treated as irreversible, so the $\Delta_r G$ values will be used to compare and analyze the likelihood of reaction pathways. In order to obtain thermodynamic Δ_r and kinetic Δ_f^\ddagger information from a chemical system, the molecular geometry of the chemical system is related to a potential energy surface.

3.2 Potential Energy Surface

The geometry of any molecular species containing N nuclei is defined by $3N-6$ degrees of freedom. Every conformation is a function of its electronic potential energy U . A point in Cartesian space defined by x, y, z can be represented by three geometric parameters q_x, q_y, q_z . In a simplified system of two geometric parameters q_1 and q_2 , the plot of $U(q_1, q_2)$ produced would be a three dimensional surface. In the case of more than two geometric parameters $q_1, q_2 \dots q_n$, a surface becomes an n -dimensional hyper-surface [200, 201]. The thermochemical and kinetic parameters discussed in the previous section require the energy differences between reactants, products and transition states. Stationary points, at which the gradient of the n -dimensional hypersurface is 0, represent points of relative stability and are where reactants, products, and transition states can be found. What distinguishes reactants and products from transition states is the nature of their stationary points. Reactants and products can be found at local minima on the potential energy surfaces, whereas transition states are found at first-order saddle points, i.e. points

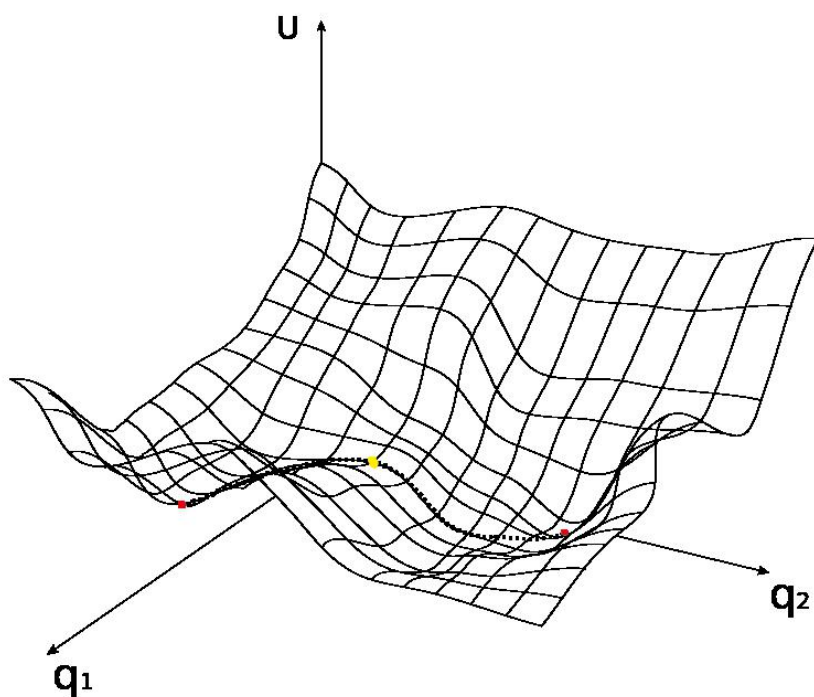


Figure 3.1: Potential energy surface, showing minima in red and transitions states shown in yellow

where the potential energy U is at a maximum for one variable but a minima for all other variables. For a sufficiently large molecule or chemical system, computation of the entire potential energy surface is computationally too expensive. Instead 'single-point' calculations are performed, where a single minima/maxima on the potential energy surface is located.

A reaction scheme can thus be analyzed as a series of these stationary points, in the form of a potential energy diagram.

However, in real chemical systems the molecules do not occupy a fixed point, molecules vibrate about their equilibrium positions. These vibrations occur at various frequencies. A non-linear molecule with N nuclei has $3N-6$ normal mode frequencies. Along with providing useful information on the infrared spectrum of the chemical species under investigation, calculation of the frequencies provides the zero-point energy (ZPE) as shown in Figure 3.3. The zero-point energy is the energy a

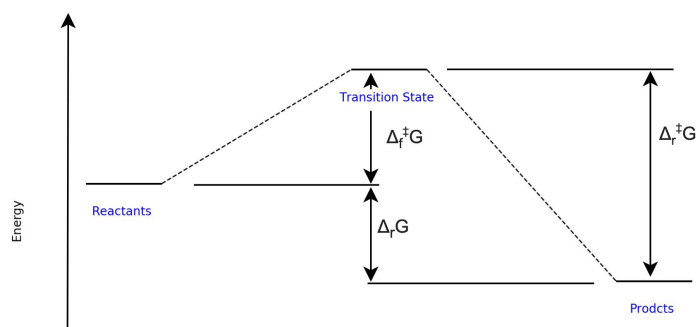


Figure 3.2: Example reaction coordinate diagram with the Gibbs energy of forward reaction $\Delta_f^\ddagger G$, energy of backward reaction $\Delta_r^\ddagger G$ and the Gibbs free energy change of reaction $\Delta_r G$

molecule posses at absolute zero as a result of vibrations. Instead of a occupying the bottom of a potential energy well, a molecule will vibrate at an energy slightly above this level.

Another assumption that has been made in constructing the relation $U(q_1, q_2 \dots q_n)$ is that the nuclear coordinates q_n are fixed in space. For the systems of interest in this thesis, only *adiabatic* surfaces will be considered and potential energy diagrams, meaning the nuclear coordinates will be treated as fixed. The underlying assumption behind this is the Born-Oppenheimer approximation.

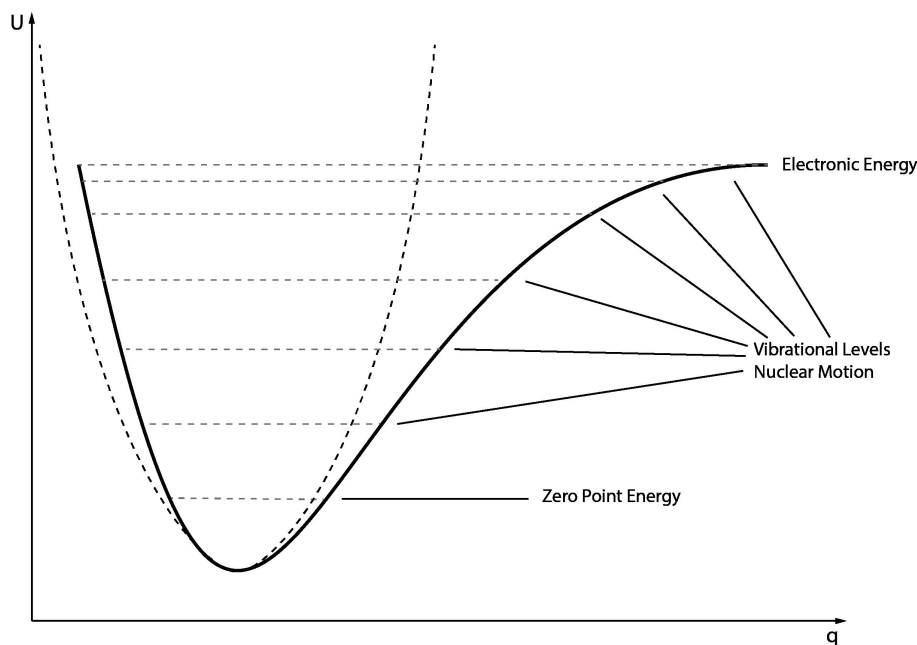


Figure 3.3: Example potential energy curve including vibrational energies. The quadratic approximation is shown here with a dotted line, which treats vibration as a harmonic oscillator.

3.3 Born-Oppenheimer Approximation

To simplify calculations involving chemical systems Born and Oppenheimer demonstrated that nuclei can be fixed in space in relation to the electrons [202]. The assumption was based on the fact that because the nuclei are much heavier than electrons ($m_N \gg m_e$) nuclei can be treated as fixed points in space. As discussed above, this allows potential energy diagrams to be constructed as a function of nuclear coordinates, essentially giving molecular configurations a defined shape. However, the Born-Oppenheimer approximation also means that the underlying equations giving energetic information about the system only need to be solved in terms of their electronic terms, which will be discussed in detail in the following sections.

3.4 Geometry Optimization

Computation of the entire potential energy surface for systems of interest in this thesis would be computationally prohibitive. Instead, we investigate single points on the surface, but in a stricter sense we are interested in minima and maxima on the surface where reactants, products and transition states are located. Repeated

calculations of the potential energy U at an assigned series of geometries are an inefficient way of locating these stationary points, and have limited use in the work here (a bond scan is an example where this method *is* used). Instead, U is calculated along with its first partial derivatives ($\delta U/\delta q_1, \delta U/\delta q_2, \dots, \delta U/\delta q_N$) with respect to the molecule's $3N-6$ coordinates (N being the number of nuclei). The first partial derivatives yields the gradient which is used by a number of optimization methods and reveals whether the optimization has reached a stationary point.

For certain calculations, like transitions state searches, the second partial derivatives with respect U ($\delta^2 U/\delta q_1^2, \delta^2 U/\delta q_2^2, \dots, \delta^2 U/\delta q_N^2$) are calculated. The second derivatives with respect to U is computed as a matrix of partial derivatives known as the Hessian or the force constant matrix. The diagonalization of the Hessian yields the normal vibrational modes of the molecule under investigation and proves you have a minima.

In practical terms, before a calculation is initiated, a geometry is guessed for the molecule or molecular system. Various the optimization procedures exist for finding stationary points such as the steepest-descent method and the conjugate gradient method, but they will not be explored in detail here. Calculating U from the molecular structure q_1, q_2, \dots, q_n is at the core of computational chemistry. From a classical perspective this can be achieved using molecular mechanics. However, for reactions and calculations where small high accurate systems are concerned, usage of quantum chemical methods are essential. It is here where the fundamentals of quantum mechanics and the key quantum chemical methods used in this thesis will be introduced.

3.5 Quantum Mechanics

The quantum chemical methods used in the work have its basis in quantum theory. Quantum theory emerged from investigations into black body radiation and the photoelectric effect. In classical physics, a black body will emit radiation as a series of oscillators, where each oscillator had its own vibration mode independent of energy. However, since the number of modes rises without limit as the wavelengths of electromagnetic radiation get smaller, the energy emitted from a black body possessing heat would approach infinity (meaning all matter in the universe would immediately radiate all its heat to absolute 0), as shown in figure 3.4. Similar experiments on the

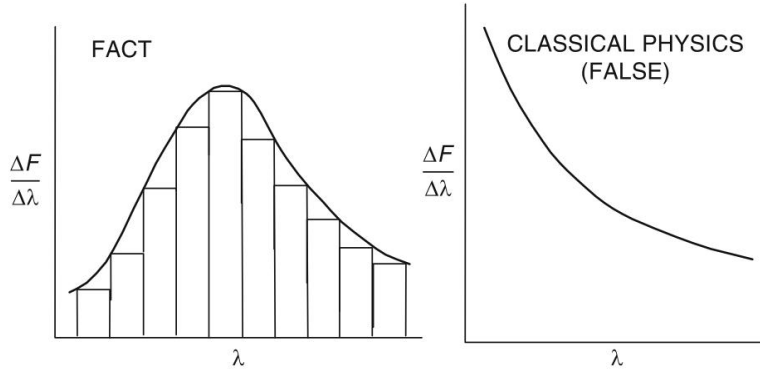


Figure 3.4: The black body ultraviolet catastrophe is illustrated here with the flux, the intensity of radiation, is plotted against wavelength. A classical system predicts that as the wavelength decreases the intensity rises indefinitely.

photoelectric effect led to classical physics being unable to explain why the kinetic energy of electrons ejected from a metal surface was independent of the intensity of light, but instead related to the frequency of light. Work by Planck in 1900 and Einstein 1905 on these problems led to the relation:

$$E = h\nu, \tag{3.8}$$

where h is the Planck constant, ν is frequency of the electromagnetic waves and E energy. Here, electromagnetic radiation is described as being formed of discrete particles, photons, with the Planck constant describing the discreteness. By contrast, classical mechanics views electromagnetic radiation as a continuous process. In the context of black-body relation, Planck's work showed that instead of a continuous series of modes emitting radiation, there instead was a set of discrete vibrational modes divisible by $h\nu$. Likewise, the photoelectric effect could be explained by the relation given in equation 3.8 where only the frequency increases the energy of the incoming particles and thus the kinetic energy of emitted electrons. On the other hand, the intensity of light merely increases the number of particles reaching the surface. Ultimately, this work showed that electromagnetic radiation can demonstrate both particle like behavior and wave-like behavior. However, the work in this thesis is concerned with matter which can also exhibits particle-like behavior.

Quantization of electrons in atoms and molecules can be observed in their spectra, which consist of discrete lines. Following the failure of the Bohr model, which

described electrons as particles which orbited undeviating along specific paths. To describe accurate spectral lines beyond hydrogen, Louis de Broglie suggested that electronic motion follows wave-like behavior:

$$\lambda = \frac{h}{mv} = \frac{h}{p}. \quad (3.9)$$

Here, λ is the wavelength, m is the mass of electron, v is the velocity of electron and p is linear momentum. The de Broglie relation was confirmed by diffraction experiments. However, as with electromagnetic radiation, electrons also exhibited particle-like behavior. The wave-particle duality is also applied to electrons, and by extension, all microscopic particles. However, in a deeper sense, electrons and sub-atomic particles are neither waves or particles but have properties of both classical analogues. A result of the wave-particle duality is the Heisenberg uncertainty principle expressed as:

$$\Delta x \Delta p_x \approx h, \quad (3.10)$$

where Δx refers to the position of the 'particle' and p_x refers to the momentum. The uncertainty principle essentially imposes limits on the simultaneously accurate measurement of the momentum and position of an electron. An example of this uncertainty has already been discussed in relation to zero-point energy (ZPE) (see figure 3.3) [203]. If our optimized geometry were to lie at the bottom of the potential well, its position and momentum would be exactly known, violating the uncertainty principle. Instead, they occupy fixed energy levels by oscillating incessantly about an equilibrium bond length. To begin to work with quantum systems, Erwin Schrödinger developed a mathematical framework based on classical wave mechanics.

3.6 Schrödinger Equation

To provide the means of predicting how the state of a quantum mechanical system changed with time, Erwin Schrödinger postulated the partial differential equation for a one particle, non-relativistic, one dimensional system:

$$-\frac{\hbar}{i} \frac{\partial \Psi(x, t)}{\partial t} = -\frac{\hbar^2}{2m} \frac{\partial^2 \Psi(x, t)}{\partial x^2} + V(x, t) \Psi(x, t), \quad (3.11)$$

where \hbar is the reduced Planck constant ($h/2\pi$), i is the imaginary unit, $\Psi(x, t)$ is the wave-function, m is the mass of the 'particle' and $V(x, t)$ potential energy

function of the system [204]. The wave-function $\Psi(x, t)$ is postulated to contain all the dynamical information about the quantum system. In the above equation the wave-function describes how the amplitude of the particle varies with time t and distance x from some chosen origin. Since $\Psi(x, t)$ is a quantum mechanical function, it cannot provide information on the exact location of a particle. Instead:

$$\Psi(x, t)^* \Psi(x, t) dx = |\Psi(x, t)|^2 dx, \quad (3.12)$$

gives the probability at time t that a particle is in the region x and $x + dx$. It is known as the probability density following the Copenhagen interpretation of quantum mechanics. The concept of a probability density expresses the *statistical* or *non-deterministic* nature of quantum mechanics. As shown in equation 3.12 probability density is computed as a product of the complex conjugate of the wavefunction Ψ^* and the wavefunction Ψ . The complex conjugate to ensure the probability density is real, since the wavefunction often contains real and imaginary parts.

Since the systems concerned in this thesis are time-independent (systems with constant energy), the wavefunction can be separated into spacial and time parts :

$$\Psi(x, t) = e^{-iEt/\hbar} \psi(x), \quad (3.13)$$

where E is postulated to be the energy. If we restrict the potential energy function $V(x, t)$ to only depend on x and insert equation 3.13 for $\Psi(x, t)$ we can write equation 3.11 as:

$$-\frac{\hbar}{i} \frac{d(e^{-iEt/\hbar})}{dt} \psi(x) = -\frac{\hbar^2}{2m} e^{-iEt/\hbar} \frac{d^2 \psi(x)}{dx^2} + V(x) \psi(x) e^{-iEt/\hbar}, \quad (3.14)$$

which simplifies to:

$$-\frac{\hbar}{i} \frac{d(e^{-iEt/\hbar})}{dt} \frac{1}{e^{-iEt/\hbar}} = -\frac{\hbar^2}{2m} \frac{d^2 \psi(x)}{dx^2} \frac{1}{\psi(x)} + V(x), \quad (3.15)$$

since:

$$\frac{d(e^{-iEt/\hbar})}{dt} = \frac{-iE}{\hbar} e^{-iEt/\hbar}, \quad (3.16)$$

inserting 3.16 in the right hand side of equation 3.15 gives:

$$E\psi(x) = -\frac{\hbar^2}{2m} \frac{d^2 \psi(x)}{dx^2} + V(x)\psi(x), \quad (3.17)$$

which is known as the *time-independent* Schrödinger equation. However, the preceding derivation has been performed for a one dimensional system. The Laplacian operator:

$$\frac{\partial^2}{\partial x^2} + \frac{\partial^2}{\partial y^2} + \frac{\partial^2}{\partial z^2} = \hat{\nabla}^2, \quad (3.18)$$

allows equation 3.17 to be written for a 3-dimensional system:

$$-\frac{\hbar^2}{2m} \hat{\nabla}^2 \psi + \hat{V} \psi = E \psi, \quad (3.19)$$

where (x,y,z) has been excluded from the functions for simplicity. Equation 3.19 can be written as:

$$\left[\frac{\hbar^2}{2m} \hat{\nabla}^2 + \hat{V} \right] \psi = E \psi. \quad (3.20)$$

This puts the equation in the form of an eigenvalue equation since we can assign the functions in the square brackets as an operator. All operators in this thesis will be written with the $\hat{}$ symbol (note the $\hat{}$ symbol on the Laplacian operator in equation 3.18). An operator has the mathematical property of acting on a function transforming it into another function. In eigenvalue equation 3.20 the operator, acts on the wavefunction or eigenfunction, yielding a value of energy E , known as the eigenvalue.

Although each wavefunction is unique to the system it represents, there are several requirements for it to be considered a 'well-behaved' wavefunction. These requirements are that the wavefunction should be: continuous, quadratically integrable, single valued, and normalized over all space.

The mathematical expression of normalization over all space is:

$$\int_{-\infty}^{\infty} \Psi^* \Psi d\tau = 1. \quad (3.21)$$

In other words, the probability that the particles represented by the wavefunction are present in all space is 1. For most chemical systems, the true wavefunction is not known and instead approximate wavefunctions are built. Building approximations to the wavefunction form a key part of quantum chemistry and provides a key source of accuracy within calculations.

Looking at the operator in the Schrödinger equation again, to relate the above equations to chemical systems, we must consider systems of multiple particles. Moreover, the operator presented in equation 3.20 is a general one. For chemical systems

involving electrons and nuclei we can be more specific of the nature of the operator acting on the wavefunction, which is generally referred to as the Hamiltonian Operator.

3.7 The Hamiltonian Operator

The Schrödinger equation for a chemical system can be expressed as an eigenvalue equation:

$$\hat{H}\psi = E\psi, \quad (3.22)$$

where \hat{H} is the Hamiltonian operator. It operates on the wavefunction yielding an energy value E [201, 200]. The Hamiltonian operator can be broken down step by step in the following way. First, the Hamiltonian operator is formed of its kinetic and potential energy operators:

$$\hat{H} = \hat{T} + \hat{V}, \quad (3.23)$$

where \hat{V} is the potential energy operator and \hat{T} is the kinetic energy operator. \hat{T} can be expressed as:

$$\hat{T} = \hat{T}_e + \hat{T}_N, \quad (3.24)$$

where \hat{T}_e is the electronic kinetic energy and \hat{T}_N is the nuclear kinetic energy. Then, \hat{V} can then be expressed as:

$$\hat{V} = \hat{V}_{ee} + \hat{V}_{Ne} + \hat{V}_{NN}, \quad (3.25)$$

where \hat{V}_{ee} is the electron-electron repulsion potential, \hat{V}_{Ne} is the nucleus-electron repulsion potential and \hat{V}_{NN} is the nucleus-nucleus repulsion potential. When the Born-Oppenheimer approximation (see section 3.3) is invoked the term \hat{T}_N can be neglected and \hat{V}_{NN} is treated as a constant in a new electronic Hamiltonian:

$$\hat{H}_{elec} = \hat{T}_e(\mathbf{r}) + \hat{V}_{ee}(\mathbf{r}) + \hat{V}_{Ne}(\mathbf{r}; \mathbf{R}), \quad (3.26)$$

where \mathbf{R} is a vector of the nuclear coordinates and \mathbf{r} is a vector of the electronic coordinates. The electronic Hamiltonian's variables are the electronic coordinates r , with the nuclear coordinates R being fixed:

$$\hat{H}_{elec} = -\frac{\hbar^2}{2m_e} \sum_i \nabla_i^2 - \sum_{N_a} \sum_i \frac{Z_a e^2}{4\pi\epsilon_0 r_{ia}} + \sum_i \sum_{j>i} \frac{e^2}{4\pi\epsilon_0 r_{e_i e_j}}, \quad (3.27)$$

where m_e is the mass of an electron, Z_a is the atomic number of some nuclei a , ϵ_0 is the vacuum permittivity constant, i represents an electron and j represents a different electron. Since the Born-Oppenheimer approximation fixes the positions of the nuclei ('clamps' the nuclei), term \hat{V}_{NN} is a constant only scaling the electronic potential energy eigenvalue U by a fixed value. This means the electronic Schrödinger equation can be expressed as:

$$(\hat{H}_{elec} + \hat{V}_{NN})\psi_{elec}(\mathbf{r}; \mathbf{R}) = U_{elec}(\mathbf{R})\psi_{elec}(\mathbf{r}; \mathbf{R}). \quad (3.28)$$

Arising from these set of equations and the Born-Oppenheimer approximation is the fact that the electronic Schrödinger equation is solved in the space of fixed nuclei positions. The $U_{elec}(\mathbf{R})$ provides the energy for the potential energy surface shown in figures 3.2, 3.1 and 3.3. To obtain the entire energy of the molecule in question, the positions of the nuclei need to be optimized. Optimization has been discussed in a general sense in section 3.4, but here we introduce the nuclear Schrödinger equation for motion to complete the picture. When the positions of the nuclei move the electronic wavefunction in equation 3.28 changes from $\psi(\mathbf{r}; \mathbf{R})$ to $\psi(\mathbf{r}; \mathbf{R}')$ with $U_{elec}(\mathbf{R})$ changing to $U_{elec}(\mathbf{R}')$. As a result, as the nuclear positions \mathbf{R} change the electronic energy varies smoothly, according to the solved electronic Schrödinger equation. Thus, $U_{elec}(\mathbf{R})$ forms part of the energy for nuclear motions. The Schrödinger equation for nuclear motion is given as:

$$\hat{H}_N \psi_N(\mathbf{R}) = U_{total} \psi_N(\mathbf{R}), \quad (3.29)$$

where ψ_N is the nuclear wavefunction and \hat{H}_N is the Hamiltonian for nuclear motion containing the $U_{elec}(\mathbf{R})$:

$$\hat{H}_N = \hat{T}_N(\mathbf{R}) + U_{elec}(\mathbf{R}). \quad (3.30)$$

Where $\hat{T}_N(\mathbf{R})$ is the term excluded in the electronic Schrödinger in equation 3.24. The solutions U_{total} to equation 3.29 provide the energies of the vibrational levels for a specific electronic state, shown as the dotted levels in figure 3.3. In this section, the details of solving the Schrödinger equation have been neglected. It is a fact of quantum mechanics that the Schrödinger equation that for systems with

more than 2 bodies cannot be solved analytically.

The variational principle allows us to build approximate methods to give inexact solutions to the Schrödinger equation. These will be dealt with in the next section.

3.8 The Variational Principle

The Schrödinger equation can only be solved analytically for systems involving less than three bodies, e.g. monoatomic hydrogen. Therefore, an approximate approach is required, if we are to have a basis for building approximate methods to solve quantum chemical systems. Moreover, an approach is required for building wavefunctions for chemical systems, where the exact wavefunction is unknown.

The variational theorem states that the using a set of trial wavefunctions ϕ we can obtain an approximate energy which is higher than or equal to the ground state energy, expressed mathematically as:

$$\int \Phi^* \hat{H} \Phi \geq E_0 \quad (3.31)$$

where E_0 is the ground state energy and ϕ is any well-behaved trial wavefunction. Equation 3.31 is expressing the probability density acted on by the Hamiltonian, integrated over some unspecified boundary conditions. To prove the variation theorem, we begin by expressing the trial wavefunction as a linear combination of orthonormal eigenfunctions of \hat{H} :

$$\Phi = \sum_i c_i \phi_i, \quad (3.32)$$

where each ϕ_i is a eigenfunction of the energy value E_i . Here, all the possible eigenfunctions of the trial wavefunction, Φ , are weighted by an expansion coefficient c_i .

The expansion of the wavefunction as a linear combination of orbitals $c\phi_i$ is known as a basis set expansion. Each eigenfunction in equation 3.32 corresponds to its own energy eigenvalue:

$$\hat{H}\phi_i = E_i\phi_i \quad (3.33)$$

so in a deeper sense each expansion coefficient c_i expresses a weighted probability

that the measurement E_i will occur. Inserting equation 3.32 into the left hand side of equation 3.31 gives:

$$\int \sum_i c_i^* \phi_i^* \hat{H} \sum_j c_j \phi_j d\tau = \int \sum_i c_i^* \phi_i^* \sum_j c_j \hat{H} \phi_j \quad (3.34)$$

Using equation 3.33 we can write equation 3.34 in terms of energy:

$$\int \sum_i c_i^* \phi_i^* \sum_j c_j E_i \phi_j = \sum_i \sum_j c_i^* c_j E_j \int \phi_i^* \phi_j \quad (3.35)$$

in order to simplify calculations we use orthonormal eigenfunctions ϕ_i . Orthonormal functions have the property where all terms are 0 when $i \neq j$ and 1 when $i = j$. Strictly, the previously described property alone is referred to as orthogonality, but *orthonormality* imposes the condition that the eigenfunctions ϕ_i are normalized too. To express the orthonormality of eigenfunctions the kronicker delta δ_{ij} replaces the intergrals on the right hand side of equation 3.35:

$$\sum_i \sum_j c_i^* c_j E_j \delta_{ij} \quad (3.36)$$

Since δ_{ij} is 0 when $i \neq j$ we can express equation 3.36 as composed of i parts only:

$$\int \phi^* \hat{H} \phi d\tau = \sum_i c_i^* c_i E_i = \sum_i |c_i|^2 E_i \quad (3.37)$$

In equation 3.31 we expressed the variation theorem in terms of the groundstate energy E_1 , the lowest energy eigenvalue. Therefore we can write equation 3.37 as:

$$\int \phi^* \hat{H} \phi d\tau = \sum_i |c_i|^2 E_i \geq \sum_i |c_i|^2 E_0 = E_0 \sum_i |c_i|^2 \quad (3.38)$$

Since ϕ is normalized we can write $\int \phi^* \phi$, and thus:

$$1 = \int \phi^* \phi d\tau = \int \sum_i c_i^* \phi_i^* \sum_j c_j \phi_j d\tau = \sum_i \sum_j c_i^* c_j \int \phi_i^* \phi_j d\tau = \sum_i \sum_j c_i^* c_j \delta_{ij} \quad (3.39)$$

and therefore:

$$1 = \sum_i |c_i|^2 \quad (3.40)$$

so, finally, we can write equation 3.38 as:

$$\int \phi^* \hat{H} \phi d\tau = E_i \geq E_0 \geq E_0, \quad (3.41)$$

which is the variation theorem expressed in terms of orthonormal wavefunctions. When the functions are non-orthogonal we can write equation 3.41 as:

$$\frac{\int \phi^* \hat{H} \phi d\tau}{\int \phi^* \phi} \geq E_0 \quad (3.42)$$

An equivalent way of writing equation 3.42 is in terms of bra-ket notation:

$$\frac{\langle \phi | \hat{H} | \phi \rangle}{\langle \phi | \phi \rangle} \geq E_0 \quad (3.43)$$

where the "bra-" $\langle \phi |$ represents the complex conjugate terms and the "-ket" $| \phi \rangle$ represents the right hand integral terms. In a deeper sense, the bra-ket notation expresses the integrals as vectors in Hilbert space with the "-ket" representing a Hilbert space vector, and the "bra-" representing the complex adjoint of the ket vector. Bra-ket provides a more convenient way of writing integrals in quantum mechanics.

What emerges from this is the variational theorem, a method for reaching approximate solutions using a trial wavefunction. These trial wavefunctions are often built with variational parameters inside them, which can be optimized to reach an energy minimum. However, with the variation theorem we still have the problem of systems involving more than two particles since electron-electron repulsion terms cannot be separated within the electronic Hamiltonian. It is therefore necessary to separate our guess wavefunctions into one-electron wavefunctions, known as the independent particle approximation (IPA). HF builds on the IPA by approximating 2-electron interactions. The Hartree-Fock method provides a means for approximating and solving a multi-electron system in terms of one- and two-electron functions.

3.9 Hartree-Fock Self-Consistent Field Method

3.9.1 The Slater Determinant

The Hartree-Fock method has its origins in 1928 when Douglas Hartree proposed constructing the multi-electron wavefunction as a product of 1-electron wavefunctions:

$$\Phi_0 = \phi_0(1)\phi_0(2)\dots\phi_0(n) \quad (3.44)$$

where Φ_0 is a product of 1 electron wavefunctions, and serves as our guess polyatomic wavefunction. $\phi_0(1)$ is the the wavefunction guess for electron 1 and $\phi_0(n)$ electron n . To begin optimizing Φ_0 , the first one-electron wavefunction $\phi_0(1)$ is solved where electron-electron repulsion is taken as the repulsion between electron 1 and an averaged field of electrons $\phi_0(2)\dots\phi_0(n)$. When the one-electron Schrödinger equation of 1 $\phi_0(1)$ is solved in this field, an improved wavefunction $\phi_1(1)$ is found. The process then repeats for electron 2 and its wavefunction $\phi_0(2)$ in the field of one-electron functions, until electron n $\phi_0(n)$. The cycle then repeats again for electron 1 and its wavefunction $\phi_1(1)$, in a newly optimized field. The cycle continues until the wavefunctions no longer optimize further in relation to the field. Then one-electron wavefunctions can be said to be *consistent* with the field, hence the term *self-consistent field* (SCF) [205].

Vladimir Fock found that the treatment of the polyatomic wavefunction in equation 3.44 as simply a product of 1-electron functions failed to represent the fermionic nature of electrons [206]. Fermions have half-integer spin quantum numbers, for electrons these are $-1/2$ or $+1/2$. The one-electron wavefunctions in Hartree's method in equation 3.44 neglects spin quantum numbers. Another deficiency Fock found related to the Pauli Exclusion principle, which states that no two fermions can possess the same quantum numbers, giving each electron in the system its own distinguishable set of quantum numbers. Representing the multi-particle wavefunction in equation 3.44 as simply the product of one-electron orbitals leads to their treatment as an indistinguishable set of particles. A correct treatment would allow for the exchange of any two particles to lead to a change in sign on the overall wavefunction, which would give the wavefunction its *anti-symmetric* requirement for fermions and ensures each particle occupies its own unique set of quantum numbers. To rectify the issues of Hartree's original representation of the wavefunctions, John Slater suggested that the multi-electron wavefunction be represented as:

$$\Phi(1, 2\dots n) = \frac{1}{\sqrt{n!}} \begin{vmatrix} \phi_1(1)\alpha(1) & \phi_1(1)\beta(1) & \dots & \phi_n(1)\beta(1) \\ \phi_1(2)\alpha(2) & \phi_1(1)\beta(2) & \dots & \phi_n(2)\beta(2) \\ \vdots & \vdots & \ddots & \vdots \\ \phi_1(n)\alpha(n) & \phi_1(n)\beta(n) & \dots & \phi_n(n)\beta(n), \end{vmatrix} \quad (3.45)$$

where α and β are spin functions respectively, ensuring that each electron has its own unique spin quantum number. The products of the spatial orbital $\phi_n(n)$ and spin function α/β in equation 3.45 are known as spin orbitals. Another way of writing the spin orbitals is:

$$\phi_1 = \phi_1\alpha, \quad (3.46a)$$

$$\bar{\phi}_1 = \phi_1\beta, \quad (3.46b)$$

which condenses the notation. Equation 3.45 became known as a Slater determinant. Placing the spin orbitals in a determinant maintains the anti-symmetric property, since the exchange of any 2 rows leads to a change of sign for the total determinant [207].

3.9.2 Formation of the Hartree-Fock Energy Expression

In order to derive an expression for the Hartree-Fock (HF) energy, we recall that for a series of normalized wavefunctions we can express the energy as:

$$E_{HF} = \langle \Phi | H_{elec} | \Phi \rangle, \quad (3.47)$$

where Φ is our n -dimensional Slater determinant in equation 3.45. To expand equation 3.47 we recall that an n -dimensional electronic can be written as an electronic Hamiltonian:

$$\hat{H}_{elec} = \overbrace{\sum_{i=1}^n \left(-\frac{1}{2} \nabla_i^2 - \sum_{N_a}^{Nuclei} \frac{1}{r_{ia}} \right)}^{1\text{-electron terms}} + \overbrace{\sum_{i=1}^{2n-1} \sum_{j=i+1}^{2n} \frac{1}{r_{ij}}}^{2\text{-electron terms}}. \quad (3.48)$$

Here, the Hamiltonian has been written in terms of atomic units which sets all the constants in equation 3.26 to 1. In this expansion we are considering a closed-shell case, with $2n$ electrons. Open-shell systems are more complex and will be discussed in Section 3.10.2. The 1-electron parts of the Hamiltonian, containing electron kinetic energy and nuclear-electron repulsion, can be condensed into a 'core Hamiltonian' operator:

$$\hat{H}_{elec} = \overbrace{\sum_{i=1}^{2n} \hat{H}_{(i)}^{core}}^{1\text{-electron terms}} + \overbrace{\sum_{i=1}^{2n-1} \sum_{j=i+1}^{2n} \frac{1}{r_{ij}}}^{2\text{-electron terms}}. \quad (3.49)$$

Separating the Hamiltonian into 1-electron and 2-electron terms allows them to be separated when the energy equation 3.47 is expanded.

Expanding the energy equation 3.47, which includes the expansion of the Slater determinant, leads to a set of integrals:

$$E_{HF} = (n!)^{-1} \int [(\phi_1^*(1)\phi_1^*(2)\dots\phi_n^*(n)) - (\phi_1^*(2)\phi_1^*(1)\dots\phi_n^*(n)) + \dots] \hat{H}_{elec} \quad (3.50)$$

$$[(\phi_1(1)\phi_1(2)\dots\phi_n(n) - \phi_1(2)\phi_1(1)\dots\phi_n(n) + \dots)] d\tau,$$

where singly permuted terms lead to -1 coefficients and doubly permuted terms have $+1$ coefficients for the expanded spin orbital products. In total, the Slater determinants on each side of the operator will have $n!$ products. It can be shown that all the integrals on the right hand side of equation 3.50 are all equal, allowing us to write the expansion as:

$$E_{HF} = \int [\phi_1^*(1)\phi_1^*(2)\dots\phi_n^*(n)] \hat{H}_{elec} \quad (3.51)$$

$$[(\phi_1(1)\phi_1(2)\dots\phi_n(n) - \phi_1(2)\phi_1(1)\dots\phi_n(n) + \dots)] d\tau.$$

At this point we can then separate out the expansion in terms of the 1-electron and 2-electron terms in the electronic Hamiltonian.

First, equation 3.51 is written solely in terms of the 1-electron core Hamiltonian:

$$\int \phi_1^*(1)\phi_1^*(2)\dots\phi_n^*(n) \left(\hat{H}_{(1)}^{core} + \hat{H}_{(2)}^{core} + \dots \hat{H}_{(n)} \right) \quad (3.52)$$

$$[(\phi_1(1)\phi_1(2)\dots\phi_n(n) - \phi_1(2)\phi_1(1)\dots\phi_n(n) + \dots)] d\tau,$$

where the sum of each core Hamiltonian for each electron $1 - n$ is shown. Taking the first set of integrals in equation 3.52, where there are no permutations, and the core Hamiltonian we get:

$$\int \phi_1^*(1)\phi_1^*(2)\dots\phi_n^*(n) \left(\hat{H}_{(1)}^{core} + \hat{H}_{(2)}^{core} + \dots \hat{H}_{(n)} \right) (\phi_1(1)\phi_1(2)\dots\phi_n(n)) d\tau. \quad (3.53)$$

We can separate equation 3.53 further according to a product of integrals for each core Hamiltonian, and then simplify the integrals using the orthogonal property of the wavefunctions. In order to demonstrate this simplification we expand equation 3.53 in terms of the core Hamiltonian $\hat{H}_{(1)}^{core}$ of electron 1. Since $\hat{H}_{(1)}^{core}$ does not operate on electrons $1 - n$ we can write the expansion 3.53 as:

$$\int \phi_1^*(1) \left(\hat{H}_{(1)}^{core} \right) \phi_1(1) d\tau_1 \int \phi_1^*(2) \phi_1(2) d\tau_2 \dots \int \phi_n^*(n) \phi_n(n) d\tau_n, \quad (3.54)$$

and due to orthogonality of the overlap integrals the (recalling $\delta_{i=i} = 1$) integrals simplifies to:

$$\int \phi_1^*(1) \left(\hat{H}_{(1)}^{core} \right) \phi_1(1) d\tau_1, \quad (3.55)$$

which demonstrates the power of choosing orthogonal functions to represent the wavefunction, since the problem becomes greatly simplified. In the expansion of equation 3.52, if the integrals contain one or more permutations they will vanish due to disagreements in the overlap integrals ($\delta_{i \neq j} = 0$). Thus for each core Hamiltonian for n -electrons, only integrals expanded with no permutations will remain, giving the general expression for equation 3.51 for a $2n$ electron case as:

$$\sum_{i=1}^n 2H_{ii} = \langle \Psi | \sum_{i=1}^{2n} \hat{H}_{(i)}^{core} | \Psi \rangle, \quad (3.56)$$

where H_{ii} refers to:

$$H_{ii} = \int \psi_i^*(1) H_{(1)}^{core} \psi_i(1) d\tau_1. \quad (3.57)$$

Giving the first term in the expansion of HF energy for a $2n$ electron system.

Moving on to the expansion of the 2-electron terms, once again we express the HF equation 3.50 solely in terms of the 2-electron terms in the core Hamiltonian:

$$\int \phi_1^*(1) \phi_1^*(2) \dots \phi_n^*(n) \left(\frac{1}{r_{12}} + \frac{1}{r_{13}} \dots \frac{1}{r_{ij}} \dots \frac{1}{r_{(n)(n-1)}} \right) \quad (3.58)$$

$$[(\phi_1(1)\phi_1(2)\dots\phi_n(n) - \phi_1(2)\phi_1(1)\dots\phi_n(n) + \dots)] d\tau,$$

where the sum of the 2-electron repulsion terms for electrons 1 – 2. Taking the first set of integrals in equation, where there are no permutations, 3.58 we get:

$$\int \phi_1^*(1) \phi_1^*(2) \dots \phi_n^*(n) \left(\frac{1}{r_{12}} + \frac{1}{r_{13}} \dots \frac{1}{r_{ij}} \dots \frac{1}{r_{(n)(n-1)}} \right) \quad (3.59)$$

$$(\phi_1(1)\phi_1(2)\dots\phi_n(n)) d\tau.$$

Once again we can separate the integrals further by writing them as a product integrals for each 2-electron term. Since the 2-electron repulsion term $\frac{1}{r_{ij}}$ does not

act on any electrons other than ij , we can write the expansion of electrons 1 and 2 as:

$$\int \phi_1^*(1)\phi_1^*(2) \left(\frac{1}{r_{12}}\right) \phi_1(1)\phi_1(2) \int \phi_2^*(3)\phi_2(3)\dots \int \phi_n^*(n)\phi_n(n). \quad (3.60)$$

Due to the orthogonality of the orbitals, the overlap integrals simplify to 1. In the general case of expanded terms from the Slater determinant which contain no permutations the integrals are represented symbolically as:

$$J_{ij} = \int \phi_i^*(1)\phi_j^*(2) \left(\frac{1}{r_{12}}\right) \phi_i(1)\phi_j(2), \quad (3.61)$$

which is referred to as the Coulomb integral, which represents the repulsion between two electrons 1 and 2 between in spin orbitals i and j . In general, the coulomb integral J_{ij} represents 2-electron terms involving no permutations in the expansion of the Slater determinant. Moving on to terms involving single permutations, such as the second set of integrals in the expansion in equation 3.51, which is expressed as:

$$- \int \phi_1^*(1)\phi_1^*(2) \left(\frac{1}{r_{12}}\right) \phi_1(2)\phi_1(1) \int \phi_2^*(3)\phi_2(3)\dots \int \phi_n^*(n)\phi_n(n), \quad (3.62)$$

where the the overlap integrals are once again simplified to 1. In the general case the integrals expanded from the Slater determinant involving single permutations are represented symbolically as:

$$K_{ij} = \int \phi_i^*(1)\phi_j^*(2) \left(\frac{1}{r_{12}}\right) \int \phi_i(2)\phi_j(1), \quad (3.63)$$

which is referred to as the exchange integral. The exchange integral does not have an explicit physical meaning, but is often interpreted as representing the repulsion between-like spins. In the case where a single permutation occurs between electrons of different spin the exchange integral will vanish, resulting in the total expression for the 2-electron terms for the closed shell $2n$ case to contain 2 coulomb repulsion terms for every 1 exchange terms:

$$\sum_{i=1}^n \sum_{j=1}^n (2J_{ij} - K_{ij}) = \langle \Psi | \sum_{i=1}^{2n-1} \sum_{j=i+1}^{2n} \frac{1}{r_{ij}} | \Psi \rangle. \quad (3.64)$$

Terms involving 2 or more permutations in the expansion of the Slater determinant in equation 3.59 will all contain disagreement in the overlap integrals, so

equation 3.64 contains only terms involving zero and single permutations. In total, combining the expansions of the 1 and 2 electron terms we arrive at an expression for energy for a $2n$ system:

$$\epsilon_i = \langle \Phi | H_{elec} | \Phi \rangle = 2 \sum_{i=1}^n H_{ii} + \sum_{i=1}^n \sum_{j=1}^n (2J_{ij} - K_{ij}). \quad (3.65)$$

These are known as the Slater-Condon rules.

3.9.3 Formation of the Hartree Fock Equations

In order to minimize the energy in the energy equation 3.65 the spin orbitals are optimized, with the constraint orthonormality such that the overlap integrals are 0 or 1 according to the kronicker delta δ_{ij} . At the minimum energy, E_{HFmin} and the overlap integrals $S_{ij} \equiv \langle \phi_i | \phi_j \rangle$ must both be constants with variations of the spin orbitals $\delta\phi$, therefore their linear combination can be expressed as:

$$\epsilon_{min} + \sum_i^n \sum_j^n \epsilon_{ij} S_{ij} = \text{constant for } \delta\phi, \quad (3.66)$$

where ϵ_{ij} is known as unknown set of constants which maintain the orthonormality of the overlap integrals S_{ij} . The method of obtaining a set of constants ϵ_{ij} in order to minimize a function under a constraint is known as the Lagrangian method of unknown multipliers, where ϵ_{ij} is our unknown multiplier. Substituting the equation for E_{HF} into equation 3.66 and differentiating with respect to ϕ 's we get:

$$2 \sum_{i=1}^n \delta H_{ii} + \sum_{i=1}^n \sum_{j=1}^n (\delta 2J_{ij} - \delta K_{ij}) + \sum_i^N \sum_j^N \epsilon_{ij} \delta S_{ij} = 0, \quad (3.67)$$

to obtain a minimum energy. Since the we are differentiating with respect to the spin orbitals we can write the components of 3.67 as:

$$\delta S_{ij} = \int \delta \phi_i(1)^* \phi_j(1) d\tau_1 + \int \phi_i^*(1) \delta \phi_j(2) d\tau_1, \quad (3.68a)$$

$$\delta H_{ii} = \int \delta \phi_i^*(1) H^{\hat{core}} \phi_i(1) d\tau_1 + \int \phi_i(1)^* H^{\hat{core}} \delta \phi_i(1) d\tau_1, \quad (3.68b)$$

$$\begin{aligned} \delta J_{ij} = & \int \delta \phi_i^*(1) \phi_j^*(2) \left(\frac{1}{r_{12}} \right) \phi_i(1) \phi_j(2) d\tau_1 d\tau_2 + \int \phi_i^*(1) \delta \phi_j^*(2) \frac{1}{r_{12}} \phi_i(2) \phi_j(2) d\tau_1 d\tau_2 \\ & + \text{complex conjugates}, \end{aligned} \quad (3.68c)$$

$$\delta K_{ij} = \int \delta\phi_i^*(1)\phi_i^*(2) \left(\frac{1}{r_{12}}\right) \phi_i(2)\phi_i(1)d\tau_1d\tau_2 + \int \phi_i^*(1)\delta\phi_i^*(2) \frac{1}{r_{12}}\phi_i(2)\phi_i(1)d\tau_1d\tau_2$$

+ complex conjugates.

(3.68d)

Using the approximation, we can define the Coulomb operator as:

$$\hat{J}_i(1) = \int \phi_i^*(2) \left(\frac{1}{r_{12}}\right) \phi_i(2)d\tau_2, \quad (3.69)$$

where $\hat{J}_i(1)$ is a pseudo 1-electron operator. This allows us to write the partial differential δJ_{ij} as:

$$\int \delta\phi_i^*(1)\hat{J}_j(1)\phi_i(1)d\tau_1 + \int \delta\phi_j^*(1)\hat{J}_i(1)\phi_j(1)d\tau_1 + \text{complex conjugate}. \quad (3.70)$$

Similarly, if we define the exchange operator as:

$$\hat{K}_i(1)\phi_j(1) = \int \phi_i^*(1) \left(\frac{1}{r_{12}}\right) \phi_j(2)d\tau_2\phi_i(1), \quad (3.71)$$

which is written as operating on an orbital ϕ_j since it involves an orbital exchange. Defining the exchange operator as equation 3.71 allows us to write the partial differential δK_{ij} :

$$\int \delta\phi_i^*(1)\hat{K}_j(1)\phi_i(1)d\tau_1 + \int \delta\phi_j^*(1)\hat{K}_i(1)\phi_j(1)d\tau_1 + \text{complex conjugate}, \quad (3.72)$$

which leads to the total partial differential equation 3.67 to be written in terms of the coulomb and exchange operators:

$$2 \sum_{i=1}^n \int \delta\phi_i [\hat{H}_{core}(1)\phi_i^*(1) + \sum_{j=1}^n (2\hat{J}_j(1) - \hat{K}_j(1))\phi_i^*(1) + \frac{1}{2} \sum_{j=1}^n \epsilon_{ij}\phi_j^*(1)]d\tau_1$$

+ complex conjugates = 0.

(3.73)

Here the total sum of the other integrals is represented by '*complex conjugates*'. Two interpretations could arise from equation 3.73: that the total sum of all the integrals cancel to equal 0 or that each integral is individually equal to 0. However, since the spin orbitals $\delta\phi_i$ and $\delta\phi_i^*$ are independent, each integral must individually equal 0. As a consequence, for all $i = 1$ to n , each integral can be expressed as:

$$\left[\hat{H}_{(1)}^{core} + \sum_{j=1}^n (2\hat{J}_j(1) - \hat{K}_j(1)) \right] \phi_i(1) = \sum_{j=1}^n \epsilon_{ij} \phi_j(1), \quad (3.74)$$

where the terms in the square brackets are known as the Fock operator \hat{F} , condensing equation 3.74:

$$\hat{F}(1)\phi_i(1) = \sum_{j=1}^n \epsilon_{ij}\phi_j(1) \quad (3.75)$$

It is important to note here that the usage of (1) in the previous equations indicates that these i equations are all 1-electron equations, solving for electron 1. The Fock operator is therefore a pseudo 1-electron operator in contrast to the Hamiltonian operator which is a multi-electron operator. In order to obtain the solutions to equation 3.75 we need it to be in the form of an eigenvalue equation. In its current form, an operator acts on a function to produce a *sum* of functions multiplied by a constant ϵ_{ij} . In order to derive an eigenvalue equation from the equation we can rewrite it as a matrix equation:

$$\hat{F}\phi = \epsilon\phi, \quad (3.76)$$

where ϕ is a column matrix of spin orbitals i to n , and ϵ is a square matrix of elements e_{ij} . The matrix equation 3.76 will be in eigenvalue form ($\hat{F}\phi_i = k\phi_i$) if all the off diagonal elements of ϵ where $\epsilon_{i \neq j}$ equal 0. In other words ϵ is a diagonal matrix. In its current form ϵ is not a diagonal matrix, but it can be diagonalized in the following way. For ϵ there exist matrices \mathbf{P} and \mathbf{P}^{-1} , as well as a diagonal matrix ϵ' such that:

$$\epsilon = \mathbf{P}\epsilon'\mathbf{P}^{-1}. \quad (3.77)$$

Substituting 3.77 in the matrix equation 3.76 yields:

$$\hat{F}\phi = \mathbf{P}\epsilon'\mathbf{P}^{-1}\phi. \quad (3.78)$$

Multiplying by \mathbf{P} on the left and \mathbf{P}^{-1} on the right gives:

$$\hat{F}\mathbf{P}^{-1}\phi'\mathbf{P} = (\mathbf{P}^{-1}\mathbf{P})\epsilon'\mathbf{P}^{-1}\phi'\mathbf{P}, \quad (3.79)$$

and since $\mathbf{P}^{-1}\mathbf{P} = 1$, equation 3.79 simplifies to:

$$\hat{F}\phi' = \epsilon'\phi'. \quad (3.80)$$

The equations 3.80 are known as the Hartree-Fock equations, and the diagonal elements of ϵ yield the energies of the orbitals i . Here, we can now refer back to equation 3.44. The derived HF equation 3.80 provides the means to iteratively reach a minimized energy in the same way, where an initial guess of the molecular orbitals ϕ_i (which are in turn individual spin orbitals in terms of the α β spin operators) allows us to then construct the Fock operator \hat{F} , which then in turn provides an improved ϕ_i and an energy ϵ_i for that orbital. The iterative process continues until ϵ_i no longer varies. The dependence of the Fock operator \hat{F} on the molecular orbitals ϕ_i means that equation 3.80 is not a true eigenvalue equation. Nonetheless, the dependence of the Fock operator on the wavefunctions it acts upon provides the means for the iterative optimization procedure, known as a self-consistent field method.

Since the wavefunctions ϕ used in the equations 3.75 are meant to represent whole molecular orbitals, they may be computationally expensive to optimize due to their complexity. Furthermore, a procedure whereby the wavefunctions are varied has not been explicitly defined. The Roothaan-Hall equations provide a means for representing the complex molecular orbitals ϕ as a linear combination of simpler functions and will be discussed in the next section.

3.9.4 Roothaan-Hall Equations

In 1951 Roothaan and Hall proposed that in order to minimize the energy in the HF energy equation 3.65, the molecular orbitals could be expanded as a series of basis functions χ :

$$\phi_i = \sum_{s=1}^r c_{si} \chi_s, \quad (3.81)$$

where the basis functions χ are weighted by expansion coefficients c_{ki} and expanded up to s times [208, 209]. The choice of basis functions χ to represent the spin orbitals will be discussed in section 3.12. Substituting the molecular orbitals in equation 3.80 with the linear combination of basis functions in equation 3.81 gives:

$$\sum_s c_{si} \hat{F} \chi_s = \epsilon_i \sum_s c_{si} \chi_s, \quad (3.82)$$

where the matrix form has been neglected demonstrate how the molecular orbitals are represented in terms of basis sets. Multiplying equation 3.82 by χ_r^* and

integrating gives:

$$\sum_{s=1}^r c_{si} \left(\langle \chi_r | \hat{F} | \chi_s \rangle - \epsilon_i \langle \chi_r | \chi_s \rangle \right) = 0, \quad (3.83)$$

where we can rewrite the integrals as:

$$\sum_{s=1}^r c_{si} (F_{rs} - \epsilon_i S_{rs}) = 0, \quad (3.84)$$

which can be expressed in matrix form as:

$$\mathbf{FC} = \mathbf{SC}\epsilon \quad (3.85)$$

which concludes the derivation of the Roothaan-Hall equations. However, if total energy is expressed as a sum of the individual orbital energies:

$$E(\text{overestimation}) = 2 \sum_{i=1}^n \epsilon_i, \quad (3.86)$$

there is an overestimation of the total energy. The overestimation comes from the fact that we are counting the repulsion between electrons i and j twice in equation 3.65. We recover the artificial increase in energy by instead using:

$$E_{HF} = 2 \sum_{i=1}^n \epsilon_i - \sum_{i=1}^n \sum_{j=1}^n (2J_{ij} - K_{ij}), \quad (3.87)$$

which gives the total expression for the HF electronic energy.

3.9.5 Deficiencies With the HF Method

The Roothaan-Hall method provides an iterative way of implementing the HF method, as well as allowing the wavefunction to be constructed as a linear combination of basis functions. Referring back to the start of the HF section to the original SCF equation proposed by Hartree, equation 3.44 was solved as a series of 1-electron functions where the wavefunctions were guessed and then iteratively refined in an average field of other electrons. In a similar way, the Roothaan-Hall procedure starts with some initially chosen basis sets χ_s and guessed coefficients c_{si} , which leads to the evaluation of the overlap integrals S , H_{core} and the potential energy integrals. The energy is then varied via the coefficients c_{si} , elements of \mathbf{C} . The newly optimized coefficients c_{si} form a newly optimized set of basis functions for the overlap integrals and the Fock operator. The process continues until the

coefficients c_{si} no longer vary. The HF method will not be directly employed in this thesis, but the SCF procedure it uses and the deployment of basis sets are common to all the methods used in the work here.

Despite providing the first method for variationally obtaining energies for polyatomic multi-electron systems, the HF method as described has a number of disadvantages. Firstly, electron correlation is neglected. Electron correlation refers to the repulsion between individual electrons. In the HF method, electrons experience repulsion from other particles as a smeared-out cloud of charge, but a more accurate picture would take into account local electron-electron interactions. Neglect of electron correlation means that energies arising from the HF method are always higher than the true non-relativistic energy:

$$E_{corr} \equiv E_e - E_{HF}. \quad (3.88)$$

The correlation energy, E_{corr} , associated with the electron-electron repulsion is known as *dynamic* correlation.

A second problem is the fact that the derivation just described has been for closed-shell systems. In our closed-shell derivation electrons have been added as pairs of electron associated with the same spatial molecular orbitals and different spin orbitals, described as a *Restricted Hartree-Fock* method. The work in this thesis deals extensively with free radicals, open-shell systems with odd numbers of electrons. Correlation energy associated with the misrepresentation of the system's state is known as *static* correlation. Arising from the HF methods, a quantum chemist has two techniques to recover some of the correlation energy- that can be employed simultaneously, or individually. Firstly, the modification of the construction of the Slater determinant wavefunction such as allowing the spin orbitals to be associated with different spatial orbitals. Secondly, post-HF methods, which involve modifications to the construction of the multi-electron wavefunctions, such as the use of multiple Slater determinants. Both these techniques will be described in the next section.

3.10 Recovering Correlation Energy

The total correlation energy arising from the incorrect description of the systems state and local electron-electron interactions, can be expressed as:

$$E_{corr} = E_{static} + E_{dynamic}. \quad (3.89)$$

This section will outline methods to recover these correlation energies.

3.10.1 Restricted Open-Shell Hartree-Fock and Unrestricted Hartree-Fock

The wavefunction 3.45 constructed in the previous section was built in a closed shell configuration, with each spatial orbital being associated with α and β spin orbitals. A wavefunction whose spatial orbitals are each associated with an α and β is termed a restricted Hartree-Fock wavefunction (RHF). We can express this RHF wavefunction for n orbitals as:

$$|\Phi(1, 2\dots n)\rangle = |\phi_1\bar{\phi}_1\phi_2\bar{\phi}_2\dots\phi_n\bar{\phi}_n\rangle. \quad (3.90)$$

In the open-shell case, where $\alpha > \beta$ electrons (or vice-versa), restricted open-shell Hartree-Fock (ROHF) method assigns extra α spin orbital(s) with a doubly occupied spatial orbital. The ROHF wavefunction can be expressed as:

$$|\Phi(1, 2\dots n)\rangle = |\phi_1\bar{\phi}_1\phi_2\bar{\phi}_2\dots\phi_n\rangle, \quad (3.91)$$

where a single electron fills the last spatial orbital.

By contrast, unrestricted hartree-fock (UHF) assigns different spatial orbitals for both the α and β spins. The UHF wavefunction is expressed as:

$$|\Phi(1, 2\dots n)\rangle = \left| \phi_1^\alpha \bar{\phi}_1^\beta \phi_2^\alpha \bar{\phi}_2^\beta \dots \phi_n^\alpha \right\rangle. \quad (3.92)$$

Both approaches have their advantages and disadvantages. In the ROHF case, since the extra α spin state is assigned to a doubly occupied spatial orbital, it is restricted spatially despite having a different environment to α the β electrons. The restriction on the spatial component could be problematic in the case of homolytic fissions for instance, where α and β electrons are situated on different atoms. As a result of this spatial restriction, the ROHF energy is higher than UHF energy

where the α and β electrons are assigned different spatial orbitals, which can be individually optimized. On the other hand, the UHF wavefunction is often not an eigenfunction of the spin operator \hat{S}^2 . As a result, the UHF cannot purely describe the multiplicity of the system of interest, and is often 'contaminated' by higher spin states. This contamination by higher spin states can be seen in figure 3.5 where the low energy orbitals in the UHF doublet are not completely degenerate.[210]

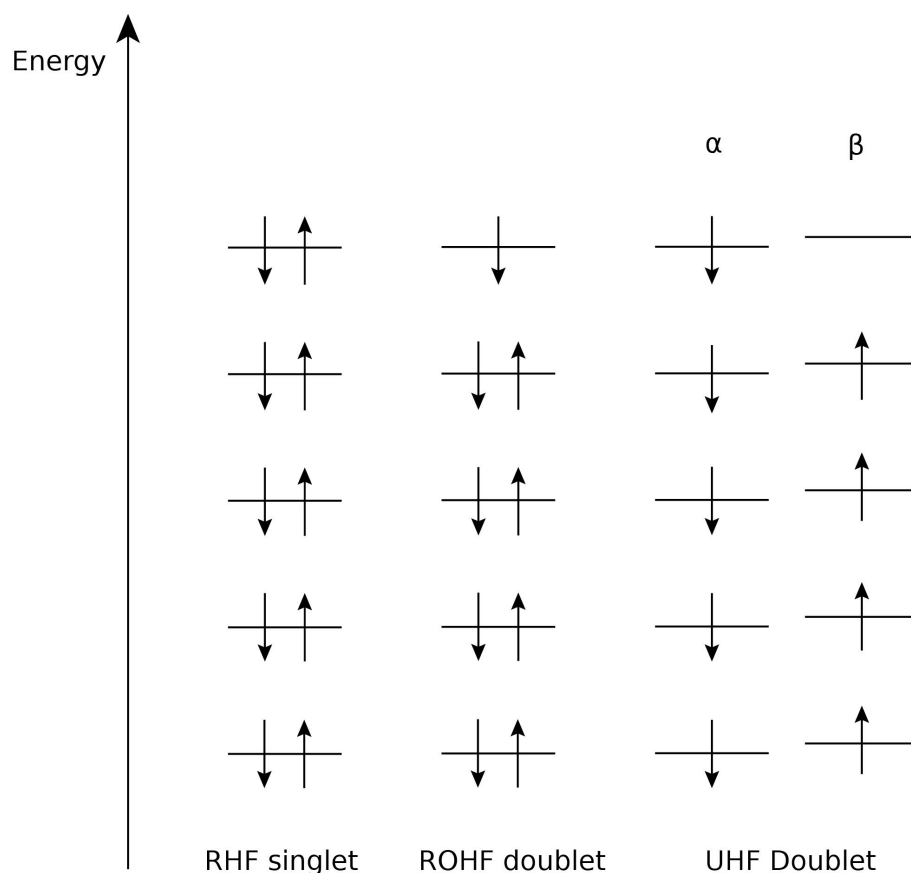


Figure 3.5: Restricted Hartree-Fock, Restricted open-shell Hartree-Fock and Unrestricted Hartree-Fock wavefunctions visualized

The use of unrestricted or restricted open-shell orbitals allows us to recover some of the static correlation energy. However, the dynamic correlation is still not taken into account when these orbitals are employed in a pure HF calculation. The next section will describe post-HF methods, which broadly aim to recover both static and dynamic correlation.

3.10.2 Post-Hartree Fock Methods

The current HF methods described thus far have all used single determinants. However, when breaking bonds homolytically to form doublets, triplets etc. (radical species), the single determinant fails to describe the multiconfigurational nature of these systems. Introducing the first post-HF method, Configuration interaction (CI) overcomes this by constructing the wavefunction as multiple determinants called configuration state functions (CSFs):

$$|\Psi\rangle = \overbrace{b_0 |\Phi_0\rangle}^{\text{ground state}} + \overbrace{\sum_{ra} b_a^r |\Phi_a^r\rangle}^{\text{singly excited}} + \overbrace{\sum_{a<b,r<s} b_{ab}^{rs} |\Phi_{ab}^{rs}\rangle}^{\text{doubly excited}} \dots, \quad (3.93)$$

where contribution of each determinant is varied via the expansion coefficients b . Each determinant in equation 3.93 is constructed from a ground state, singly excited, or doubly excited configurations. Representing all the possible configurations for a given set of occupied and virtual orbitals is termed a full CI calculation. Even for small molecules, the number of determinants in a full CI calculation is too computationally too expensive to deal with. For instance, one of the simplest hydrocarbons CH_4 requires 13123110 determinants for a full CI calculation using a minimal basis. Even with an incomplete basis it is necessary to reduce the size of the CI calculation by truncating the number of excited determinants due to computational expense. A commonly employed CI method is CISD, which just includes the singly and doubly excited CSFs. However, CI calculations have the disadvantage that they are neither *size extensive* nor *size consistent* [211]. Size extensivity refers to the property of a method that produces a linear growth in energy as the size of the system increases. Size consistency refers to the property of a method that treats two infinitely dissociated species as two separate entities. Coupled with the high computational cost, the size extensivity and consistency issues means that CI is rarely useful for all but small systems. In order to deal with these issues whilst still employing multiple determinants, the multiconfiguration SCF (MCSCF) method can be introduced.

In the MCSCF method, the multi-electron wavefunction is still written as a linear combination of CSFs, but the variation comes from the b expansion coefficients as well as the molecular orbitals which construct the CSFs. There are a several types of MCSCF, with the key difference between each type being the way the configurations for the determinants are selected. Qualitatively, many chemical systems have a multi-determinant nature, like conjugated systems where a single determinant fails

to describe the resonance between the orbitals. One of the most popular forms of the MCSCF methods is complete active space SCF (CASSCF). In CASSCF the 'active space' are MOs with whom a full CI is performed. Since this becomes too expensive for larger systems, a variation of CASSCF, restricted active space SCF (RASSCF) is sometimes employed. RASSCF portions the active space into single, double and triple excitations; and so on. Employing MCSCF requires a judicious choice of the active space. Incorrect choice of the active space can lead to incorrect potential energy surfaces, which can lead to transition states 'flattening' [212]. Furthermore, MCSCF much like CI is expensive to employ for larger systems. As an alternative to the expensive CI and MCSCF methods, perturbation theory can be used.

Møller-Plesset (MP) perturbation theory was developed to recover correlation energy from the unperturbed HF wavefunction [213]. Perturbation theory is not unique to quantum chemistry, but originates from a wider set of methods in physics developed to reach approximate solutions to complex problems by adding perturbations to simpler mathematical models of those problems. One of the earliest examples of perturbation theory is in reaching approximate solutions to many-body celestial mechanics problems [214]. Nonetheless, MP perturbation theory was developed as a way of systematically recovering correlation energy from the original HF equation.

A second order correction calculation is termed an MP2 calculations, with further corrections being termed MP3, MP4; and so on. MP calculations are generally computational cheaper than CI and MCSCF calculations. Furthermore, MP calculations are size consistent. MP calculations have the disadvantage that when used with unrestricted wavefunctions spin contamination can produce serious errors [215]. Moreover, MP calculations only work when the perturbation to reach the correct solution is small. Therefore, the starting geometries can not be too far from the stationary point. When the starting guess is far away from the solution, there is little guarantee that the calculation will converge. The final post-HF we will introduce is the coupled-cluster method.

Coupled-cluster (CC) is similar to CI and MCSCF in that it recovers correlation energy by using electron excitations.

A common CC method use is coupled cluster singles and doubles (CCSD), which includes the \hat{T}_1 and \hat{T}_2 excitation operators. The method CCSD(T), which includes a perturbation inclusion of the triple excitation operator \hat{T}_3 , is often referred to as

'the gold standard' of computational chemistry due to its accurate computation of bond lengths and energies. However, CCSD(T) is often too computationally demanding to be used for larger systems.

A common issue in many of the Post-HF methods is the computational expense required. For the work in this thesis, where the agglomeration of large aromatic systems characterizes jet fuel deposition, many of these methods are too expensive to be used practically. The next section will introduce Density Functional Theory (DFT), which takes a different approach entirely to HF and post-HF methods, recovers electron correlation energy. DFT is computationally cheap and scales $N^{3.5}$ compared to $N^{8.5}$ for CCSD(T). Moreover, DFT is usually less sensitive to the basis sets used.[216]

3.11 Density Functional Theory

Density functional theory is not based on the wavefunction, in contrast to HF and post-HF. DFT rests on the proof that all the electronic properties of a molecule can be found from its ground-state electron probability density $\rho_0(x, y, z)$ [217]. Using the ground-state electron density $\rho_0(x, y, z)$ has the advantage in that it is a function of only three variables, in contrast to $4n$ coordinates using the wavefunction. Furthermore, electron density is a property which directly measurable in contrast to the abstract concept of the wavefunction. The key advantage of DFT is that it can recover correlation energy whilst being relatively computational cheap compared to post-HF methods. As a result of these advantages, it is employed extensively in this thesis. The following section will elucidate the theories behind DFT and describe how it will be employed in the work in this document.

3.11.1 The Hohenberg-Kohn Theorems

Calculating the properties of atoms and molecules has its origins in early work on an ideal electron gas [218] [219]. Moreover, modern implementations of DFT rely on the Hohenberg-Kohn theorems. The first Hohenberg-Kohn theorem states that the properties of a molecule in its ground state is a functional of its ground state probability density:

$$E_0 = E[\rho_0(x, y, z)]. \quad (3.94)$$

A functional is a mathematical operation that transforms a function (in this case density) into a number. The second Hohenberg-Kohn theorem is analogous to the variation theorem for wavefunction described in section 3.8. The second theorem states that any trial electron density function will give energy equal or higher than the true energy, which is expressed as:

$$E_v[\rho_t] \geq E_0[\rho_0]. \quad (3.95)$$

Here, E_v and ρ_t refer to the variational energy and trial electron density respectively. Unfortunately, there are several issues with the above theorems. Firstly, there is no indication how to find the electron density ρ_0 . Moreover, the functional relating energy to the electron density ρ_0 is not known. As a result, approximations in finding the electron density and the functionals must be made. These approximations lead to functionals which are not variational. Nevertheless, with judicious choice of functional, it is still possible to obtain molecular structures with a high degree of accuracy. The most widely applied method for obtaining approximate energies and obtaining electron density is the Kohn-Sham approach.

3.11.2 Kohn-Sham Equations

In principle, DFT makes it possible to calculate electronic properties without having to find the wavefunction. However, the original Hohenberg-Kohn theorems offered no way of finding the energy. The Kohn-Sham (KS) approach overcomes these issues in two ways. Firstly, expressing the total energy functionals as a sum of many smaller functionals, where only a relatively small functional is the unknown one. Secondly, building electron density as an initial guess of 'KS orbitals' which are iteratively optimized (similar to the HF method). In this sense, the KS theory still relies on a 'KS wavefunction' formed from basis sets. However, in the KS approach, the wavefunction has no physical significance. By contrast, HF occupied orbital energies correspond well to the negative of the energy to remove an electron from that orbital.

For the derivation of the KS equations, we consider a fictitious non-interacting reference system of n interacting electrons $\rho_f(r)$ that each experience the same external potential $v_s(r_i)$. The external potential $v_s(r_i)$ acts on fictitious density $\rho_f(r)$ to yield exact energy eigenvalues of the densities of a real system. To find an expression for the external potential $v_s(r_i)$, we consider the total energy expression for a molecule:

$$E_0[\rho_0] = T_{ni}[\rho_0] + V_{ne}[\rho_0] + V_{ee}[\rho_0] + \overbrace{\Delta T[\rho_0] + \Delta V_{ee}[\rho_0]}^{E_{xc}} \quad (3.96)$$

Here $T_{ni}[\rho_0]$ represents the kinetic energy for non interacting electrons, $V_{ne}[\rho_0]$ the nuclear-electron repulsion, $V_{ee}[\rho_0]$ electrostatic electron-electron repulsion, $\Delta T[\rho_0]$ is a correction term for non-interacting electrons and $\Delta V_{ee}[\rho_0]$ is a correction term for the deviation between the real electron-electron repulsion energy compared to a charge-coulomb repulsion energy. It is this last term which makes DFT a correlated method. These last two terms are summed into one term 'the exchange correlation' E_{XC} functional. However, the exact form of the exchange-correlation function E_{XC} is unknown. Instead, various approximations have been proposed, and it is up to the user to find which approximation suits their system the best. Different approximations to the exchange-correlation functional will be discussed in Section 3.11.3.

In the total expression for energy, equation 3.96, we have used the ground state density ρ_0 . However, we are considering a system of non-interacting electron of fictitious density $\rho_f(r)$. In the Kohn-Sham approach, the fictitious density is said to be equal to the true ground state density, which is expressed as a linear combination of spatial-orbitals:

$$\rho_0 = \rho_f = \sum_{i=1}^{2n} \left| \Phi(1)_i^{KS} \right|^2. \quad (3.97)$$

Using the expression for fictitious density in equation 3.97, we can now expand the total energy expression 3.96 in terms of the known functionals. Starting the kinetic energy for non-interacting electrons, the kinetic energy for non-interacting electrons $T_{ni}[\rho_0]$ can be written as the expectation value of the sum of one-electron kinetic energy operators:

$$T_{ni}[\rho_0] = -\frac{1}{2} \sum_{i=1}^{2n} \langle \Phi(1)_i^{KS} | \nabla_1^2 | \Phi(1)_i^{KS} \rangle. \quad (3.98)$$

The nuclear-electron repulsion, $V_{ne}[\rho_0]$ is written as the product of ground state density and the external potential:

$$V_{ne}[\rho_0] = \int \rho(\mathbf{r}) \nu(\mathbf{r}) d\mathbf{r} = - \sum_{nuclei A} Z_A \int \frac{\rho_0(\mathbf{r}_1)}{r_{1a}} d\mathbf{r}_1, \quad (3.99)$$

where ν is the potential for attraction of electron i to the nuclei and Z_A the nuclear charge on nucleus A. The electron-electron repulsion $V_{ee}[\rho_0]$ is be written as:

$$V_{ee}[\rho_0] = \frac{1}{2} \int \int \frac{\rho_0(\mathbf{r}_1)\rho_0(\mathbf{r}_2)}{r_{12}} d\mathbf{r}_1 d\mathbf{r}_2 \quad (3.100)$$

Using equations 3.98, 3.99 and 3.100 and combining the last two terms into the exchange correlation term, the energy expression 3.96 now becomes:

$$E_0 = - \sum_{nucleiA} Z_A \int \frac{\rho_0(\mathbf{r}_1)}{\mathbf{r}_{1a}} d\mathbf{r}_1 - \frac{1}{2} \sum_{i=1}^{2n} \langle \Phi(1)_i^{KS} | \nabla_1^2 | \Phi(1)_i^{KS} \rangle + \frac{1}{2} \int \int \frac{\rho_0(\mathbf{r}_1)\rho_0(\mathbf{r}_2)}{r_{12}} d\mathbf{r}_1 d\mathbf{r}_2 + E_{XC}[\rho_0]. \quad (3.101)$$

In a similar procedure to HF, substituting our expression of the KS density (equation 3.97) into our expression for the energy (equation 3.101) as well as varying E_0 with respect to Φ_i^{KS} , subject to the constraint of maintaining orthonormality, leads to the KS equations:

$$\left[-\frac{1}{2} \nabla_i^2 - \sum_{nucleiA} \frac{Z_A}{\mathbf{r}_{1A}} + \int \frac{\rho(\mathbf{r}_2)}{r_{12}} d\mathbf{r}_2 + \frac{\delta E_{xc}[\rho(\mathbf{r})]}{\delta \rho(\mathbf{r})} \right] \Phi_i^{KS}(1) = \epsilon_i^{KS} \Phi_i^{KS}(1). \quad (3.102)$$

Combining the two-body terms in equation 3.102 we find an expression for the external potential $v_s(r_i)$ acting on our fictitious density $\rho_f(r)$. The term in equation 3.102 square brackets is termed the Kohn-Sham operator, and is expressed as:

$$\hat{h}^{KS} \Phi_i^{KS}(1) = \epsilon_i^{KS} \Phi_i^{KS}(1). \quad (3.103)$$

The Kohn-Sham operator is analogous to the Fock operator \hat{F} shown in equations 3.74 and 3.75. In order to optimize the density with respect to minimizing the energy of the orbitals ϵ_i^{KS} , we can employ the Roothaan-Hall approach described in Section 3.9.4. Using the Roothaan-Hall equations, the KS orbitals in equation 3.103 are written as a series of basis functions χ which are varied by expansion coefficients c_{si} (equation 3.81). The expansion of the KS MOs Φ_i^{KS} in terms of their basis functions χ and expansion coefficients c_{si} , allows us to form a matrix equation much like equation 3.85:

$$\mathbf{hC} = \epsilon \mathbf{SC}, \quad (3.104)$$

where h is the matrix of Kohn-Sham operators, C the matrix of expansion coefficients, ϵ the matrix orbital energies, and S the overlap matrix. Using the matrix equation 3.104, an iterative procedure can be employed to minimize the energy of the orbitals, in much the same way as the HF method. Coefficients c are guessed, yielding a trial density from equation 3.97. This can then be inputted into the KS operator, which then forms the secular matrix equation 3.104, yielding new coefficients c and ϵ . This iterative procedure continues until the electron density converges. Equation 3.104 then produces the minimized electronic energy.

The KS approach to DFT is remarkably similar to HF. The similarities include: employing a SCF procedure to minimize the energies, optimizing a series of basis functions to minimize energy and the affinity of the Fock and KS operators. The KS operator's advantage over the Fock operator is that it can recover correlation energy with the E_{xc} term. In some sense, the KS approach is a step away from the original conception of DFT as a wavefunction-free method. The usage of 1-electron orbitals means that the problem has $3n$ dimensionality (where n is the number of electrons) as opposed to 3 (x, y, z) if the direct density is employed. Orbital-free DFT (or 'pure' DFT) has its beginnings in the Thomas-Fermi for an ideal electron gas [218, 220]. Subsequent improvements have been made to the Thomas-Fermi orbital free DFT [221]. However, in its current form, due to the lack of accurate approximations to the kinetic-energy functional T_{ni} , it has poor accuracy. As a consequence, KS DFT is ubiquitous in the literature, and will be solely employed in this thesis.

3.11.3 Approximations to the Exchange Correlation Functional

The true form of the exchange-correlation (XC) functional E_{xc} in the total Kohn-Sham energy expression is unknown. As a consequence, approximate EX functionals must be employed. The approximate functionals can be categorized and placed on a metaphorical 'Jacobs Ladder'. A functional class on a higher rung of Jacob's Ladder introduces new physical components to the XC functional not included in the previous rungs. However, in contrast to the systematic improvements in accuracy offered by increasingly expensive post-HF wavefunction methods, the increasingly complex functionals offer no guarantee that they will reach more accurate solutions. The key difference between post-HF methods and DFT XC functionals is the fact that many DFT functionals are semi-empirical, with constants fitted from experimental

data. The semi-empirical nature of some functionals means that they can be produce accuracy for certain systems, but offer poor accuracy for others. Non-empirical DFT functionals are constructed using known features of the exact functional, but since the number of known constraints are highly limited, the accuracy associated with non-empirical functionals is often poor [222]. Despite these weaknesses, a general trend of improving accuracy rising up the ladder is observed, leading up to the 'heaven' of chemical accuracy.

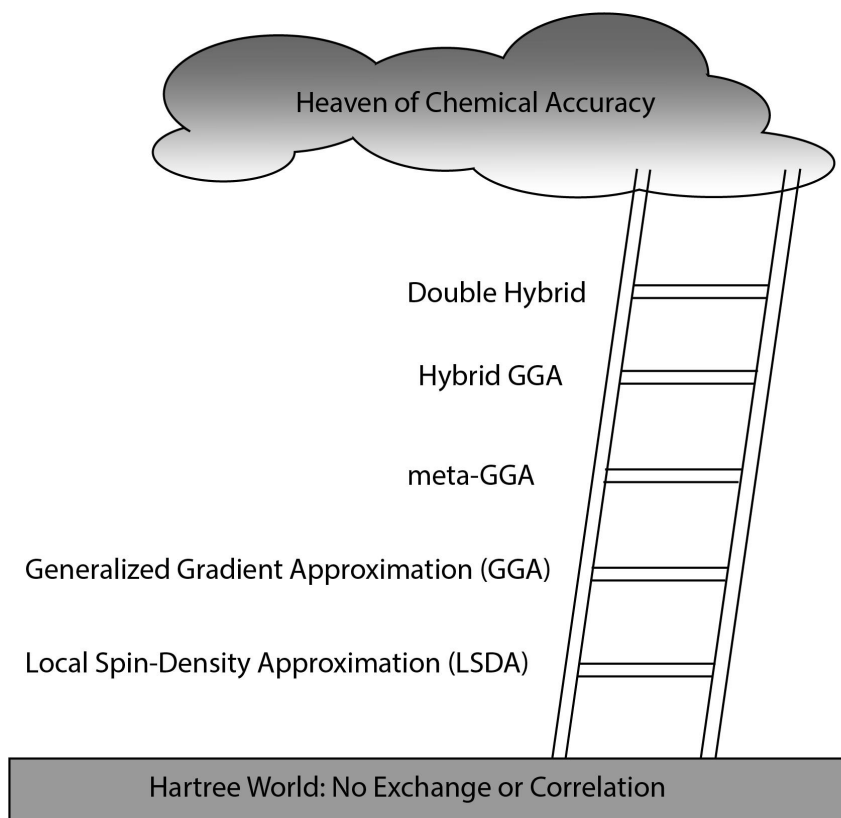


Figure 3.6: Jacob's Ladder of DFT functionals

Starting at the bottom of the ladder in figure 3.6, local spin-density approximation (LSDA) functionals approximate the electron density as a uniform electron gas. In LSDA functionals the α and β spin densities are varied independently. In general, the LSDA functionals are split into their exchange and correlation functionals:

$$E_{xc}^{LSDA} = E_x^{LSDA} + E_c^{LSDA}. \quad (3.105)$$

Splitting the exchange correlation functional into two separate functionals allows each one to modeled separately. The exact form of the LSDA exchange functional

was conceived by Slater in 1951 [223]:

$$E_x^{LSDA} = -\frac{3}{2} \left(\frac{3}{4\pi} \right)^{1/3} \sum_{\sigma}^{\alpha,\beta} \int \rho(\mathbf{r})_{\sigma}^{4/3} d\mathbf{r}. \quad (3.106)$$

The exact form of the LSDA correlation functional (purely dynamical correlation) is unknown. Nonetheless, approximate LSDA correlation functionals like VWN5 [224] and PW92 [225] provide accurate electronic energies. LSDA functionals are popular for condensed matter systems where the electron density is slowly varying. However, for molecular systems of highly varying electron density the accuracy of LSDA is extremely poor, underestimating the exchange energy by 10% [212]. In order to improve on LSDA, we need to consider an additional property of electron density, its non-uniformity.

At the second rung of Jacobs Ladder we find Generalized Gradient Approximation (GGA) functionals, which utilize electron density and its gradient. The density gradient $\nabla\rho(\mathbf{r})$ is found from the first derivative of electron density. Therefore, the general expression for a GGA exchange correlation functional is:

$$E_{xc}^{GGA}[\rho^{\alpha}, \rho^{\beta}] = \int f(\rho^{\alpha}(\mathbf{r}), \rho^{\beta}(\mathbf{r}), \nabla\rho^{\alpha}(\mathbf{r}), \nabla\rho^{\beta}(\mathbf{r})) d\mathbf{r}. \quad (3.107)$$

Here, the spin densities and their gradients are variables in some function f . In a similar way to LSDA, E_{xc}^{GGA} is usually split into its exchange and correlation parts. The general form of the GGA exchange functional is given as:

$$E_x^{GGA} = E_x^{LSDA} + \Delta E_x^{GGA}, \quad (3.108)$$

where $E_{X,\sigma}^{LSDA}$ is the uniform electron gas exchange density per unit volume corrected by some inhomogeneity function $\Delta E_{x,\sigma}^{GGA}$. An example of a commonly-used exchange functional used is the B88 functional [226]:

$$E_x^{B88} = E_x^{LSDA} + \Delta E_x^{B88} = E_x^{LSDA} - b \sum_{\sigma}^{\alpha,\beta} \int \frac{(\rho(\mathbf{r})^{\alpha})^{4/3} x_{\sigma}^2}{1 + 6bx_{\sigma} \ln [x_{\sigma}^2 + (x_{\sigma}^2 + 1)^{1/2}]} d\mathbf{r}, \quad (3.109)$$

where b is an empirical parameter fitted to known HF energies and:

$$x = \frac{|\nabla\rho(\mathbf{r})^{\sigma}|}{(\rho(\mathbf{r})^{\sigma})^{4/3}}. \quad (3.110)$$

Popular GGA correlation functionals are the Lee-Yang-Parr (LYP) functional [227] and the Perdew 1986 functional [228]. The Perdew-Burke-Ernzerhof (PBE) exchange and correlation functional is widely employed in solid systems and contains no empirical constants [229].

At the third rung of Jacobs Ladder we have meta-GGA functionals. Meta-GGA functionals further improve on GGA functionals in two ways. First, by including the Laplacian of the density, $\nabla^2\rho(\mathbf{r})_\sigma$ and including the kinetic energy density, which is given by:

$$\tau_{sigma} = \sum_i^{n_\sigma} |\nabla\Phi_{i,\sigma}^{KS}|^2. \quad (3.111)$$

Here, τ_σ is the kinetic energy density, which is formed from the absolute sum squared of the occupied KS orbitals $\Phi_{i,\sigma}^{KS}$ [230]. In a similar vein to equation 3.107, the general expression for a meta-GGA functional is:

$$E_{xc}^{MGGA}[\rho^\alpha, \rho^\beta] = \int f(\rho^\alpha(\mathbf{r}), \rho^\beta(\mathbf{r}), \nabla\rho^\alpha(\mathbf{r}), \nabla\rho^\beta(\mathbf{r}), \nabla^2\rho(\mathbf{r})^\alpha, \nabla^2\rho(\mathbf{r})^\beta) d\mathbf{r}. \quad (3.112)$$

Inclusion of either the Laplacian of the density or the kinetic energy density term depends on the precise functional. Furthermore, either term can be found in the exchange or correlation parts. A popular meta-GGA functional is B95, which contains empirical parameters [231]. Meta-GGA functionals tend to perform better than GGA functionals, albeit at a higher computational cost. Nevertheless, GGA functionals may perform better than meta-GGA functionals in certain cases. A recent study found that PBE, a GGA functional, performs better for hydrogen bonded systems than some meta-GGA functionals [232]. The idiosyncratic strengths and weaknesses of LDA, GGA and meta-GGA functionals leads us on to the next rung of Jacobs Ladder- hybrid functionals. Hybrid functionals mix contributions of different exchange correlation functionals together as well as combining some contribution from Hartree-Fock exchange.

Hybrid functionals are popular, and were first contrived by Becke who proposed the B3PW91 functional:

$$E_{xc}^{B3PW91} = E_{xc}^{LSDA} + 0.2(E_x^{exact} - E_x^{LSDA}) + 0.72\Delta E_x^{B88} + 0.81\Delta E_c^{PW91}, \quad (3.113)$$

where the B3PW91 E_{xc} is given by contributions from the: LSDA exchange correlation energy E_{xc}^{LSDA} , the B88 correction to the exchange correlation ΔE_x^{B88} , the PW91 correction to the correlation function ΔE_c^{PW91} and the 'exact' exchange energy E_x^{exact} [233]. The 'exact' exchange energy term is provided by the HF definition of exchange:

$$E_x^{exact} = -\frac{1}{4} \sum_{i=1}^n \sum_{j=1}^n \langle \Phi_i^{KS}(1)\Phi_j^{KS}(2) | \frac{1}{r_{12}} | \Phi_j^{KS}(1)\Phi_i^{KS}(2) \rangle. \quad (3.114)$$

If the orbitals in equation 3.114 were chosen to be HF orbitals, the exact HF exchange energy would be obtained. The parameters in front of the last three terms in the PW91 equation 3.113 are found by fitting to numerous atomization energies, making PW91 semi-empirical. The parameters decide the weighting of each contributing term to the total exchange correlation energy. Other hybrid functionals are formed in similar ways to PW91- containing weighted contributions from lower rung functionals and/or the exact exchange functionals. One of the most popular hybrid functionals is B3LYP, which is almost identical to PW91, replacing the E_c^{PW91} functional with E_c^{LYP} . The contribution of HF exchange E_x^{exact} is repeatedly found to improve accuracy, but the fractional contribution is highly system-dependent. Additionally, inclusion of E_x^{exact} can add additional computational expense. At the highest point in Jacob's ladder we find double-hybrid functionals. Double-hybrid functionals improve on hybrid functionals by using the MP2 second-order energy correction. Of course, the addition of an MP2 calculation further adds computational expense.

In general, most DFT functionals struggle with long range interactions like Van Der Waals forces. In order to correct the issues of long range interactions, an energy correction term is often applied. Addition of a dispersion energy correction term to the total energy is known as DFT-D. DFT-D3 is one of the best dispersion correction terms for correcting for long range interactions and will be used extensively in this thesis [234]. As an alternative to adding dispersion corrections, some functionals have non-local correlation functionals as part of their total exchange correlation functional- termed vdW-DF. An example of a vdW-DF functional is optPBE, which adds an non-local correlation functional to the widely used PBE functional [235].

Several thousand DFT functionals have been proposed. Each functional has its particular strengths and weaknesses. It is up to the user to work out which

functional best suits their needs. The 'best' functional can be defined by historical use in the literature, benchmarking studies and direct comparison of energetics with real experimental values. Compared to post-HF methods, there is no systematic way of achieving higher accuracies. However, the 'gold standard' post-HF methods CCSD(T) has limited applicability due to scaling $N^{8.5}$. By contrast, DFT scales roughly $N^{3.5}$, so large molecular systems can still be modeled with high accuracy within acceptable time-frames.

3.12 Basis Sets

The formation of the Roothan-Hall equations (Section 3.9.4) and the Kohn-Sham Equations (Section 3.11.2) introduced the concept of basis functions (χ) to build the total wavefunction and total ground-state density respectively. A set of basis functions is referred to as a basis set.[200] A linear combination of basis functions is used to build the molecular orbitals (Equation 3.81). In this section, we will detail several important basis sets and those that are used in this thesis.

3.12.1 Slater-Type Orbitals

The simplest basis set is the Slater-type orbitals.[207] Slater-type orbitals (STOs) are close approximations to the atomic wavefunctions. Their form is:

$$\chi_{abc}^{STO} = Nx^a y^b z^c e^{-\zeta r}. \quad (3.115)$$

where χ is our STO basis function, N is a normalization constant and ζ controls the width of the orbital, and r controls the radius of the orbital. STOs are said to have the correct properties of hydrogen 1s orbitals because the function decays exponentially from a cusp at the nucleus. Figure 3.7 shows a typical Slater-type function for hydrogen. Unfortunately, STOs are computationally expensive to use, arising from the evaluation of two-electron integrals.[236] In order to overcome the issue with computational cost, STOs can be built from a linear combination of Gaussian functions, which are easier to integrate.[237]

$$\chi_{abc}^{GTO} = Nx^a y^b z^c e^{-\zeta r^2}. \quad (3.116)$$

An STO-1G basis function is built from 1 Gaussian function, and STO-3G is built from 3, and adding more leads the basis function to become more 'Slater-like'. The effect of adding successive Gaussian functions is illustrated in Figure 3.7.

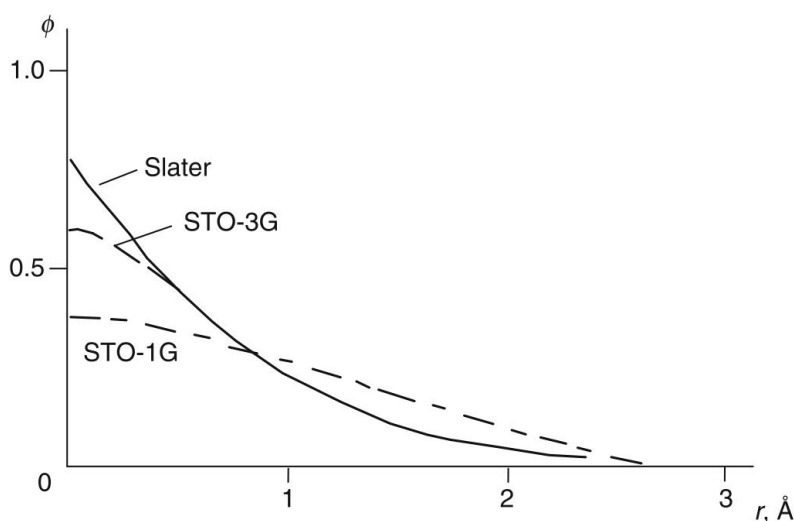


Figure 3.7

3.12.2 Pople Basis Sets

To address some of the issues encountered with STOs, we can use multiple basis functions for each atomic orbital. The terminology of using multiple basis sets for each atomic orbital is *double zeta* for two, *triple zeta* for three etc. Nevertheless, this can become quite expensive too, so splitting the valence electrons into an inner shell, outer shell, and core electrons is done to reduce the cost. For example 3-21G refers to a split-valence basis set which uses 2 Gaussian functions on the inner shell, and 1 on the outer shell, and 3 Gaussian functions for the core orbitals. Using multiple basis functions for an atomic orbital allows for nodal features to be added. However, for d orbitals, we need to add polarization functions which allows the atomic orbitals to be displaced along a particular direction. 3-21G with polarization functions is termed 3-21G^(*), which mixes contributions from higher angular momentum orbitals. For example, if we want to add polarization functions to an s orbital, we would mix it with a p orbital.[238] These basis sets are often referred to as Pople Basis sets.

To further improve on the accuracy of Pople Basis sets, we can add diffuse functions. Diffuse functions help model more diffuse electron clouds, found in systems containing heteroatoms with lone pairs, anions and excited state electrons. A Gaussian function with a small value of ζ is added to the existing functions, leading the 3-21G^{*} function to be termed 3-21G^{*}+G.[200] Overall, it is clear that moving from a minimal basis to adding more functions (increasing the basis set size) that improves the accuracy of calculations. It is here the concept of the *basis set limit* can be

introduced, which posits that in variational methods using successively larger basis sets leads to lower energies.[239] Building on this concept, Dunning and co workers built a series of basis sets design to converge smoothly to the basis set limit, which will be discussed next.[240]

3.12.3 Dunning's Correlation Consistent Basis Set

Dunning's *correlation consistent* (cc) basis sets are designed to successively recover correlation energy from valence electrons. Practically, this means that additional functions, added to the basis set at the same stage contribute similar amounts of correlation energy. An additional advantage compared to the Pople and STO basis sets, previously described is that they were built using CI methods as opposed to pure HF.[212] The nomenclature of Dunning's correlation consistent basis sets: cc-pVDZ, cc-pVTZ,...cc-pVnZ, where n to the number of contracted basis sets added to the core electrons.[240]

In this thesis, the cc-pVTZ basis set is used extensively. For metals, the number of core electrons starts to become very expensive to calculate. Additionally, for extended systems like metal surfaces, the electron density effectively has 'infinite' range within the solid. It is here that we can introduce the concept of plane-wave basis sets combined with pseudopotentials.

3.12.4 Plane Wave Basis Sets and Projector Augmented Wave Method

3.12.4.1 Bloch's Theorem

Part of this thesis focuses on the calculation of periodic solid state systems. In extended solid systems there are essentially an infinite number of electrons. Consequently, they are impossible to calculate as an extended system without restricting the solid size and artificially creating edges to the solid. To alleviate this problem we can use Bloch's theorem which states that the wavefunction ψ of an electron n in a periodic system can be written as:

$$\psi_n(\mathbf{r}) = u_n(\mathbf{r})e^{i\mathbf{k}\cdot\mathbf{r}}, \quad (3.117)$$

where n is the band number (energy level in the solid), \mathbf{r} is a positional lattice vector, u is a periodic function with the same periodicity of the solid, and \mathbf{k} is a wave-vector which defines the momentum in the crystalline lattice. The exponent

part of equation 3.117 is a plane-wave. The periodicity of the function $u_n(\mathbf{r})$ means that:

$$\mathbf{u}_n(\mathbf{r}) = \mathbf{u}_n(\mathbf{r} + \mathbf{R}), \quad (3.118)$$

where \mathbf{R} is any vector which is a multiple of the unit cell, where the unit cell is the smallest unit of the repeating periodic system. Resulting from Bloch's theorem is the ability to calculate the properties of an extended system by just calculating the approximate solutions of ψ_n of a single unit cell.[241]

3.12.4.2 Application of Bloch's Theorem to Solid State Calculations

In the last section of the basis set introduction we introduced plane waves as a means of modeling an 'infinite' systems of solids. When combined with periodic boundary conditions, they can be used to run quantum chemistry calculations on bulk solids and surfaces. Practically, a calculation involving periodic boundary conditions leads to the optimization of a volume and the atomic positions in that volume (for solid systems the volume is usually a unit cell or a supercell). This is illustrated in Figure 3.8.

The atoms in the chosen volume then 'feel' interactions in adjacent volumes, where the total wavefunction can be written as equation 3.117. We can express the periodic part of the wavefunction as:

$$u_n(\mathbf{r}) = \sum_{\mathbf{G}} C_{\mathbf{G}nk} e^{i\mathbf{G}\mathbf{r}}. \quad (3.119)$$

$C_{\mathbf{G}nk}$ are variation coefficients. \mathbf{G} are reciprocal lattice vectors within the chosen periodic volume, which are found from transforming the lattice vectors l into reciprocal space via:

$$\mathbf{G}l = 2\pi m, \quad (3.120)$$

where m is an integer. Combining equations 3.117 and 3.119 leads to a total expression for the wavefunction:

$$\Psi(x) = \sum_{\mathbf{G}} C_{\mathbf{G}nk} e^{i(\mathbf{G}+\mathbf{k})\cdot\mathbf{r}}. \quad (3.121)$$

This allows an system with an infinite number of electrons to be calculated as a finite set of electrons in a unit cell. However, Equation 3.121 is an expression the periodic wavefunction for an infinite set of reciprocal space vectors \mathbf{k} . Practically it

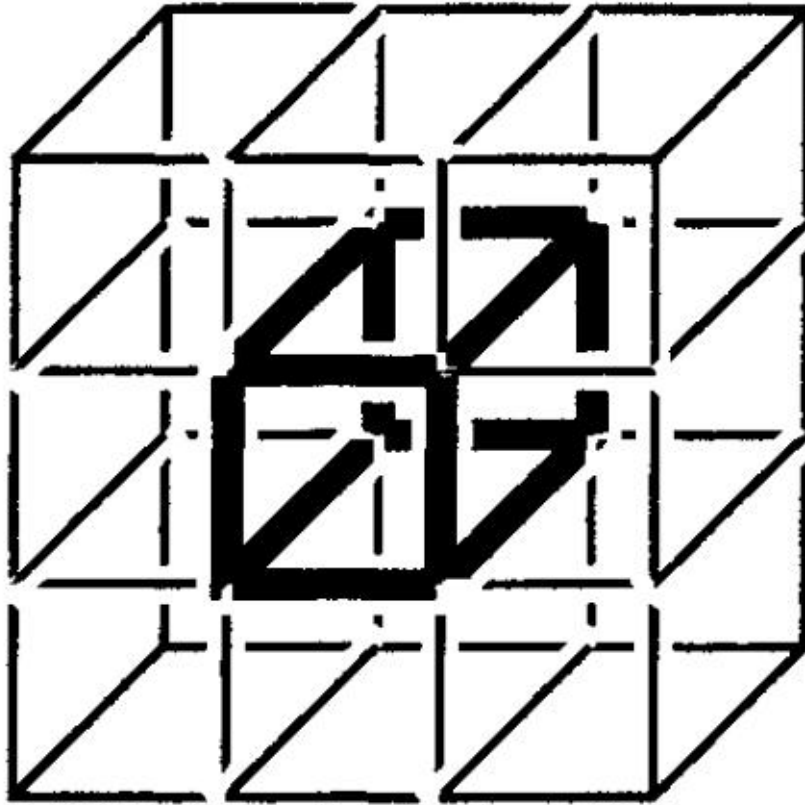


Figure 3.8: A simplified periodic system.

would be impossible to use a wavefunction with infinite terms. Therefore, a select number of reciprocal space vectors \mathbf{k} are selected, discretizing the problem. We can then substitute Equation 3.121 into the Kohn-Sham equations 3.102 allowing us to run DFT calculations on periodic systems.[242]

3.12.4.3 Pseudopotential Approximation

An issue associated with building the total wavefunction with plane-waves is that the number of waves required for rapidly varying states, such as near the cusp of the nucleus, becomes computationally very expensive. To overcome this issue, the projector-augmented wave method (PAW), is introduced which combines two techniques.[243] Firstly, the core-electrons are frozen and pre-calculated in an atomic environment. Secondly, the rapidly oscillating plane-waves are transformed to pseudized smooth waves, which are easy to compute. This is represented visu-

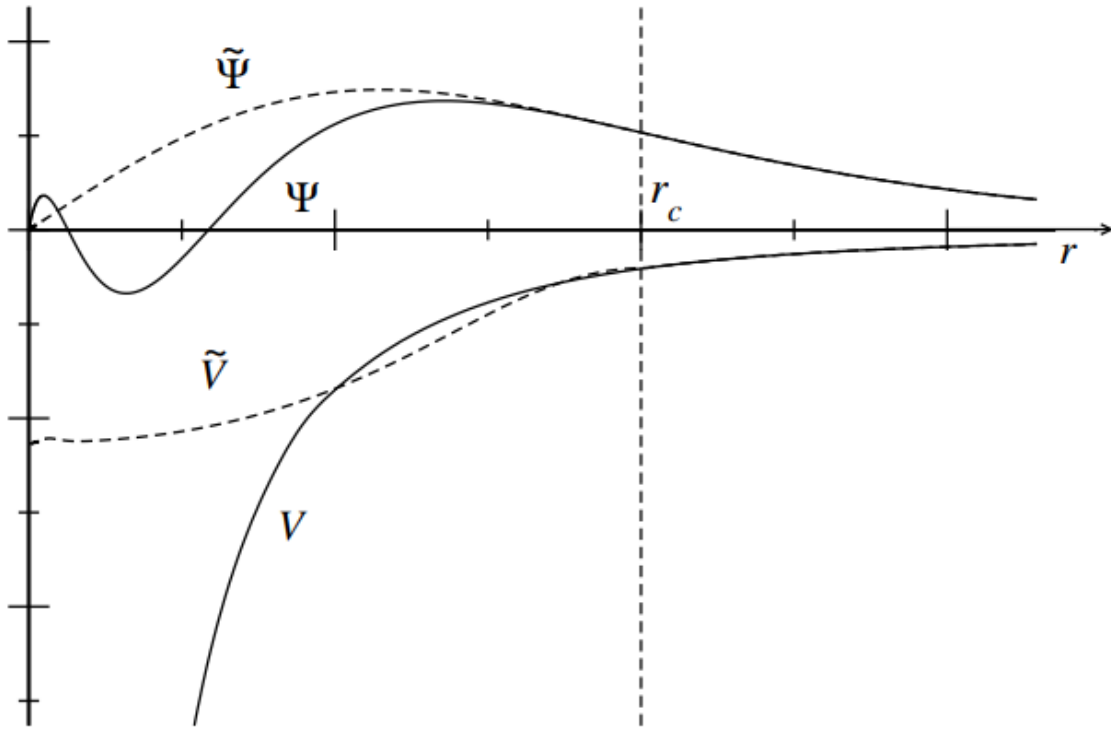


Figure 3.9: Projector augmented wave method.

ally in Figure 3.9, where $\tilde{\Psi}$ is the approximated wavefunction and r_c is the cutoff radius for the frozen core. In the PAW method, everything outside r_c is allowed to optimize. Practically this leads to reduction in accuracy, but aside from H and Li, calculation of atomic systems becomes impossible using pure plane-waves.

Chapter 4

Investigations into the SMORS Mechanism

Abstract

The SMORS mechanism describing the formation of insoluble material in bulk jet fuel was investigated using density functional and experimental techniques. The first part of the SMORS mechanism, the formation of quinones from the oxidation of indigenous fuel phenols, was shown to proceed via two possible pathways. First, a single-step pathway yielding two quinones and a hydrogen peroxide. Secondly, a two-step pathway yielding a quinone, *p*-chinole and singlet oxygen. The second step of the SMORS mechanism, the reaction of quinones with electron-rich heterocycles in fuels, was shown to proceed via a homolytic aromatic substitution pathway. These findings, allow us to propose a modified SMORS mechanism, built on our enhanced mechanistic understanding of fuel deposit formation.

4.1 Introduction

Liquid-phase jet fuel thermal oxidative degradation in conventional fuels is largely driven by minor heteroatomic species.[24] The process of jet fuel thermal degradation can be split into three main stages: 1) autoxidation of the bulk fuel yielding oxidized species, 2) agglomeration of oxidized components to high molecular weight species, 3) formation of insolubles.[33] There is a better understanding of step 1 than step 2, and this is reflected in the existing pseudo-detailed mechanisms for deposition, where there are more steps representing autoxidation reactions.[193, 24, 74]

To understand the agglomeration and insoluble formation processes in more detail, researchers have taken the approach of correlating initial polar concentrations with mass of deposit.[244, 63, 65] Phenols and electron-rich nitrogen compounds, indoles and carbazoles, were found to correlate well with mass of deposit.[65] In fact, phenol and electron-rich nitrogen compounds have been found to interact synergistically to enhance deposit formation in fuels.[63, 170] To explain this synergistic effect, Beaver *et al.* proposed the Soluble Macromolecular Oxidatively Reactive Species (SMORS) mechanism.[32] Several articles have subsequently used this mechanism to explain observed deposition effects,[245, 47, 68, 66] but none have explored the SMORS mechanism in depth.

The original SMORS mechanism proposed by Beaver *et al.* is described in detail in the following reference[32] and in Section 2.3.1. It relies on the formation of electrophilic quinones from the oxidation of phenol. These quinones are then proposed to undergo electrophilic aromatic substitution reactions (EAS) with electron-rich heteroatomic compounds in fuel.[163] Using indole as a model for nitrogen heterocycle leads to the formation of a 3-indolyl hydroquinone. The EAS product between quinone and nitrogen heterocycles is proposed to undergo further EAS steps to successively larger structures, ultimately forming insoluble particles in fuel.[245]

In recent years, density functional theory (DFT) has become an increasingly popular tool to investigate thermal oxidative reactions in fuel.[94, 29, 54, 76] Early work by Zabarnick *et al.* used the B3LYP//6-31G(d) level of theory to investigate X–H bond dissociation energies of various fuel heteroatoms to understand their chain-breaking properties.[29] Building on these methods, Parks *et al.* used the B3LYP//cc-pVTZ level of theory to propose a copper catalyzed hydroperoxide decomposition cycle.[94] Further work by Parks *et al.* successively elucidated thermally oxidation pathways of a variety of sulfur classes.[54]

It is the aim of this work to investigate the SMORS mechanism at a molecular level using DFT methods, while proposing alternative pathways where appropriate. Additionally, our DFT calculations will enhance the understanding of the SMORS mechanism itself, and allow us to propose alternative pathways. Moreover, a greater mechanistic understanding of the SMORS mechanism will eventually lead to enhanced predictive capabilities in the form of pseudo-detailed mechanisms.

4.2 Materials and Methods

4.2.1 Computational Details

All calculations were performed in Gaussian09 (E.01) using the B3LYP functional.[246][233] Grimme’s DFT-D3(BJ) dispersion correction was applied to all the calculations to account for long-range effects.[247] A PCM solvation model, with *n*-dodecane as the chosen solvent, was selected to replicate the hydrocarbon bulk.[248] The basis set chosen was cc-pVTZ on an *ultrafine* grid. This basis set adds polarization functions, allowing orbital hybridization to be taken into account.[240] Transition states were optimized using the QST1/3 method depending on the reaction studied. All transition states were verified by the presence of one imaginary frequency corresponding to the saddle point. Additionally, intrinsic reaction coordinate (IRC) calculations were performed to verify the transition state corresponded to the expected reactants and products. Unrestricted (broken symmetry) calculations were performed on open-shell systems, where the HOMO and LUMO were mixed (`guess=mix` option). Entropy values were corrected using the GoodVibes script, which employs a quasi-harmonic correction corrected at 298 K.[249, 250, 251] The quinone oxidation pathway in Section 4.3.2 was further validated with single point DLPNO-CCSD(T)[252, 253, 254, 255, 256] calculations using the ORCA quantum chemistry package.[257] DLPNO-CCSD(T) allows near CCSD(T) accurate calculations at a fraction of the cost by identifying electron pairs with significant contributions to correlation energy, where the correlation energies for the other pairs are obtained at the MP2 level of theory.

4.2.2 Surrogate Fuels

Details of the experimental setup can be found in the Appendix (Section 10.1.4).

4.3 Results and Discussion

In this section we will present the DFT calculations for each step of SMORS, in conformity with reference.[32]

4.3.1 Formation of the Keto-Peroxyl Radical

The first set of calculations was focused on the generation of keto peroxy radical, indicated as **(P1)** in Figure 4.1. In the generalized SMORS reaction scheme, the first step involves the abstraction of a hydrogen atom from a phenol (representing an indigenous antioxidant) by a hydroxy radical $\text{ROO}\cdot$. As shown in Figure 4.1, the Gibbs free energy barrier corresponding to the transition state of this reaction (**TS1**) is $\Delta_{\ddagger}G = +12.65 \text{ kcal mol}^{-1}$; the overall reaction is slightly endergonic, with a $\Delta_rG(\text{ROO}\cdot) = +0.40 \text{ kcal mol}^{-1}$.

Comparing the hydrogen abstraction step for the reaction between phenol and different *n*-dodecane fuel radical classes ($\text{R}\cdot$, $\text{RO}\cdot$, $\text{ROO}\cdot$)[24], the $\text{RO}\cdot$ pathway provides the lowest barriers. The calculated values for each pathway associated for each radical class are presented in Table 10.1 and the comparison for each pathway is shown in Figure 4.1. The higher associated barriers $\Delta_{\ddagger}G$ for the $\text{R}\cdot$ and $\text{ROO}\cdot$ species compared to $\text{RO}\cdot$ are likely due to the higher level of distortion associated with these barriers. Energies of formation Δ_rG for the radical classes go from highest to lowest $\text{RO}\cdot > \text{R}\cdot > \text{ROO}\cdot$. The ability of the electron-rich oxygens to share spin density with the ring can justify the lower peroxy radical reactivity, leading to enhanced radical stability. On the other hand, the alkyl radical is stabilized solely by the inductive effects from the adjacent carbons.[26]

The next step in the SMORS mechanism is the reaction of dissolved oxygen with the resulting phenoxy radical. In order to study this step computationally, triplet oxygen was selected for the calculation, because of its higher stability and commonality in nature.[258] Our results indicate that the reaction between dissolved oxygen and the phenoxy radical is endergonic, with a $\Delta_rG = +15.23 \text{ kcal/mol}$. The transition state with a barrier of $\Delta_rG = +21.50 \text{ kcal/mol}$ was identified for this reaction (**TS2** in Figure 4.1), which is in good agreement with the previous work.[259] Overall, the formation of keto-peroxy radical (**P1** in Figure 4.1) is endergonic, indicating that high temperatures would be needed for this species to form. However, the exergonicity of the reactions of phenol with $\text{R}\cdot$ and $\text{RO}\cdot$ more than compensates for this, making the hydrogen abstraction using $\text{R}\cdot$ or $\text{RO}\cdot$ exergonic overall and making these reactions more favorable than the reaction with $\text{ROO}\cdot$. Nevertheless, the concentration of these chain-carrying radicals will be important too, with $\text{ROO}\cdot$

Species	$\Delta_{\ddagger}S$ (kcal mol ⁻¹ K ⁻¹)	$\Delta_{\ddagger}H$ (kcal mol ⁻¹)	$\Delta_{\ddagger}G$ (kcal mol ⁻¹)	Δ_rS (kcal mol ⁻¹ K ⁻¹)	Δ_rH (kcal mol ⁻¹)	Δ_rG (kcal mol ⁻¹)
R·	-2.749E-02	8.24	9.97	-1.440E-03	-18.88	-17.98
RO·	-2.037E-02	0.29	1.32	1.24E-03	-3.31	-20.79
ROO·	-2.327E-03	8.94	10.40	9.00E-06	0.40	0.40

Table 4.1: Calculated energy change of reaction Δ_{\ddagger} and formation Δ_r values for reaction of phenol with different dodecane fuel radicals calculated at the B3LYP-D3//cc-pVTZ *n*-dodecane PCM level of theory. Enthalpy values are corrected with GoodVibes at 298K. All Δ_{\ddagger} values are calculated from stable pre-collision complexes located from an IRC calculation.

being primary chain carriers due to their higher concentration.[33]

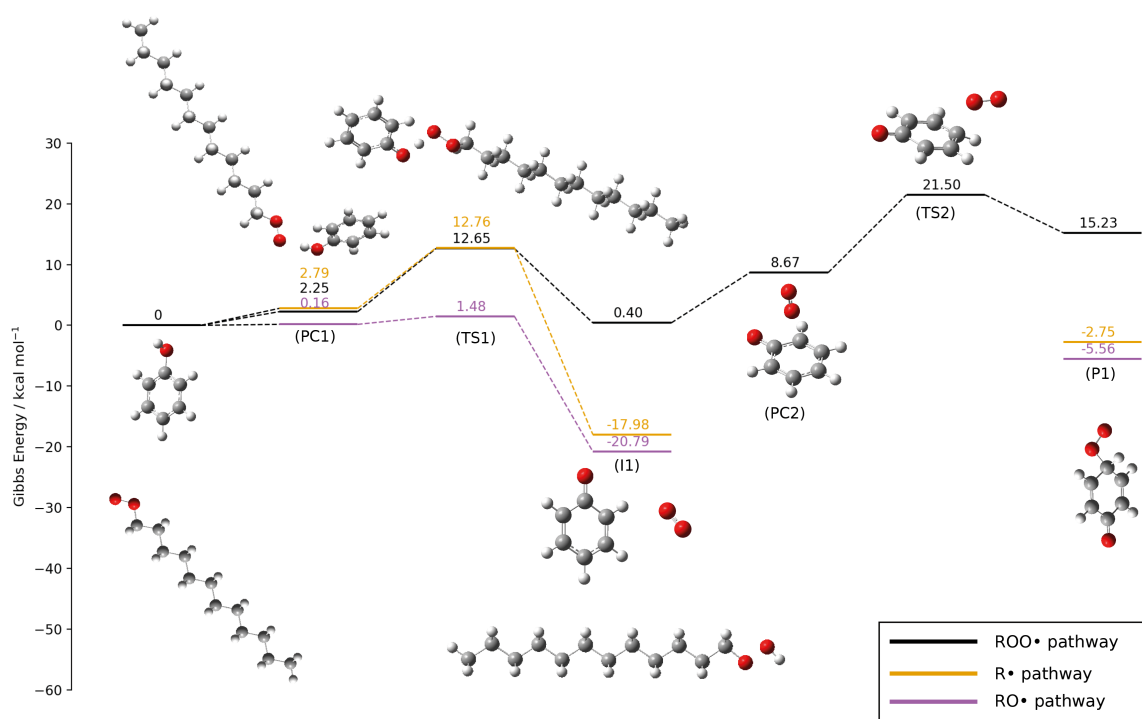


Figure 4.1: Potential energy surface (Gibbs energy) for the formation of the keto peroxy radical calculated at the B3LYP-D3//cc-pVTZ level of theory using *n*-dodecane (PCM) as a solvent.

4.3.2 Formation of Quinones

The next step proposed in the SMORS mechanism is the chain termination of two keto-peroxyl radicals, resulting in the formation of a quinone, a hydroquinone and oxygen. Quinones have been found to form from substituted and unsubstituted phenols in fuels under oxidative conditions.[155, 74] The formation of quinones from phenols is universally found to occur *via* a termination step.[260, 261, 100] In the SMORS mechanism proposed by Beaver *et al.* it has been suggested that this step is likely to proceed with the formation of a tetraperoxide (ROOOOR) intermediate, formed from the recombination of two keto-peroxyl radicals. Beaver *et al.* then propose quinones are formed by the decomposition of the ROOOOR via a Russell Mechanism, leading to the final products.[262] However, our DFT calculations suggest that this is unlikely. The final SMORS species are $104.89 \text{ kcal mol}^{-1}$ (indicated as the red level in Figure 4.2) lower than the starting state of keto-peroxyl radicals. However, it is highly unlikely that the α hydrogen (labelled as 1 in Figure 4.2) would be able to move to the para-oxygen (labelled as 2 in Figure 4.2), given that the distance of 4.75 \AA is prohibitive to hydrogen transfer. Indeed no transition state was found for this hydrogen transfer.

Because the termination of two radicals is unlikely, the production of keto-peroxyl radicals and subsequent tetroxide formation in competition with *n*-dodecane autoxidation and other phenol H-abstraction pathways was explored using a pseudo-detailed mechanism. The details of the pseudo-detailed mechanism are presented in Section 10.1.3.1 of the appendix. The final concentrations of the species from our pseudo-detailed mechanism is presented in Table 10.3. Despite the competing steps, the formation of the tetroxide is still competitive with the other autoxidation and hydrogen abstraction steps, with the concentrations greater or similar to *n*-dodecane autoxidation products found.

Alternative to the proposed oxidation products in reference [32], several pathways yielding a p-chinole (**a**), quinone (**b**), and singlet oxygen (**c**). These are shown as **P2a,b,d** in Figure 4.2. Additionally, a pathway yielding two quinones (**a**) and hydrogen peroxide (**d**) were found (**P2c** in Figure 4.2).

The first step is the formation of the tetraperoxide. A barrier of $13.36 \text{ kcal mol}^{-1}$ (**TS3**) for peroxyl radical recombination and the formation of the tetraperoxide

(**I2**) was found in our calculations, which is similar to the previous work on peroxy radicals.[263]. Furthermore, the formation of the tetraperoxide (**I2**) is endergonic, with a Gibbs energy $+8.05 \text{ kcal mol}^{-1}$ above the separated species. This can be attributed to the instability of the linear ROOOOR structure.[264] It is worth mentioning that no stable ROOOOR species was found on the triplet surface, which is in agreement with previous work.[265]

The decomposition of ROOOOR can proceed through several pathways which are discussed here. First, a modified Russell Mechanism pathway was explored, leading to the formation of quinone (**I2** \rightarrow **TS4a** \rightarrow **P2a,b,d**) However, the Russell mechanism pathway was found to have a high Gibbs free energy barrier of $\Delta_{\ddagger}G=+34.91 \text{ kcal mol}^{-1}$. Such a high energy barrier indicates that the Russell mechanism is unlikely to contribute significantly to quinone formation, when compared to other calculated pathways in this section. We note that experimental work has found little evidence for the Russell Mechanism[262] in peroxy self-reactions producing ROH, RCHO and O₂ products.[266, 267, 268]

Given that the Russell Mechanism decomposition of the tetraperoxide was found to have a large free energy barrier, we considered other pathways. As a consequence, an exergonic single-step channel was identified (**I2** \rightarrow **TS4c** \rightarrow **P2c**), yielding a two quinones and a hydrogen peroxide **P2c**. First, the tetraperoxide decomposes via **T4c** ($\Delta_{\ddagger}G=10.87 \text{ kcal mol}^{-1}$), predicting a simultaneous transfer of two α -hydrogens to two oxygens in the ROOOOR chain and the cleavage of two O-O bonds. The IRC calculation for this transition state can be found in Figure 10.1 in the Appendix. Production of hydrogen peroxide from peroxy self-reactions has been detected in previous work.[100] But, to the best of our knowledge, this is the first time a concerted hydrogen peroxide production step has been located.

A second pathway consists of a two-step channel yielding a quinone, p-chinole, and singlet oxygen species was identified (**I2** \rightarrow **TS4b** \rightarrow **I3b** \rightarrow **TS5b** \rightarrow **P2a,b,d**). This includes a transition state **TS4b** ($\Delta_{\ddagger}G=25.27 \text{ kcal mol}^{-1}$) involving a simultaneous cleavage of one O-O and transfer of an α -hydrogen to an oxygen. The resultant intermediate formed (**I3b**) is a stable hydrotrioxide (ROOOH) species hydrogen bonded to a quinone species ($\Delta_rG=-51.58 \text{ kcal/mol}$). Subsequently, the hydrotrioxide species can decompose via a transition state **TS5b** of $\Delta_{\ddagger}G=44.26 \text{ kcal/mol}$, characterized by a four membered cyclic structure. This level of energy barrier is in

agreement with the previous work.[265, 263] The high barriers for **TS4b** and **TS5b** show that this channel is prohibitive for the production of quinone.

Finally, a further two-step channel leading to a quinone, p-Chinole and singlet oxygen species was identified (**I2** → **I3d** → **TS5d** → **P2a,b,d**). The first step in this pathway is the exergonic decomposition of the ROOOOR species ($\Delta_r G = -3.27 \text{ kcal mol}^{-1}$), yielding two keto hydroxyl radicals and a singlet oxygen.[269, 48] In a related work, a potential energy surface scan of the CCSD//6-31G(d) level of theory on this step with ethane peroxy radicals indicates that this is a barrierless process.[263] In our case also, no transition state was found. Following the decomposition of the tetraperoxide, an α -hydrogen from one peroxy radical is then transferred linearly to the other peroxy O atom, yielding **P2a,b,d** with an energy barrier of $\Delta_{\ddagger} G = +18.84 \text{ kcal mol}^{-1}$ corresponding to **TS5d** in Figure 4.2.

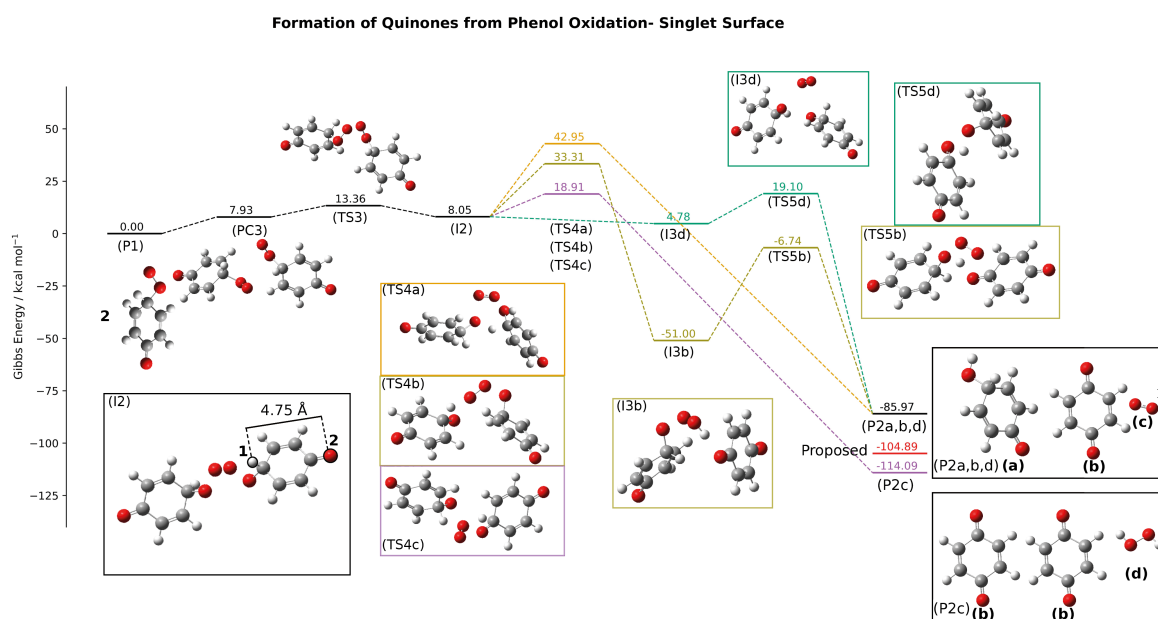


Figure 4.2: Potential energy surface (Gibbs energy) of the keto-peroxy radical yielding quinones on the singlet surface, calculated at the B3LYP-D3//cc-pVTZ using *n*-dodecane (PCM) as a solvent. The red level indicates energy of the proposed quinone oxidation products, where no pathway could be found to form them.

To identify competing oxidation pathways, other non-quinone producing path-

ways were considered, as shown in Figure 4.3. On the singlet surface, an exergonic aromatic substitution pathway is identified, leading to ROOR species and singlet oxygen (**P1** → **PC4a** → **TS6a** → **P4**), without producing quinone. In this pathway, at **TS6a** a rocking movement of the peroxy radical towards an α -carbon on the other peroxy radical is observed. This is in association with the simultaneous cleavage of a C–O liberating singlet oxygen is observed. However, the high energy barrier of **TS6a** ($\Delta_{\ddagger}G=+59.46$ kcal mol⁻¹) means that the termination of ROOOOR (**I2**) via **TS3** is strongly preferred, suggesting this pathway can be excluded.

On the triplet surface, an exergonic pathway was identified, which leads to the production of two hydroxy radicals and a triplet oxygen (**P1** → **PC4b** → **TS6b** → **P3**). The first step of this pathway is the formation of a dimeric pre-reaction complex (**PC4b**). Following **PC4b**, a high energy transition state (**TS6b**) was characterized via the simultaneous scission of O–O bonds on each peroxy radical and the formation of new O–O bonds between terminal oxygens. The very high barrier associated with **TS6b** ($\Delta_{\ddagger}G=+51.49$ kcal/mol) means that this pathway will not proceed beyond **PC4b**.

If all the pathways are compared, then the formation and decomposition of ROOOOR via two routes offers the most likely pathway to quinones with both having similar kinetic barriers. First, the single-step pathway (**I2** → **TS4c** → **P2c**) giving two quinones and hydrogen peroxide. Secondly, the two-step pathway (**I2** → **I4d** → **TS5d** → **P2a,b,d**), yielding a quinone, p-chinole and singlet oxygen. The single-step pathway is more favorable thermodynamically, with an exergonicity of the reaction of 28.12 kcal mol⁻¹ lower. Nevertheless, both pathways have similar kinetic barriers. Thus, there is likely to be a distribution of products.

DLPNO-CCSD(T) calculations were performed for the pathways in this section, where the same reactive trend was observed, which validates our method chosen. The results are shown in Section 10.1.3 of the appendix.

In real fuels, unsubstituted phenols form a majority of phenolic species. Nevertheless, they also form quinones when oxidized, and are expected to undergo similar reactions here.[155, ?] Nonetheless, this should be investigated further.

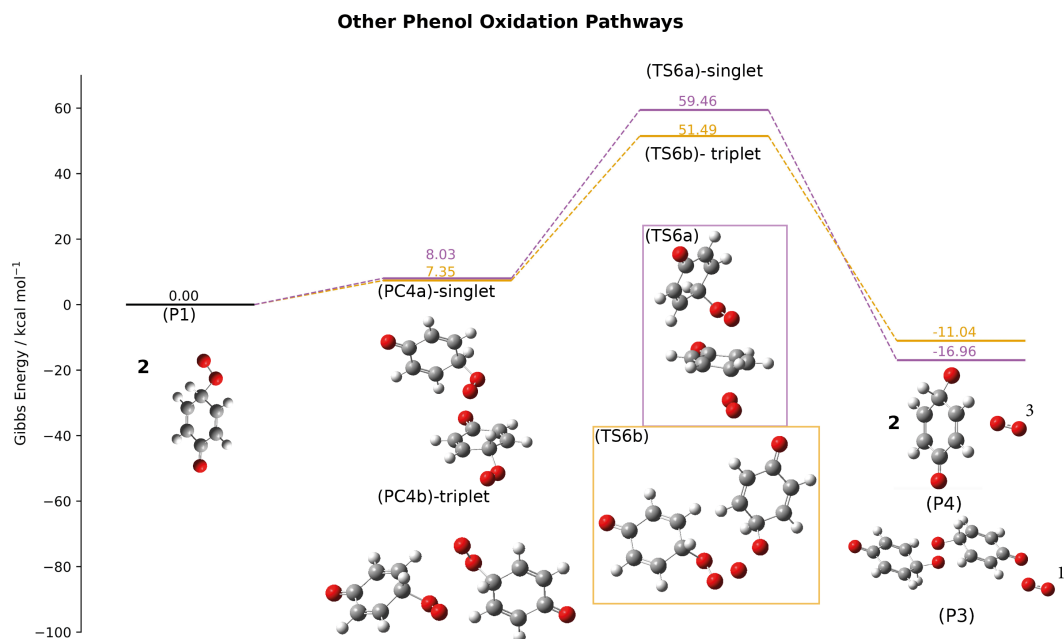


Figure 4.3: Reactions of Keto-Peroxy Radical yielding non-quinone products on the triplet and singlet surfaces, calculated at the B3LYP-D3/cc-pVTZ *n*-Dodecane PCM level of theory

4.3.3 Quinone Heteroatom Coupling Step

4.3.3.1 Proposed SMORS Electrophilic Aromatic Substitution Step

The next step in the originally proposed SMORS mechanism; the electrophilic aromatic substitution (EAS) between indigenous electron-rich compounds and electrophilic quinones was found to be thermodynamically and kinetically prohibited. EAS reactions usually proceed with the initial attack of an electron-rich aromatic (the carbazole in this case) to an electron deficient species (quinone in our study), breaking aromaticity. The second step is the subsequent release of a species, most commonly H^+ , at the site of electrophilic attack, completing the substitution reaction and re-establishing aromaticity.[270] The EAS between indole and benzoquinone (**P2**) proposed by Beaver *et al.* is presented in Figure 4.4.[32]. Following the addition of benzoquinone, a zwitterionic σ -complex forms (Indole+Quinone-).[271]

Following the EAS scheme in Figure 4.4, no stable intermediate was found. The aprotic nature of *n*-dodecane solvent is unable to provide stability to the charged intermediate. However, even with a PCM water solvent model no stable benzoquinone-indole intermediate structure was found.

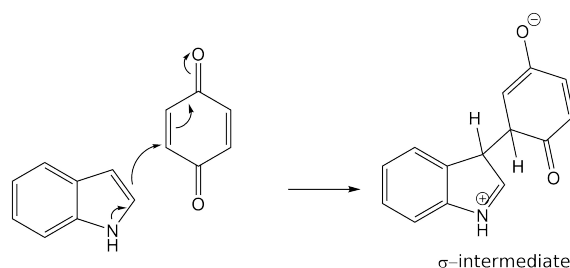


Figure 4.4: Proposed SMORS EAS step

Despite these limitations, the EAS transition state was identified between methyl substituted-carbazole proposed in Beaver *et al.*[32] and quinone, using a lower level of theory (B3LYP//cc-pvDZ). The intermediate product (**I4**) could only be obtained from a constrained optimization by freezing the C–C bonds. Without freezing the C–C bonds, the zwitterionic structure in 4.4 optimized to two separate indole and quinone species. The $\Delta_{\ddagger}G=+177.11$ kcal mol⁻¹ barrier between benzoquinone and carbazole implies the original SMORS EAS proposal is kinetically prohibited. Recent work on EAS reactions indicate that in aprotic/apolar solvents interactions are likely to proceed through a concerted route, precluding the formation of a charged intermediate. The concerted routes studied found that in apolar solvents tend to involve autocatalysis of the attacking electrophile with another electrophile.[272, 273] Two quinone species reacting with a single indole was studied to explore an autocatalytic concerted route. However, in our case no concerted route to the coupled SMORS species was identified.

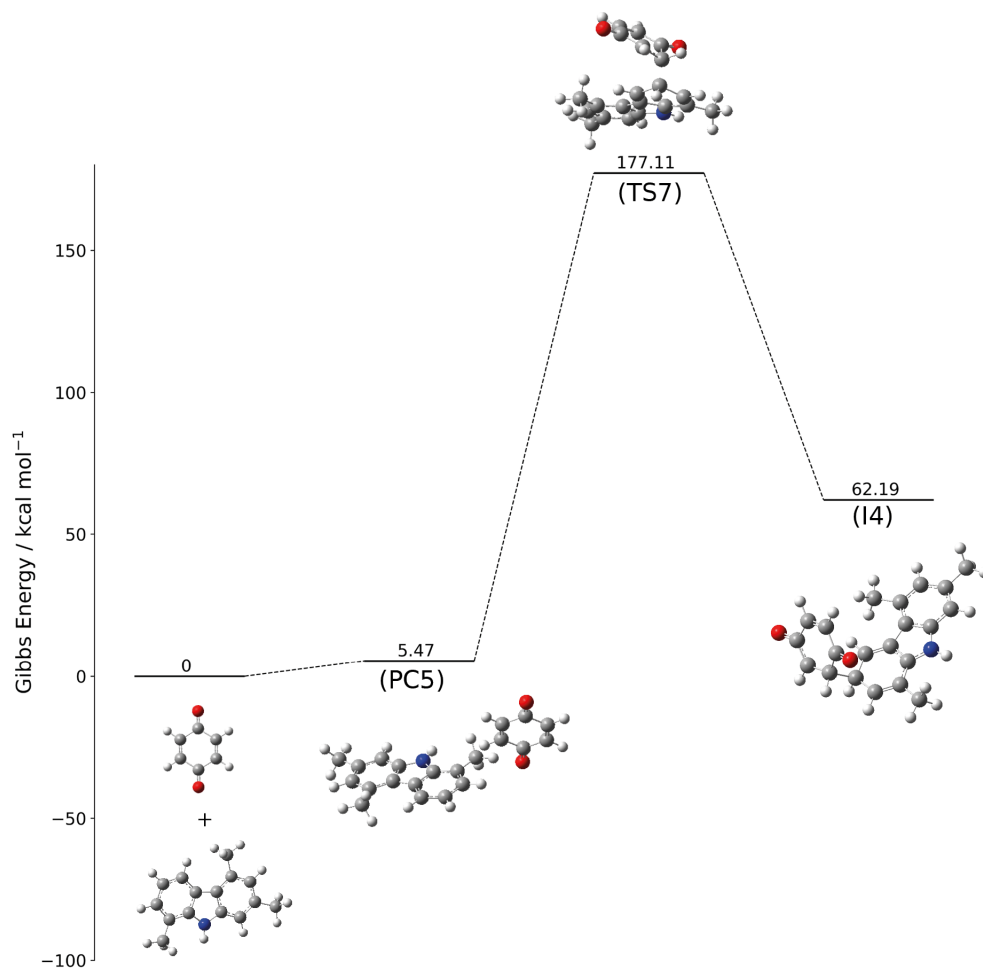


Figure 4.5: Potential energy surface (Gibbs free energy) of the reaction between carbazole and quinone, calculated at the B3LYP//cc-pVDZ *n*-Dodecane PCM level of theory.

4.3.3.2 Alternative Acid-Catalyzed EAS Step

The condensation reaction between benzoquinones and indoles has been reported previously to be catalyzed by acid.[274, 275] In fuels, it is proposed that the autoxidation of indigenous sulfur compounds can lead to the formation of sulfonic

acids.[54] In addition, previous work has suggested that strong acids may play a role in catalyzing deposit formation.[33] Therefore, an acid-catalyzed pathway was considered as a possible route for SMORS formation.

This alternative SMORS scheme is presented in Figure 4.6. A protonated quinone was selected to model this pathway since protonation of the indole would preclude it from reacting with the electrophilic quinone species. From the overall reaction scheme presented in Figure 4.6, it can be concluded that a protonated quinone is able to proceed through a more favorable kinetic pathway. In addition, the formation of the aromatized hydroquinone carbazole species as proposed in the SMORS mechanism is possible and thermodynamically favorable ($-78.13 \text{ kcal mol}^{-1}$).

The pre-reaction complex (**PC5**) for this reaction is exergonic. The barrier of the addition step (**TS7**) is small at $\Delta_{\ddagger}G=+6.83 \text{ kcal mol}^{-1}$ above **I5**. When compared to the non-catalyzed EAS scheme (Figure 4.4), the positive charge delocalized around the quinone species will activate the nucleophilic 3-position of the quinone. A hydrogen transfer (**TS8**) is then achieved through a pseudo-ring like structure, with a small barrier of $+7.10 \text{ kcal mol}^{-1}$. The resultant structure from this hydrogen transfer contains a hydroquinone moiety (**I6**). The formation of this species is thermodynamically favorable with a Gibbs free energy change of $-18.43 \text{ kcal mol}^{-1}$ compared to the starting structures.

Protonation of quinone will also proceed with a barrier. In our DFT calculations the quinone was protonated by a dodecane sulfonic acid, known to form from the oxidation of indigenous sulfur compounds in fuel. It was found that the protonation step was barrierless but highly endergonic in *n*-dodecane with a large thermodynamic barrier of $\Delta_rG=+77.57 \text{ kcal mol}^{-1}$. As shown in Figure 4.6, an overall Gibbs energy of $-0.59 \text{ kcal mol}^{-1}$ change is associated with the entire catalytic cycle, from the protonation of the quinone by the dodecane sulfonic acid to the formation of the SMORS species. This indicates that the overall pathway is only mildly exergonic. Nevertheless, a protonated quinone allows the EAS step to proceed with modest kinetic barriers. However, with such a large thermodynamic barrier to quinone protonation in *n*-dodecane, protonation is unlikely unless the resultant ionic species are stabilized by a more polar solvent. The protonation step in water was calculated to have a thermodynamic cost of $\Delta_rG=+25.43 \text{ kcal mol}^{-1}$. Small amounts of water

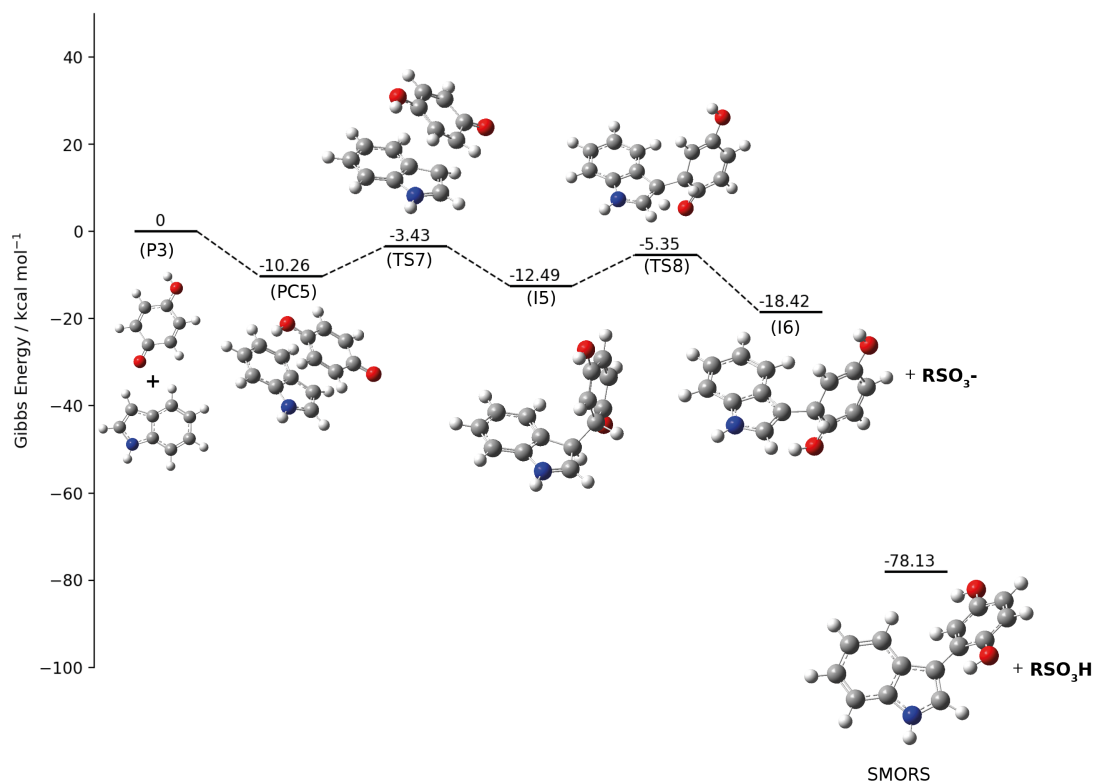


Figure 4.6: Acid catalyzed EAS step calculated at the B3LYP//cc-pVTZ *n*-dodecane PCM level of theory.

have been detected as micelles in jet fuel.[276] We hypothesize that these micelles could offer a site for protonation in fuels.

4.3.3.3 Alternative Oxidative Coupling Pathway

Although an acid catalyzed pathway was shown to proceed with modest kinetic barriers, protonation of quinone in *n*-dodecane comes at a high thermodynamic cost. Therefore, we investigated additional mechanisms. Another possible pathway for the coupling between indoles and quinones in the SMORS mechanism is an oxidative coupling route. Oxidative coupling products have previously been detected in real and surrogate fuels.[155, 68] Undeniably, chain termination between an indole and a quinone radical would occur spontaneously. However, the termination of two dissimilar radical species is unlikely due to the low concentration of free-radicals in solution.[100, 62] Nevertheless, the termination reaction between an indole and a

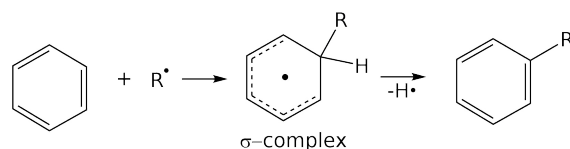


Figure 4.7: Generalized HAS mechanism.[278]

quinone radical will lead to a small proportion of SMORS. Alternatively, we investigated the possibility of a homolytic aromatic substitution (HAS) reaction between indole radicals and quinone, and indoles and quinone radicals. HAS has been described as the 'radical analogue of the more facile EAS'.[277] In our study an EAS pathway could not be located. Therefore HAS serves as another alternative pathway to forming the SMORS product.

The general HAS mechanism is presented in Figure 4.7. The first step is manifested by the attack of a radical species on an aromatic ring. The formation of a σ -complex (analogues to the Wheland intermediate in Figure 4.4) is then followed by the loss of hydrogen leading to re-aromatization of the ring.

Following the HAS framework, the scheme depicted in Figure 4.7 is proposed for the reaction of quinone radical with an indole. The σ -complex formed from the initial attack of the quinone radical at the indole **C3** site is presented as **I8b**. It appears that the formation of the hydroquinone moiety is not immediately accessible *via* abstraction of a hydrogen atom from the σ -complex, which is how the general HAS mechanism proceeds (Figure 4.7). Instead, internal hydrogen transfer leads to the formation of intermediate **I9**, which contains a semiquinone moiety. Semiquinones are known for their exceptional stability owing to their resonance stabilization.[259] Nevertheless, hydrogen abstraction from indigenous fuel compounds (RH in Figure 4.7) will lead to the formation of the SMORS product.

DFT calculations for the HAS pathway are presented in Figure 4.9. For comparison, two HAS reaction pathways were calculated for quinone and indole radicals, respectively. For indole, multiple positions for hydrogen abstraction are available, but the **C3** is generally the preferred site for C-C bond formation.[279] Our calculations indicate that the route leading to the formation of quinone radicals is kinetically and

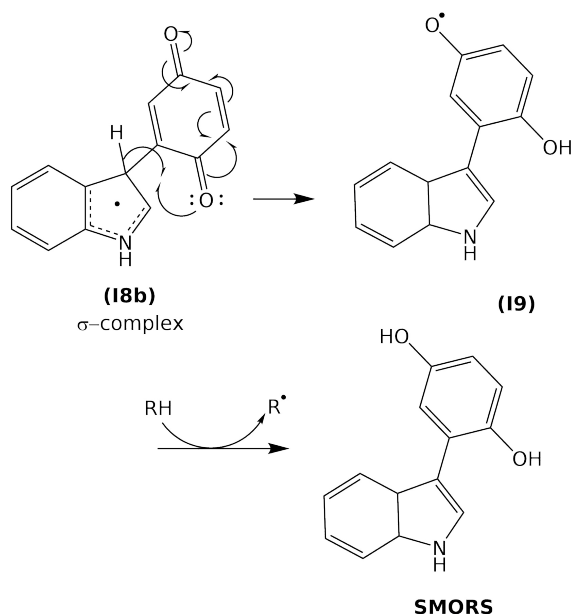


Figure 4.8: HAS mechanism applied to the SMORS indole + quinone substitution step

thermodynamically preferred ($0 \rightarrow \text{PC6b} \rightarrow \text{TS9b} \rightarrow \text{I7b}$) over the formation indole radicals ($0 \rightarrow \text{PC6a} \rightarrow \text{TS9a} \rightarrow \text{I7a}$). The transition state for both species is characterized by a linear hydrogen transfer to a dodecane hydroxy radical, where the barrier to quinone hydrogen abstraction (TS9b) is $5.04 \text{ kcal mol}^{-1}$ lower in Gibbs free energy than the indole abstraction barrier (TS9a). Additionally, the resultant quinone radical (I7b) is $8.12 \text{ kcal mol}^{-1}$ lower in energy than the indole radical (I7a). Here, it must be noted that when comparing all the products formed from the quinone production (P2), hydrogen abstraction from p-chinole ($(\text{a})\text{P2}$) is strongly preferred over quinone due to the formation of a highly stable semiquinone radical. Not shown in Figure 4.9, the abstraction of an α -hydrogen from p-chinole ($(\text{a})\text{P2}$) has a $\Delta_{\ddagger}G + 5.54 \text{ kcal mol}^{-1}$ barrier and a resultant $\Delta_rG - 47.13 \text{ kcal mol}^{-1}$. Consequently, the p-chinole species is more likely to form radicals than indole and quinone here. However, the subsequent attack of the p-chinole radical at the **C3** of an indole to form a HAS σ -complex has a high barrier $\Delta_{\ddagger}G 36.47 \text{ kcal mol}^{-1}$, meaning it can be precluded as a contributor to the HAS pathway.

The next step in the HAS scheme is the attack of the radical to the aromatic ring forming a σ -complex. With respect to the indole radical + quinone pathway, 1,4-benzoquinones are not strictly aromatic. Nevertheless, it has been noted that both substituted and non-substituted 1,4-benzoquinones are able to form resonance struc-

tures which could stabilize the resultant σ -intermediate.[280] Both the quinone and indole radical attack pathways (**I7**→**PC7**→**TS10**→**I8**) proceed exergonically. However, in relation to **I7**, the attack of a quinone radical has a lower free-energy barrier (**TS10b**) $\Delta_{\ddagger}G=6.87$ kcal mol⁻¹ compared to the attack of the indole radical (**TS10a**) $\Delta_{\ddagger}G=8.09$ kcal mol⁻¹. For both **TS10a** and **TS10b**, the transition state is characterized by a rocking motion between the C–C bonds formed. The resultant indole radical-quinone σ -intermediate (**I8a**) is 4.84 kcal mol⁻¹ more stable than the quinone radical-indole σ -intermediate (**I8b**).

Following the formation of the σ -intermediates, a subsequent hydrogen transfer leads both intermediates to form **I9** which is a stable semiquinone radical. Formation of **I9** is strongly preferred from quinone radical-indole σ -intermediate (**I8b**→**TS11b**→**I9**). The free energy barrier for **TS11b** is small ($\Delta_{\ddagger}G=2.76$ kcal mol⁻¹). The re-aromatization step **TS11b** for this pathway is characterized by a pseudo-cyclic transition state structure, where a hydrogen from the **C3** position on the indole is transferred to a quinone (=O) moiety ortho- to the C–C bond. By contrast, re-aromatization of the indole radical-quinone intermediate **I8b** proceeds via a high energy barrier (**TS11a**) $\Delta_{\ddagger}G=47.64$ kcal mol⁻¹ meaning this pathway should be discounted as a major HAS pathway. **TS11a** is part of a hydrogen transfer from the quinone **C2** carbon, where the planar quinone moiety has to be bent to allow hydrogen transfer. This bending of the quinone moiety out-of-plane likely leads to the high barrier for **TS11a**.

The final step to produce the resultant **SMORS** species leading to re-aromatization of the semiquinone compound **I9** via abstraction of hydrogen. Dodecanol produced in the first abstraction step (**0**→**TS9b**→**I7b**) was modelled as the species for hydrogen abstraction, allowing the efficiency of this radical propagation step to be assessed. The re-aromatization step with dodecanol proceeds endergonically (**I9**→**PC8**→**T12**→**SMORS**), showing the semiquinone compound **I9** is more stable than the dodecane hydroxy radical. However, overall the pathway to produce the final **SMORS** product is exergonic by -18.24 kcal mol⁻¹ relative to the reactants state. This indicates this propagation cycle leading to **SMORS** is thermodynamically favorable. The stability of **I9** indicates that completion of the final re-aromatization step is disfavored. Formation of a **SMORS** trimer is likely given that the **SMORS** trimer (Figure 4.11) is 14.15 kcal mol⁻¹ more stable than **I9**. In this case, an additional indole and dodecane hydroxy radical are consumed.

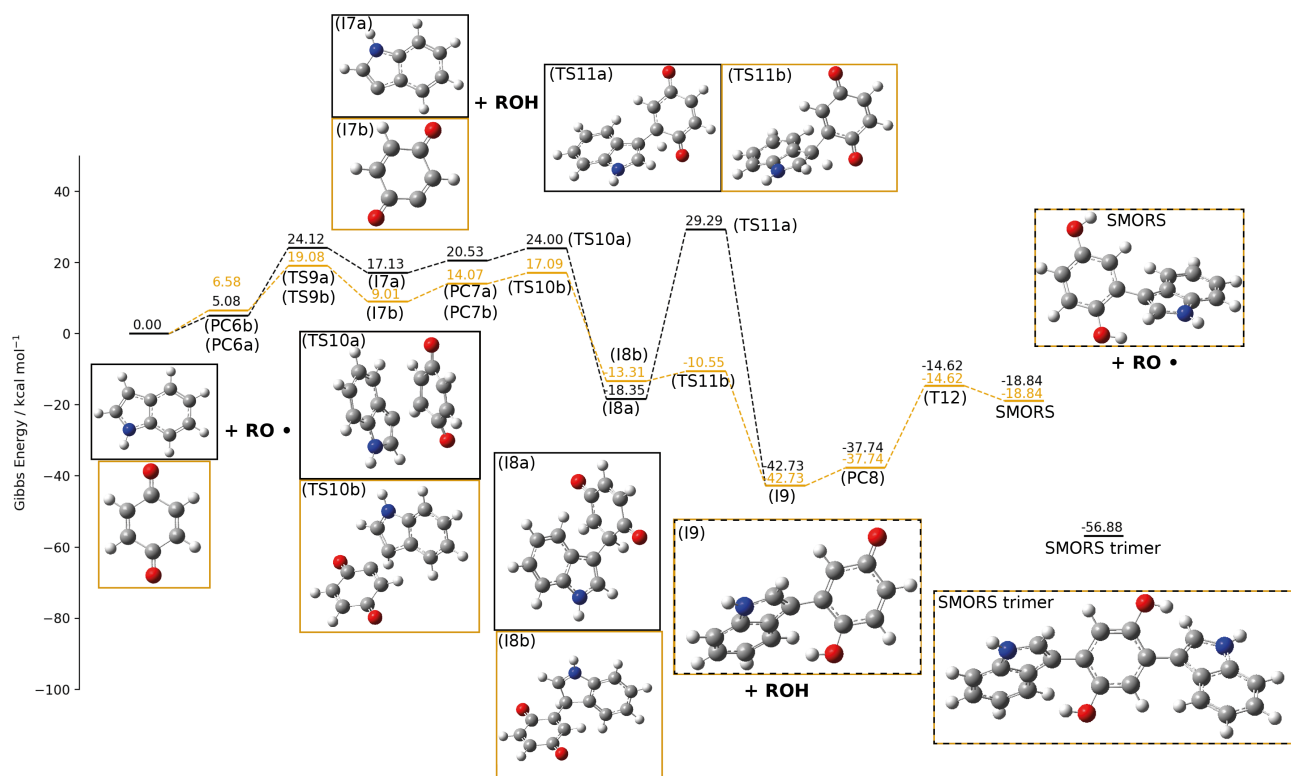


Figure 4.9: HAS step calculated at the B3LYP//cc-pVTZ *n*-dodecane PCM level of theory. The R group in this figure refers to an *n*-Dodecane moiety.

Our calculations show that SMORS can form under both acid-catalyzed and oxidative conditions, in line with literature precedent.[281, 282] In order to investigate the formation of trimers under acid-catalyzed and oxidative conditions a series of small scale testing was performed, as illustrated in the following section.

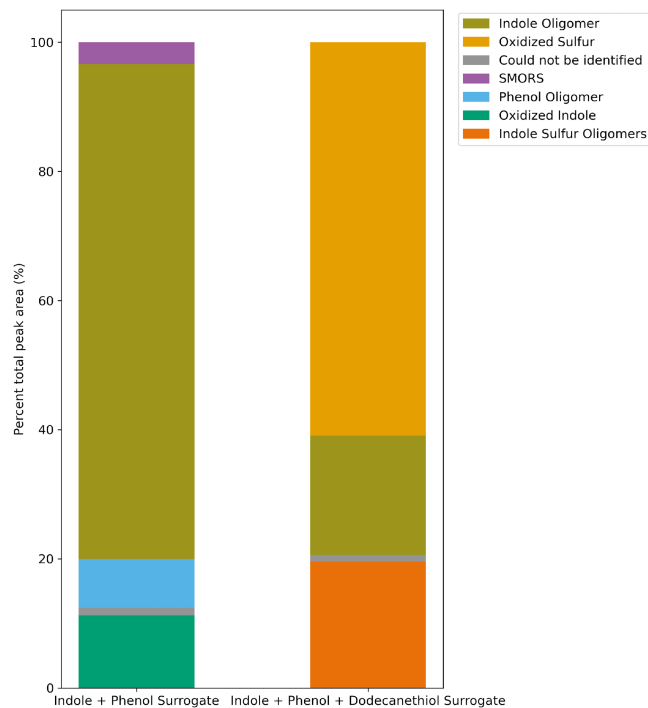
4.3.4 Flask Tests

Our calculations have shown that acid catalysis and/or oxidative conditions can lead to the formation of SMORS. To examine the effect of acids on the SMORS mechanism, two indole + phenol based model fuels were prepared, one containing acid forming dodecanethiol (IP-S) and one without (IP). The details of these tests are presented in the Appendix, in Section 10.1.4, along with a list of the molecular formula from (-)LCMS (negative mode LCMS), as well as the proposed structures. Each (-)LCMS peak was characterized in terms of species class by assigning the formula of the base peak to a species class. Subsequently, the areas associated

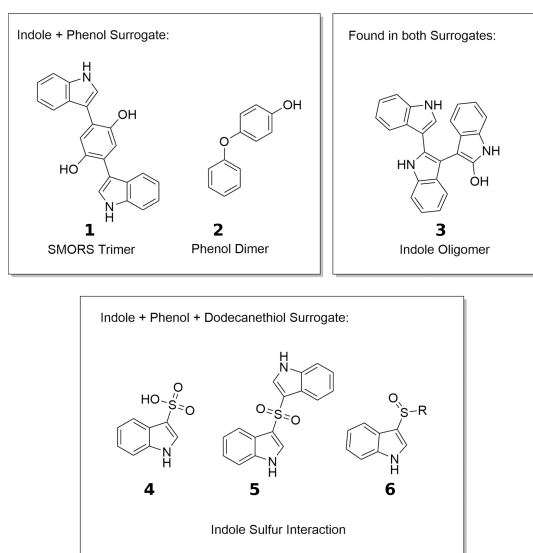
with each class were grouped, allowing the % total area for each species class to be presented. This allows the relative abundance of each deposit class detected by (-)LCMS to be determined. The species classes and their associated percentage peak areas are presented in Figure 4.10a.

From (-)LCMS results, it is clear that the addition of thiol led to indole + sulfur oligomer formation, and suppressed the formation of SMORS. The heavy molecular weight materials corresponding to the IP-S surrogate contained compounds with molecular formulas associated with indole sulfonylation (**44.10b**), arylated sulfonylation (**54.10b**), and sulfenylation (**64.10b**) reactions. These products have previously been detecting when indole and thiols have been combined under oxidative conditions.[279, 283, 272] A SMORS trimer (**14.10b**) is directly observed in the IP surrogate deposit, suggesting that the SMORS process can proceed without the need of a strong acid catalyst, as weak carboxylic acids can still form from the autoxidation of bulk fuel.[284] This observation lends support to the HAS mechanism over an acid-catalyzed mechanism.

The formation of phenol dimers (**24.10b**) in the sulfur-free IP surrogate deposit suggests that phenols are oxidized in the liquid phase. By contrast, no phenol oxidation products are observed in the sulfur containing IP-S surrogate. Instead, oxidized sulfur compounds form the largest proportion of the deposit. Co-elution of phenolic and oxidized sulfur compounds can be ruled out because phenolic compounds in IP elute at different retention times to oxidized sulfur compounds in IP-S (Tables 10.4 and 10.5 in the Appendix).



(a) (-)LCMS peak areas associated with the deposits generated from the *n*-dodecane 0.1 mol L^{-1} indole + phenol and 0.1 mol L^{-1} indole + phenol + dodecanethiol surrogates.



(b) Selected putative structures detected in the deposit. Detailed information of the deposit structures are present in Section 10.1.4 of the Appendix

4.3.5 Discussion and Implication for Fuels

The fact that different components in fuels interact with each other, either enhancing or slowing down deposit formation, is an uncontroversial idea. In fact, synergistic deposition enhancement between indole, phenol, and sulfur compounds in fuel has been observed in recent tests.[63] However, the mechanism by which this behind this synergistic behavior is still unclear. Our DFT and experimental results lead us to propose a modified SMORS mechanism. The first step in our mechanism is the oxidation of phenols (**1**) to quinones (**9**) are presented in Figure 4.2. The key weakness of the original SMORS proposal was the formation of quinones via a Russell Mechanism. Instead, we propose that quinones are produced via two main pathways, leading to a distribution of products. The first pathway, a two-step mechanism, involves the decomposition of the tetraperoxide (**5**) chain followed by hydrogen transfer. This leads to the production of one quinone (**7**), p-chinole (**6**), and singlet oxygen (**8**). The second pathway, a single step-mechanism, involves the concerted decomposition of the tetraperoxide (**5**). This leads to the production of two quinones (**7**) and a hydrogen peroxide (**9**). The hydrogen peroxide (**9**) species is likely to undergo fission, yielding two HO· radicals, further propagating the chain-mechanism.

The second part of this modified SMORS mechanism is the coupling of quinone and indoles is proposed to occur via a HAS pathway, presented in Figure 4.12. The original EAS pathway, requires a stable, charged, σ -intermediate could not be located computationally in *n*-dodecane. Instead, a HAS pathway offers a route to a stable radical σ -intermediate via the attack of a quinone radical (**11**) on an indole (**13**). Quinone radicals could also attack other electron-rich fuel heterocycles like pyrroles and carbazoles, generalizing the scheme.

This is the first time a HAS pathway has been proposed as a route to fuel deposit formation. A HAS pathway also offers additional flexibility being a deposit formation route which does not rely on free-radical termination to lead to C–C/C–O bond formation, and instead can be considered to be a propagation step. Beyond phenol and indole coupling, other fuel species could react to form via HAS reactions. A recent review focusing on HAS has shown these reactions can occur for both aromatic and heterocyclic compounds, including pyrrole and phenyls present in fuel. A particularly interesting facet of this review in relation to this work is the usage

species, despite the fact that deposition in conventional aviation fuels are highly correlated with nitrogen and phenol content.[65, 163] Additionally, a common weakness in existing pseudo-detailed mechanisms is the implicit deposition steps. The work here presents an explicit generalized scheme for nitrogen and phenol deposit formation. The effect on kinetic and thermochemical parameters on the variations between different nitrogen species and different phenol structures using this generalized scheme can be studied, allowing for the eventual addition of explicit deposition steps in pseudo-detailed mechanisms.

4.4 Conclusions and Next Steps

The highly-cited SMORS mechanism to explain phenol and fuel heteroatom coupling in fuels was investigated by experimental and DFT methods. Several key modifications are made to the original proposed mechanism. First, in contrast to the proposed one-step Russell Mechanism, formation of quinone was shown to occur via a two-step mechanism. This occurs via the decomposition of a tetraperoxide, formed via the termination of two keto-peroxyl radicals, leading to two reactive hydroxy radicals and singlet oxygen. Hydroxy radicals then undergo a hydrogen transfer reaction to form quinone and a p-chinole, in contrast to the quinone, hydroquinone and triplet oxygen products in the original mechanism. The second important modification is the coupling step between quinone and electron-rich compounds. In apolar solvents, an electrophilic aromatic substitution (EAS) step was found to form unstable intermediates and was found to proceed with prohibitively high barriers. Instead, a homolytic aromatic substitution (HAS) mechanism was found to be the most likely pathway according to DFT calculated energies and experimental observations. Based on these findings, we propose a new modified SMORS pathway (Figures 4.11 and 4.12). Additionally, HAS reactions should begin to be explored as a new coupling pathway for fuel species.

Chapter 5

The Interaction of Nitrogen Heteroatomics with Sulfur

Abstract

The mechanism behind the synergistic interactions between nitrogen and sulfur compounds in fuels was explored using a series of simplified surrogate fuels. Indole combined with dodecane-sulfide, disulfide, and thiol in a flask oxidizer setup all led to increased deposits in comparison to indole alone. LCMS and GCMS analysis indicates that the addition of sulfur led to nitrogen-sulfur cross-coupling, indole alkylation, and accelerated indole-indole coupling. Additionally, the liberation of SO_3 from all the sulfur compounds led to sulfonated indoles forming. Hansen solubility parameters were employed to assess the solubility of the suggested structures. Additionally, when pyrrole and quinoline were combined with dodecanethiol differing effects occur. Addition of dodecanethiol to pyrrole led to rapid polymerization products. Whereas for quinoline, where no coupling products were detected, quinoline decomposition products were detected instead. From these results, a mechanism is proposed involving direct protonation of the nitrogen compounds catalyzing coupling.

5.1 Introduction

Jet fuel deposition is largely driven by minor heteroatomic species, present as less than 0.1% by mass. The heteroatomic fraction is further subdivided into categories including: sulfur species, antioxidants, nitrogen species, and dissolved metals.[24] The nitrogen species of significant concentration in fuels include nitrogen heterocycles such as indole, quinoline, pyridine, and pyrrole.[28] Nitrogen and sulfur com-

pounds have long been known to synergistically act together to form deposits. However, there is debate as to whether 6- or 5-membered nitrogen heterocycles interact with indigenous sulfur the strongest. Several studies have indicated that 5-membered heterocycles (indole, pyrrole) are significantly more adverse for fuel thermal stability when compared with 6-membered heterocycles (pyridine) and amines.[171, 172, 156] In addition, an extensive investigation correlating the heteroatom type and the mass of deposit produced from conventional Jet A-1 fuels found that species primarily of concern were 5-membered nitrogen heterocycles, phenols, and polar oxygenated species.[65]

Conversely, work by Zabarnick *et al.* showed that in a polar-free solvent, 6-membered heterocycles had a greater deposition propensity than both 5-membered heterocycles pyridines and indoles. However, when all the nitrogen compound classes were combined with hexylsulfide, the level of deposit increased significantly for all the nitrogen classes.[63] Likewise, in Oswald and Alexis's work, the addition of sulfur compounds was often necessary to induce deposition.[64] It is the aim of this paper to expand our understanding of the mechanisms of the synergistic interaction between nitrogen heterocycles and sulfur compounds leading formation of insolubles in fuel.

Total sulfur is limited by a number of jet fuel standards[129]. However, various classes of sulfur species behave differently during fuel thermal degradation. Consequently, a correlation between total sulfur and surface deposition is not an appropriate approach in understanding thermal stability.[51] For example, the deposition tendency of straight chain thiols is consistently found to be the highest amongst all the classes.[140, 62, 130, 153] By contrast, heteroatomic sulfur compounds are found to be relatively benign.[151, 152, 153] It is commonly accepted that sulfur species tend to slow down the oxidation process in fuels by reacting directly with hydroperoxides forming sulfur acids.[140] It is thought that the deposition tendency of sulfur compounds is linked to their formation of acids and other sulfur oxidation products.[285, 52, 139, 142]

Several studies have investigated the synergistic deposition effects between nitrogen and sulfur species, and proposed contrasting potential theories to explain the effects. These theories include: an acid-base pathway where the basic nitrogen

reacts with acids from the oxidation of sulfur compounds,[33, 63] a free radical oxidative pathway where oxidative coupling occurs between electron-rich sulfur and nitrogen species,[63, 148, 64] an acid-catalyzed cross-coupling pathway,[170, 33] and a mechanism involving the decomposition of sulfur compounds forming SO₂ and alkenes.[52] None of the above theories have received extensive mechanistic scrutiny, and the pathways leading to deposits remain largely unknown.

For our work, investigation into the synergistic interactions between nitrogen and sulfur fuel species, a customizable surrogate fuel was considered using lab grade solvents. In order to characterize the thermally stressed surrogates, a twin LCMS and GCMS approach was taken. With GCMS, enhanced heteroatom concentrations combined with a pre-concentration technique [155] will allow for thermally stressed components at lower concentrations to be characterized. GCMS has been found to be successful at characterizing bulk fuel components,[74] so the effect of heteroatoms on bulk fuel can be elucidated. LCMS will allow for the larger, less volatile deposit precursors and deposits to be characterized in terms of molecular formula and weight. Here, knowledge of the starting components in the surrogate will allow structures to be proposed from the molecular formula.[68] Both GCMS and LCMS will offer semi-quantitative data in terms of the relative areas of the peaks associated with each compound class. An investigation combining these techniques to a multicomponent surrogate fuel heteroatoms is novel within the area of jet fuel, and the wider fuel-fouling area.

The successful characterization of the nitrogen and sulfur deposits will improve our understanding of their interactions at molecular level, and ultimately lead to the construction of predictive models with improved sensitivity and accuracy to different fuel chemistry. In our study, ab-initio density functional theory was used to assess proposed various fuel reactions. Additionally, Hansen Solubility Parameters (HSPs) were employed to assess the solubility of the detected deposit species.

5.2 Materials and Methods

5.2.1 Surrogate Fuels

The bulk surrogate fuel in this investigation was composed solely of *n*-dodecane (ACROS Organics, >99%), which is the average carbon chain length of jet fuel.[286]

The bulk surrogate fuels use in this study are shown in Table 5.1. All the heteroatoms added to the fuel were added in at 0.1 mol L^{-1} indole (Sigma Aldrich, >99% purity), pyrrole (Sigma Aldrich, >98% purity) and quinoline (Oakwood chemicals, >98% purity) were chosen as the representative of polar nitrogen. The role of indole and pyrrole in deposition is widely reported in the literature.[63, 172, 156, 64] However, quinoline compounds have lower effect on the formation of deposit in fuels.[65] Furthermore, three different straight-chain sulfurs components were added to separately surrogate fuels including: di-N-hexyl sulfide (Insight Biochemical, >99%), di-N-hexyl disulfide (Alfa Aesar, >85%), and dodecanethiol (Oakwood Chemicals, >98%). These sulfur compounds were selected on the basis of their commonality in aviation fuels and their varying effect on deposition.[51, 63] Methanol ($\geq 99.8\%$, SLS), toluene ($\geq 99.5\%$, SLS) and acetone(>99%, SLS) were used for the dissolution of deposit procedure.

Heteroatom Classes	Compounds Added to <i>n</i> -dodecane
Polar Nitrogen	Indole
Polar Nitrogen + Sulfur	Indole + Di-n-Hexyl Sulfide
Polar Nitrogen + Sulfur	Indole + Di-n-Hexyl Disulfide
Polar Nitrogen + Sulfur	Indole + 1-Dodecanethiol
Polar Nitrogen + Sulfur	Pyrrole + 1-Dodecanethiol
Polar Nitrogen + Sulfur	Quinoline + 1-Dodecanethiol

Table 5.1: Surrogate fuels employed in this work, all compounds were added at 0.1 mol L^{-1}

5.2.2 Method of Thermal Stressing

All tests were carried out in pressurized glass round bottom flasks to eliminate any effect of wall surface catalysis.[287] 5 mL of surrogate fuel and a 12 mm PTFE magnetic stirrer bar was added to the 50 mL volume flasks and sealed for the rest of the tests. The stirrer bar was set to 600 rpm for the duration of the test. Each test was carried out at $140 \text{ }^\circ\text{C}$ with a 1 bar bar molecular oxygen atmosphere above the heated

surrogate fuel. The oxygen pressure was maintained at 1 bar with glass inserts connected to a cylinder left open during the duration of each test. To maintain the temperature, a heating block was used. A lower temperature typically encountered in jet fuel systems was chosen due to limits of the device used.[245] A pure oxygen atmosphere was used to ensure that the fuel was completely saturated with oxygen, an essential reagent of autoxidation and deposition chemistry.[71] Enhanced oxygenated conditions allowed for greater production of autoxidation/deposition products, providing easier analysis and detection. The tests were carried out for 8 h for all surrogates.

5.2.3 Characterization

Prior to each test, 10 mL of total surrogate was prepared, which was split into two equal parts, with one was kept as a blank. After thermal stressing, the liquid portion of the thermally stressed mixture was taken off the top, and solid deposits were allowed to settle to the bottom of the flask. Liquid-liquid extraction with 1 mL of methanol was then performed on the stressed liquid. Methanol was analyzed by GCMS to explore the effect on the bulk solvent and search for any detectable precursors. In order to characterize the deposits, 5 mL of tri-solvent composed of 1:1:1 methanol, toluene, and acetone was used to dissolve the deposits.[288, 289, 170] In summary, at the end of each test, three samples were produced for analysis: a) the stressed bulk, b) tri-solvent consisting of dissolved deposits, and c) a blank surrogate.

The GCMS instrument used in this work was an Agilent Technologies 7200 Accurate Mass GC-MS QToF. A split ratio of 100:1 was selected, equipped with an Agilent hp5-ms low-bleed column. The oven temperature program was set at 45 °C for 2 min, then 10 °C/min ramp to 90 °C, followed by a 2 °C/min ramp to 130 °C, and eventually a 10 °C/min ramp to 225 °C. The injector temperature was set at 250 °C. Structures proposed by GCMS are compared with mass spectral fragmentation data from the NIST library. In most cases, the highest match/R-match factor was selected as the structure. However, in some cases, due to knowledge of the starting structures, some structures with a lower match factor were selected.

For the LCMS analysis an Agilent Technologies 6530 Accurate Mass LC-MS QToF instrument was used. The samples were injected into the a Agilent Zorbax Extend-

C18 2.1 mm×50 mm, 1.8 μm column. The mobile phase was run at a 20 : 1 ratio of 70 : 30 acetonitrile:water containing 0.1% formic acid to water for the first 10 min. For the next two minutes the ratio was changed to 1 : 20 70 : 30 acetonitrile:water containing 0.1% formic acid. Subsequently, for the remaining 3 min the final solvent mixture was 20 : 1 ratio of 70 : 30 acetonitrile:water containing 0.1% formic acid to water. The mass spectrometer on the LCMS was operated at 350 °C with a pressure of 45 psi. Data was collected over a 50-3000 m/z range, with a 4000 V capillary voltage, fragmenter voltage of 125 V. A Duel ESI ion source allowed for real-time mass accuracy calibration, allowing for probably chemical formulas of the ions to be elucidated. All the solutions were analyzed in positive ((+)LCMS) and negative mode ((-)LCMS), ensuring all functional groups were analyzed for.

The Agilent LCMS MassHunter software allows for the determination of a probable chemical formula based on the mass of the molecular ion detected. In many cases, multiple formulas are suggested, but given the knowledge of the starting compounds, one is selected. The deviation from the predicted formula and the measured mass of the compound will be presented in ppm.

5.2.4 Computational Details

All calculations were performed using the same settings detailed in Section 4.2.1.

5.2.5 Hansen Solubility Analysis

Hansen solubility parameters have historically been a useful tool to assess and predict the solubility/miscibility of various solvents and solutes.[290] Here, we will use Hansen solubility parameters (HSP), calculated from the HSPIP software, to assess the solubility of the structures proposed from our analysis.[291] We built a HSP sphere to calculate the probable solubility of the detected deposit molecules. These are detailed alongside the structures. A relative energy difference (RED) between the HSP sphere and the calculated HSP parameters of the molecule chosen larger than 1 implies the molecule is likely to be insoluble in your main solvent (*n*-dodecane in this case), whereas a RED less than 1 implies the molecule is soluble. Further detail on the calculation and equations associated with HSP can be found in Section 10.2.1 of the Appendix.

5.3 Results and Discussion

5.3.1 Pure Indole Deposition

Our analysis of the 8h indole run has demonstrated that indoles tend to couple-oxidatively to form deposits when present in a fuel-like solvent. Putative structures compounds detected by LCMS are in Figures 10.19 and 10.21 in the Appendix. The deposits formed from an indole containing solvent tend to be solely formed from indole units with oxidized bulk fuel seemingly not present in the deposit structure at significant levels. Instead, the oxidation of the bulk fuel appears to be suppressed by the indole as indicated by GCMS analysis of the stressed solution presented in 10.22 of the Appendix. In contrast to this, GCMS chromatograms of the stressed *n*-dodecane chromatogram which is populated by peaks containing various oxygenated groups shown in Figures 10.14 and 10.15 in the Appendix. This is interesting as it is in contrast to previous studies showing indole had neither pro or antioxidant tendencies.[63, 170] The key difference here may be the high concentration of indole added to our mono-component surrogate, where previous studies used smaller amounts of indole. Studies with real fuels have consistently shown that nitrogen has been present at higher elemental concentrations than the parent fuel,[156, 292, 293, 33] which reinforces the validity of chemical comparisons between surrogate and real fuels.

5.3.2 Effect of Sulfur with Indole

In this section, the effect on adding various sulfur compounds to the indole surrogate on the structure of deposits will be discussed. After 8 hr stressing the appearance of each flask was markedly different. The pictures of the flasks after 8 hr thermal stressing are presented in Figure 10.17 in the appendix. Gravimetric analysis of the deposit masses indicates that the order of deposition in terms of the sulfur compounds added is dodecanethiol (RSH) > di-*n*-Hexylsulfide (RSR) > di-*n*-hexyldisulfide (RSSR) > pure indole (I) which is presented at the bottom of Figure 5.1 (Table 10.7). Thiols have consistently been shown to have the most severe effect on deposition in fuels compared to other sulfur compounds. [130, 294, 51]

The deposit masses generated and the appearance of each flask are related to the

structure of the deposit, with a higher deposit mass correlated to a higher proportion of the deposit containing alkylated indole oligomers. Comparative chromatograms in positive ((+)LCMS) and negative (-)LCMS ion mode are presented in Figures 10.27 and 10.28. The LCMS chromatogram peaks are labelled according to the class of deposit structure. Because some peaks contained multiple ions, the most intense ion signal was selected as the dominant species to assign to the peak class. However, it should be noted that signal height is not necessarily correlated with concentration within each peak.[68] The relative peak areas by species class are presented in Figure 5.1. The structures associated with all the peaks are presented in Tables 10.13 and 10.14, and their associated chromatograms are presented in Section 10.2.7. Looking at both chromatograms, the I+RSH deposits exhibit the largest number of peaks, implying there is a larger amount of decomposition products. This is not surprising given that the I+RSH deposit gave the largest mass. The addition of sulfur compounds to the indole surrogate led four key compound classes: 1) indole sulfur oligomers, 2) indole oligomers, 3) oxidized sulfur species, and 4) alkylated nitrogen structures. Interestingly, in both (-)LCMS and (+)LCMS, the higher the deposit mass, the greater the proportion of the deposit structure was composed of alkylated-indole oligomers. However, the proportion of indole-sulfur products in the deposit is the largest in the RSR+I deposit. Overall, it is clear that addition of sulfur compounds: accelerates coupling between indoles and changes the deposit structure by reacting with indole. The deposit structure for each class will now be discussed in detail.

Selected structures associated with each major species class will now be discussed, putative structures for each class presented in Figure 5.1 are shown in Figures 5.2, 5.3, 5.4, and 5.6. First, the structures for indole oligomers compound class will be discussed. In all of the deposits analyzed, indole oligomers were found. However, for the I deposit, indole oligomers formed the entire deposit structure. Indole dimers found in I, I+RSR, and I+RSH are presented as structures **3** and **1** in Figure 5.2, which are indicative of oxidative coupling products. Similarly, indole trimers **2** and tetramers **4** are found, suggesting that even when dimers are insoluble (indicated by their RED score > 1), further heterogeneous coupling reactions can occur leading to further deposit growth. Similar oligomerization products were observed in another model fuel study using 2-methyl indole.[68] Nevertheless, the oligomers detected using 2-methyl indole appeared to contain more oxygenated functional groups com-

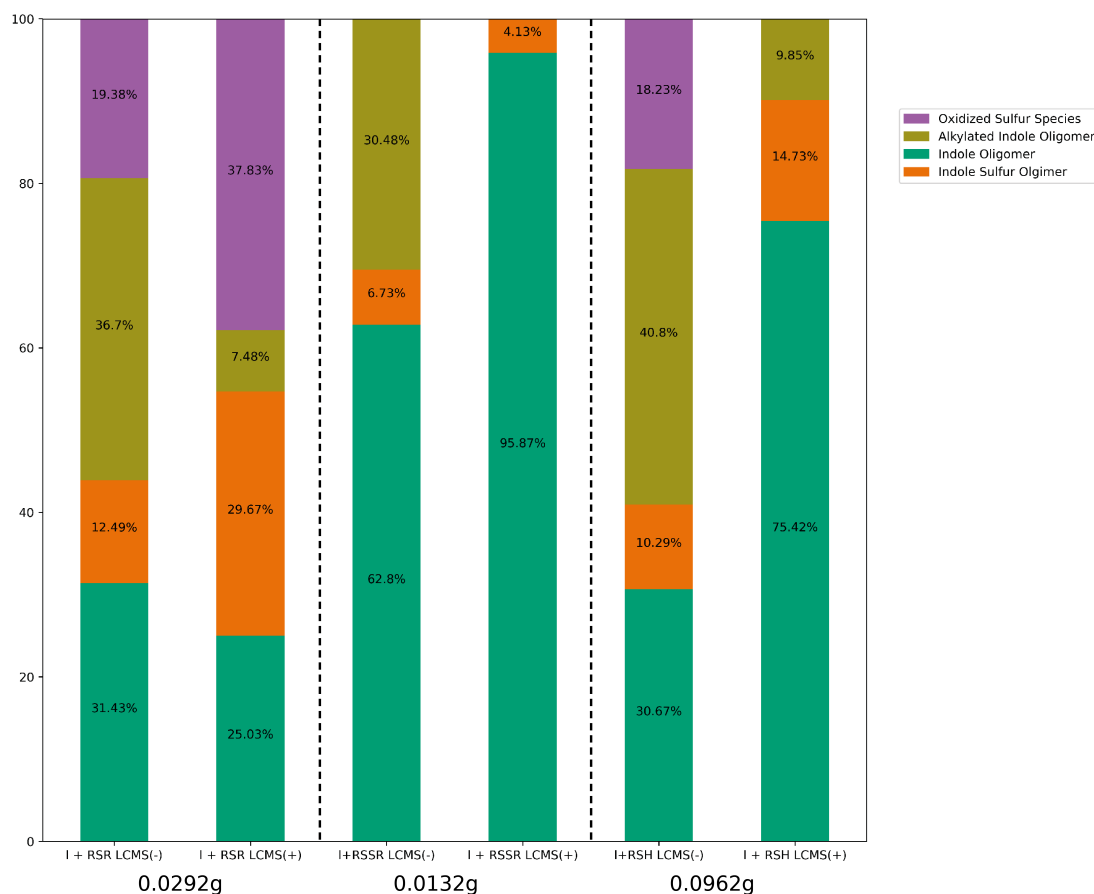


Figure 5.1: Relative peak areas for the four deposit species classes shown the key, with associated mass of deposit generated in 5 mL surrogate shown. Detail of the peaks associated with each class are shown in the LCMS chromatograms in Section 10.2.7 of the Appendix.

pared to our indole oligomers, which do not always contain oxygen group, even as tetramer oligomers.

GCMS analysis of the stressed surrogate solutions also reveal information about the structure of the indole oligomers. Detailed structures of the compounds detected in the GCMS solutions are presented in Section 10.2.6 of the Appendix. Several oligomers containing nitrile and indole-ring opening moieties are found in all the indole and sulfur surrogate solutions (for example, compound h-k in Table 10.10). In addition, the compound $C_{15}H_{10}N_2$ was detected in the I+RSR and I+RSH LCMS analysis of the deposit, also suggestive of a dimer containing indole decomposition moieties. The fact these compounds are only detected in the indole + sulfur surrogates and not the pure indole surrogate is suggestive of the sulfur compounds

accelerating indole oxidation.

Structures associated with the indole sulfur oligomer compound class will now be

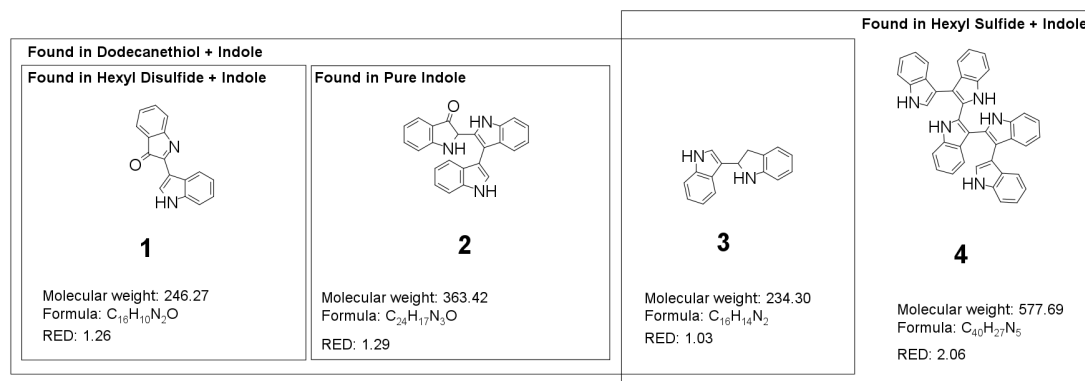


Figure 5.2: Examples of compounds found in the indole oligomer compound class found in the indole+sulfur deposits. The RED score indicates the solubility of the proposed structure, with RED > 1 indicating an insoluble structure in *n*-dodecane.

explored. Out of sulfur containing the deposits analyzed, the highest proportion of deposit containing the indole sulfur oligomer class was the RSR+I deposit. Interestingly, in all (-)LCMS analysis of the deposit, the compound C₈H₇NSO₃ was detected, which is assigned to structure **7** in Figure 5.3. Sulfur dioxide has been observed as a decomposition product of sulfur compounds in model and real fuels.[141, 51, 52] Compound **7** is indicative of a SO₃ molecule reacting with indole. Sulfonation of indole usually occurs at the 3-position, owing to the enhanced stability of intermediates compared to electrophilic substitution at the 2-position.[295] As a consequence, the most likely structure in Figure 5.3 is presented as the -SO₃H group at the 3-position. **7** could contribute to deposit in several ways. Firstly, the -SO₃H group will significantly reduce the solubility of the indole moiety in hydrocarbons. The RED score for this structure is 2.03, indicating that this structure is likely to be highly insoluble in *n*-dodecane. The RED score is one of the largest out of all calculated scores for the deposit structures. Despite dodecane sulfonic acid (structure **10**) containing an -SO₃H group, the majority of the molecule is composed of the C12 chain, leading to a total calculated RED score of 0.54. As the alkyl chain shortens, the total proportion of the molecule which shares structural similarities (δD , δP , δH Hansen parameters) with the bulk solvent is reduced. This effect of chain length on RSO₃H solubility is particularly well demonstrated when comparing the RED scores for hexyl sulfonic acid (structure **9**) to dodecane sulfonic

acid (structure **10**), where the RED scores are 0.54 and 1.22 respectively, owing to the proportion of the molecule containing an *n*-dodecane-like structure. Regarding the sulfonylated indole species **7**, the $-\text{SO}_3\text{H}$ group is attached to an indole containing an aromatic structure with a polar NH moiety, which is highly dissimilar to *n*-dodecane base solvent. Alternatively, structure **7** could accelerate deposition because of the electron withdrawing effect of the $-\text{SO}_3\text{H}$, increasing the propensity of nucleophilic aromatic substitution.[283] Nevertheless, $-\text{SO}_3\text{H}$ groups are widely accepted as protecting groups for coupling reactions.[296]

Compounds containing sulfoxide groups compounds in the indole sulfur oligomer class are found in the I+RSR and I+RSH deposit. The C/H ratio of several compounds detected in the I+RSR and I+RSH deposit including $\text{C}_{17}\text{H}_{24}\text{N}_2\text{OS}$, $\text{C}_{33}\text{H}_{39}\text{N}_3\text{OS}$, and $\text{C}_{20}\text{H}_{31}\text{NOS}$ are indicative of a sulfur containing alkyl chain attached to an indole oligomer. The proposed structure of $\text{C}_2\text{OH}_{31}\text{NOS}$ is presented in Figure 5.3 as structure **6**. Structure **6** is indicative of the product of indole sulfenylation, usually occurring in the presence of thiols and an oxidant source. Indole sulfenylation products tend to form at the C3 position on the indole.[279] Nevertheless, the RED score of compound **6** indicates it is likely soluble in *n*-dodecane owing to the large alkyl chain, meaning only larger oligomers containing shorter sulfur alkyl chains are likely to contribute significantly to deposits.

Finally, indole+sulfur oligomers containing sulfoxide/sulfone bridges were detected in all the sulfur+indole deposits. The C/H ratio and number of nitrogens $\text{C}_{16}\text{H}_{12}\text{N}_2\text{OS}$, $\text{C}_{16}\text{H}_{12}\text{N}_2\text{O}_2\text{S}$, and $\text{C}_{24}\text{H}_{23}\text{N}_3\text{OS}$ are all indicative of indole oligomers containing sulfoxide/sulfone bridges. A putative structure is presented for $\text{C}_{16}\text{H}_{12}\text{N}_2\text{OS}$ as structure **5** in Figure 5.3. Structure **5** could form from the reaction of an indole with a sulfonylated $\text{C}_8\text{H}_7\text{NSO}_3$ (structure **7**) species. Both of these arylated sulfonylated compounds could be intermediates to dimers, where C-S bond cleavage and the release of SO_3/SO_2 leads to the formation of C-C bonds. Despite this, cleavage of the C-S bond is a challenge without transition-metal catalysts, which are not present in our surrogates.[283] Nevertheless, the detection of both arylated sulfonylated compounds adds credence to the theory that compounds **7** could accelerate coupling. Alternatively, direct reaction of SO_2/SO_3 and $\text{R}\cdot$ could leading to sulfonyl radicals ($\text{RSO}_2\cdot$), which can then couple further. SO_2 in particular is a good radical trap, and the subsequently formed $\text{RSO}_2\text{R}'$ is able to readily decompose to release more radicals.

Next, focusing on the oxidized sulfur species class, we see an array of products as-

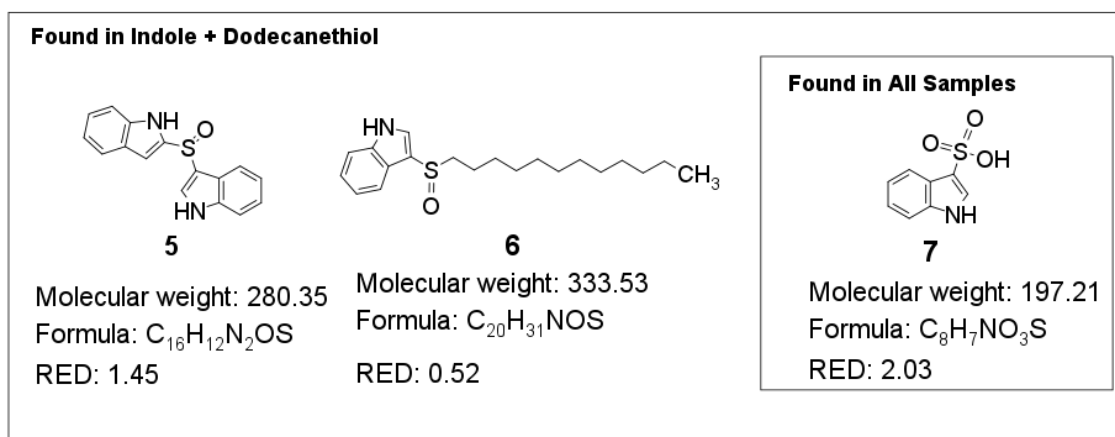


Figure 5.3: Examples of compounds found in the indole-sulfur oligomers compound class found in the indole+sulfur deposits.

sociated with sulfur oxidation in the I+RSR and I+RSH deposit. Interestingly, no oxidized sulfur species were detected in the I+RSSR deposit. Nevertheless, the presence of the sulfonylated structure **7** in the I+RSSR deposit is suggestive of oxidized sulfur species being formed, but below the limit of detection.

Focusing on the oxidized sulfur species in I+RSH, a large peak in (-)LCMS (labelled on Figure 10.28) pertains to C₁₂H₂₆O₃S which is dodecane sulfonic acid shown as structure **10** in Figure 5.4. Similarly, in the I+RSR deposit, hexane sulfonic acid is found with the formula C₆H₁₄O₃S assigned to structure **9**. In the I+RSR deposit, the compound C₁₂H₂₆S is also found, corresponding to a sulfoxide species (structure **8**). Sulfoxides are a known product of sulfide oxidation, and likely a precursor to C-S scission allowing hexane sulfonic acid (structure **9**) to form.[297]

Finally, we will explore the alkylated indole species class detected. Selected structures for this class are presented in Figure 5.6. First, it is notable that no alkylated indole species were detected in the pure indole deposit. This is likely due to the fact that the oxidation of *n*-dodecane is suppressed by the presence of indole, as discussed in Section 5.3.1. The source of the alkylated compounds in the sulfur surrogates is proposed to come through two key mechanisms: 1) reaction of indole oligomers with oxidized *n*-dodecane compounds and 2) sulfur decomposition products leading to the formation of alkenes and SO₃ via the mechanism in Figure 5.5. Regarding mechanism 1), several *n*-dodecane autoxidation products were detected

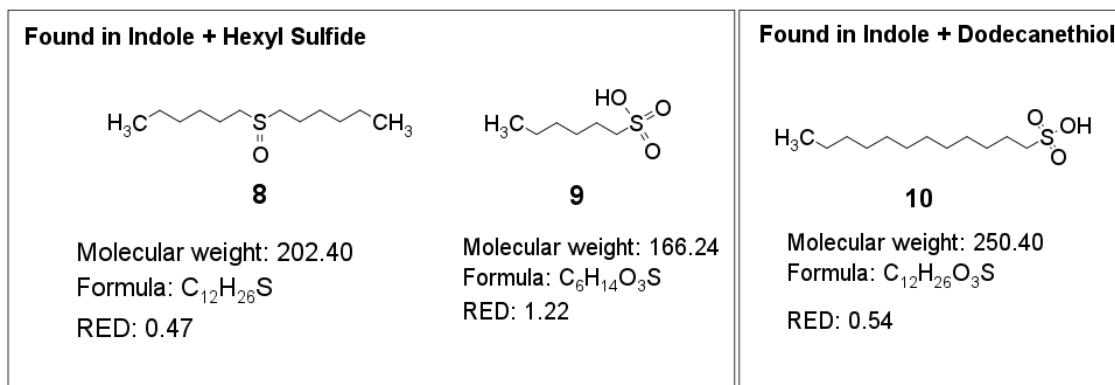


Figure 5.4: Examples of compounds found in the oxidized sulfur class compound class found in the indole+sulfur deposits.

in the LLE enhanced GCMS analysis of the stressed sulfur indole solutions which are presented in 10.2.6. These *n*-dodecane autoxidation products could react with indole oligomers. Nevertheless, *n*-dodecane autoxidation products still appear to form a minor part of the stressed solution like the pure indole surrogate, so it would be expected that some alkylated products would be detected in the pure indole deposit. Instead, mechanism 2) is more likely, given the fact the SO₃ reaction products like **5** and **7** are detected in all the indole + sulfur deposits, so alkenes are likely readily formed too. Indeed, alkenes are well known to readily couple with other species under free-radical oxidative conditions.[298]

Exploring the alkylated indole class in detail in each surrogate, in the I+RSR de-

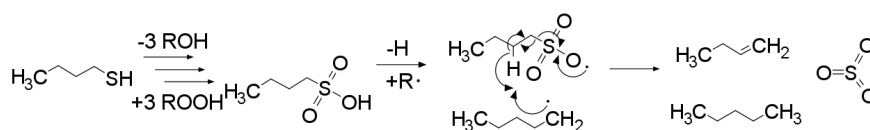


Figure 5.5: Mechanism of SO₃ production in fuels.[52] First RSH is successively oxidized to a sulfonic acid. The sulfonic acid then undergoes hydrogen abstraction and reacts with another alkyl radical, this subsequently yields an SO₃ molecule, an alkane, and an alkene.

posit, several compounds are found containing more carbons expected than given the number of nitrogens. These include the compounds C₃₀H₂₃N₃O, C₃₈H₃₀N₄O, C₂₂H₂₂N₂O₂, and C₂₉H₂₃N₃. These structures are all consistent with alkylated indole oligomers. Exploring one structure from the I+RSR deposit in detail, C₂₂H₂₂N₂O₂ is presented

as **13** in Figure 5.6. Structure **13** shows an indigo moiety bonded to a hexene moiety. Given that indigo was directly detected in the GCMS trace as compound r in Table 10.10 and hexene would be an expected decomposition product of hexane sulfonic acid via mechanism 2) in Figure 5.6, **13** is likely to correspond to $C_{22}H_{22}N_2O_2$.

Similar alkylated indole products are found in the I+RSH deposit, again indicated by more carbons than expected given the number of nitrogens in the molecular formula. These I+RSH deposit products include the compounds $C_{36}H_{37}N_3$, $C_{44}H_{40}N_4O$, $C_{36}H_{35}N_3O$, and $C_{20}H_{29}NO$. $C_{36}H_{37}N_3$ is assigned structure **12**, showing a dodecene, likely arising from dodecane sulfonic acid decomposition, bonded with an indole oligomer. $C_{20}H_{29}NO$ is assigned **11**, which likely arises from an oxidized dodecane species (detected in the I+RSH LLE GCMS) reacting with indole. Interestingly, the RED score of **11** of 0.51 implies this molecule is likely soluble in *n*-dodecane, and is potentially entrained in the I+RSH deposit. The long alkyl chain contributes to the solubility of **11** in *n*-dodecane. Shorter alkyl chains in the I+RSSR deposit structures could lead to compounds with lower solubility, which can explain the wider distribution of deposit products compared to the I+RSH deposit.

In the I+RSSR deposit, fewer alkylated indole oligomers are detected. This reflected in the fact that oxidized sulfur species are not detected in this deposit, lending support to the mechanism in Figure 5.5 being a source of the indole alkylated deposits.

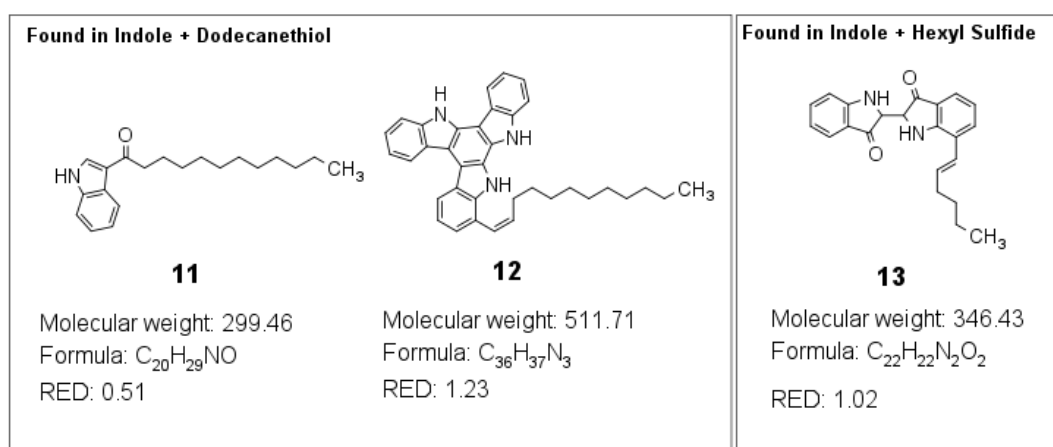


Figure 5.6: Examples of compounds found in the alkylated indoles compound class found in the indole+sulfur deposits.

5.4 Reaction of Sulfur with Other Nitrogen Heterocycles and Compounds

To further investigate the synergistic effect between nitrogen and sulfur compounds, we explored the interaction between other representative nitrogen compounds and thiols. Dodecanethiol was chosen as the representative sulfur in these tests due to its significant interaction with indole. Two other fuel representative nitrogen heterocycles were selected- pyrrole and quinoline. Each test was carried out according to the method of thermal stressing detailed in the method section.

After 8 h thermal stressing each flask contained differing levels of visible deposits and the solutions exhibited different colors. The flasks are depicted in Figure 10.33 of the Appendix. Although, gravimetric analysis was not performed for these tests, it is clear that the addition of dodecanethiol had a pronounced effect of increasing the amount of visual deposits. In particular, the pyrrole flask produced a black deposit which was only partially soluble in the trisolvant mixture. As a consequence, for pyrrole + dodecanethiol, the trisolvant mixture was filtered through a glass microfibre 0.6 μm filter before analysis. The black deposit is likely polypyrrole, proposed to form by other researchers under oxidative conditions in fuel,[64] and is notoriously difficult to dissolve due to the highly constrained nature of the polymer backbone.[299] By contrast, the pure quinoline solution appeared to yield no visible deposits, but the addition of dodecanethiol led to a fine deposition around the flask.

The GCMS chromatograms of each solution with the indication of products detected at each region is presented in Figure 5.7. Similarly to the indole GCMS analysis (Figure 10.22), GCMS was not able to detect surrogate deposit precursors. Once again, this is likely due to the volatility of the precursors, precluding them from entering the GCMS column. Nevertheless, it is notable that *n*-dodecane autoxidation products were observed for both pyrrole and quinoline, but the same GCMS analysis found that indole (Figure 10.22) suppressed the autoxidation of the bulk solvent. Pyrrole has been noted for its antioxidant properties too,[300] but in this case it is clear that indole shows greater antioxidant properties.

GCMS analysis also revealed that pyrrole was consumed below the detection limit in the pure-pyrrole test. By comparison, the other solutions in Figure 5.7 all indi-

cated the presence of starting nitrogen compounds. To understand the deposition mechanism further, LCMS analysis was performed on the dissolved deposit.

Like in the indole tests, LCMS analysis was performed for these tests in (+)LCMS

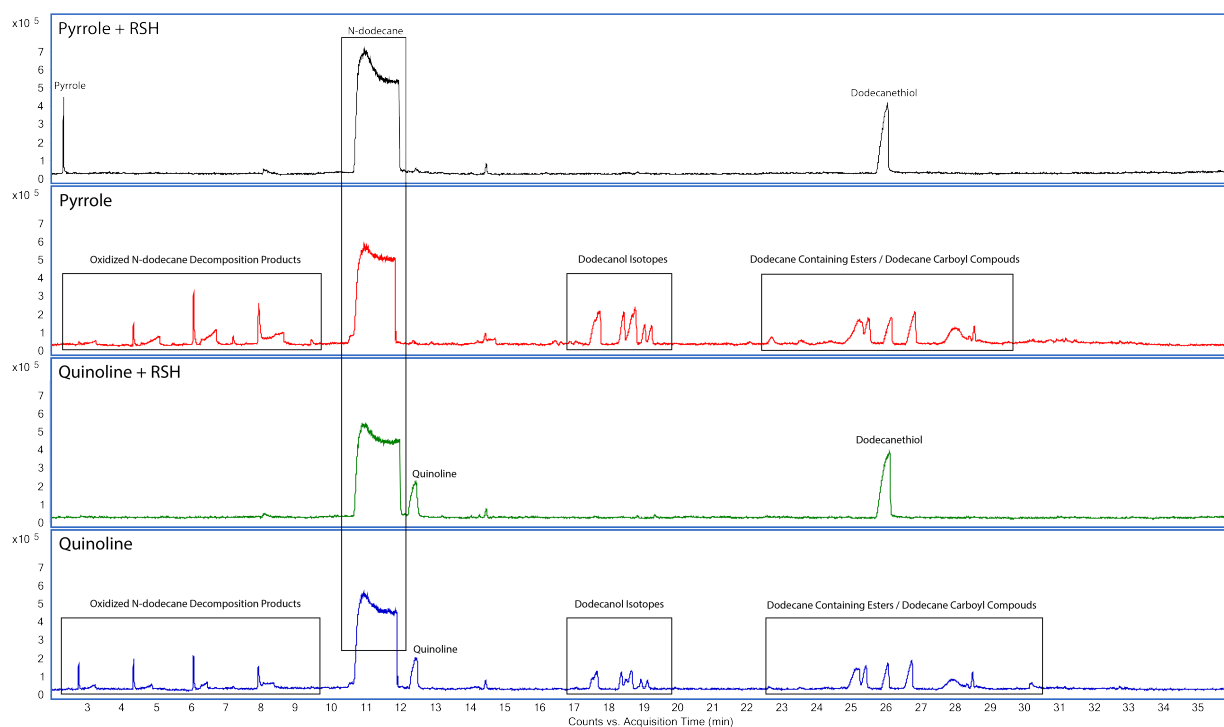


Figure 5.7: GCMS chromatogram of the solutions of pyrrole, pyrrole+dodecanethiol, quinoline, and quinoline+dodecanethiol after 8h stressing at 140 °C.

and (-)LCMS mode to capture a wide range of possible deposit products. The ions detected in these tests are presented in Table 10.15.

Four main classes of species were observed in both the nitrogen deposit structures: 1) *n*-dodecane autoxidation products 2) nitrogen oligomers, and 3) alkylated nitrogen compounds. The chromatograms and ions detected by LCMS are presented in Section 10.2.8.2. The addition of sulfur had a large effect on the structure of the deposit for each nitrogen species.

Analysis of the pyrrole deposits produced structures entirely composed of the *n*-dodecane autoxidation products class. These compounds are $C_{12}H_{24}O_3$ and $C_{12}H_{22}O_2$ both associated with acidic *n*-dodecane species, assigned structures **14** and **15**. In section B and C of the pyrrole (+)LCMS chromatogram several low-intensity over-

lapping peaks are found, which could not easily be identified. However, it is likely this section contained *n*-dodecane autoxidation products too because the peaks were found at same retention times as *n*-dodecane autoxidation products found in the pure quinoline (+)LCMS deposits. Additionally, the absence of pyrrole in the GCMS analysis of the solution implies pyrrole did take part in the formation of deposit. Nevertheless, nitrogen containing structures were not identified in the LCMS chromatogram here.

Upon the addition of sulfur, pyrrole deposits contained structures associated entirely with pyrrole cross-coupling and oxidized sulfur. Suppression of *n*-dodecane autoxidation is clear from the GCMS results in Figure 5.7, so it is not surprising that no *n*-dodecane autoxidation products were found in LCMS analysis of the deposit. Several products containing C/N ratio of 4:1 indicating several pyrrole oligomers $C_8H_{10}N_2O$ and $C_{16}H_2ON_4O$, assigned structures **17** and **18**. Products with C/N ratios higher than expected were also found in the pyrrole + dodecanethiol deposit. These include the compounds $C_{13}H_{11}N_3$ and $C_{25}H_{20}N_6O_3$. The C/H ratios of these compounds are indicative of pyrrole chain containing a pyridine moiety. For example, the compound $C_{25}H_{20}N_6O_3$ is assigned structure **16**, consisting for 4 pyrrole units and one pyridine, possibly formed from ring opening with pyrrole and subsequent re-aromatization. Alternatively, since pyrrole polymerization proceeds via a chain-growth mechanism, whereby the formation of a radical/positive charge on the subsequent dimer leads to further reactions at the 2-position, the reaction of trace pyridine is likely to halt/slow this process. Due to pyridine's 6-membered structure, a pyridine unit is likely to interfere with the polymer conjugation properties of polypyrrole.[301] As a consequence, compound **16** is likely to have a lower propensity to undergo further coupling compared to a pyrrole trimer. Thus, **16** is likely to remain soluble towards the trisolvant compared to the larger polypyrrole species formed.

Analysis of the pure quinoline deposit shows a mixture of oxidized *n*-dodecane, oxidized quinoline, and alkylated quinoline products. Oxidized *n*-dodecane compounds include acid decomposition products $C_4H_6O_4$ and $C_5H_8O_3$, and directly oxidized *n*-dodecane including $C_{12}H_{22}O_4$, $C_{12}H_{22}O_4$, and $C_{12}H_{26}O_6$. The oxidized *n*-dodecane compounds then directly react with quinoline. Compounds $C_{16}H_{19}NO$ and $C_{17}H_{21}NO$ are indicative of cross-coupling reactions with *n*-dodecane decomposition products. **20a** and **20b** are considered possible structures of $C_{16}H_{19}NO$. **20a**

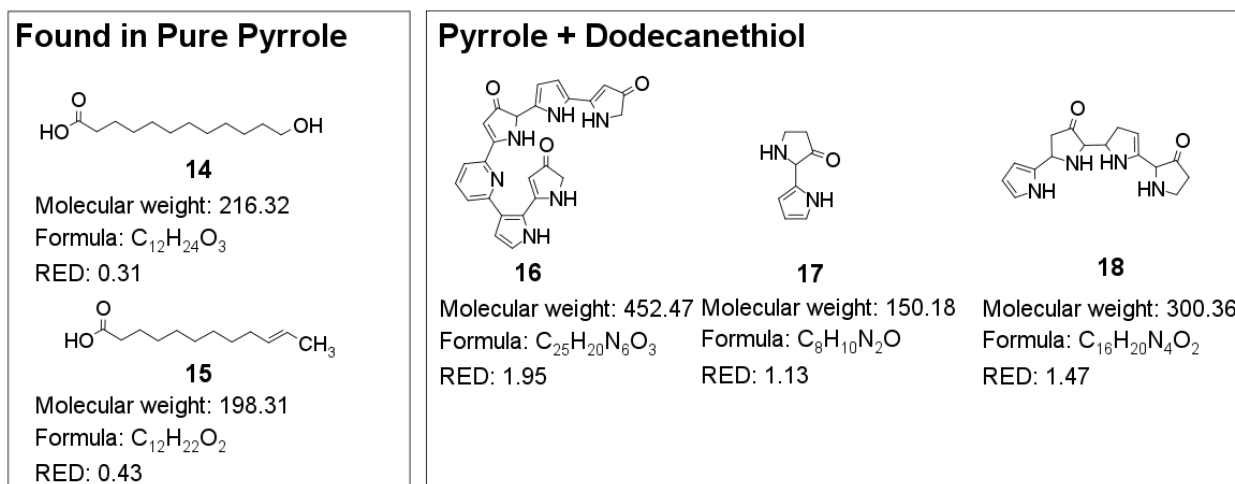


Figure 5.8: Selected putative structures from the compounds detected by LCMS detected in the pyrrole and pyrrole+dodecanethiol deposit. The RED based on calculated HSP are presented for each structure.

is analogous to the alkylation products observed in the indole+di-*n*-hexylsulfide and indole+dodecanethiol runs (for example **12**, **19**). **20b** is proposed to occur via coupling between oxidized *n*-dodecane species detected in the GCMS chromatogram in Figure 5.7. Interestingly, all the quinoline structures proposed in section A (+)LCMS are soluble in *n*-dodecane according to the RED scores given. RED scores below one for the cross-coupling products arise from the large alkyl chain, increasing the similarity with the base solvent. Since no deposits were observed visually from the pure quinoline run, these structures could collect at the bottom of the flask after the solution was extracted. Finally, the compound C₉H₇NO is associated with an oxidized quinoline, likely structure **19**. **19** is proposed as the most likely site oxidation is the ortho-position according to previous work on quinoline oxidation.[302]

Addition of dodecanethiol to the quinoline surrogate led to the suppression of *n*-dodecane autoxidation products, and quinoline oxidation products. Again, the GCMS chromatograms in Figure 5.7 indicate that *n*-dodecane autoxidation is suppressed here, so the formation of alkylated quinoline is not observed here. In fact, the formation of oxidized quinoline compounds is also suppressed by the addition of dodecanethiol. Instead, the compounds are detected in section B C₂₅H₂₆N₄O and C₂₈H₂₂N₄O of the (+)LCMS contain fewer carbons that would be expected with quinoline tetramer. Since ring-opening reactions were observed in the indole runs upon addition of sulfur compounds (Tables 10.12, 10.10 and 10.11), the compounds

associated with quinoline in this run could also be formed from ring-opening products of quinoline. Supporting this assertion, sulfur acids and SO₃ have shown to readily decompose quinolines.[303, 304]

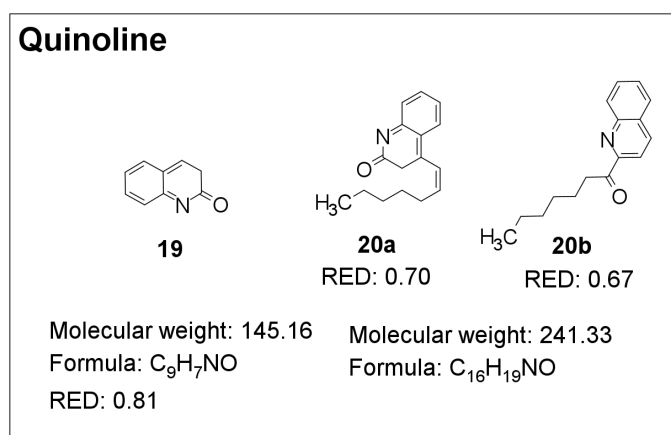


Figure 5.9: Selected putative structures from the compounds detected by LCMS detected in the quinoline deposit. The RED based on calculated HSP are presented for each structure.

Overall, the addition of a typical fuel sulfur, *n*-dodecanethiol, appears to lead to two effects. Firstly, the suppression of *n*-dodecane autoxidation products is evident from the GCMS and LCMS data, where these products are only observed in the pure nitrogen deposit and solution. The second effect is the promotion of coupling for pyrrole, where direct coupling products are only observed when dodecanethiol is added to the flask. This is also seen with the indole tests, where addition of sulfur compounds led to an apparent increased amount of coupling product ions observed. By contrast, the 6-membered quinoline shows no neat quinoline coupling species, even upon addition of dodecanethiol. Instead, the compounds formed are associated with reactions between decomposed nitrogen coupling products. Also, the addition of dodecanethiol appeared to suppress the formation of quinoline alkylation/alkenylation products (**36-39**). The implications for these results will be discussed in the next section, with potential mechanisms proposed.

5.5 Mechanism Discussion and Implication for Jet Fuels

In the introduction to this work three mechanisms proposed by researchers which lead to nitrogen and sulfur compounds forming fuel deposits were highlighted: 1) an acid-base pathway leading to salt formation,[33, 63], 2) an acid-catalyzed coupling pathway,[170, 33] 3) a free-radical oxidative coupling pathway between nitrogen and sulfur species,[63, 64] and 4) a pathway involving the in-situ formation of H_2SO_4 from SO_2 . [52] The semi-quantitative investigation into nitrogen-sulfur interactions in fuel has revealed several important findings. Firstly, the addition of reactive sulfur compounds to fuel nitrogen heteroatoms does not appear to lead to salt formation in our study, as suggested by some researchers.[63, 33] Considering oxidative-coupling between nitrogen and sulfur compounds, several sulfenylation reactions were found in the indole runs (**6**, **17**, $\text{C}_{27}\text{H}_{27}\text{N}_3\text{OS}$), but oxidative coupling products *between* nitrogen compounds appeared to be make up the a large part of the total deposit structure, too. Nevertheless, the third mechanism proposed in the literature, formation of SO_2 is given credence in our study due to the detection of sulfonylated species **7** in the indole sulfur tests. However, other sulfonylated species were not detected in the other nitrogen sulfur runs. Despite this, the sulfonation of indole led to a compound with high insolubility in our *n*-dodecane solvent. Nonetheless, the presence of the $-\text{RSO}_3$ group is likely to protect indole from further coupling, so the insolubles formed from compound **7** are likely to form as fine deposits rather than larger macromolecular structures. According to the barriers calculated (Table 10.17 in Section 10.4), the sulfonation of several fuel-typical 5-membered nitrogen heterocycles can more easily proceed than 6-membered heterocycles, potentially giving one reason why 5-membered heterocycles led to enhanced deposit in the presence of sulfur in some studies.[171, 172, 156]

It is also notable that the identity of the sulfur species in the indole test led to interesting differences in the structure of deposit. The I+RSH and I+RSR deposits contained indole-sulfur cross-coupling products, likely forming from the reaction with $\text{R}\cdot$ and $\text{RS}\cdot$. However, the most notable effect between the sulfur classes appeared to be related to the extent of coupling products produced, indicated by the number and area of peaks produced in the dissolved deposit (Figures 10.27 and 10.28). This effect is particularly seen when comparing the pyrrole + dodecanethiol

test to the pure pyrrole test, where no pyrrole coupling products appear to form after our 8 h test. By contrast, upon addition of dodecanethiol, pyrrole coupling products are observed but no direct sulfur+nitrogen coupling is found (Tables 10.15 and 10.16). The addition of dodecanethiol to the quinoline surrogate fuel did not lead to the detection of quinoline coupling products. Instead, the main products detected were ions indicative of reactions between ring opening products of quinoline. These findings indicate the addition of sulfur appears to play a role in catalyzing coupling between some nitrogen species.

To explain this effect, it is proposed that sulfonic acid plays a role in accelerating coupling by protonating the heteroatom, supporting the acid-catalyzed theory of coupling.[33, 170] Our proposed mechanism is illustrated in Figure 5.10. In our explanation we use pyrrole as our model 5-membered heteroatom and pyridine to illustrate the 6-membered case. Protonation on pyrrole is more favorable at the C2 position.[305] On the other hand, pyridine tends to be protonated at nitrogen, since the lone pair is more available to protonation. Pyrrole protonation at the C2 position leads to C3 and C5 activation due to the positive charge dissociated round the ring via more resonance forms, leading to nucleophilic 5-membered heterocycles to attack these positions. The resulting pyrrole dimer from nucleophilic attack still bears the positive charge, leading further coupling. It is for this reason acids are employed in the production of polypyrrole.[306] By contrast, protonated 6-membered heterocycles are unable to form resonance structures meaning the positive charge remains on the protonated nitrogen site. Nevertheless, due to the strong electron withdrawing effects of the protonated nitrogen species, attack by nucleophiles (like other nitrogen heterocycles) leading to enhanced coupling at the C2 position.[304] Since 6-membered heterocycles show much greater basicity than 5-membered heterocycles,[307] strong acids (like sulfonic acids), the effect stronger activation effects in 5-membered heterocycles will be balanced out by the increased protonation of 6-membered rings. As a consequence, our mechanistic approach can explain enhanced coupling in for both 5- and 6-membered heterocycles.

Our proposal relies on the ability of sulfur acids in fuel to protonate in non-polar aprotic bulk fuel. A recent review has highlighted the importance of trace water in forming reverse micelles, allowing acid-base chemistry to occur in non-polar bulk solutions.[308] Another review into the water content in jet fuel has highlighted that polar compounds, including sulfonic acids and polar nitrogen compounds, tend to

coalesce round water droplets found in fuel, potentially offering a site where the protonation steps could occur.[276] Nevertheless, despite the low concentration of water, as highlighted in Figure 5.10, once protonation occurs on one nitrogen species the positive charge remains on the dimer allowing polymerization/oligomerization to larger macromolecules until the nitrogen oligomer is deprotonated.

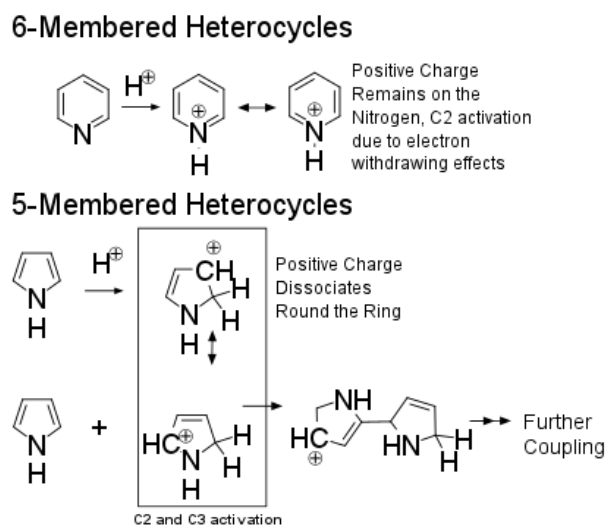


Figure 5.10: Proposed mechanism of acid catalyzed for 5-membered nitrogen heterocycles in fuel

To explore the coupling sites via protonation, a series of DFT calculations were performed on various protonated nitrogen fuel species to calculate the electrostatic potentials (ESP) mapped onto total electron density. The results of the calculations are presented in Figure 10.34 in the Appendix. The chosen protonation sites were selected as the most favorable based on previous literature supplied in the figure caption. Panel 10.34A shows that pyridine protonated at the N1 position leads to electron deficiency primarily at the N1 site. Nevertheless, the C2/C6 carbons appear to show areas of weak electron deficiency too, which can help explain why pyridine shows increased deposit in the presence of sulfur acids.[64] Protonated quinoline demonstrates lower charge dissociation, where the benzene ring attached to the pyridine moiety leads to greater electron density at the C2 position. By contrast, pyrrole, which shows greater deposit enhancement when combined with acid species, protonation at the C2 leads to electron deficiency at the C5 site, and to a lesser extent the C3 site. Indole protonated at the C3 site also leads to electron

deficiency at the C2 position. This likely explains why coupling products were observed in the C2 position in the GCMS results in section 10.2.6. Interestingly, the carbazole ESP plot shows that protonation has little effect on the electron density at other sites, potentially explaining why Zabarnick *et al.* showed that carbazole deposition was not accelerated by the addition of sulfur. [63]

Two notable differences between our surrogates and real fuels 1) use of an artificially high concentration of antioxidant and 2) use of a simplified bulk fuel containing aromatics, should be discussed. Firstly, use of artificially high concentration of antioxidants likely increased the level of self-reaction. In a real fuel, an antioxidant would be expected to couple with fuel components at a higher rate, leading to a greater concentration of bulk fuel-nitrogen side products. Secondly, using a more realistic fuel containing aromatics would also lead to an increase in bulk fuel-nitrogen side products. Particularly because aromatics have a higher propensity to undergo C–H abstraction than alkyl components.[29] Additionally, the addition of aromatics is known to increase the solubility of polar compounds, therefore the level of deposit is likely to change between a pure n-dodecane fuel and a fuel containing aromatics.[276]

Our findings in this work will help researchers more to a more comprehensive understanding of jet fuel deposition. The work has highlighted that greater understanding into the protonation mechanisms in fuels will need to be performed. Nevertheless, integration of our findings into a predictive mechanism will lead to greater sensitivity to fuel chemistries.

5.6 Conclusions and Next Steps

In this work a combination of experimental and computational techniques was used to propose several mechanisms to deposits generated by nitrogen heteroatoms and sulfur compounds. When indole and several common fuel sulfur compounds (di-*n*-hexyl sulfide, di-*n*-hexyl disulfide and dodecanethiol) are combined in a flask oxidizer LCMS and GCMS analysis shows that sulfur compounds tend to accelerate coupling between indoles. This accelerating coupling effect is found to in the order dodecanethiol > di-*n*-hexyl sulfide > di-*n*-hexyl disulfide. Interestingly, di-*n*-hexyl sulfide and dodecanethiol exhibited indole alkylation and sulfenylation/sulfonylation cross-coupling products, indicative of decomposition of the chain to R· and RS·. In all the sulfur compounds, SO₃ gas is generated, indicated by the detection of

sulfonated indoles in all the sulfur deposits. Additionally, the decomposition of sulfur compounds producing SO_3 creates alkenes as a by-product, which were found to form alkenylation compounds in the sulfur nitrogen deposits. The calculated Hansen Solubility Parameters of the sulfonated indole compounds suggests many of these are highly insoluble in *n*-dodecane, leading to another source of deposit in fuels.

Expanding our investigation to two other common fuel nitrogen compounds, quinoline and pyrrole, the addition of dodecanethiol leads to the rapid polymerization of pyrrole. By contrast, quinoline appears not to show any coupling products, but instead demonstrates decomposition products likely catalyzed by sulfonic acid formed from the oxidation dodecanethiol.

Based on our analysis, a mechanism was proposed involving sulfur acids from oxidized sulfur. Favorable protonation sites on 5-membered rings lead to the activation carbon sites around the ring to coupling, initiating a oligmerization chain reaction. Protonation of basic 6-membered rings does not lead activation of coupling sites to the same extent, but still leads to enhanced C2 activation to nucleophilic attack due to strong electron withdrawing effects of the protonated nitrogen. We show this difference clearly with calculated electrostatic potential plots. Our proposal will enable greater prediction of fuel deposits engines with higher thermal efficiency, and enable models to be built with greater sensitivity to fuel blends.

Chapter 6

Understanding the Wall Deposition Mechanism

Abstract

Elemental analysis of deposits formed on a simulated jet fuel burner feed arm suggest a higher concentration of oxidized polar fuel species at the wall-deposit interface. To investigate this, the adsorption energies of various jet fuel species classes were calculated using plane-wave DFT methods on two oxides Fe_2O_3 -(0001) and Cr_2O_3 -(0001), which were chosen to represent a stainless steel surface. A mixed termination approach was chosen to encapsulate the heterogeneous nature of stainless steel surfaces. On metal-terminated Fe_2O_3 and Cr_2O_3 , the order of the absolute adsorption energies was $\text{RSO}_3\text{H} > \text{RSO}_2\text{H} > \text{RCOOH} > \text{RSH} > \text{ROH} > \text{RCOH} > \text{RH}$. Dissociative chemisorption was observed for all the acid species, with sulfur acids having a higher absolute adsorption energy on Cr_2O_3 but carboxylic acids having a higher adsorption energy on Fe_2O_3 . On oxygen-terminated Fe_2O_3 , the order of the absolute adsorption energies was $\text{RSO}_2\text{H} > \text{RSR} > \text{RSO}_3\text{H} > \text{RSH} > \text{ROH} > \text{RCOH} > \text{RCOOH} > \text{RH}$. On the other hand, for oxygen-terminated Cr_2O_3 , the order of the absolute adsorption energies were $\text{RSO}_2\text{H} > \text{RSR} > \text{RSH} > \text{RSO}_3\text{H} > \text{RCOH} > \text{ROH} > \text{RCOOH} > \text{RH}$. In contrast to the metal terminated surface, acids do not chemisorb on the oxygen terminated surfaces. Instead, the sulfur acids are found to form surface hydroxyl species from the dissociation of the acidic $-\text{OH}$ group. The reactivity of the surfaces followed the general pattern: metal terminated- $\text{Fe}_2\text{O}_3 >$ metal-terminated Cr_2O_3 , oxygen-terminated $\text{Fe}_2\text{O}_3 \approx \text{Cr}_2\text{O}_3$.

6.1 Introduction

Irrespective of the source of an aviation fuel, one of the crucial technical suitability considerations for the utilization of fuel is its resistance to thermal oxidative degradation. Thermal oxidative stability is a regulated property, since jet fuel has a secondary function as a cooling fluid, prior to the combustion chamber.[309] Thermal oxidative degradation will become increasingly important in the future as more thermally efficient jet engines are brought into service, resulting in larger heat loads on the bulk fuel.[74] The development of a robust theoretical framework for thermal oxidative degradation through an understanding of the molecular interactions between fuel species and components will enhance the prediction of the growth of surface carbonaceous deposits in aero-engine fuel systems.[24] However, this requires a comprehensive quantitative/qualitative analysis of a large number of chemical species interacting with the surface during fuel thermal degradation. The complex chemical composition of aviation fuel means that efforts to understand the mechanisms behind deposition, to date, have involved a combination of theoretical studies and experimental work carried out under simplified conditions.[24, 89, 77]

Experimentally, jet fuel system simulators such as the Aviation Fuel Thermal Stability Test Unit (AFTSTU) are capable of assessing fuel thermal degradation in service conditions.[89] The AFTSU rig replicates conditions in a range of current and future aero-engines, ensuring that the fuel arrives at the simulated burner feed arm in a condition which is representative of a system in terms of fluid flow, thermal exposure, surface chemistry, etc.

From a theoretical point of view, density functional theory (DFT) has emerged as an increasingly important tool to understand thermal oxidative degradation. DFT allows proposed reaction pathways to be evaluated in terms of calculated thermodynamic and kinetic parameters. Publicly available DFT studies pertinent to jet fuel thermal stability have mainly focused on liquid phase chemistry in bulk fuel.[310, 311, 54] Within recent years, plane-wave pseudopotential methods implemented in DFT have become useful tools for investigating surface chemistry.[312, 313, 314] Within the scope of fuels, DFT calculations using the Vienna Ab Initio Package (VASP) have explored the reactivity of surfactants on stainless steel surfaces in automotive engines.[312] Particularly relevant to our research area, a recent study has employed plane-wave DFT calculations to study the adsorption of bio-fuel species

on stainless steel.[315] To our knowledge, no DFT studies have investigated the reaction of thermally oxidized conventional jet fuel species occurring at the surface-fuel interface, i.e. reactions occurring between the fuel and pipe walls.

The term thermal oxidative stability refers to the ability of an aviation fuel to withstand chemical changes caused by reactions with oxygen dissolved in the liquid phase.[316] Thermal oxidative degradation can be divided into two key processes: (i) autoxidation of the fuel, (ii) subsequent formation of insoluble species leading to deposits. The autoxidation of the bulk fuel produces several oxidized fuel species including acids ($\text{RC}(=\text{O})\text{OH}$), alcohols (ROH) and carbonyl compounds (RCHO). Minor heteroatomic species (such as nitrogen and sulfur-containing species) are also oxidized via reactions with hydroperoxides (ROOH). Of these heteroatomic species, indigenous sulfur compounds are known to be strongly deleterious to fuel thermal stability. In particular, thiols,[317, 318, 319] successively react with hydroperoxides to form sulfenic (RSOH), sulfinic ($\text{RS}(=\text{O})\text{OH}$) and sulfonic ($\text{RS}(=\text{O})_2\text{H}$) acids.[54, 53]

The oxidized species RCHO , ROH , $\text{RC}(=\text{O})\text{OH}$ along with sulfur-containing species RSOH , $\text{RS}(=\text{O})\text{OH}$, $\text{RS}(=\text{O})_2\text{OH}$ formed through the autoxidation process are believed to take part in agglomeration processes. These oxidized species then eventually bind to heated surfaces, forming carbonaceous deposits.[320] However, it is yet unclear which chemical mechanisms or fuel species are involved in different stages of deposition. It has been reported that deposits generated in aviation fuel systems are ‘varnish-like’ or ‘lacquer-like’, as they are difficult to remove mechanically.[115, 166] The high temperatures ($500 - 800^\circ\text{C}$) required to completely remove deposits using thermal gravimetric analysis (TGA) and carbon burn-off methods suggest that deposits are chemically bonded to the heated surfaces.[321, 89]

Direct analysis of deposits from lab scale tests, and subsequent characterization of constituent elements and functional groups has collectively helped to propose potential mechanisms of deposition. Stainless steel (SS) 316 is the most common material found in the fuel lines of an aero-engine. Therefore, it has received extensive attention as a substrate for deposition.[321, 69, 178] For example, Ervin *et al.* used X-ray Photoelectron Spectroscopy (XPS) to confirm the higher concentration of S-O bonds at early stages of deposit growth.[321] Moreover, atomic emission

spectroscopy (AES) measurements carried out by Kauffman *et al.* demonstrated a higher concentration of sulfur and oxygen at the deposit-surface boundary.[69] The presence of S–O bonds allowed both papers to postulate that organic sulfur acids formed from autoxidation of reactive sulfur play a key role at the early stage of deposition. Complementary to this, Venkataraman *et al.* reported that deposits show high levels of oxygen-containing functional groups together with the presence of carboxyl moieties via thermogravimetric analysis-mass spectroscopy (TGA-MS). The latter was confirmed by XPS.[322] In addition, sulfonic and carboxylic acids have been shown to react with SS316L surfaces. However, the mode of interaction in this case has not been fully elucidated.[323] In contrast to the involvement of oxidized fuel species in wall attachment, Beaver *et al.* proposed that aryl thiols are important for deposit formation.[320] Mohan *et al.* also theorize that thiols and disulfides directly form metal sulfides on a variety of SS surfaces.[324] Finally, metal sulfides have also been shown to form at higher pyrolytic temperatures on stainless steel by several researchers.[322, 325]

Morphological analysis of fuel deposits reveals that the thermally stressed fuels initially form a thin film of deposit on SS. This film then manifests itself as particle growth at specific sites.[321] Kauffman *et al.* postulated that site-specific growth could occur at grain boundaries on stainless steel.[69] Stainless steel primarily is passivated by a chromium layer. However, grain boundaries reveal local chromium depleted zones which exposes iron-based oxides.[28] Furthermore, steel passivation layers tend to contain both chromium and iron oxides of differing phases. Thus, local oxides could interact with deposits in different ways. Unfortunately, because of the high molecular weight and amorphous nature of jet fuel deposits, direct analysis of deposits can only provide limited information about their structure. Furthermore, it is difficult to study deposit growth *in situ*, because of the difficulty of sampling and the rapidity of deposit layering at the nano-scale.

The aim of this article is to identify which indigenous/oxidized fuel species have the greatest propensity to adsorb on clean stainless-steel surfaces using DFT calculations of their adsorption energy and adsorption mode. A complication in this is the fact that SS is heterogenous in structure, whereas predictive numerical mechanisms require the wall to be treated as a mono-component surface with uniform reactive properties.[24] Thus, the adsorption energies of fuel species for two main surface oxides, hematite and chromia, will be compared. Two main classes of species

and their main autoxidation products will be assessed. Firstly, bulk hydrocarbons (RH) which will be represented by a simple alkane as the most common species in conventional and alternative fuels.[28, 326] The bulk hydrocarbon autoxidation products investigated will be carbonyl (RCHO), alcohol (ROH) and carboxylic acid (RC(=O)OH) species. Secondly, sulfur species represented by a thiol (RSH) and sulfide (RSR), which are found in conventional fuels. The main products of thiol (RSH) autoxidation, sulfinic (RS(=O)OH) and sulfonic (RS(=O)₂OH) will also be assessed. The DFT results were compared with the elemental analysis of carbonaceous deposits at the early stage of deposition, obtained from the wetted surface of a simulated burner feed arm, as part of Aviation Fuel Thermal Stability Test Unit (AFTSTU).

6.2 Methods

6.2.1 Surface Model

Stainless steel is heterogeneous in structure, so noted above. Therefore, α -Cr₂O₃ and α -Fe₂O₃ oxides were chosen as the surfaces to represent stainless steel in this study. Fe₂O₃ and Cr₂O₃ are isostructural species. Both are found in corundum type structures. The (0001) lattice planes were used for both given that they are common in steel. [327] Both metal and oxygen-terminated surfaces will be studied, in-line with recent computational work exploring the reactivity of stainless steel. [314] Nevertheless, we acknowledge that a metal-terminated surface has frequently been shown to have the highest stability for pure α -Cr₂O₃ and α -Fe₂O₃. [328, 327, 329]

To construct the surfaces, bulk hexagonal unit cells and ions were allowed to relax. Subsequently, two layers were frozen using the relaxed-bulk structure and optimized unit cell, and a 20 Å vacuum was added above the surface. The non-frozen ions were subsequently relaxed, creating the clean surface geometry. Each bulk and surface unit cell consisted of a slab roughly 12 Å thick which was built from four stoichiometric units. All structures were assigned their most stable magnetic ordering at standard conditions. Thus, Fe₂O₃ exhibits ferromagnetic coupling within each Fe bilayer and anti-ferromagnetic coupling between neighboring bilayers along the (0001) direction. [330] In contrast, Cr₂O₃ exhibits anti-ferromagnetic coupling within the bilayers and ferromagnetic coupling between adjacent Cr layers. [331]

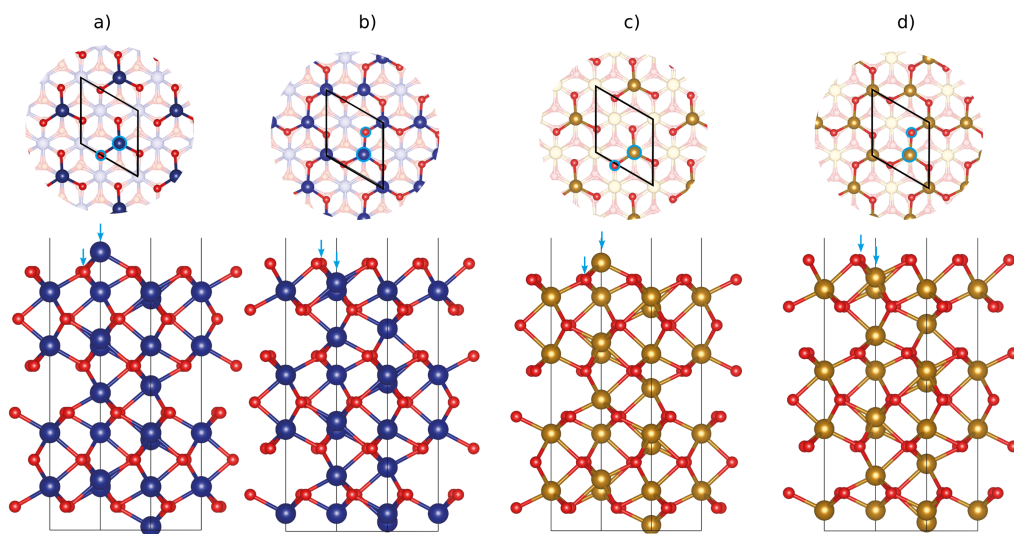


Figure 6.1: Surfaces used in this study, blue atoms represent chromium, brown atoms represent iron and red atoms represent oxygen. Panel a) correspond to metal terminated Cr_2O_3 ($\text{Cr}-\text{O}_3-\text{Cr}$). Panel b) corresponds to oxygen terminated Cr_2O_3 ($\text{O}_3-\text{Cr}-\text{Cr}$). Panel c) metal terminated Fe_2O_3 ($\text{Fe}-\text{O}_3-\text{Fe}$). Panel d) oxygen terminated Fe_2O_3 ($\text{O}_3-\text{Fe}-\text{Fe}$). Green arrows and circles indicate the chosen adsorption sites for this study, at the top site metal and oxygen for each respective surface.

All surface models were prepared using the pymatgen python package. [332, 333] The molecules were placed 1.6 Å above the surface aligned with functional groups 2 potential sites corresponding to metal and oxygen top-sites. These sites were selected out of all possible adsorption sites (Figure 6.1) likely to be important. For each top-site, the slab and adsorbate geometries were optimized to a minimum. Each calculation corresponds to a high-coverage scenario, because a (1×1) unit cell was chosen. A high coverage scenario was chosen, because of the number of species, configurations and surfaces that were tested, given the available resources. Additionally, a high-coverage scenario allows the lateral interaction between adjacent polar species on heated surfaces.

6.2.2 Computational Details

All density functional theory calculations were performed using the Vienna Ab Initio Simulation Package (VASP), version 5.4.4. [334, 335, 336] The generalized gradient approximation (GGA) was used with the optimized Perdew, Burke, and Enzerhof functional (OptPBE). [337] OptPBE improves the accuracy of the original PBE functional by adding a non-local correlation energy using a model response functional which uses electron densities. [338] Addition of this vdW-DF allows long-range dispersion interactions to be accounted for, where localized GGA functionals are often inaccurate. [339] Inclusion of long-range interactions makes the OptPBE functional particularly suitable for surface interactions. Our own testing of the OptPBE, PBE, and the meta-GGA SCAN functionals demonstrate that PBE under-binds for chemisorbed and physisorbed fuel species on both oxides. These results are presented in Table 6.1. To describe the highly correlated 3d-electrons in α -Fe₂O₃ and α -Cr₂O₃ the rotationally invariant approach proposed by Dudarev *et al.* was chosen as the DFT +U method. [340] For Fe the U-J parameter was 4.0 eV, which gave a band gap of 2.07 eV and magnetic moment of 4.14 μ_B , close to the experimental band gap of 2.4 eV and measured magnetic moment range of 3.32 – 4.20 μ_B . [341] For Cr a U-J parameter of 4.0 eV gave a band gap of 3.22 eV and a magnetic moment of 2.91 μ_B , compared to the experimental values of 3.4 eV and 3.8 μ_B band gap and magnetic moment, respectively. [323] The core electrons were replaced by projector augmented wave (PAW) potentials. [342, 343] The wave function of the valence electrons was cut-off at 600 eV. [344, 345] For both α -Fe₂O₃ and α -Cr₂O₃, a Monkhorst-Pack

$7 \times 7 \times 1$ k -point grid was used for the surface calculations, where a dipole correction was added to account for the asymmetry of the slabs. For the bulk calculations a $7 \times 7 \times 7$ Monkhorst-Pack k -point grid was employed. Bader charge analysis was performed by the code written by the Henkelman group.[346, 347, 348, 349]

The adsorption energies, E_{ads} , were calculated as follows:

$$E_{ads} = (E_{sys} - E_{slab} - N_{mol} \times E_{mol}) / N_{mol} \quad (6.1)$$

where E_{sys} is the energy associated with the optimized structure of the adsorbate on the slab, E_{slab} is the energy associated with the clean slab, and E_{mol} is the energy of the adsorbate calculated in a large $20 \times 20 \times 20 \text{Å}$ box. N_{mol} is the number of adsorbates per unit cell.[312]

We will also consider the energy contribution of lateral interactions below. They were calculated using:

$$E_{lateral} = E_{molsurf} - E_{mol}, \quad (6.2)$$

where $E_{molsurf}$ is the energy of the frozen adsorbate, obtained from the geometry of the fully-relaxed structure on the slab after the slab is removed (as described in the surface model section).

6.2.3 Justification for using the OptPBE

Due to the difficulty in obtaining reliable experimental data for adsorption energies, often the comparison of different functionals is used to justify the choice of functional.[314] As a result, we compared OptPBE with PBE (GGA) and the SCAN (meta-GGA) functional. The cutoff energy used for these tests was 450 eV and a gamma centered $4 \times 4 \times 2$ k -point grid was used. The SCAN functional has been shown to give accurate results for covalent and long-range systems for both solid state and molecular systems, often improving on the accuracy of more expensive hybrid functionals.[350] The ethane sulfonic acid adsorbate was selected for testing each functional since it was expected that this group would exhibit the both strong chemisorption and long-range interactions. The adsorption energies for each functional are presented in Table 6.1. It is clear that PBE underbinds at the chemisorption site (oxygen top-site), and the physisorption site (metal top-site).

By contrast both the SCAN and OptPBE functional gave similar results at each site. The OptPBE functional was chosen for this study because of its lower overall computational cost.

Table 6.1: Calculated adsorption energies eV of ethane sulfonic acid on metal terminated Fe_2O_3 and Cr_2O_3 using different functionals

	Fe_2O_3		Cr_2O_3	
	Metal top-site	Oxygen top-site	Metal top-site	Oxygen top-site
PBE	-0.31	-1.55	-0.36	-1.73
OptPBE	-1.26	-2.48	-1.01	-2.56
SCAN	-0.90	-2.11	-0.93	-2.76

6.3 Results and Discussion

6.3.1 Results from the Aviation Fuel Thermal Stability (AFTSU) Rig

Figure 6.2 presents the distribution of the elements in an area covering small parts of stainless steel and deposit layer generated in the AFTSU rig. These results suggest that Fe atoms are more concentrated in stainless steel and reduce significantly throughout deposit. On the other hand, the Cr component is closer to the steel wall surface, indicating the passivating layer.[351] With the exception of the early stage of deposit, close to the surface, C atoms are evenly distributed throughout the different stages of deposition. This suggests that deposition at later stages is dominated by C-C interactions. O atoms are more concentrated at the early and later stages of deposition; sulfur atoms show more contribution at early stage and become patchy throughout deposit. Interestingly, the concentration of oxygen and sulfur is located at similar spots at the wall-deposit interface, suggesting the involvement of an oxidized sulfur species.

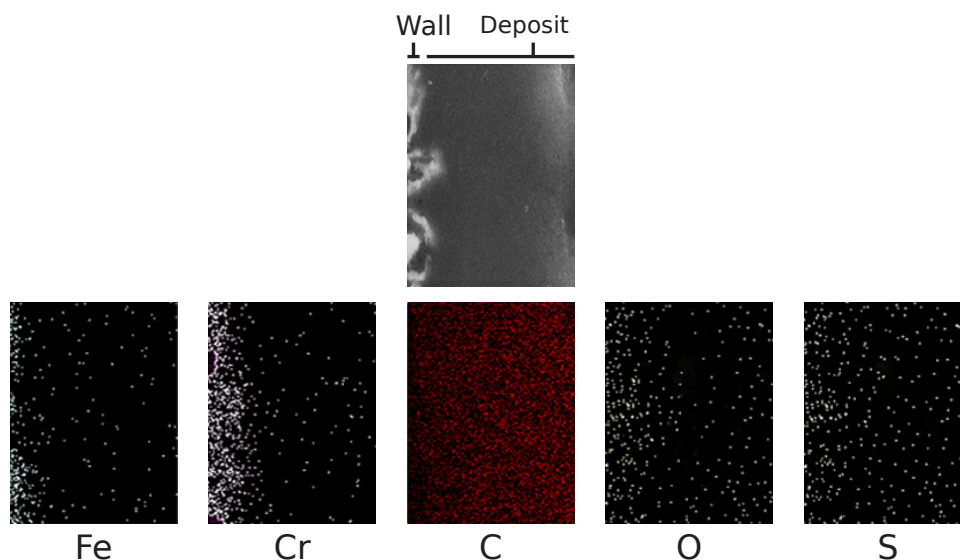


Figure 6.2: Map of constituent elements detected via EDX of deposit generated in an AFTSU burner feed-arm corresponding to an arbitrary point, the corresponding SEM image of the area is shown at the top

As noted above, the late stage development of the deposit is outside the scope of

this work, but our results are consistent with a deposition layer composed largely of polar species. In this work we will focus on the origins of the fuel-wall interactions at the early stage using DFT calculations.¹

6.3.2 Computational Results

In this section, DFT-calculated adsorption energies for oxidized and indigenous fuel species on Fe_2O_3 and Cr_2O_3 are presented and discussed. Geometry optimization of the clean M-terminated (metal terminated) surfaces led to the inward relaxation of the top metal sites, leading to a contraction in the interlayer metal top-layer and oxygen layer. For clean O-terminated (oxygen terminated) surfaces, geometry optimization also led to an inward relaxation of the top-site oxygens. The optimized clean surface geometries are present in the appendix Figure 10.35. The surface energy for the M-terminated Fe_2O_3 and Cr_2O_3 surfaces were 1.52 J m^{-2} and 2.03 J m^{-2} respectively, matching well with previous data.[352, 353] The O-terminated surfaces had higher surface energies 3.09 J m^{-2} and 3.69 J m^{-2} for Fe_2O_3 and Cr_2O_3 , owing to the dipole induced by the non-stoichiometric surface.

The results will be related to the AFTSU experimental work and existing observations for fuel systems.[321, 320, 69, 322] Since this study is primarily concerned with the reactivity of the functional groups of various fuel species with stainless steel, a short ethane carbon chain was used rather than more typical jet fuel species. Indeed, the average chain length of a jet fuel hydrocarbon is C_{12} .[316] This was computationally too costly, given the available resources, due to the large gap which would be required between the slabs. Thus, a C_2 chain was selected instead, to minimize the computational cost. Additionally, a shorter chain reduces the number of possible conformations of the alkyl tail. Nevertheless, in general, a longer alkyl tail increases adsorption energy due to adjacent VdW packing (see Figure 10.38 in the Appendix for the effects of tail length), observed in recent work on high-coverage surfactant adsorption on SS.[312] A shorter tail reduces the complexity of the calculations without sacrificing insight into different fuel species. Figure 6.3 shows the adsorption energies for each of the surface terminations and for the given fuel species. Tables 10.19 and 10.18 in the Appendix give details of the adsorption energies, and tabulate the contribution of lateral VdW interactions to the total adsorption energies.

¹The results here were not conducted by the author of the thesis but by Dr Simon Blakey and Dr Ehsan Alborzi, and are included as part of completeness of the study.

Section 10.5.5 contains the geometries of all the adsorbates and surfaces tested.

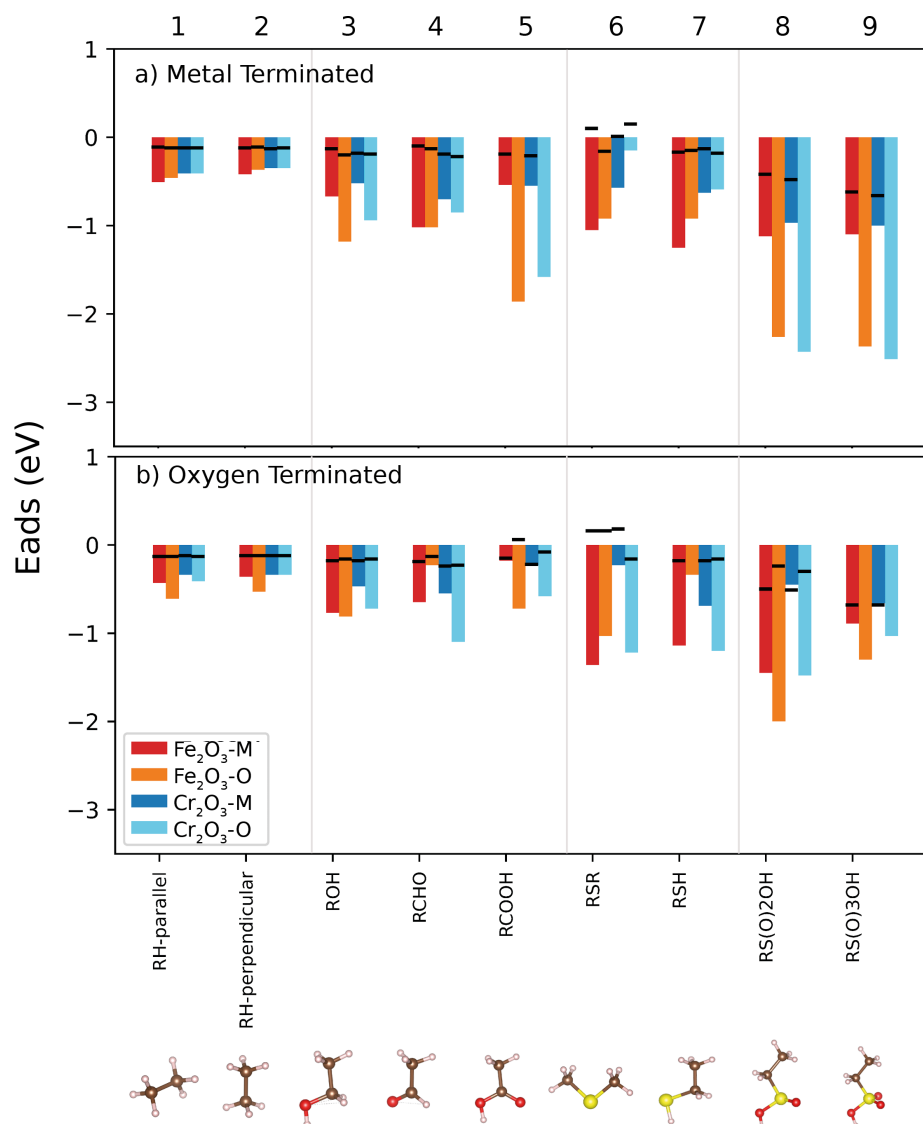


Figure 6.3: Adsorption energies calculated using OptPBE for the high coverage metal-terminated and oxygen-terminated surfaces. The key indicates whether the geometry relaxation was initiated the metal-top (-M) or oxygen-top (-O) sites. The adsorbates displayed at the bottom are the initial configurations which are set to relax on each surface. The black bars indicate the VdW contributions towards the total adsorption energy.

Our VASP calculations show that sulfur acids play an important role in binding to the heated surface in the deposition process as proposed by previous researchers.[69,

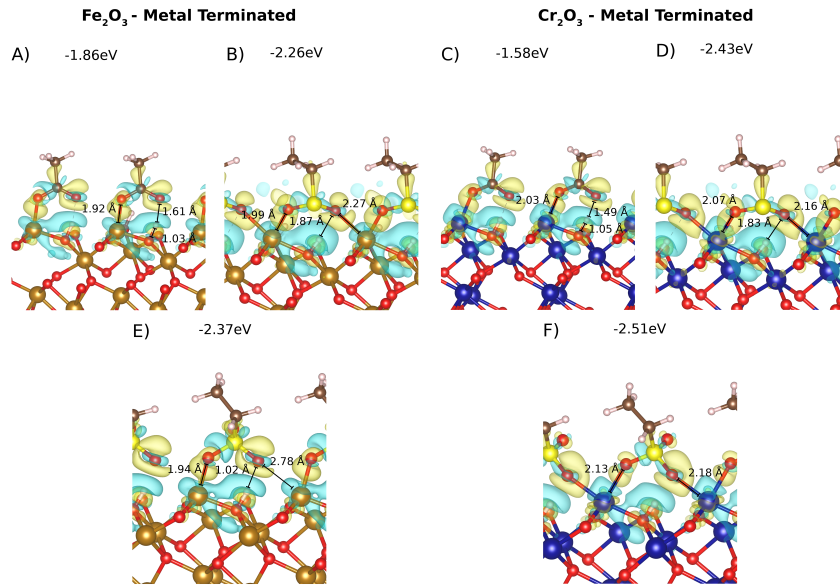


Figure 6.4: Chemisorbed geometries in our tests including charge density difference plots,

49, 321] In particular, the detection of higher concentrations of O and S at the the wall/deposit interface of the AFTS burner feed arm is consistent with the accumulation of acidic sulfur species. However, the adsorption energies show that each oxidized sulfur species exhibits individual behavior on the surface depending on the surface termination and the specific oxide under consideration.

Firstly, only M-terminated surfaces lead to dissociative chemisorption adsorption of oxidized sulfur species to the wall, where the adsorption of sulfur acids is presented in panels in **B**, **D**, **E** and **F** Figure 6.4. Hereby, dissociative adsorption of sulfur acids on Cr_2O_3 is more favorable than on Fe_2O_3 . This contradicts the assertion by previous researchers that Cr-depleted zones could provide a favorable site for deposition.[69] Nevertheless, the deposition process in conventional fuels is almost always characterized by an induction period, where components like sulfurs are oxidized.[317] Therefore, the formation of sulfur acids before the start of deposition corroborates well with previous observations.

All acids tested formed metal ester bonds (S/C–O–M) via the top site metal on the M-terminated surfaces (Figure 6.4). Ethanoic acids were adsorbed as monodentate metal-ester structures on both surfaces (Figure 6.4 **A** and **C**). However, all the sulfur acids (with the exception of sulfinic acid on Fe_2O_3) were adsorbed as bridging

bidentate metal-esters formed on adjacent M top-sites. On O-terminated surfaces, acid –OH groups tended to interact with the top O layer (Figures 10.40 and 10.44 in the appendix). In general, acids on O-terminated Fe_2O_3 had the highest absolute adsorption energies compared to O-terminated Cr_2O_3 . Interestingly, sulfur acids dissociated on O-terminated Fe_2O_3 forming surface –OH groups.

In contrast to the sulfur acids favorable binding on M-terminated Cr_2O_3 , non-oxidized sulfur compounds tended to have a higher absolute adsorption energy on M-terminated Fe_2O_3 . Thiols tended to have a higher absolute adsorption energy than sulfides on both M-terminated surfaces, where poor packing abilities of the sulfide methyl groups led to repulsive VdW interactions reducing the total adsorption energy (Figure 10.41 in the appendix). Both non-oxidized sulfur compounds are stabilized by favorable sulfur lone-pair M-top-site interactions. On O-terminated surfaces, in general sulfides had higher absolute adsorption energies. In fact, on the O-terminated surfaces, at the M-top-sites, sulfides form sulfoxides upon adsorption. Thiol adsorption is characterized by favorable –SH O-top-site interactions. However, on Fe_2O_3 the adsorption of thiol also leads to the formation of surface –OH groups. In contrast with Beaver *et al.*'s SMORS proposal, no aryl sulfide formation was observed on any of our oxides tested.[320] Nevertheless, stable physisorbed structures formed on both surface terminations could block further adsorption at these sites, suggested by previous researchers.[287]

Potential alternative future fuels like power-to-liquid fuels will contain no sulfur. Instead, the major products of thermal oxidative stressing will be oxygenated species.[315] For the oxygenated species on the M-terminated surfaces, Fe_2O_3 provides the highest absolute adsorption energies. Nevertheless, both M-terminated surfaces follow a similar adsorption trend of $\text{RC}(=\text{O})\text{OH} > \text{RCOH} \sim \text{RCHO} > \text{RH}$. This result mirrors similar work on biofuel molecules on Cr_2O_3 M-terminated surfaces.[315] In general, physisorbed geometries of the oxygenated species are stabilized by O-M interactions, where stable dative bonds are formed (Figure 10.39). For the O-terminated surfaces, Fe_2O_3 tends to provide the highest stability for oxygenated species with the exception of RCHO on O-terminated Cr_2O_3 .

On both surfaces and terminations, surface-adsorbate adsorption of the oxygenated compounds is stabilized by high levels of VdW lateral interactions. Because high levels of oxygenated species has previously been correlated with high levels of deposit,[354]

an increased concentration of oxygenated species at the wall will increase the stability of oxygenated species simultaneously adsorbed at the wall. Additionally, despite the fact that no chemisorption was found for the oxygenated species we tested, formation of meta-stable physisorbed structures would still increase the residence time of these species in the fuel system. It has been shown that increased residence time results in the production of larger amounts of deposit because of the ability of species to undergo further autoxidation and agglomeration reactions.[118]

Looking into the future, fuels will contain an increasing variety of oxygenated and heteroatomic species, as drop-in fuels become more popular. Existing numerical mechanisms tend to model deposition as a single **Deposit Precursor**→**Deposit** step.[24, 74, 78] However, our AFTS experimental data shows a changing chemical composition moving away from the SS wall (Figure 6.2). In addition, our VASP results suggest that once adsorbed, fuel species would block any further reaction with the surface. Therefore, after initial adsorption, further deposition will be no longer characterized by metal-fuel interactions, but by carbon-carbon interactions. Existing work by Alborzi *et al.* has proposed a two-stage deposition mechanism based on this phenomenon.[355] However in reference[355], the thermochemical and kinetic parameters were correlated from experiments using a conventional fuel with a specific fuel chemistry. Recent work has shown that quantum chemistry calculations integrated into predictive numerical mechanisms have the potential to create more generalized mechanisms, applicable to multiple fuel chemistries.[76] Our study has demonstrated that DFT calculations can begin to explain the behavior of different fuel types. A larger study of a variety of compounds and surface types, including structural variations of adsorbates, would provide the opportunity to construct a predictive deposition mechanism using these techniques. Indeed, high throughput surface calculations could offer a way of constructing a larger data-set for the task of constructing a predictive numerical mechanism for future fuels.[356]

6.3.3 Conclusions

The adsorption of representative jet fuel species on representative stainless steel oxides (hematite and chromia) was studied using plane-wave DFT calculations. In addition, the AFTSU rig was employed to study chemical composition throughout the deposit-wall structure. Results from the AFTSU rig indicate higher levels of sulfur and oxygen at the deposit-wall interface. DFT calculated adsorption energies show

that sulfur acids and carboxylic acids are able to chemisorb on metal-terminated Fe_2O_3 and Cr_2O_3 . Interestingly, sulfur acids show a larger binding strength for metal-terminated Cr_2O_3 , whereas carboxylic acids show greater stability on metal-terminated Fe_2O_3 . Future sustainable aviation fuels (SAF) are expected to have a lower sulfur content. Therefore, higher levels of carboxylic acids are expected to be formed from autoxidation. Thus, the deposition on steel is expected to be slower and found at Cr-depleted zones.

Unoxidized sulfur compounds showed a lower reactivity towards the surface. However, thiols and sulfides were still able to form stable physisorbed structures, particularly on Fe_2O_3 . The bulk fuel component, represented by ethane, was inert towards both surfaces as expected. Oxidized bulk fuel components, ethanol and ethanal, were able to form stable physisorbed structures via dative bonds. Since the aim of the work was to guide the future formation of predictive deposition models, the generalizability of heterogeneous stainless steel was also explored within the DFT calculations. In general, metal-terminated surfaces led to a larger binding energy. In addition, binding energies were larger for both terminations of the Fe_2O_3 surface. However, many exceptions were found to this observation, notably for the chemisorption of sulfur acids on Cr_2O_3 .

Our experimental results combined with surface DFT calculations show that both techniques can be used successfully in combination to explore complex deposition phenomena in fuels. Future, fuels will have a lower proportion of heteroatomic components. However, higher temperature demands on fuels, and the expectation that conventional fuel will be continually used as a blend, means that thermal oxidative stability will still be important. In particular, our study has shown the formation of carboxylic acids from fuel autoxidation will remain a problem as long as hydrocarbon fuels are used.

Chapter 7

Predicting Thermal Stability Behavior with Quantum Chemistry

Abstract

To understand the formation of insolubles in fuels from first principles, a series of DFT calculations were run to calculate the barriers of the autoxidation and coupling reactions for several common fuel aromatics/heteroatoms. The compounds chosen were: phenol, toluene, naphthalene, pyrrole, quinoline, and indole. A homolytic aromatic substitution mechanism was identified which when integrated into a simplified pseudo-detailed mechanism, could predict deposition behavior of the compounds tested in a simple *n*-dodecane surrogate. The homolytic aromatic substitution mechanism identified starts with the formation of an AHA \cdot intermediate, formed from the attack of a A \cdot to an AH species. It was found that ROOH could re-aromatize the AHA \cdot intermediate forming a deposit dimer. Sensitivity analysis of our pseudo-detailed mechanism indicated that R \cdot and RO \cdot abstraction steps had a large influence on the final mass of deposit. However, the A \cdot +AH coupling step also had the largest influence on the rate of deposit formation. An aromatic/heteroatom model containing phenol and toluene was also built, which showed that phenol suppressed deposition from toluene, and reduced peaked in deposit mass at a 25:75 phenol:toluene ratio.

7.1 Introduction

The formation of insolubles in the liquid-phase of jet fuels is mainly driven by the formation of oligomers from fuel components.[74, 47] Oligomers successively grow starting from dimers, trimers, tetramers and so on. Each oligomer growth step is

predominantly characterized by the formation of C–C and C–O bonds. Previous research has emphasized the termination of antioxidant and/or fuel components ($A \cdot + A \cdot \longrightarrow A_2$) as a key source of fuel insolubles, and by that extension C–C/C–O bond formation.[62, 145, 24] This has led Heneghan and Zabarnick to highlight an inverse correlation between the ease of oxidation and the formation of deposits. In other words, a fuel with a lower oxidation rate arises from the higher concentration of chain-breaking $A \cdot$ radicals, and therefore have a higher concentration of $A \cdot$ to undergo termination steps producing deposit.[62] However, in some instances, this relation does not always hold. Notably, some nitrogen compounds like pyrroles and indoles tend to show low/no effects on autoxidation rates yet are severe deposit promoters.[170, 63, 65] To explain these exceptions, Heneghan and Zabarnick propose that some fuels produce termination A–A products with a higher solubility.[62] Nevertheless, there may be other chemical factors that need to be explored.

The formation of A–A via the termination of two free-radicals $A \cdot$ in solution is part of an oxidative coupling process. However, it is possible to form A–A without a termination step under oxidative conditions. Focusing on transition metal free processes, homolytic aromatic substitution (HAS) has received considerable attention as a method for cross-coupling aromatic compounds under free-radical conditions.[357, 358, 278, 359] Additionally, HAS mechanisms have been used as a way to understand the rate of radical reactions.[360, 361] The general mechanism of HAS is shown in Figure 4.7. First, an attack of an aryl radical to an arene compound generates a σ -intermediate. The σ -intermediate is then re-aromatized via elimination of a leaving group forming a dimer. In this sense, HAS reactions are analogous to electrophilic aromatic substitution (EAS) reactions, except that the σ -intermediate is not charged. EAS reactions have been proposed as a mechanism in the formation of jet fuel deposits.[32] However, in aprotic non-polar jet fuel, the stabilization of charged EAS σ -intermediates is precluded.[273] By contrast, HAS reactions have been shown to readily occur in non-polar aprotic solvents between arenes under molecular oxygen.[362] In general HAS reactions have presented a challenge to organic chemists due to poor selectivity, leading to intractable mixtures.[278] Nevertheless, in the context of jet fuel fouling, fuel deposits and gums are characterized by highly disordered coupled products composed of mainly aromatic groups.[177, 363] Overall, the HAS reactions between aromatic fuel species should be investigated as possible route to deposits. Particularly as HAS offers a route to form C–C bonds without terminating the free-radical chain mechanism,

and can instead be considered a propagation step.

Several reactions for the formation of insolubles/deposits are represented in pseudo-detailed mechanisms in the public literature.[24, 61] However, at present, they are implicit. As a result, they do not represent specific chemical transformations, but are composed of 'pseudo' species with parameters fitted to experiments. In the future, a wider range of fuel chemistries and blends will require predictive mechanisms with greater sensitivity to the starting components, without relying too heavily on fitting parameters. However, due to complexity and range of insoluble structures, a compromise needs to be met between the range of reactions and products represented.

In recent years, density functional theory (DFT) has become a popular tool to build pseudo-detailed mechanisms jet fuel deposition from 'first-principles'. [54, 76] DFT allows direct calculations of thermochemical and kinetic data, and evaluation of competing chemical reaction pathways. By contrast, previous pseudo-detailed mechanisms have been produced by producing activation energies from fitted experimental data.[24, 61] However, this leads to mechanisms which are only suitable for specific types of fuel.

It is the aim of this paper to: 1) explore the possibility of HAS as a route to insolubles formation and 2) attempt to predict insoluble formation tendencies using DFT methods. First, several two-component fuels containing bulk and heteroatoms will be stressed to produce an insoluble mass. Then, the energetic pathways from fuel heteroatoms and bulk species to dimers are calculated and compared to insolubles generated by the surrogate fuels. As a means of understanding the deposition process further, the solubility of oligomers will be considered too.

7.2 Methods and Materials

7.2.1 Surrogate Fuels for this Study

Six surrogate fuels were built with a range of compounds designed to represent the different heteroatom and aromatic compounds found in fuels. Out of the nitrogen class of compounds pyrrole (Sigma Aldrich, >98% purity), quinoline (Oakwood chemicals, >98% purity), and indole (Sigma Aldrich, >99% purity) were selected.

Pyrrole and indole are two 5-membered nitrogen heteratom compounds known to promote insoluble formation, with pyrrole being a particularly problematic insoluble promoter.[65, 172] Quinoline has been shown to also promote insolubles, but to a lesser degree than pyrrole and indole.[65, 63] Next, phenol (ACROS Organics, >99%) was chosen to represent the phenolic class of compounds, again shown to promote insolubles in a variety of real and surrogate fuels.[65, 155, 161, 77] Finally, two aromatic components, naphthalene (Fluorochem, >99%) and toluene (SLS, $\geq 99.5\%$) were chosen for their presence in the mono-aromatic and di-aromatic class in fuels.[37] Each of the above six components were added as 0.1 mol L^{-1} to *n*-dodecane (ACROS Organics, >99%).

7.2.2 Method of Thermal Stressing and Deposit Measurement

To produce the insoluble masses, 5 mL of fuel was added to a 50 mL borosilicate round bottom pressurized flask. The flask was heated to 140 °C for 24 h under 1 bar. After heating, the flask was allowed to cool and insolubles were then filtered through a 0.1 μm glass fiber filter to give the total weight of insolubles in the bulk. The flask was then washed with trisolvent and then washed into a flask. The flask was then dried in a vacuum oven to remove any liquid residue, weighed, and then compared with the weight of the clean flask- giving the total weight of adherent insolubles left in the flask.[364] The sum of the insolubles weights on the filter and in the flask gave a mass total insolubles per surrogate. The deposit experiments were repeated at least 3 times for each surrogate to improve the accuracy of the total insolubles measurement.

7.2.3 Hansen Solubility Parameters and Computational Details

The details for the Hansen Solubility Parameters can be found in Section 10.2.1 and 5.2.5. The computational details for this section were the same employed in the Chapter 4 presented in Section 4.2.1.

7.2.4 Pseudo-Detailed Mechanism in Fuels

In order to compare the total insolubles to the number of dimers predicted by DFT, several new reaction steps were proposed which will be elucidated in the results and discussion. To capture the autoxidation reactions in the bulk, the basic autoxidation scheme (BAS) was used which gave good agreement with oxygen and hydroperoxide depletion with experiment. The BAS scheme was optimized for a range of C10-C14 hydrocarbons, whereby the thermochemical and kinetic parameters were obtained using *n*-dodecane as the model fuel. Further details of the BAS scheme can be found in reference[76]. To construct the mechanism, the Eyring equation was used, with A being formed from the entropy barrier and E_a formed from the enthalpy barrier. All the forward and reverse barriers were calculated from a stable pre-reaction and post-reaction complex.

For each surrogate fuel, different mechanisms were constructed to study oxygen depletion and deposit formation. For oxygen depletion, the level of oxygen was fixed at 1.8 mmol L^{-1} . [365] For the deposition mechanism, oxygen was removed as a limiting reagent (kept constant at 1.8 mmol L^{-1}) to reflect the continuous supply of oxygen in our deposit forming rig. The mechanism was integrated in MATLAB using the ode45 solver. The mechanism gave a molar concentration of a dimer, which was then related to a mass via the molecular weight of the proposed dimer.

7.3 Results and Discussion

7.3.1 Homolytic Aromatic Substitution Mechanism

The key bottleneck in any HAS reaction is the re-aromatization and liberation of hydrogen from the σ -intermediate. The loss of $\text{H}\cdot$ in this step is not well understood. Nevertheless, one paper exploring HAS reactions between aryl iodides and arenes using oxygen as an oxidant, proposed a re-aromatization step involving oxygen this is shown as reaction 1) in Figure 7.1 Because hydroperoxides (ROOH) and oxygenated species like alcohols (ROH) form under oxidative conditions in fuels, these were also considered as possible reagents to remove hydrogen from the σ -intermediate. ROOH reacting with the σ -intermediate is proposed to form $\text{RO}\cdot$ and H_2O , is shown as reaction 2) in Figure 7.1. ROH reacting with the σ -intermediate is proposed to form $\text{R}\cdot$ and H_2O , is shown as reaction 3) in Figure 7.1.

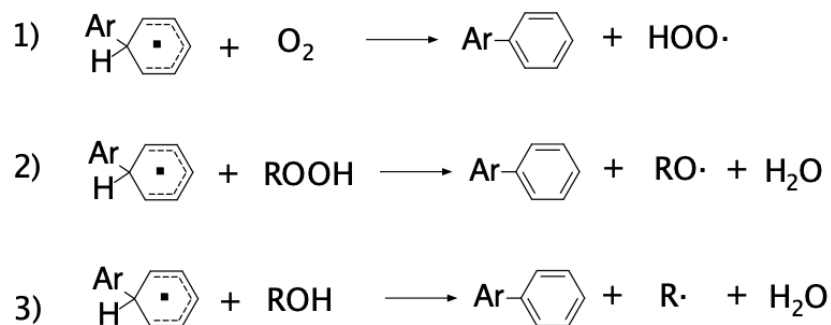


Figure 7.1: HAS reactions considered for fuel coupling reactions. Each step shows the σ -intermediate formed from an $\text{A}\cdot + \text{AH}$ reaction, and the species chosen to re-aromatize the intermediate.

Considering the mechanisms presented in Figure 7.1, we explored the possibility of these reactions in phenolic coupling. Phenols have widely been recognized as being detrimental to fuel thermal stability.[65] HAS mechanisms have previously been considered as a possible pathway the oxidative coupling of phenols.[361]

The calculated HAS pathways for phenol are presented in Figure 7.2. First, the formation of the σ -intermediate is endergonic and has a free-energy barrier of $\Delta_{\ddagger}G = +25.64 \text{ kcal mol}^{-1}$ leading to an intermediate $\text{PhOPhO}\cdot$. The para- position of the phenol was chosen as the site of oxidative coupling of another phenoxy radical given that this is the generally the more favorable site.[165] The first mechanism in Figure 7.1, involving the re-aromatization with oxygen, could not be identified for phenol. A key challenge with the oxygen transition state is the choice of spin multiplicity. Given that oxygen is in the triplet state, and the system σ -intermediate is in the doublet state, an open-shell doublet or a quartet surface can be chosen.

The other two mechanisms presented in Figure 7.1 involve ROH and ROOH. The ROOH pathway in Figure 7.2 shows a lower barrier to re-aromatization of the σ -intermediate compared to the ROH by $30.22 \text{ kcal mol}^{-1}$. Additionally, the ROOH is thermodynamically favored, namely due to the enhanced stability of the $\text{RO}\cdot$ radical compared to $\text{R}\cdot$. The IRCs for both these pathways are presented in Figures 10.45 and 10.46 in the appendix. The ROOH and ROH re-aromatization transition states are characterized by a rotation of the terminal OH moiety towards an available hydrogen at the para-coupling site.

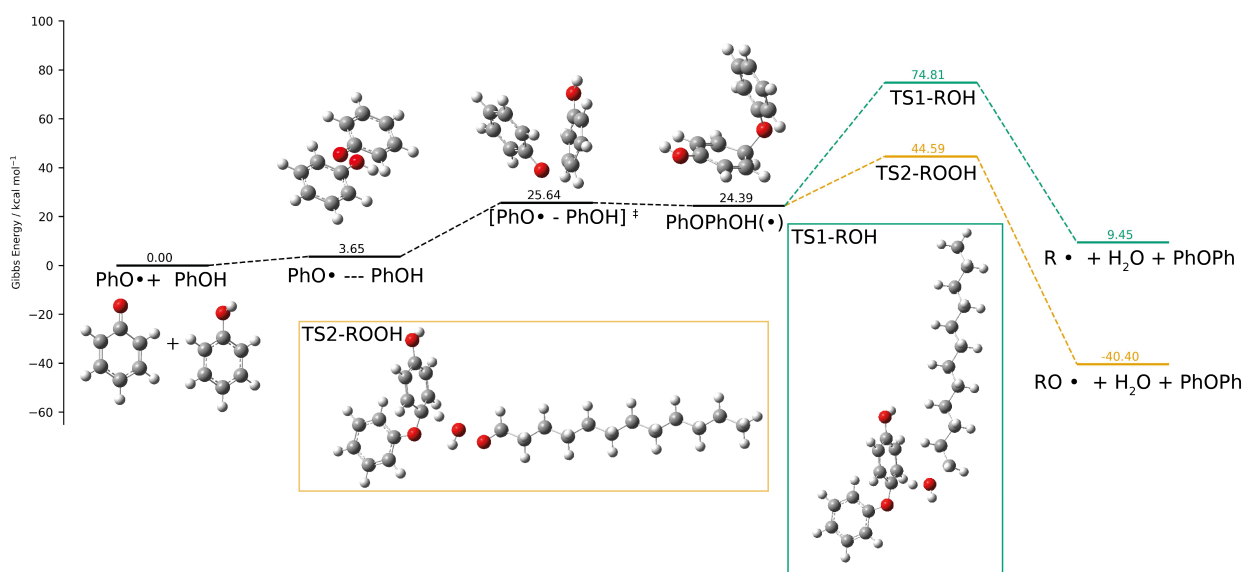


Figure 7.2: Comparison of different HAS pathways at the B3LYP-D3//cc-pVTZ level of theory using *n*-dodecane (PCM) as a solvent. The first step of the process in black shows the $A\cdot + AH \longrightarrow AHA\cdot$ reaction of a phenol and a phenoxy radical, leading to the σ -intermediate. The subsequent levels in green shows the re-aromatization step with ROH and the level in orange shows the re-aromatization step with an ROOH species.

7.3.2 Comparison of Antioxidant Oligomer Solubility and Pathway to Deposit

To justify the assumption that the formation of insolubles results from the coupling of AH species, we calculated Hansen solubility parameters for oligomers for our chosen heteratoms of increasing size. Previous research has hypothesized that aromatic compounds in fuel rapidly become insoluble as they grow in size.[27] Figure 7.3 shows the change in RED score as the oligomer chain grows, where relative energy difference (RED) > 1 (see Section 5.2.5) indicates an oligomer that has become insoluble in *n*-dodecane. For real fuels, these results will vary, particularly as the aromatic content will increase the 'likeness' of the solvent to other extended aromatic structures.[276] Nevertheless, because our model fuels in this study contain *n*-dodecane as the base solvent, the Hansen plots here are a useful tool to explore deposition tendency in our model fuels. Oligomer structures were chosen

based on the favored coupling site for each heteroatom based on literature data and our calculations.[165, 306, 304] The phenol chain growth is shown as an example. What is clear is that in general as the oligomer grows in size, the solubility in *n*-dodecane decreases. However, different oligomers reach the insolubility threshold in fewer units, where a single unit is the monomer, 2 units is a dimer and so on. For example, comparing toluene and naphthalene, naphthalene reaches the insolubility threshold after 2 units have coupled. This is consistent with previous observations that di-aromatics form deposit more rapidly because they 'require fewer consecutive reaction steps to produce high-molecular-weight'.[27]

Interestingly, heteroatom size does not influence the solubility of the resultant oligomers. Instead, the lower solubility is related to the dD parameter in the HAS framework, representing Van Der Waals forces between the solvent and heteroatom. As the oligomers grow, the difference in polarity and hydrogen bonding begins to decrease (indicated by the decreasing dP and dH parameters), but the difference in dispersion forces dD increases.

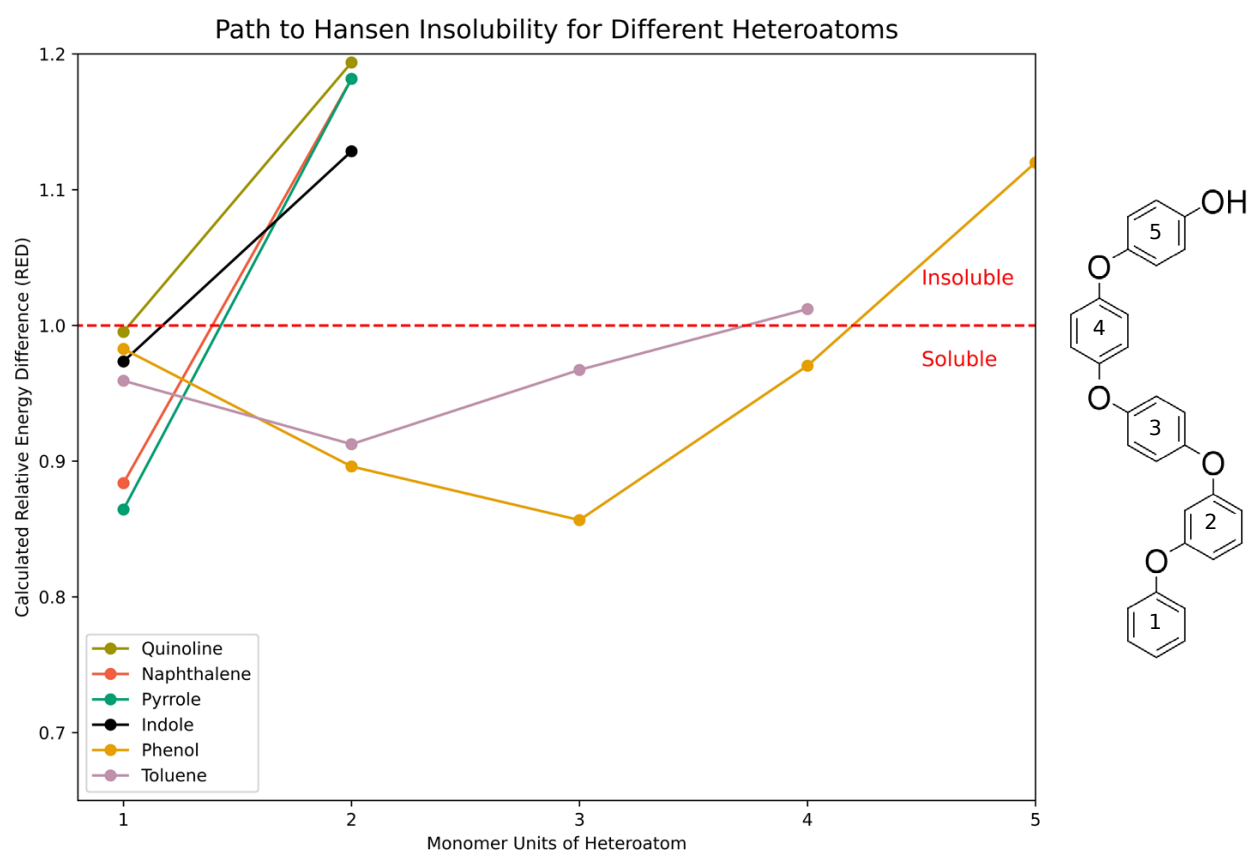


Figure 7.3: Effect of oligomer unit size on solubility calculated using the HSPiP software. It is clear some heteroatoms reach insoluble threshold in fewer units than others. Phenol and toluene is particularly interesting, becoming initially more soluble in *n*-dodecane before reaching the threshold. For phenol this is due to the growth of oligomer leading to a lower proportion of the molecule containing the *H*-bonding –OH group, but as the molecule grows the Van Der Waals dD difference grows eventually leading to an insoluble.

7.3.3 Predicting Deposition formation using DFT

7.3.3.1 H-abstraction and Coupling Mechanisms for Each Heteratom

Based on the solubility modelling presented in Figure 7.3, it was clear that the coupling of fuel heteratoms would lead to insoluble formation in our *n*-dodecane surrogate. Following the proposed HAS pathway, we calculated the H-abstraction and subsequent barriers to form dimers via the HAS pathway. The barriers for these reactions are presented in detail in Table 10.20 of the appendix. The termination reaction was barrierless for all the species, and the pre-exponential factor was kept constant for each of the species at 3×10^9 .^[24]

The H-abstraction site and the coupling site for each species was selected based on literature and our own testing, and is summarized in Figure 7.4. For phenol, H-abstraction occurs at the O-site, with coupling between the subsequent phenoxy radical and the para-carbon site of a phenol.^[165] For naphthalene, the C3 site was favored over the C2 position in terms of both abstraction and coupling barrier heights. For quinoline, the C2 site is the most favored site for coupling and H-abstraction, and the barriers for abstraction were lower at the C2 site compared to the C3 site.^[366] For toluene, the para position was selected for coupling and H-abstraction based on our own testing and literature data.^[367]

For indole and pyrrole, the favored coupling and H-abstraction site were different. For indole, the N1 site was found to be the most favorable site for H-abstraction, but the C3 site is the most favored for coupling. Nevertheless, C–N linkages are detected very rarely and are found to be thermodynamically prohibited for indole oligomers.^[368, 369] As a consequence, we compared the overall pathway to dimers at the C3 position via H-abstraction at the N1 and C3 positions. The results for the indole dimer formation calculations are found in Figure 10.48 of the appendix. Overall, the C3 H-abstraction pathway shows the highest barriers. Therefore, the N1 H-abstraction pathway for indole was chosen. Similarly, for pyrrole, H-abstraction at the N1 position is favored, yet polypyrrole is formed of C2-C2 linkages.^[306] Comparing both pyrrole coupling C2 coupling pathways with H-abstraction at the N1 or C2 position, presented in Figure 10.47, both pathways have similar barrier heights. Nevertheless, the initial H-abstraction reaction at the N1 position is more favorable, and leads to an intermediate **I1b** $\Delta G - 24.49 \text{ kcal mol}^{-1}$ lower in energy than the C2 pathway. As a consequence, following the N1 pathway, pyrrole would have antiox-

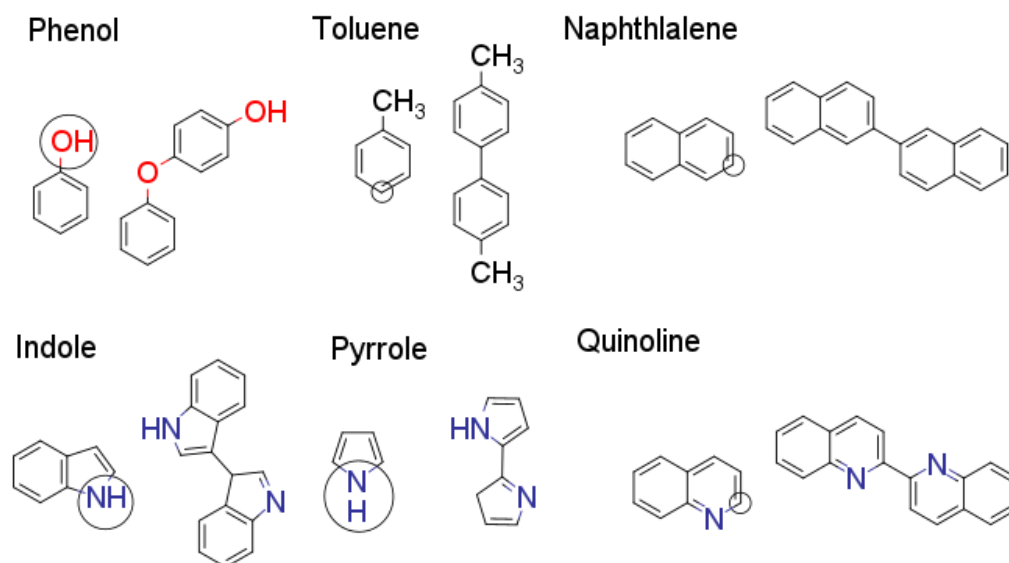


Figure 7.4: H-abstraction Sites and Dimers Selected for the Pseudo-Detailed Mechanisms. The selected H-abstraction site is circled, and resultant dimer is shown for each species.

identant properties, which is reflected in the petroOxy measurements (Figure 7.6b). Therefore the N1 abstraction pathway for pyrrole was chosen.

Based on the above proposed coupling and H-abstraction sites, we computed the barriers for AH species reacting with *n*-dodecane $R\cdot$, $RO\cdot$, and $ROO\cdot$ radicals and subsequently forming dimers via a HAS process. The Gibbs potential energy surfaces for our chosen heteroatoms undergoing H-abstraction to the formation of dimers are presented in Figure 7.3 for $RO\cdot$. The values for the reactions with the other radicals are presented in Table 10.20 of the appendix.

The first section (reaction A) of Figure 7.5, showing the abstraction of hydrogen from our selected AH species. Here, we can see there is a clear difference in the reactivity and thermochemistry. To begin with, phenol shows the lowest barriers for hydrogen abstraction out of all the species tested. Phenol has long been known as a powerful antioxidant in fuels.[24] By contrast, toluene exhibits the highest barrier and the overall Gibbs energy abstraction reaction is endergonic at $+28.32 \text{ kcal mol}^{-1}$. The overall order of the Gibbs energy barrier to hydrogen abstraction (section A) is, in descending order: toluene > naphthalene > quinoline > pyrrole > indole > phenol.

The resultant radicals formed indicate that phenol, pyrrole, and indole all exhibit antioxidant properties, by undergoing an exergonic H-abstraction reactions. By contrast, naphthalene, toluene, and quinoline undergo endergonic H-abstraction reactions showing no antioxidant qualities. At this point in the reaction process, two $A\cdot$ radicals can terminate to form a dimer. Nevertheless, this termination process is a rare occurrence due to the low-concentration of $A\cdot$ species in fuel (for example, for pyrrole the peak concentration in our mechanism was $5.17\text{E-}13\text{ mol L}^{-1}$).

The HAS reaction between an $A\cdot$ and AH first proceeds with an attack of the radical. The radical attack is shown as pathway B) in Figure 7.5. For this step, the antioxidant species formation is endergonic and proceeds with high Gibbs energy barriers for phenol and indole of $\Delta_{\ddagger}G=25.63\text{ kcal mol}^{-1}$ and $\Delta_{\ddagger}G=24.36\text{ kcal mol}^{-1}$ respectively. By contrast, pyrrole proceeds with a lower barrier of $\Delta_{\ddagger}G=19.20\text{ kcal mol}^{-1}$. On the other hand, the non-antioxidant species show lower barriers for pathway B). In fact, naphthalene and toluene show the highest barriers for the H-abstraction step, but lowest barriers out of all the species for step B) at $\Delta_{\ddagger}G=12.87\text{ kcal mol}^{-1}$ and $\Delta_{\ddagger}G=13.50\text{ kcal mol}^{-1}$ respectively. Additionally, the formation of the σ -intermediate is the most exergonic for naphthalene and toluene. The relationship between the antioxidant tendency and the ease of coupling is likely related to the aromatic structure. Species with more antioxidant qualities will also have higher levels of aromaticity to stabilize radicals, but also will have higher barriers to aromaticity-breaking radical attack.

The final step in the dimer forming process is the re-aromatization step via loss of hydrogen from the σ -intermediate. Interestingly, the barriers for this step are similar for our aromatics tested, in the range of $23.87 - 17.47\text{ kcal mol}^{-1}$. This step is clearly less related to the structure of the AH compound. Nevertheless, the concentration of ROOH available to complete this step, is related to the antioxidant qualities of the AH species in fuels. For example, for phenols, due to their antioxidant properties, the concentration of ROOH is expected to be low.[24] As a consequence, termination reactions likely provide a higher source of C-C/C-O coupling. To explore how these interrelated pathways yield deposits for different fuel components, we created different pseudo-detailed mechanisms to compare each fuel.

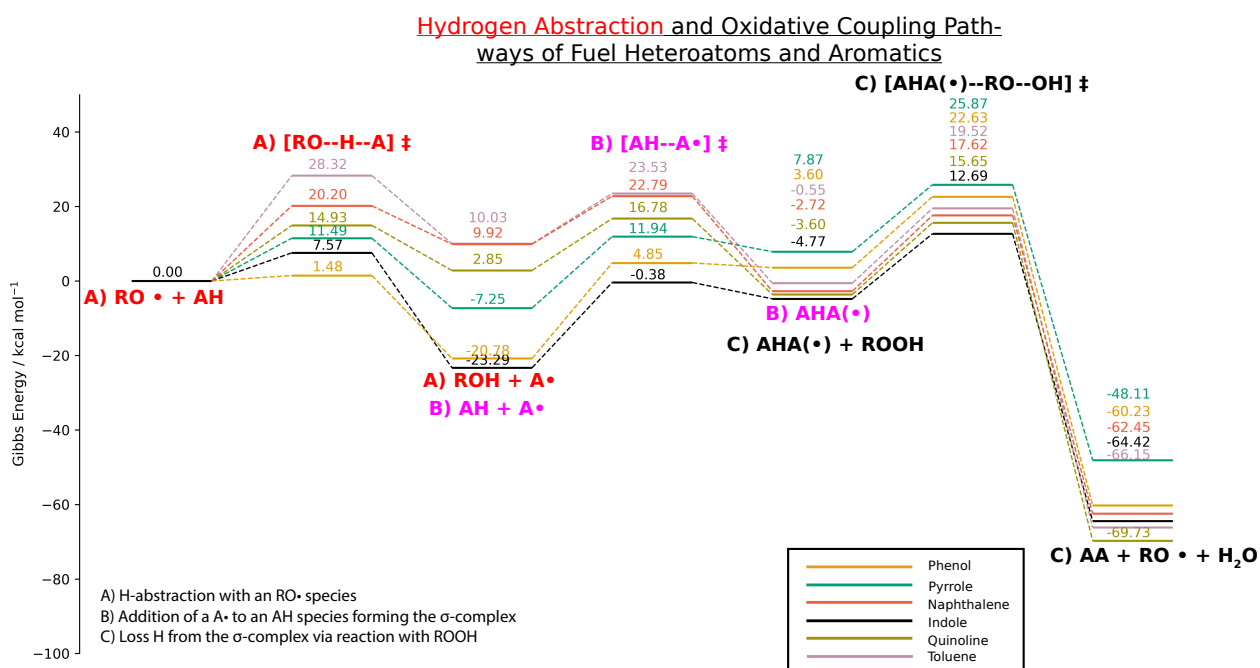


Figure 7.5: Growth to a deposit dimer for our chosen heteroatoms, calculated at the B3LYP-D3/cc-pVTZ *n*-dodecane PCM level of theory. The barriers were calculated from stable pre-reaction complexes. The R species was *n*-dodecane. The antioxidant species (phenol, indole and pyrrole) show exergonic H-abstraction in step A.

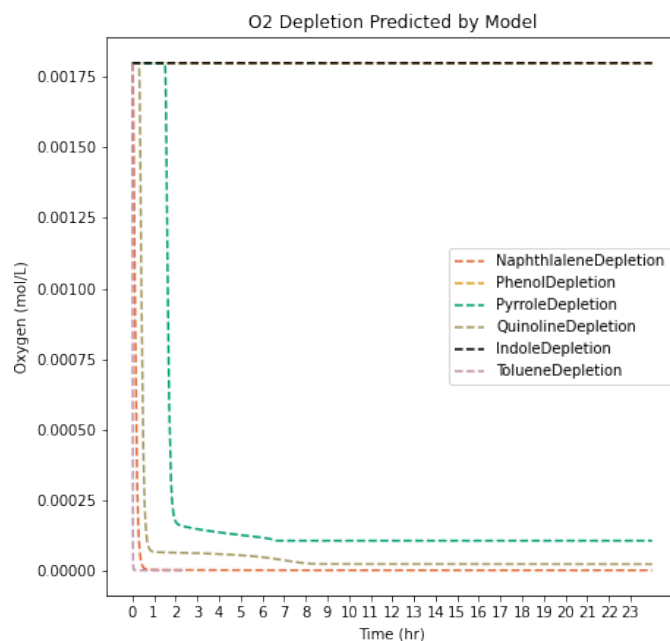
7.3.3.2 Comparison of Experimental Results and Psuedo-Detailed Models

Antioxidant Behavior

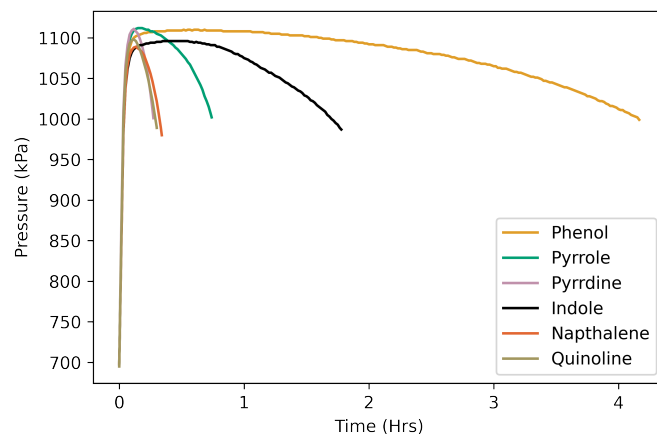
First, the antioxidant behavior of our surrogate fuels was explored in relation to our models. The O₂ depletion predicted by our model alongside the petroOxy depletion curves are presented in Figure 7.6. Although the petroOxy device cannot measure the O₂ depletion in the bulk, the device can be used to assess the antioxidant behavior of different fuels.[76] Our model successfully predicts that pyrrole, indole, and phenol are all antioxidant species, as shown by the increased induction period in the petroOxy curves. In addition, the petroOxy device indicates that indole and phenols are stronger antioxidants than pyrrole, which is also reflected in the O₂ depletion curves in our mechanism. However, the difference between indole and phenol in the petroOxy curves is not reflected in the mechanism. Nevertheless, this difference between the surrogates is better reflected in the AH + RO· abstraction barrier in Figure 7.5. Exploring the GCMS results for indole in our previous study, in Figure 10.22, no *n*-dodecane autoxidation products are observed after 8h. By contrast, pyrrole and quinoline both show lesser antioxidant qualities and lead to *n*-dodecane autoxidation products in Figure 5.7. Similarly, for our model, no oxygen is consumed leading to no autoxidation products.

Deposition Behavior

The amount of insoluble dimers predicted by our model compared with the total insolubles measured is presented in Figure 7.7. It should be noted that the comparison here is focused on the *correlation* between amount of dimers predicted, and total deposit produced by experiment. As a consequence, the correlation produced will reflect how well the model predicts deposition behavior. A quantitative comparison will require pathways beyond dimers to be calculated, which is beyond the scope of this study. The model predicts the insoluble formation behavior between our different surrogates well, with pyrrole producing the largest amounts of insolubles. Interestingly, phenol and indole are shown to produce the lowest amount of deposit in both our experiments and model. By contrast, in real fuels, indoles, and particularly phenol concentration are shown to correlate well with final insoluble mass.[65] A key difference between our simplified surrogates and real fuels are the synergistic effects between fuel classes, which are not captured in our two-component surrogates. In particular, sulfur is shown to interact strongly with 5-membered nitrogen



(a) O₂ Depletion Predicted by our model



(b) Petroxy depletion behavior

Figure 7.6: O₂ depletion behavior of our surrogate- comparison between model and experiment. The model shows the change in O₂ concentration over time. The petroOxy depletion curves show the change in headspace pressure, and although they are not a direct measure of O₂ depletion, they can differentiate between antioxidant qualities of different species.

heterocycles, and phenols with other nitrogen compounds.[63, 170] For example, in a simplified surrogate, previous work has shown trends between deposition propensity of 5- and 6-membered heterocycles break down, where quinoline-like compounds have shown to produce more deposit than indole compounds.[63] Nevertheless, the use of surrogates is still important to understand the chemical interactions within species classes.

Interestingly, in our experiment and models, toluene and naphthalene produced more insolubles than phenol and indole. This is interesting as fuel thermal degradation is often viewed as solely driven by heteroatoms.[24] Exploring the barriers for toluene and naphthalene in detail in Table 10.20, we see that lower barriers to the $AH + A \cdot \longrightarrow AHA \cdot$ reaction are found with the aromatic species. Sensitivity analysis (Figure 7.9) of our models suggests this coupling step is strongly related to the final insoluble mass. However, in a 2-component fuel, combining an antioxidant heteroatom and aromatic, the formation of aromatic insolubles will be significantly reduced due to the size of the H-abstraction barrier in comparison to the other heteroatoms used in this study (Figure 7.5). Instead, the heteroatom antioxidant class will form the majority of the $A \cdot$ radicals going on to form deposit. To strengthen this hypothesis, using our calculated values, a fuel model was built containing both phenol and toluene.

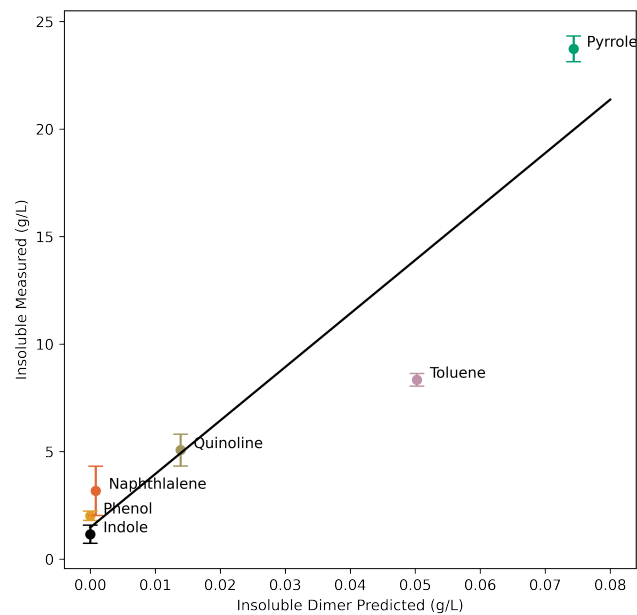
The effect of heteroatoms suppressing deposition from non-antioxidant species is demonstrated in Figure 7.8, where insolubles are generated from model fuels containing different ratios of toluene and phenol is tested. The model was built using the same BAS scheme base described in the section 7.2.4, with the addition of both toluene and phenol pathways. In this simplified model, toluene-derived insolubles are suppressed upon introduction of phenol. This effect can help explain why fuel deposits/insolubles often have an elemental composition of heteroatoms higher than conventional fuels also containing aromatic hydrocarbons.[33] Another interesting effect of blending is the peak in phenol insolubles at 25:75 phenol:toluene ratios above a 100% phenol mix, which implies that above a certain concentration, phenols will prevent the formation of insolubles. The peak concentration of hydroperoxide steadily drops at different % phenol concentrations, which is related to the extent the autoxidation chain is suppressed. The peak of phenol deposition could be related to the ROOH concentration, allowing more σ -intermediates to be re-aromatized. This shows our model can replicate the effect of changing concentrations of antioxidant

on total insolubles.

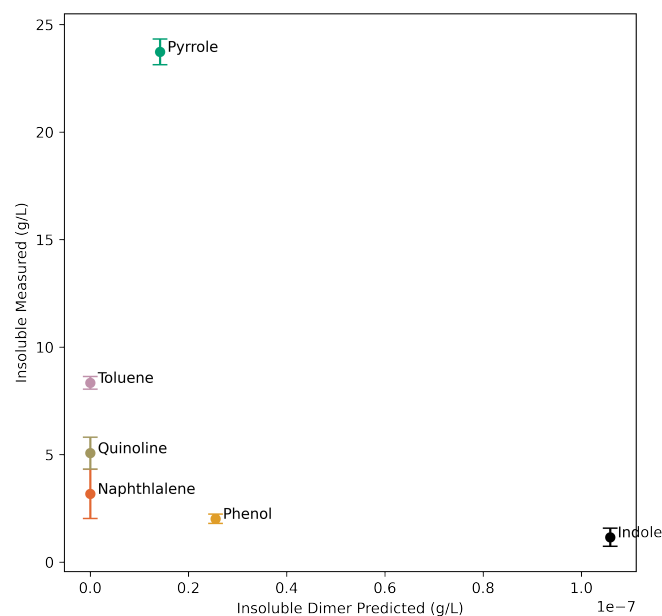
For some of the fuels the pseudo-detailed mechanisms reflect the behavior of 'peak' deposition temperature. The effect of temperature on the concentration of deposits for each mechanism is shown in section 10.6.5 of the Appendix. For quinoline, a peak deposition level is reached at 460K. Whereas for toluene, as the temperature increases the level of deposit decreases. All the other fuel models show an increase in concentration of deposit as the temperature rises. This demonstrates these deposit mechanisms can reflect the complex behavior of observed in real fuels of increasing and decreasing levels of deposit depending on fuel temperature.[370]

Finally, our results here lend credence to a HAS pathway leading to deposit. When the HAS pathway is removed from the mechanism in Figure 7.7b, no discernible trend is found between the formation of dimers and insolubles measured. In fact, the HAS pathway appears particularly important for species with low/no antioxidant tendency, but with a tendency to still form insolubles.

Sensitivity analysis of our bespoke mechanisms is presented in Figure 7.9. The reaction numbers cited here correspond to those given in Table 10.20. For our mechanisms, the reaction **29**, $A\cdot + AH \longrightarrow AHA\cdot$, has the largest influence on the level of deposit with the exception of phenol. Increasing the rate of reaction **29** leads to more $AHA\cdot$ species which can readily form deposit. Reaction **32**, $A\cdot + ROOH \longrightarrow AH + ROO\cdot$, removing hydroperoxides from the system also has an influence on the level of deposit. As the rate of reaction **32** increases, hydroperoxides are removed from the system leading to fewer $AHA\cdot + ROOH$ re-aromatization reactions leading to deposit dimers. The change of ROOH and insoluble concentration presented in Figure 7.10 demonstrates that as insolubles are produced ROOH is depleted. For all the species tested, the $RO\cdot$ (reaction **26**) and $R\cdot$ (reaction **27**) hydrogen abstraction steps have a large influence on the level of deposit, with faster rates leading to more $A\cdot$ species able to undergo coupling reactions. By contrast, the rate of the $ROO\cdot$ abstraction barrier (reaction **16**) has a negligible influence on deposition for most species because this reaction in general has high barriers already. Finally, for phenol, reaction **26**, $AH + R\cdot \longrightarrow A\cdot + RH$ also influences the formation of deposit more than the other species, and is more important than the coupling step (reaction **29**). This is likely because the termination pathway dominates the formation of deposits here, thus leading to a direct correlation between



(a) Correlation between mass of dimer predicted by our model and insolubles measured.



(b) Correlation between mass of dimer predicted by our model and insolubles measured when the HAS pathway is excluded.

Figure 7.7: Insoluble formation behavior- comparison between dimers predicted and total deposits in experiment. Temperature of the experiment and pseudo-detailed *n*-dodecane chemical mechanism containing the A and E_a values shown in Table 10.20. The temperature was set at 431 K both the model and the experiment. 211

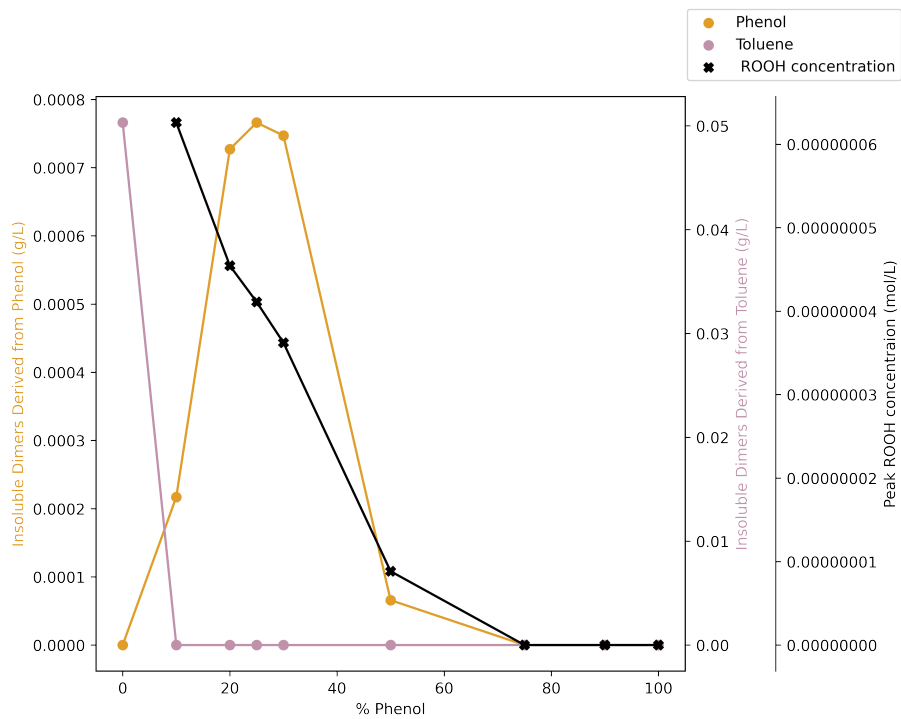


Figure 7.8: Effect of phenol % in a phenol toluene aromatic total of 0.1 mol L^{-1} on the insolubles derived from phenol and toluene.

the concentration of $A \cdot$ and the amount of deposit dimer.

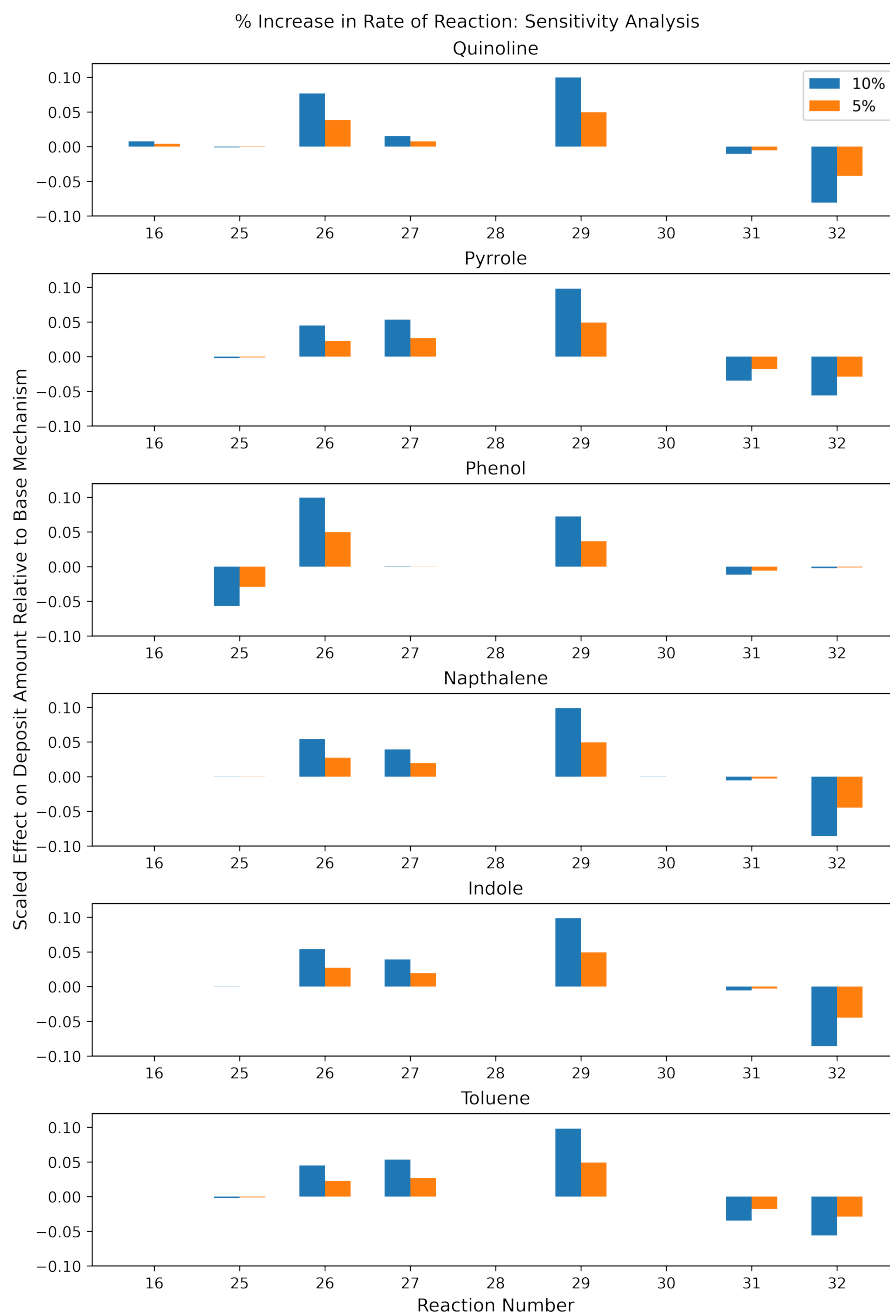


Figure 7.9: Sensitivity analysis of the bespoke insoluble pseudo-detailed mechanisms. For the sensitivity analysis, the rate of reaction is increased by a factor of 10% (blue) and 5% (orange) and the resultant increase in insolubles is shown relative to the base pseudo-detailed mechanism. The reaction number corresponds to Table 10.20 in the appendix

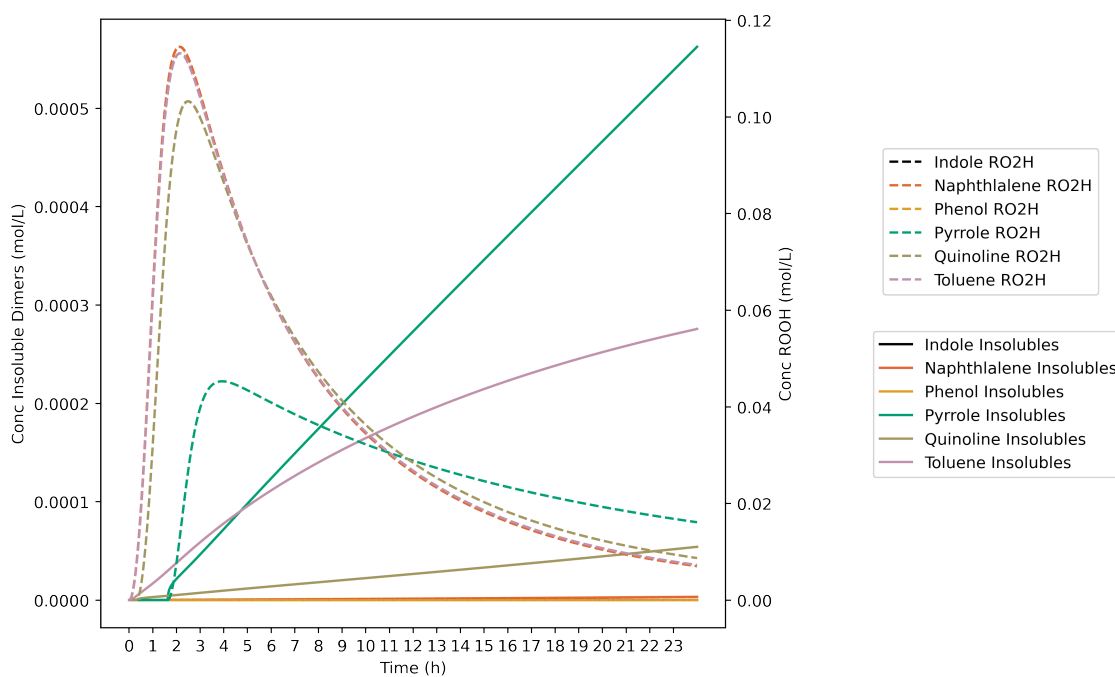


Figure 7.10: Change in the concentration of insolubles and ROOH over the course of the 24h pseudo-detailed models. The thick lines show the change in insoluble dimer concentration, whereas the dotted lines show the change in ROOH concentration. The results clearly show that for each species, as ROOH is depleted, the level insolubles begin to increase.

7.4 Implication for Fuels

The formation of fuel insolubles is influenced by both the H-abstraction and coupling propensity of the heteroatoms/aromatics present in fuel. By simplifying the insoluble formation process into the formation of dimers, we were able to show clear differences between the insoluble formation and antioxidant tendency between surrogate fuels. Nevertheless, the formation of dimers represents a small subsection of the insoluble/deposit structure. To expand the mechanism to reach an insolubles formation model which can provide a quantitatively accurate description, additional pathways need to be considered. This is a challenge, particularly as there are likely thousands of possible side reactions between and within species classes.[47] Even in our surrogate fuels, side reactions are likely to occur between AH and RH species, where the oxidation of *n*-dodecane is not significantly repressed. In fact, this is demonstrated when comparing the structure of insolubles found in the *n*-dodecane indole (Section 10.2.5) and quinoline deposits (Figure 5.9), where indole deposits are mostly indole-indole oligomers but quinoline deposits are composed in quinoline *n*-dodecane side reactions.

To address this challenge, several approaches using techniques benchmarked in this study can be used. The first approach involves scaling the deposit forming dimer steps to experimental deposit measurements. This would lead to a semi-empirical mechanism, which moves away from the first-principles approach using DFT. Nevertheless, the DFT thermochemical and kinetic parameters will allow the gross differences between species class and structure to be explored. This approach relies on the assumption that the formation of deposit dimers relates to a general property of 'coupling propensity'. Some preliminary calculations imply this assumption is generally correct, where a propanal doublet attacking various nitrogen compounds give barrier sizes (presented in Figure 10.49 in the appendix) in the same order of magnitude as the dimerization barriers for step B) in Figure 7.5.

A second, more computationally intensive approach, would be a set of high throughput calculations on additional deposit forming pathways. This approach would use HAS and termination reactions to calculate the pathways to various oligomers. Hansen solubility parameters will guide a 'cut-off' point for energetic pathways to oligomers to form insolubles. Nevertheless, insoluble species are still likely to react to form larger molecular weight species, which adds an additional challenge to this

approach.

7.5 Conclusions

The formation of insolubles in fuel is driven by coupling reactions between aromatics. In this work we have shown the importance of HAS in explaining the formation of these insolubles. DFT calculations revealed that the hydroperoxides play a key role in facilitating the HAS pathway. As a result of these findings, we showed that kinetic values calculated for a simplified two-component (dodecane and aromatic) surrogate can reveal differences in antioxidant and deposition tendency of different aromatics compared to the experiment. In addition, when the HAS pathway is excluded, the predicted deposition trends break down. Exploring the behavior of the mechanism further, we show that the addition of antioxidant to an antioxidant+aromatic model leads the suppression of insolubles composed of the aromatic. Instead, the antioxidant+aromatic model leads to insolubles only composed of the antioxidant. Finally, sensitivity analysis reveals that the formation of hydroperoxides ($\text{AH} + \text{ROO}\cdot \longrightarrow \text{A}\cdot + \text{ROOH}$) and the homolytic coupling ($\text{AH} + \text{A}\cdot \longrightarrow \text{AHA}\cdot$) have a strong influence on the final deposit mass.

Chapter 8

Discussion, Future Work and Conclusions

This discussion will revisit the key research questions identified from the literature search, evaluate how this thesis has answered these questions, and propose future directions for the work.

8.1 Key Research Questions

- **Can DFT successfully model the SMORS pathway?** Due to the deficiencies of the SMORS highlighted in the third section of the literature, is it possible to model the pathway using DFT methods? If the proposed pathway is unfeasible, what other routes to SMORS species can be conceived?
- **How do nitrogen and sulfur species interact synergistically in jet fuel?** There is still considerable debate as to how nitrogen and sulfur species in fuels. Can experimental and DFT techniques be used to help understand the mechanisms behind nitrogen and sulfur interactions in fuels?
- **How do oxidized fuel species interact with the heated walls to form the initial deposit layer?** Investigations into the early stages of deposition have been a challenge experimentally, can we use DFT methods to elucidate which species are likely involved with the early stages of deposition?
- **How can researchers approach constructing predictive deposition mechanisms with DFT methods?** The autoxidation stage of deposition has been modeled with DFT and integrated into pseudo-detailed mechanisms

with success. By contrast, the deposition process presents a significant challenge due to the complexity of reactions. Using simplistic surrogate fuels, how can DFT be related to the deposition process?

8.2 Summary of Each Chapter and Critical Evaluation of the Work

Chapter 4 focused on using DFT techniques to evaluate the widely cited SMORS mechanism. The first step in the SMORS mechanism, formation of phenols, the originally proposed concerted Russell Mechanism route was shown to be kinetically prohibited. Instead, DFT calculations suggested two competitive routes. The first route involved the decomposition of a tetraperoxide intermediate forming a hydrogen peroxide and two quinones. The second route involved the barrierless decomposition of the tetraperoxide, which yielded two hydroxy radicals and singlet oxygen. The two hydroxy radicals can then further react to form a p-chinole ($-OH$ species) and a quinone.

The next step of the proposed SMORS mechanism is the reaction between indole and quinone, proposed to occur via an electrophilic aromatic substitution (EAS) mechanism. The EAS reaction between quinone and indole could not be located with our DFT methods, and neither a water and *n*-dodecane solvation model could not stabilize the σ -intermediate generated in the EAS process. Instead, two alternative pathways were explored: 1) an acid catalyzed route and 2) a homolytic aromatic substitution (HAS) route. Our calculations offered plausible routes to indole-quinone coupling for both pathways. However, flask tests combined with LCMS analysis indicated that the addition of acid forming sulfur suppressed the formation of SMORS species, thus favoring the HAS proposal for indole-quinone coupling in fuels. As a consequence of these findings, a modified SMORS scheme is proposed. This chapter successfully answers the question: 'Can DFT successfully model the SMORS pathway?' by exploring the existing mechanism and proposing new mechanistic routes.

In the experimental work in chapter 4, several interesting nitrogen-sulfur compounds were detected by LCMS. Consequently, the flask oxidizer technique used in the SMORS chapter was chosen as a method for exploring nitrogen and sulfur interactions.

Chapter 5 explored the interaction of nitrogen and sulfur (N+S) compounds in fuel insoluble production using flask tests followed by GCMS, LCMS, and gravimetric analysis. LCMS analysis indicated that the addition of sulfur to indole (a common nitrogen compounds found in fuel) had two key effects. Firstly, deposition was accelerated by increased coupling between indoles, forming indole oligomers. Secondly, the structure of the insolubles changed, with sulfonated, sulfenylated, and alkylated indole oligomers detected as part of the gross structure. Each insoluble compound detected via LCMS was assessed with Hansen Solubility Parameters (HSP), to explore how the structure related to solubility. It was shown that sulfides and thiols had a similar distribution of structural classes, whereas the disulfides class produced acids below the detectable limits. Species from the sulfonated indoles structural class were suggested to form from SO₃ production via the decomposition of sulfonic acids arising from the oxidation of sulfur compounds. SO₃ is able to undergo EAS reactions with various N-compounds in *n*-dodecane via an autocatalytic route, identified by DFT calculations. A second product of the decomposition of sulfonic acids are alkenes. Reaction of alkenes with indoles could explain the presence of alkylated indole products detected in the flask, particularly as GCMS analysis of the solution indicated that the autoxidation in the bulk is suppressed by indole and sulfur compounds.

To expand the mechanistic work on nitrogen and sulfur interactions further, thiols were combined with pyrrole and quinolines in surrogates. For pyrroles, the addition of thiols greatly accelerated coupling. In the pure pyrrole flask, no coupling products were detected after 8 h of thermal stressing. By contrast, the addition of thiol led to the formation of many polypyrrole-like compounds, suggesting that thiols help accelerate coupling between pyrrole units. When pure quinoline was tested, several alkylated quinoline deposit structures were detected. However, when a thiol was added to quinoline, hazy deposits in the flask were detected as oxidized thiol and decomposed quinolines were found- but no coupling products were found. As a consequence of these findings, we proposed a mechanism based on the protonation of nitrogen compounds as a means to accelerate coupling. We acknowledge that protonation in inorganic solvents is precluded, and thus propose that water micelles may play a role here. Overall, the work in the chapter 5 helped elucidate new nitrogen-sulfur structures and proposes a new pathway to explain their synergistic deposition mechanism.

Extending the work on acids in fuel, the literature review identified that acids may also play a role in allowing deposits to bind to the wall. Chapter 6 uses plane-wave DFT methods to investigate the binding of indigenous and oxidized fuel compounds to stainless steel surfaces. A mixed termination and oxide modelling approach was used due to the heterogenous nature of stainless steel surfaces. Benchmarking showed that inclusion of dispersion in the DFT functional was essential for the calculation of accurate adsorption energies at the surface. The only species to chemisorb on the surface were the acids tested on the metal terminated surfaces. DFT calculations found that sulfonic acid bonded to metal terminated Cr_2O_3 had the largest adsorption energy out of all the termination and species combinations. The adsorption of the sulfur acids is generally characterized by dissociative bridging bidentate adsorption, with the exception of sulfonic acid on metal terminated Fe_2O_3 . Interestingly, ethanoic acids showed a larger adsorption energy for metal terminated Fe_2O_3 compared to Cr_2O_3 , suggestive that heteroatom-free fuels are likely to deposit at Cr depleted zones. Dissociation of acids in this work were calculated in a vacuum, and therefore did not require water micelles proposed for insoluble formation in chapter 5. The work in this chapter further highlights the importance of acids in the deposition process, and successfully pioneers a new DFT technique to investigate wall effects.

Building on the DFT methods in this thesis, moving away from purely mechanistic investigations, chapter 7 focused on using DFT techniques to *directly* predict the deposition behavior of different fuel chemistries. The HAS mechanism identified in chapter 4 as route to insolubles, was used as a base mechanism for the coupling of 6 different fuel aromatics and heteroatoms (toluene, naphthalene, pyrrole, indole, quinoline and phenol). Using DFT, for the 6 compounds, the barriers for the HAS mechanism to a dimer and hydrogen abstraction via dodecane $\text{R}\cdot$, $\text{RO}\cdot$ and $\text{ROO}\cdot$ were calculated. The barriers allowed for the creation of 6 compound dependent pseudo-detailed mechanisms, which were integrated into an existing pseudo-detailed mechanism for *n*-dodecane. To compare the mechanisms created, 6 surrogate fuels were tested in the petroxy as well as their insoluble producing tendency. Hansen solubility parameters were able to show that the successive coupling between our compounds led to insoluble particles in fuels. Each of the 6 fuels were stressed for 24h to produced insolubles. The DFT calculated pseudo-detailed mechanisms were able to predict the antioxidant behavior of surrogates demonstrated in the petroxy device, where phenols, indoles and pyrroles all showed antioxidant tendencies. This is

also reflected in our pseudo-detailed mechanisms, where the autoxidation mechanism is suppressed for indole and phenol, but not for quinoline. In addition, analysis of stressed surrogates tested in chapter 5 at the same conditions as our pseudo-detailed mechanisms showed *n*-dodecane autoxidation products for indole but not for quinoline.

The pseudo-detailed mechanisms also successfully predicted the differing deposition tendencies of the mono-component surrogates. When the HAS pathway was excluded from the pseudo-detailed mechanisms, the prediction of insoluble production tendency breaks down, which lends support to the inclusion of the HAS mechanism in the SMORS chapter. A more complex two-component mechanism was then built containing phenol and toluene, which showed that the addition of phenol completely suppressed toluene derived insoluble production, and instead the majority of the deposits were composed of phenol. The phenol deposition tendency peaked at a 25:75 phenol:toluene blend. Sensitivity analysis of these mechanisms suggests that both hydrogen abstraction steps for $R\cdot$ and $RO\cdot$ and coupling steps have a large influence on deposition tendency. However, the addition step $A\cdot + AH \longrightarrow AHA\cdot$ had the largest influence on deposition tendency for most fuels. Chapter 7 successfully shows how DFT can predict deposition behavior of simplified surrogate fuels based on starting chemistry.

8.3 Limitations and Future Work Directions

Chapter 4 focuses directly specifically on phenol and indole as model species for the DFT investigation. To validate the new generalized SMORS mechanism, future work should use a greater variety of compounds to explore the relationship between compound structure and ease of SMORS production. A larger body of calculations will enable fuel researchers to understand whether the SMORS mechanism can truly be generalized for phenol and nitrogen heterocycles. In addition, in order to be integrated into new predictive mechanisms, a larger kinetic dataset will allow for greater predictability a variety of fuel chemistries. Larger bodies of calculations can be achieved through high-throughput calculations, which are an increasingly popular technique to build large DFT datasets for complex reaction systems.[356, 371, 372]

Chapter 5 suffers a similar weakness to the first chapter in that it focused on a small fraction of compounds found in fuels. Nevertheless, the three nitrogen compounds and four sulfur compounds were chosen to represent species classes, where small structural changes (for example methyl groups) were assumed to not change the major chemical transformations within each class. This assumption should be tested in future investigations using similar LCMS techniques. In addition, the work here can be developed from a semi-quantitative to a quantitative investigation using internal standards.

The mechanism proposed in the chapter 5, where sulfur acids protonate nitrogen compounds to accelerate coupling, should be explored further. It is unclear exactly how protonation could occur in non-polar fuels. Nevertheless, doping fuels with deuterated acids would allow researchers to 'track' the protonation process of accelerating coupling. Additionally, the removal/addition of small amounts of water to fuels in a controlled environment will help to explore the idea of micelles offering a site for protonation to occur.

Moving to chapter 6, the plane-wave DFT techniques here present an exciting new avenue to investigate fuel deposition. Improving the work, a larger surface (which was precluded in our tests due to available resources) will allow researchers to differentiate high and low coverage scenarios for deposition. In addition, because our investigation is purely thermodynamic focused, a natural next step is the investigation of the kinetics of dissociative adsorption of acids on metal terminated surfaces using the nudged elastic band (NEB) method. Barriers calculated here will allow for deposition steps to be integrated explicitly in new pseudo-detail mechanisms.

Moving beyond the investigations into pure metal surfaces in chapter 6, the layering of deposit, characterized by interaction between deposited species and addition fuel species, presents a significant challenge. In contrast to the homogeneous crystalline nature of Fe_2O_3 and Cr_2O_3 , the carbonaceous deposit layer is almost certainly heterogeneous in composition.[177, 373]

Chapter 7, successfully uses DFT to predict deposition behavior tendency of different surrogates, but for a fuel-applicable mechanism exact quantitative deposition behavior needs to be reached. Reaching a mechanism with greater quantitative prediction will require the thousands of deposition pathways to be accounted for.

This presents a challenge with the computational and labor time to prepare each calculation. Nevertheless, as highlighted previously in this section, high-throughput calculations can offer a route to build these datasets. Additionally, structural variations within species classes can be assessed to see how they affect the kinetics of deposition, allowing for the class 'generalizability' to be evaluated. Due to the complexity of side reactions, and other synergistic contaminants like dissolved metals and sulfur compounds, the task of building a complete dataset using high throughput techniques is likely to preclude researchers for many years. As a consequence, in the short-term, a smaller dataset will allow for a more simplified but still chemistry specific model to be built.

8.4 Conclusion

This thesis has proposed new fuel thermal oxidative degradation pathways within the bulk and on heated surfaces, where experimental and DFT techniques have allowed new mechanisms to be proposed. In the bulk, the homolytic aromatic substitution (HAS) mechanism is found to play a role in the inter-species coupling and the formation of insolubles. Based on the HAS framework, new mechanisms and predictions were made using DFT calculations.

To explain the increased formation of deposit between nitrogen and sulfur species in the bulk, experimental work indicates that sulfur compounds act as catalysts and react directly with nitrogen species. Acids are proposed to play a role via protonation reactions, accelerating the rate of coupling. Acids were also shown to play a key role in the deposition step, where DFT calculations showed that acids readily chemisorb on stainless steel surfaces. These wall-DFT calculations indicated quantitative adsorption energies, where Cr_2O_3 offers the highest adsorption energies for sulfur acids and Fe_2O_3 surfaces the highest adsorption energies for carboxylic acids.

In the future, a wider variety of fuels will be employed as aviation continues to attempt to decarbonize. New sustainable fuels derived from bio and air capture sources will contain low/no heteroatoms. On the other hand, new crude oil deposits which will be exploited, will contain more heteroatoms. Adding to the complexity of the problem, it is expected both conventional and sustainable fuels will be blended.

These fuels will be subjected to increasing thermal stress, whilst engines burn hotter in an effort to increase thermal efficiency. For this reason, it is more essential than ever that a deeper chemical understanding of thermal oxidative stability is achieved. A deeper chemical understanding will lead to mechanisms with greater predictive capabilities, and ultimately a more sustainable and safer future for aviation.

Chapter 9

Published Work from this Thesis

- Understanding Thermal Stability of Future Jet Fuels Using Computational Chemistry *C. Adams, S. Blakey, A. Meijer, E. Alborzi, C. Parks* 3rd ECATS Conference, Making aviation environmentally sustainable. 2020
- Density Functional Study of the Deposition and Adsorption of Fuel Species on Stainless Steel *C. Adams, E. Alborzi, A. JHM Meijer, S. Blakey, M. Pourkashanian* IASH 2022, the 17th International Conference On The Stability, Handling and Use of Liquid Fuels. 2022
- Predicting the Insoluble Formation Tendencies of Fuel Heteroatoms and Aromatics with Computational Techniques *C. Adams, E. Alborzi, M. Conte, K. Hughes, A. JHM Meijer, S. Blakey, M. Pourkashanian* International Conference On The Stability, Handling and Use of Liquid Fuels. 2022
- **Submitted** Mechanistic Investigation Into The Formation of Insolubles in Bulk Fuel Jet Fuel Using Quantum Chemical and Experimental Techniques *C. Adams, E. Alborzi, A. JHM Meijer, K. Hughes, M. Pourkashanian* FUEL 2022

Bibliography

- [1] Organization of Petroleum Exporting Countries, “World Oil Outlook 2040,” 2017.
- [2] IEA, “Key World Energy Statistics,” *Statistics*, 2015.
- [3] United Nations, “Summary of the Paris Agreement,” *United Nations Framework Convention on Climate Change*, pp. 27–52, 2015.
- [4] O. US EPA, “Basic Information about Nonpoint Source (NPS) Pollution,” 2018.
- [5] I. Renewable Energy Agency, *Renewable Power Generation Costs in 2017*. 2018.
- [6] B. Khandelwal, A. Karakurt, P. R. Sekaran, V. Sethi, and R. Singh, “Hydrogen powered aircraft : The future of air transport,” *Progress in Aerospace Sciences*, vol. 60, pp. 45–59, jul 2013.
- [7] A. Yoshino, “The birth of the lithium-ion battery,” *Angewandte Chemie International Edition*, vol. 51, no. 24, pp. 5798–5800, 2012.
- [8] Chevron, “Aviation Fuels,” tech. rep., 2007.
- [9] IATA, “Economic Performance Of The Airline Industry Key Points,” tech. rep., 2018.
- [10] G. Liu, B. Yan, and G. Chen, “Technical review on jet fuel production,” *Renewable and Sustainable Energy Reviews*, vol. 25, pp. 59–70, 2013.
- [11] M. Bernabei, R. Reda, R. Galiero, and G. Bocchinfuso, “Determination of total and polycyclic aromatic hydrocarbons in aviation jet fuel,” *Journal of Chromatography A*, vol. 985, pp. 197–203, jan 2003.

- [12] E. Corporan, T. Edwards, L. Shafer, M. J. DeWitt, C. Klingshirn, S. Zabar-nick, Z. West, R. Striebich, J. Graham, and J. Klein, “Chemical, Thermal Stability, Seal Swell, and Emissions Studies of Alternative Jet Fuels,” *Energy & Fuels*, vol. 25, pp. 955–966, mar 2011.
- [13] Royce Rolls, *The Jet Engine*. 1996.
- [14] S. Blakey, L. Rye, and C. Willam Wilson, “Aviation gas turbine alternative fuels: A review,” 2011.
- [15] Shell, *The Aeroshell Book*. 12 ed., 2012.
- [16] S. Boichenko, O. Vovk, and A. Iakovlieva, “Chemical Technology Overview Of Innovative Technologies For Aviation Fuels Production,” Tech. Rep. 3, 2013.
- [17] J. I. Hileman, P. E. Donohoo, and R. W. Stratton, “Energy Content and Alternative Jet Fuel Viability,” *Journal of Propulsion and Power*, vol. 26, pp. 1184–1196, nov 2010.
- [18] M. Gómez-Carracedo, J. Andrade, M. Calviño, D. Prada, E. Fernández, and S. Muniategui, “Generation and mid-IR measurement of a gas-phase to predict security parameters of aviation jet fuel,” *Talanta*, vol. 60, pp. 1051–1062, jul 2003.
- [19] S. C. Pandey, D. K. Ralli, A. K. Saxena, and W. K. Alamkhan, “Physicochem-ical characterization and applications of naphtha,” tech. rep., 2004.
- [20] M. S. Stark, J. J. Wilkinson, J. R. L. Smith, A. Alfadhil, and B. A. Pochopien, “Autoxidation of Branched Alkanes in the Liquid Phase,” *Industrial & Engi-neering Chemistry Research*, vol. 50, pp. 817–823, jan 2011.
- [21] A. T. A. Group, “Beginner’s Guide to Aviation Biofuels. Edition 2,” 2011.
- [22] S. D. Anuar Sharuddin, F. Abnisa, W. M. A. Wan Daud, and M. K. Aroua, “A review on pyrolysis of plastic wastes,” *Energy Conversion and Management*, vol. 115, pp. 308–326, may 2016.
- [23] T. Kandaramath Hari, Z. Yaakob, and N. N. Binitha, “Aviation biofuel from renewable resources: Routes, opportunities and challenges,” *Renewable and Sustainable Energy Reviews*, vol. 42, pp. 1234–1244, 2014.

- [24] N. J. Kuprowicz, S. Zabarnick, Z. J. West, and J. S. Ervin, “Use of measured species class concentrations with chemical kinetic modeling for the prediction of autoxidation and deposition of jet fuels,” *Energy and Fuels*, vol. 21, no. 2, pp. 530–544, 2007.
- [25] J. Holladay, “Sustainable Aviation Fuel, Review of Technical Studies,” tech. rep., U. S. Department of Energy, 2020.
- [26] M. Dwyer, S. Blakey, E. Alborzi, and A. Meijer, “The role of hydrocarbon composition on the thermal stability of aviation fuels,” in *IASH 2017, the 15th International Symposium on Stability, Handling and Use of Liquid Fuels Rome*, no. September, 2017.
- [27] M. J. DeWitt, Z. West, S. Zabarnick, L. Shafer, R. Striebich, A. Higgins, and T. Edwards, “Effect of Aromatics on the Thermal-Oxidative Stability of Synthetic Paraffinic Kerosene,” *Energy & Fuels*, vol. 28, pp. 3696–3703, jun 2014.
- [28] R. Kamin and M. Ortman, “DoD Fuel Stability Program Program Drivers,” in *CRC conference*, no. May, 2019.
- [29] S. Zabarnick and D. K. Phelps, “Density functional theory calculations of the energetics and kinetics of jet fuel autoxidation reactions,” *Energy and Fuels*, vol. 20, no. 2, pp. 488–497, 2006.
- [30] Z. J. West, R. K. Adams, and S. Zabarnick, “Homogeneous catalysis of liquid-phase hydroperoxide decomposition in hydrocarbons,” *Energy and Fuels*, vol. 25, no. 3, pp. 897–904, 2011.
- [31] E. G. Jones, L. M. Balster, and W. J. Balster, “Autoxidation of aviation fuels in heated tubes: Surface effects,” *Energy and Fuels*, vol. 10, no. 3, pp. 831–836, 1996.
- [32] B. Beaver, L. Gao, C. Burgess-Clifford, and M. Sobkowiak, “On the mechanisms of formation of thermal oxidative deposits in jet fuels. Are unified mechanisms possible for both storage and thermal oxidative deposit formation for middle distillate fuels?,” *Energy and Fuels*, vol. 19, no. 4, pp. 1574–1579, 2005.
- [33] R. N. Hazlett, J. A. Schreifels, W. M. Stalick, R. E. Morris, and G. W. Mushrush, “Distillate fuel insolubles: formation conditions and characterization,” *Energy and Fuels*, vol. 5, no. 2, pp. 269–273, 1991.

- [34] S. S. Doliente, A. Narayan, J. F. D. Tapia, N. J. Samsatli, Y. Zhao, and S. Samsatli, “Bio-aviation Fuel: A Comprehensive Review and Analysis of the Supply Chain Components,” *Frontiers in Energy Research*, vol. 8, no. July, pp. 1–38, 2020.
- [35] W. F. Taylor and T. J. Wallace, “Kinetics of deposit formation from hydrocarbon fuels at high temperatures: General Features of the Process,” *Industrial and Engineering Chemistry Product Research and Development*, vol. 6, no. 4, pp. 258–262, 1967.
- [36] D. R. Clarke, M. Oechsner, and N. P. Pature, “Thermal-barrier coatings for more efficient gas-turbine engines,” *MRS Bulletin*, vol. 37, pp. 891–898, oct 2012.
- [37] . John M. Andrésen, James J. Strohm, , Lu Sun, and C. Song*, “Relationship between the Formation of Aromatic Compounds and Solid Deposition during Thermal Degradation of Jet Fuels in the Pyrolytic Regime,” 2001.
- [38] C. G. Kabana, S. Botha, C. Schmucker, C. Woolard, and B. Beaver, “Oxidative stability of middle distillate fuels. Part 1: Exploring the soluble macromolecular oxidatively reactive species (SMORS) mechanism with jet fuels,” *Energy and Fuels*, vol. 25, no. 11, pp. 5145–5157, 2011.
- [39] M. Jones, “Engine Fuel Filter Contamination,” *Aero Quarterly*, pp. 14–19, 2008.
- [40] S. P. Heneghan, S. Zabarnick, D. R. Ballal, and W. E. Harrison, “JP-8+100: The Development of High-Thermal-Stability Jet Fuel,” *Journal of Energy Resources Technology*, vol. 118, p. 170, sep 1996.
- [41] S. Zabarnick, “Chemical Kinetic Modeling of Jet Fuel Autoxidation and Antioxidant Chemistry,” *Industrial & Engineering Chemistry Research*, vol. 32, pp. 1012–1017, 1993.
- [42] P. Aksoy, G. Omer, R. Cetiner, D. A. Fonseca, M. Sobkowiak, S. Folcone-Miller, B. G. Miller, and B. Beaver, “Insight into the Mechanisms of Middle Distillate Fuel Oxidative Degradation . Part 2 : On the Relationship between Jet Fuel Thermal Oxidative Deposit, Soluble Macromolecular Oxidatively Reactive Species, and Smoke Point,” no. 8, pp. 2052–2055, 2009.

- [43] K. Qian, R. P. Rodgers, C. L. Hendrickson, M. R. Emmett, and A. G. Marshall, "Reading Chemical Fine Print: Resolution and Identification of 3000 Nitrogen-Containing Aromatic Compounds from a Single Electrospray Ionization Fourier Transform Ion Cyclotron Resonance Mass Spectrum of Heavy Petroleum Crude Oil," 2001.
- [44] V. R. Katta, E. G. Jones, and W. M. Roquemore, "Modeling of deposition process in liquid fuels," *Combustion science and technology*, vol. 139, no. 1, pp. 75–111, 1998.
- [45] X. Pei, L. Hou, and Z. Ren, "Flow Pattern Effects on the Oxidation Deposition Rate of Aviation Kerosene," *Energy and Fuels*, vol. 29, no. 9, pp. 6088–6094, 2015.
- [46] E. Ranzi, M. Dente, A. Goldaniga, G. Bozzano, and T. Faravelli, "Lumping procedures in detailed kinetic modeling of gasification, pyrolysis, partial oxidation and combustion of hydrocarbon mixtures," *Progress in Energy and Combustion Science*, vol. 27, no. 1, pp. 99–139, 2001.
- [47] M. Commodo, I. Fabris, C. P. T. Groth, and Ö. L. Gülder, "Analysis of aviation fuel thermal oxidative stability by electrospray ionization mass spectrometry (ESI-MS)," *Energy and Fuels*, vol. 25, no. 5, pp. 2142–2150, 2011.
- [48] M. Dwyer, *Investigating The Role Of Aviation Fuels Hydrocarbon Chemistry On Its Autoxidation*. PhD thesis, University of Sheffield, 2019.
- [49] E. N. Antonio, C. Wicking, S. Filip, M. P. Ryan, and S. Heutz, "Role of Iron Speciation in Oxidation and Deposition at the Hexadecane-Iron Interface," *ACS Applied Materials and Interfaces*, 2020.
- [50] G. w. Mushrush, "Fuel instability 1: Organo-sulfur hydroperoxide reactions," *Fuel science & technology international*, vol. 10, no. 9, pp. 1523–1560, 1992.
- [51] P. M. Rawson, R. L. Webster, D. Evans, and S. Abanteriba, "Contribution of sulfur compounds to deposit formation in jet fuels at 140 °C using a quartz crystal microbalance technique," *Fuel*, vol. 231, no. May, pp. 1–7, 2018.
- [52] D. W. Naegeli, "The role of sulfur in the thermal stability of jet fuel," in *Proceedings of the ASME Turbo Expo*, vol. 2, 1999.

- [53] L. A. van Bergen, G. Roos, and F. De Proft, "From thiol to sulfonic acid: Modeling the oxidation pathway of protein thiols by hydrogen peroxide," *The journal of physical chemistry A*, vol. 118, no. 31, pp. 6078–6084, 2014.
- [54] C. M. Parks, A. J. Meijer, S. G. Blakey, E. Alborzi, and M. Pourkashanian, "Computational studies on the reactions of thiols, sulfides and disulfides with hydroperoxides. Relevance for jet fuel autoxidation," *Fuel*, vol. 316, no. January, p. 123326, 2022.
- [55] E. Alborzi, C. M. Parks, P. Gadsby, A. Sheikhansari, S. G. Blakey, and M. Pourkashanian, "Effect of Reactive Sulfur Removal by Activated Carbon on Aviation Fuel Thermal Stability," *Energy and Fuels*, vol. 34, no. 6, pp. 6780–6790, 2020.
- [56] A. P. Watkinson and D. I. Wilson, "Chemical Reaction Fouling: A Review," tech. rep., 1997.
- [57] J. Voigt, "Atmospheric Oxidation and Antioxidants.," *Angewandte Chemie*, vol. 78, pp. 1027–1027, nov 1966.
- [58] N. M. Emanuel, E. T. Denisov, Z. K. Maizus, N. M. Emanuel, *et al.*, "Liquid-phase oxidation of hydrocarbons," 1967.
- [59] I. Hermans, J. Peeters, and P. A. Jacobs, "Autoxidation of ethylbenzene: The mechanism elucidated," *Journal of Organic Chemistry*, vol. 72, pp. 3057–3064, apr 2007.
- [60] C. J. Hammond, J. R. Lindsay Smith, E. Nagatomi, M. S. Stark, and D. J. Waddington, "A mechanistic study of the liquid phase autoxidation of nonan-5-one," *New Journal of Chemistry*, vol. 30, no. 5, pp. 741–750, 2006.
- [61] Z. Liu, S. Tang, Z. Li, Z. Qin, S. Yuan, L. Wang, L. Wang, X. Zhang, and G. Liu, "An improved kinetic model for deposition by thermal oxidation of aviation hydrocarbon fuels," *Fuel*, vol. 258, no. June, p. 116139, 2019.
- [62] S. P. Heneghan and S. Zabarnick, "Oxidation of jet fuels and the formation of deposit," *Fuel*, vol. 73, pp. 35–43, jan 1994.
- [63] S. Zabarnick, Z. J. West, L. M. Shafer, S. S. Mueller, R. C. Striebich, and P. J. Wrzesinski, "Studies of the role of heteroatomic species in jet fuel thermal

- stability: model fuel mixtures and real fuels,” *Energy and Fuels*, vol. 33, no. 9, pp. 8557–8565, 2019.
- [64] A. A. Oswald and F. Noel, “Role of Pyrroles in Fuel Instability,” *Journal of Chemical and Engineering Data*, vol. 6, no. 2, pp. 294–301, 1961.
- [65] L. M. Balster, S. Zabarnick, R. C. Striebich, L. M. Shafer, and Z. J. West, “Analysis of polar species in jet fuel and determination of their role in autoxidative deposit formation,” *Energy and Fuels*, vol. 20, no. 6, pp. 2564–2571, 2006.
- [66] K. M. Christison, R. M. Lorenz, L. Xue, and O. D. Sparkman, “Exploring the Molecular Origin of Jet Fuel Thermal Oxidative Instability through Statistical Analysis of Mass Spectral Data,” *Energy and Fuels*, vol. 33, no. 2, pp. 830–836, 2019.
- [67] M. N. Siddiquee and A. de Klerk, “Heterocyclic Addition Reactions during Low Temperature Autoxidation,” *Energy & Fuels*, vol. 29, pp. 4236–4244, jul 2015.
- [68] R. Epping, S. Kerkerling, and J. T. Andersson, “Influence of different compound classes on the formation of sediments in fossil fuels during aging,” *Energy and Fuels*, vol. 28, no. 9, pp. 5649–5656, 2014.
- [69] R. E. Kauffman, “The effects of different sulfur compounds on jet fuel oxidation and deposition,” in *Proceedings of the ASME Turbo Expo*, vol. 3, 1995.
- [70] D. R. Kendall and J. S. Mills, “Thermal Stability of Aviation Kerosines: Techniques To Characterize Their Oxidation Properties,” vol. 25, no. 3, pp. 83–108, 1986.
- [71] S. Zabarnick, P. Zelesnik, and R. R. Grinstead, “Jet Fuel Deposition and Oxidation: Dilution, Materials, Oxygen, and Temperature Effects,” tech. rep., 1996.
- [72] E. A. Klavetter, S. J. Martin, and K. . Wessendorf, “Monitoring Jet Fuel Thermal Stability Using a Quartz Crystal Microbalance,” tech. rep., 1993.
- [73] D. ASTM, “7545-14. standard test method for oxidation stability of middle distillate fuels—rapid small scale oxidation test (rssot),” *West Conshohocken (PA): ASTM International*, 2014.

- [74] T. Jia, L. Pan, S. Gong, J. Xie, X. Wang, Y. Fang, J. J. Zou, and X. Zhang, “Mechanistic insights into the thermal deposition of highly thermal-stable jet fuel,” *Fuel*, vol. 276, no. May, p. 118100, 2020.
- [75] K. Bacha, A. Ben-Amara, A. Vannier, M. Alves-Fortunato, and M. Nardin, “Oxidation stability of diesel/biodiesel fuels measured by a petrooxy device and characterization of oxidation products,” *Energy and Fuels*, vol. 29, no. 7, pp. 4345–4355, 2015.
- [76] E. Alborzi, M. R. Dwyer, C. M. , A. Sheikhsari, D. C. Mielczarek, M. Zanganeh, A. J. Meijer, S. G. Blakey, and M. Pourkashanian, “Construction of a reduced chemical kinetic mechanism for autoxidation of n-paraffinic solvent – A model for aviation fuel,” *Fuel*, vol. 294, no. January, p. 120170, 2021.
- [77] T. Jia, M. Zhao, L. Pan, C. Deng, J.-j. Zou, and X. Zhang, “Effect of phenolic antioxidants on the thermal oxidation stability of high-energy-density fuel,” *Chemical Engineering Science*, p. 117056, 2021.
- [78] T. Duangthip and J. S. Ervin, “Simulations of Jet Fuel Thermal Oxidative Degradation: Part I. The Effect of Metal Surface Catalysis on the Thermal Oxidation of Jet Fuel,” tech. rep., 2006.
- [79] Jamie S. Ervin, Thomas A. Ward, Theodore F. Williams, , and J. Bento, “Surface Deposition within Treated and Untreated Stainless Steel Tubes Resulting from Thermal-Oxidative and Pyrolytic Degradation of Jet Fuel,” 2003.
- [80] E. Alborzi, P. Gadsby, M. S. Ismail, A. Sheikhsari, M. R. Dwyer, A. J. H. M. Meijer, S. G. Blakey, and M. Pourkashanian, “Comparative study of the effect of fuel deoxygenation and polar species removal on jet fuel surface deposition,” *Energy & Fuels*, vol. 33, no. 3, pp. 1825–1836, 2019.
- [81] E. G. Jones, W. J. Balster, and M. E. Post, “Degradation of a Jet A Fuel in a Single-Pass Heat Exchanger,” *Journal of Engineering for Gas Turbines and Power*, vol. 117, no. 1, p. 125, 1993.
- [82] W. A. Rubey, R. C. Striebich, M. D. Tissandier, D. A. Tirey, and S. D. Anderson, “Gas Chromatographic Measurement of Trace Oxygen and Other Dissolved Gases in Thermally Stressed Jet Fuel,” *Journal of Chromatographic Science*, vol. 33, pp. 433–437, aug 1995.

- [83] Z. J. West, S. Zabarnick, and R. C. Striebich, "Determination of hydroperoxides in jet fuel via reaction with triphenylphosphine," *Industrial & Engineering Chemistry Research*, vol. 44, no. 10, pp. 3377–3383, 2005.
- [84] D. R. Hardy and M. A. Wechter, "Characterization of Soluble Macromolecular Oxidatively Reactive Species (SMORS) from Middle Distillate Diesel Fuels: Their Origin and Role in Instability," *Energy and Fuels*, vol. 8, no. 3, pp. 782–787, 1994.
- [85] R. C. Striebich, J. Contreras, L. M. Balster, Z. West, L. M. Shafer, and S. Zabarnick, "Identification of polar species in aviation fuels using multidimensional gas chromatography-time of flight mass spectrometry," *Energy and Fuels*, vol. 23, no. 11, pp. 5474–5482, 2009.
- [86] A. D. Smith, "Analysis Of Fouling Rate And Propensity For Eight Crude Oil Samples In Annular Test Section," in *International Conference on Heat Exchanger Fouling and Cleaning - 2013*, vol. 2013, pp. 1–8, 2013.
- [87] C. Panchal and A. Watkinson, "Development of an analytical model for organic-fluid fouling," tech. rep., Argonne National Laboratory (ANL), Argonne, IL, oct 1994.
- [88] D. L. Daggett, A. Veninger, C. Lewis, S. Bullock, and R. Kamin, "The Development of an Aviation Fuel Thermal Stability Test Unit," tech. rep., 1995.
- [89] E. Alborzi, S. Blakey, H. Ghadbeigi, C. Pinna, and C. Lewis, "Investigation of surface deposition in a simulated fuel injector feed arm with sudden expansion/contraction," *Fuel*, vol. 186, pp. 534–543, 2016.
- [90] E. Alborzi, S. Blakey, H. Ghadbeigi, and C. Pinna, "Prediction of growth of jet fuel autoxidative deposits at inner surface of a replicated jet engine burner feed arm," *Fuel*, vol. 214, pp. 528–537, 2018.
- [91] G. L. Dieterle and K. E. Binns, "Extended Duration Thermal Stability Test of Improved Thermal Stability Jet Fuels," in *International Gas Turbine and Aeroengine Congress and Exposition*, p. V003T06A013, 1995.
- [92] A. J. Varandas, "CBS extrapolation of Hartree-Fock energy: Pople and Dunning basis sets hand-to-hand on the endeavour," *Physical Chemistry Chemical Physics*, vol. 21, no. 15, pp. 8022–8034, 2019.

- [93] R. Paton, I. Funes-Ardoiz, G. Luchini, J. V. Alegre-Requena, and Y. Guan, “patonlab/goodvibes: Calculate quasi-harmonic free energies from gaussian output files with temperature and other corrections.”
- [94] C. M. Parks, E. Alborzi, S. G. Blakey, A. J. Meijer, and M. Pourkashanian, “Density Functional Theory Calculations on Copper-Mediated Peroxide Decomposition Reactions: Implications for Jet Fuel Autoxidation,” *Energy and Fuels*, vol. 34, no. 6, pp. 7439–7447, 2020.
- [95] D. C. Mielczarek, M. Matrat, A. B. Amara, Y. Bouyou, P. Wund, and L. Starck, “Toward the accurate prediction of liquid phase oxidation of aromatics: A detailed kinetic mechanism for toluene autoxidation,” *Energy & Fuels*, vol. 31, no. 11, pp. 12893–12913, 2017.
- [96] I. Coordinating Research Council, “Coordinating Support Of Fuels And Lubricant Research And Development (R & D),” *Handbook of Aviation Fuel Properties*, no. Third Edition, 2004.
- [97] G. E. Fedor and D. W. Naegeli, “Peroxide Formation In Jet Fuels,” pp. 1267–1276, 1988.
- [98] J. S. Ervin and T. F. Williams, “Dissolved Oxygen Concentration and Jet Fuel Deposition,” tech. rep., 1996.
- [99] M. A. Roan and A. L. Boehman, “The Effect of Fuel Composition and Dissolved Oxygen on Deposit Formation from Potential JP-900 Basestocks,” 2004.
- [100] E. T. Denisov and I. B. Afanas’ ev, *Oxidation and antioxidants in organic chemistry and biology*. CRC press, 2005.
- [101] N. M. N. M. Emanuel, G. E. G. E. Zaikov, and Z. K. Z. K. Maizus, *Oxidation of organic compounds : medium effects in radical reactions*. Elsevier Science, 1984.
- [102] J. Igarashi, R. K. Jensen, J. Lusztyk, S. Korcek, and K. U. Ingold, “Autoxidation of alkylnaphthalenes. 2. Inhibition of the autoxidation of n-hexadecane at 160.degree.C,” *Journal of the American Chemical Society*, vol. 114, pp. 7727–7736, sep 1992.

- [103] V. L. Singleton, "Oxygen with phenols and related reactions in musts, wines, and model systems: Observations and practical implications," *American Journal of Enology and Viticulture*, vol. 38, no. 1, pp. 69–77, 1987.
- [104] B.-Z. Zhu, H.-T. Zhao, B. Kalyanaraman, J. Liu, G.-Q. Shan, Y.-G. Du, and B. Frei, "Mechanism of metal-independent decomposition of organic hydroperoxides and formation of alkoxy radicals by halogenated quinones.," *Proceedings of the National Academy of Sciences of the United States of America*, vol. 104, pp. 3698–702, mar 2007.
- [105] R. L. Webster, D. J. Evans, P. M. Rawson, B. S. Mitrevski, and P. J. Marriott, "Oxidation of neat synthetic paraffinic kerosene fuel and fuel surrogates: Quantitation of dihydrofuranones," *Energy and Fuels*, vol. 27, pp. 889–897, feb 2013.
- [106] R. L. Webster, P. M. Rawson, C. Kulsing, D. J. Evans, and P. J. Marriott, "Investigation of the Thermal Oxidation of Conventional and Alternate Aviation Fuels with Comprehensive Two-Dimensional Gas Chromatography Accurate Mass Quadrupole Time-of-Flight Mass Spectrometry," *Energy and Fuels*, vol. 31, no. 5, pp. 4886–4894, 2017.
- [107] E. Engelmann, G. Just, W. Pritzkow, M. Rudolf, G. Spindler, T. D. Tien, V. Voerckel, and V. Wittekind, "Kinetic Modelling of the Oxidation of Medium Paraffins further evidence for the importance of bifunctional intermediates," *Journal für Praktische Chemie*, vol. 328, no. 4, pp. 484–487, 1986.
- [108] K. Chatelain, A. Nicolle, A. Ben Amara, L. Catoire, and L. Starck, "Wide range experimental and kinetic modeling study of chain length impact on n-alkanes autoxidation," *Energy & Fuels*, vol. 30, no. 2, pp. 1294–1303, 2016.
- [109] S. P. Heneghan, S. Zabarnick, D. R. Ballal, and W. E. Harrison, "JP-8+100: The Development of High-Thermal-Stability Jet Fuel," *Journal of Energy Resources Technology*, vol. 118, p. 170, sep 2008.
- [110] W. F. Taylor, "Kinetics Of Deposit Formation From Hydrocarbons," *Ind. Eng. Chem. Prod. Res. Dev.*, vol. 8, pp. 375–380, 1969.
- [111] W. A. Yehye, N. A. Rahman, A. Ariffin, S. B. Abd Hamid, A. A. Alhadi, F. A. Kadir, and M. Yaeghoobi, "Understanding the chemistry behind the antioxidant activities of butylated hydroxytoluene (BHT): A review," aug 2015.

- [112] P. J. Marteney and L. J. Spadaccini, “Thermal Decomposition of Aircraft Fuel.pdf,” vol. 108, no. October 1986, 1986.
- [113] J. S. Chin and A. H. Lefebvre, “Influence of Flow Conditions on Deposits From Heated Hydrocarbon Fuels,” *Journal of Engineering for Gas Turbines and Power*, vol. 115, p. 433, jun 1992.
- [114] T. Bott, *Fouling of Heat Exchangers*. 1995.
- [115] D. C. Mielczarek, *Autoxidation behaviour of hydrocarbons in the context of conventional and alternative aviation fuels*. PhD thesis, University of Leeds, 2015.
- [116] F. M. White, *Fluid Dynamics*. No. 7, 2010.
- [117] L. J. Spadaccini, D. R. Sobel, and H. Huang, “Deposit Formation and Mitigation in Aircraft Fuels,” *Journal of Engineering for Gas Turbines and Power*, vol. 123, no. 4, p. 741, 1999.
- [118] P. Gadsby, “Surface Roughness Effects on Thermally Stressed Aviation Fuel,” 2018.
- [119] F. R. Brown and F. S. Karn, “Stability studies of coal-derived liquids,” vol. 59, pp. 431–435, 1980.
- [120] J. Czarnocka and M. Odziemkowska, “Diesel fuel degradation during storage proces,” *Chemik*, vol. 69, no. 11, pp. 771–776, 2015.
- [121] S. Zabarnick, “Chemical Kinetic Modeling of Jet Fuel Autoxidation and Antioxidant Chemistry,” *Industrial and Engineering Chemistry Research*, vol. 32, no. 6, pp. 1012–1017, 1993.
- [122] J. Lee, Y. Lee, and E. Choe, “Temperature dependence of the autoxidation and antioxidants of soybean, sunflower, and olive oil,” *European Food Research and Technology*, vol. 226, no. 1-2, pp. 239–246, 2007.
- [123] W. J. Balster and E. G. Jones, “Effects of temperature on formation of insolubles in aviation fuels,” *Proceedings of the ASME Turbo Expo*, vol. 2, no. April 1998, pp. 289–293, 1997.

- [124] X. Y. Pei and L. Y. Hou, "Effect of dissolved oxygen concentration on coke deposition of kerosene," *Fuel Processing Technology*, vol. 142, no. 3, pp. 86–91, 2016.
- [125] W. F. Taylor and J. W. Frankenfeld, "Development of high stability fuel," tech. rep., Exxon Research And Engineering Co Linden Nj Government Research Lab, 1976.
- [126] K. Zhu, Z. Tao, G. Xu, and Z. Jia, "Surface deposition characteristics of supercritical kerosene rp-3 fuel within treated and untreated stainless-steel tubes. part 1: Short thermal duration," *Energy & Fuels*, vol. 30, no. 4, pp. 2687–2693, 2016.
- [127] R. N. Hazlett, A. J. Power, A. G. Kelso, and R. K. Solly, "Chemistry of Deposit Fomration in Distillate Fuels," tech. rep., 1986.
- [128] "Coordinating Support Of Fuels And Lubricant Research And Development (R&D) 2 Delivery Order 0002: Handbook of Aviation Fuel Properties-2004 Third Edition Propulsion Directorate Air Force Materiel Command Air Force Research Laboratory Wright-patterson Air Force Base, OH 45433-7251," tech. rep., 2004.
- [129] Ministry of Defence, "Turbine Fuel , Kerosine Type , Jet A-1 NATO Code : F-35 Joint Service Designation : AVTUR," *Defence Standard 91-91*, no. 7, 2011.
- [130] S. I. Tseregounis, "Effects of sulfur chemistry on deposits derived from a gasoline oxidized at 100°C," *SAE Technical Papers*, 1990.
- [131] J. M. Watkins, G. W. Mushrush, R. N. Hazlett, and E. J. Beal, "Hydroperoxide Formation and Reactivity in Jet Fuels," *Energy and Fuels*, vol. 3, no. 2, pp. 231–236, 1989.
- [132] J. C. W. Chien and C. R. Boss, "Sulfur Compounds as Antioxidants," *Jorunal of Polymer Science*, vol. 10, no. 7, pp. 1579–1599, 1972.
- [133] S. Oae and J. Doi, *Organic Sulfur Chemistry*, vol. 2. CRC Press, 1991.
- [134] F. H. Seubold and W. E. Vaughan, "Acid-catalyzed Decomposition of Cumene Hydroperoxide," *Journal of the American Chemical Society*, vol. 75, no. 15, pp. 3790–3792, 1953.

- [135] L. A. Van Bergen, G. Roos, and F. De Proft, "From thiol to sulfonic acid: Modeling the oxidation pathway of protein thiols by hydrogen peroxide," *Journal of Physical Chemistry A*, vol. 118, no. 31, pp. 6078–6084, 2014.
- [136] S. M. Deneke, "Thiol-based antioxidants," *Current Topics in Cellular Regulation*, vol. 36, no. C, pp. 151–180, 2001.
- [137] L. E. Netto, H. Z. Chae, S. W. Kang, S. G. Rhee, and E. R. Stadtman, "Removal of hydrogen peroxide by thiol-specific antioxidant enzyme (TSA) is involved with its antioxidant properties. TSA possesses thiol peroxidase activity," *Journal of Biological Chemistry*, vol. 271, no. 26, pp. 15315–15321, 1996.
- [138] N. Kharasch and C. Y. Meyers, *The Chemistry of Organic Sulfur Compounds*. Elsevier, 2013.
- [139] G. W. Mushrush, E. J. Beal, E. Slone, and D. R. Hardy, "Reaction of organosulfur compounds with naturally occurring peroxides in jet fuel," *Energy and Fuels*, vol. 10, no. 2, pp. 504–508, 1996.
- [140] G. W. Mushrush, R. N. Hazlett, D. R. Hardy, and J. M. Watkins, "Liquid-Phase Oxidation of Hexyl Sulfide and Dodecanethiol by tert -Butyl Hydroperoxide in Benzene and Tetradecane," *Industrial and Engineering Chemistry Research*, vol. 26, no. 4, pp. 662–667, 1987.
- [141] G. W. Mushrush, R. E. Pellenbarg, D. R. Hardy, G. W. Mushrush, and R. N. Hazlett, "Role of Sulfur Compounds in Fuel Instability: A Model Study of the Formation of Sulfonic Acids from Hexyl Sulfide and Hexyl Disulfide," *Energy and Fuels*, vol. 5, no. 2, pp. 258–262, 1991.
- [142] W. F. Taylor and T. J. Wallace, "Kinetics of deposit formation from hydrocarbons: Effect of Trace Sulfur Compounds," *Industrial and Engineering Chemistry Product Research and Development*, vol. 7, no. 3, pp. 198–202, 1968.
- [143] E. J. Powers and W. T. Wotring, "Stabilization of No. 2 Fuel Oils With Caustic Treating and Additives.," *ASTM Special Technical Publication*, no. 2, pp. 92–102, 1981.
- [144] A. F. Sauer, R. W. Weed and C. E. Headington, "Mechanism for organic sediment formation in heating oils," Aug 1958.

- [145] F. R. Mayo and B. Y. Lan, “Gum and deposit formation from jet turbine and diesel fuels at 130.degree.C,” *Industrial Engineering Chemistry Product Research and Development*, vol. 25, pp. 333–348, jun 1986.
- [146] J. W. Frankenfeld, W. F. Taylor, and D. W. Brinkman, “Storage stability of synfuels from oil shale. 1. general features of sediment formation in model fuel systems,” *Industrial & engineering chemistry product research and development*, vol. 22, no. 4, pp. 608–614, 1983.
- [147] D. W. Naegeli, U. S. N. A. Administration, and Space, *Thermal stability of jet fuels kinetics of forming deposit precursors : final report, NASA contract no. NAG 3-1739*. 1997.
- [148] D. R. Hardy and M. A. Wechter, “Insoluble sediment formation in middle distillate diesel fuel: further evidence concerning the role of in situ fuel acidity,” *Fuel*, vol. 69, no. 6, pp. 720–724, 1990.
- [149] M. A. Wechter and D. R. Hardy, “Effects of dodecylbenzenesulfonic acid on insolubles production in mid-distillate diesel fuel blends,” *Energy and Fuels*, vol. 10, no. 1, pp. 117–120, 1996.
- [150] S. R. Daniel and F. C. Heneman, “Deposit formation in liquid fuels 4. Effect of selected organo-sulphur compounds on the stability of Jet A fuel,” tech. rep., 1983.
- [151] M. McCollom, *Assessing diesel fuel stability : a predictive approach*. PhD thesis, 2020.
- [152] D. D. Link, J. P. Baltrus, K. S. Rothenberger, P. Zandhuis, D. K. Minus, and R. C. Striebich, “Class-and structure-specific separation, analysis, and identification techniques for the characterization of the sulfur components of JP-8 aviation fuel,” *Energy and Fuels*, vol. 17, no. 5, pp. 1292–1302, 2003.
- [153] V. V. Lobodin, W. K. Robbins, J. Lu, and R. P. Rodgers, “Separation and Characterization of Reactive and Non-Reactive Sulfur in Petroleum and Its Fractions,” *Energy and Fuels*, vol. 29, no. 10, pp. 6177–6186, 2015.
- [154] G. W. Mushrush, E. J. Beal, J. M. Hughes, S. E. Bonde, W. L. Gore, and G. E. Dolbear, “Stability studies of a jet fuel containing no organo-sulfur compounds,” *Petroleum Science and Technology*, vol. 20, no. 5-6, pp. 561–570, 2002.

- [155] L. Jones and N. C. Li, "Ageing of SRC II middle distillate from Illinois No. 6 coal," *Fuel*, vol. 62, no. 10, pp. 1156–1160, 1983.
- [156] W. F. Taylor and J. W. Frankenfeld, "Deposit Formation from Deoxygenated Hydrocarbons. 3. Effects of Trace Nitrogen and Oxygen Compounds," *Industrial and Engineering Chemistry Product Research and Development*, vol. 17, no. 1, pp. 86–90, 1978.
- [157] L. S. Helmick and G. T. Seng, "FTIR ANALYSIS OF AVIATION FUEL DEPOSITS.," *NASA Technical Memorandum*, 1984.
- [158] Z. West, "Fuel System Surface Deposits : Perspective & Preliminary Characterization Industry Concerns : ' Water Soluble Deposits '," in *CRC Aviation Meeting*, pp. 1–20, 2019.
- [159] S. Zabarnick and R. R. Grinstead, "Studies of Jet Fuel Additives using the Quartz Crystal Microbalance and Pressure Monitoring at 140 °C," *Industrial and Engineering Chemistry Research*, vol. 33, no. 11, pp. 2771–2777, 1994.
- [160] S. Kerkering, W. Koch, and J. T. Andersson, "Influence of Phenols on the Oxidation Stability of Home Heating Oils/FAME Blends," *Energy & Fuels*, vol. 29, pp. 793–799, feb 2015.
- [161] R. N. Hazlett and A. J. Power, "Phenolic compounds in Bass Strait distillate fuels: their effect on deposit formation," *Fuel*, vol. 68, no. 9, pp. 1112–1117, 1989.
- [162] S. Zabarnick, "Model studies of silylation agents as thermal-oxidative jet fuel additives," *Energy and Fuels*, vol. 13, no. 1, pp. 154–159, 1999.
- [163] M. Sobkowiak, J. M. Griffith, B. Wang, and B. Beaver, "Insight into the mechanisms of middle distillate fuel oxidative degradation. Part 1: On the role of phenol, indole, and carbazole derivatives in the thermal oxidative stability of fischer-tropsch/petroleum jet fuel blends," *Energy and Fuels*, vol. 23, pp. 2041–2046, apr 2009.
- [164] R. Clark and L. Smith, "Further studies of the effects of polar compounds on the thermal stability of jet fuel," in *Proceedings of 3rd International Conference on Long-Term Storage Stabilities of Liquid Fuels, (Institute of Petroleum, London, England)*, pp. 268–275, 1988.

- [165] S. Kobayashi and H. Higashimura, "Oxidative polymerization of phenols revisited," *Progress in Polymer Science (Oxford)*, vol. 28, no. 6, pp. 1015–1048, 2003.
- [166] D. W. Naegeli, "Thermal stability of jet fuels: Kinetics of forming deposit precursors," *Final Report for NASA Contract No. NAG*, pp. 3–1739, 1997.
- [167] J. S. Ervin, T. A. Ward, T. F. Williams, and J. Bento, "Surface deposition within treated and untreated stainless steel tubes resulting from thermal-oxidative and pyrolytic degradation of jet fuel," *Energy and Fuels*, vol. 17, no. 3, pp. 577–586, 2003.
- [168] W. F. Taylor, "Deposit Formation from Deoxygenated Hydrocarbons. I. General Features," *Industrial and Engineering Chemistry Product Research and Development*, vol. 13, pp. 133–138, jun 1974.
- [169] W. E. Harrison, H. C. Mongia, S. P. Heneghan, and D. R. Ballal, "Advanced jet fuels - JP-4 through JP-8 and beyond," *Proceedings of the ASME Turbo Expo*, vol. 3, 1995.
- [170] R. H. Clark and L. Smith, "Further studies of the effects of polar compounds on the thermal stability of jet fuel," in *3rd International Conference on Stability And Handling of Liquid Fuels*, no. 2, 1988.
- [171] R. B. Thompson, J. A. Chenicek, L. W. Druge, and T. Symon, "Stability of Fuel Oils in Storage - Effect of Some Nitrogen Compounds," *Industrial & Engineering Chemistry*, vol. 43, no. 4, pp. 935–939, 1951.
- [172] A. C. Antoine, "EFFECT OF SOME NITROGEN COMPOUNDS ON THERMAL STABILITY OF JET A.," *NASA Technical Memorandum*, jun 1982.
- [173] J. Frankenfeld and W. Taylor, "Fundamental synthetic fuel stability study. first annual report, may 1, 1979-april 30, 1981.[in storage]," tech. rep., Exxon Research and Engineering Co., Linden, NJ (USA), 1980.
- [174] J. H. Worstell, S. R. Daniel, and G. Fraunhoff, "Deposit formation in liquid fuels. 3. The effect of selected nitrogen compounds on diesel fuel," *Fuel*, vol. 60, no. 6, pp. 485–487, 1981.
- [175] J. M. Richter, B. W. Whitefield, T. J. Maimone, D. W. Lin, M. P. Castroviejo, and P. S. Baran, "Scope and mechanism of direct indole and pyrrole

- couplings adjacent to carbonyl compounds: total synthesis of acremoauxin a and oxazin 3,” *Journal of the American Chemical Society*, vol. 129, no. 42, pp. 12857–12869, 2007.
- [176] M. Brasse, J. A. Ellman, and R. G. Bergman, “A facile, metal- and solvent-free, autoxidative coupling of quinolines with indoles and pyrroles,” *Chemical Communications*, vol. 47, no. 17, pp. 5019–5021, 2011.
- [177] R. Venkataraman and S. Eser, “Characterisation of solid deposits from the thermal-oxidative degradation of jet fuel,” *International Journal of Oil, Gas and Coal Technology*, vol. 1, no. 1-2, pp. 126–137, 2008.
- [178] D. R. Kendall and J. S. Mills, “The influence of JFTOT operating parameters on the assessment of fuel thermal stability,” *SAE Technical Papers*, 1985.
- [179] D. W. McKee, “Catalytic decomposition of hydrogen peroxide by metals and alloys of the platinum group,” *Journal of Catalysis*, vol. 14, no. 4, pp. 355–364, 1969.
- [180] C. Man, C. Dong, Z. Cui, K. Xiao, Q. Yu, and X. Li, “Characterization of the Outer Layer Nanostructure in the Electrochemical Response of Stainless Steel in Aqueous Sodium Hydroxide,” *Analytical Letters*, vol. 51, no. 9, pp. 1384–1399, 2018.
- [181] K. H. Strauss, “Thermal stability specification testing of jet fuel-A critical review,” *SAE Technical Papers*, 1988.
- [182] S. A. Jadhav, “Self-assembled monolayers (SAMs) of carboxylic acids: An overview,” jun 2011.
- [183] G. Shustak, A. J. Domb, and D. Mandler, “Preparation and characterization of n-alkanoic acid self-assembled monolayers adsorbed on 316L stainless steel,” *Langmuir*, vol. 20, no. 18, pp. 7499–7506, 2004.
- [184] S. G. Pande and D. R. Hardy, “Comparison of the effects of storage in the presence of copper using laboratory vs field conditions on jet fuel thermal stability as measured by the gravimetric JFTOT,” *Energy and Fuels*, vol. 11, no. 5, pp. 1019–1025, 1997.

- [185] R. E. Morris and N. H. Turner, "Influences exerted by metal deactivator on the thermal stability of aviation fuel in the presence of copper," *Fuel Science and Technology International*, vol. 8, no. 4, pp. 327–350, 1990.
- [186] R. E. Morris, J. M. Hughes, and J. E. Colbert, "The impact of copper on the liquid-phase oxidation of jet fuel for advanced aircraft," *Energy and Fuels*, vol. 18, no. 2, pp. 490–496, 2004.
- [187] P. Gandeepan, T. Müller, D. Zell, G. Cera, S. Warratz, and L. Ackermann, "3d Transition Metals for C-H Activation," *Chemical Reviews*, vol. 119, no. 4, pp. 2192–2452, 2019.
- [188] G. A. Russell, "Deuterium-isotope Effects in the Autoxidation of Alkyl Hydrocarbons. of the Interaction of Peroxy Radicals," *Journal of the American Chemical Society*, vol. 79, no. 14, pp. 3871–3877, 1957.
- [189] S. Miyamoto, G. R. Martinez, M. H. G. Medeiros, and P. D. Mascio, "Singlet Molecular Oxygen Generated from Lipid Hydroperoxides by the Russell Mechanism: Studies Using ¹⁸O-Labeled Linoleic Acid Hydroperoxide and Monomol Light Emission Measurements," 2003.
- [190] S. P. Heneghan, C. R. Martel, T. F. Williams, and D. R. Ballal, "Effects of Oxygen and Additives on the Thermal Stability of Jet Fuels," *Journal of Engineering for Gas Turbines and Power*, vol. 117, no. 1, p. 120, 2008.
- [191] D. G. Y., M. A. S., S. P. R., and M. R.", "Modeling of the thermal stability of aviation fuels," in *198th ACS National Meeting, Symposium on the Chemical Aspects of Hypersonic Propulsion*, 1989.
- [192] S. Zabarnick, "Pseudo-Detailed Chemical Kinetic Modeling of Antioxidant Chemistry for Jet Fuel Applications," vol. 0624, no. 97, pp. 547–553, 1998.
- [193] N. J. Kuprowicz, J. S. Ervin, and S. Zabarnick, "Modeling the liquid-phase oxidation of hydrocarbons over a range of temperatures and dissolved oxygen concentrations with pseudo-detailed chemical kinetics," *Fuel*, vol. 83, no. 13, pp. 1795–1801, 2004.
- [194] N. Li, J. Long, Y. Zhao, Z. Tao, and Z. Dai, "DFT study of Oxidation Initiation for Different Compound in Gasoline," *Journal of Clean Energy Technologies*, vol. 6, no. 3, pp. 242–245, 2018.

- [195] V. M. L. Dos Santos, J. A. B. Da Silva, L. Stragevitch, and R. L. Longo, “Thermochemistry of biodiesel oxidation reactions: A DFT study,” *Fuel*, vol. 90, no. 2, pp. 811–817, 2011.
- [196] S. Arrhenius, “Über die reaktionsgeschwindigkeit bei der inversion von rohrzucker durch säuren,” *Zeitschrift für physikalische Chemie*, vol. 4, no. 1, pp. 226–248, 1889.
- [197] K. J. Laidler and M. C. King, “The development of transition-state theory,” *Journal of Physical Chemistry*, vol. 87, no. 15, pp. 2657–2664, 1983.
- [198] H. Eyring, “The Activated Complex in Chemical Reactions,” *The Journal of Chemical Physics*, vol. 107, no. 3-4, pp. 190–195, 1935.
- [199] J. H. Van’t Hoff, *Etudes de dynamique chimique*, vol. 1. Muller, 1884.
- [200] E. Lewars, *Computational Chemistry*. Springer, 2003.
- [201] I. N. Levine, D. H. Busch, and H. Shull, *Quantum chemistry*, vol. 6. Pearson Prentice Hall Upper Saddle River, NJ, 2009.
- [202] M. Born and R. Oppenheimer, “Zur quantentheorie der molekeln,” *Annalen der physik*, vol. 389, no. 20, pp. 457–484, 1927.
- [203] R. Newing, “Uncertainty principle and the zero-point energy of the harmonic oscillator,” *Nature*, vol. 136, no. 3436, pp. 395–395, 1935.
- [204] E. Schrödinger, “Über das verhältnis der heisenberg-born-jordanschen quantenmechanik zu der meinem,” *Annalen der Physik*, vol. 384, no. 8, pp. 734–756, 1926.
- [205] D. R. Hartree, “The wave mechanics of an atom with a non-Coulomb central field Part I Theory and methods,” *Mathematical Proceedings of the Cambridge Philosophical Society*, vol. 24, no. 1, pp. 89–110, 1928.
- [206] V. Fock, “Näherungsmethode zur lösung des quantenmechanischen mehrkörperproblems,” *Zeitschrift für Physik*, vol. 61, no. 1-2, pp. 126–148, 1930.
- [207] J. C. Slater, “Note on hartree’s method,” *Physical Review*, vol. 35, no. 2, pp. 210–211, 1930.
- [208] C. C. J. Roothaan, “New developments in molecular orbital theory,” *Reviews of modern physics*, vol. 23, no. 2, p. 69, 1951.

- [209] G. Hall, "The molecular orbital theory of chemical valency viii. a method of calculating ionization potentials," *Proceedings of the Royal Society of London. Series A. Mathematical and Physical Sciences*, vol. 205, no. 1083, pp. 541–552, 1951.
- [210] J. A. Pople and D. L. Beveridge, "Approximate Molecular Orbital Theory," 1970.
- [211] M. Nooijen, K. R. Shamasundar, and D. Mukherjee, "Reflections on size-extensivity, size-consistency and generalized extensivity in many-body theory," *Molecular Physics*, vol. 103, no. 15-16, pp. 2277–2298, 2005.
- [212] F. Jensen, *Introduction to Computational Chemistry Second Edition*. 2011.
- [213] R. J. Bartlett, "Many-body perturbation theory and coupled cluster theory for electron correlation in molecules," *Annual Review of Physical Chemistry*, vol. 32, no. 1, pp. 359–401, 1981.
- [214] M. C. Gutzwiller, "Moon-Earth-Sun: The oldest three-body problem," *Reviews of Modern Physics*, vol. 70, no. 2, pp. 589–639, 1998.
- [215] K. Wolinski and P. Pulay, "Generalized Moller-Plesset perturbation theory: Second order results for two- configuration, open-shell excited singlet, and doublet wave functions," *The Journal of Chemical Physics*, no. 90, pp. 3647–3659, 1989.
- [216] V. Barone, A. Bencini, F. Totti, and M. G. Uytterhoeven, "Comparison between post-hartree-fock and dft methods for the study of strength and mechanism of cleavage of hg (single bond) c bond," *International journal of quantum chemistry*, vol. 61, no. 3, pp. 361–367, 1997.
- [217] P. Hohenberg and W. Kohn, "Inhomogenous Electron Gas," *Physical Review*, vol. 136, pp. 864–871, 1964.
- [218] E. Fermi, "Zur quantelung des idealen einatomigen gases," *Zeitschrift für Physik*, vol. 36, no. 11-12, pp. 902–912, 1926.
- [219] P. A. M. Dirac, "On the theory of quantum mechanics," *Proceedings of the Royal Society of London. Series A, Containing Papers of a Mathematical and Physical Character*, vol. 112, no. 762, pp. 661–677, 1926.

- [220] L. H. Thomas, “The calculation of atomic fields,” in *Mathematical Proceedings of the Cambridge Philosophical Society*, vol. 23, pp. 542–548, Cambridge University Press, 1927.
- [221] J. D. Chai, V. L. Lignères, G. Ho, E. A. Carter, and J. D. Weeks, “Orbital-free density functional theory: Linear scaling methods for kinetic potentials, and applications to solid Al and Si,” *Chemical Physics Letters*, vol. 473, no. 4-6, pp. 263–267, 2009.
- [222] M. G. Medvedev, I. S. Bushmarinov, J. Sun, J. P. Perdew, and K. A. Lyssenko, “Response to comment on ‘density functional theory is straying from the path toward the exact functional’,” *Science*, vol. 356, no. 6337, pp. 496–496, 2017.
- [223] J. C. Slater, “A simplification of the hartree-fock method,” *Physical review*, vol. 81, no. 3, p. 385, 1951.
- [224] S. H. Vosko, L. Wilk, and M. Nusair, “Accurate spin-dependent electron liquid correlation energies for local spin density calculations: a critical analysis,” *Canadian Journal of physics*, vol. 58, no. 8, pp. 1200–1211, 1980.
- [225] J. P. Perdew and Y. Wang, “Pair-distribution function and its coupling-constant average for the spin-polarized electron gas,” *Physical Review B*, vol. 46, no. 20, p. 12947, 1992.
- [226] A. D. Becke, “Density-functional exchange-energy approximation with correct asymptotic behavior,” *Physical review A*, vol. 38, no. 6, p. 3098, 1988.
- [227] C. Lee, W. Yang, and R. G. Parr, “Development of the colle-salvetti correlation-energy formula into a functional of the electron density,” *Physical review B*, vol. 37, no. 2, p. 785, 1988.
- [228] J. P. Perdew, “Density-functional approximation for the correlation energy of the inhomogeneous electron gas,” *Physical Review B*, vol. 33, no. 12, p. 8822, 1986.
- [229] J. P. Perdew, K. Burke, and M. Ernzerhof, “Generalized gradient approximation made simple,” *Physical review letters*, vol. 77, no. 18, p. 3865, 1996.
- [230] J. P. Perdew and L. A. Constantin, “Laplacian-level density functionals for the kinetic energy density and exchange-correlation energy,” *Physical Review B*, vol. 75, no. 15, p. 155109, 2007.

- [231] A. D. Becke, “A new dynamical correlation functional and implications for exact-exchange mixing,” *J. Chem. Phys.*, vol. 104, no. October 1995, pp. 1040–1046, 1996.
- [232] N. Mardirossian and M. Head-Gordon, “Thirty years of density functional theory in computational chemistry: An overview and extensive assessment of 200 density functionals,” 2017.
- [233] A. D. Becke, “Density-functional thermochemistry. III. The role of exact exchange,” *The Journal of Chemical Physics*, vol. 98, no. 7, pp. 5648–5652, 1993.
- [234] S. Grimme, J. Antony, S. Ehrlich, and H. Krieg, “A consistent and accurate ab initio parametrization of density functional dispersion correction (DFT-D) for the 94 elements H-Pu,” *Journal of Chemical Physics*, vol. 132, no. 15, 2010.
- [235] J. Klimeš, D. R. Bowler, and A. Michaelides, “Chemical accuracy for the van der Waals density functional,” *Journal of Physics Condensed Matter*, vol. 22, no. 2, 2010.
- [236] C. D. Sherrill, “The Multiconfigurational Self-Consistent-Field Method,” *School of Chemistry and Biochemistry Georgia Institute of Technology March*, no. March, pp. 1–6, 2004.
- [237] W. J. Hehre, R. F. Stewart, and J. A. Pople, “Self-consistent molecular-orbital methods. I. Use of gaussian expansions of slater-type atomic orbitals,” *The Journal of Chemical Physics*, vol. 51, no. 6, pp. 2657–2664, 1969.
- [238] R. Krishnan, J. S. Binkley, R. Seeger, and J. A. Pople, “Self-consistent molecular orbital methods. xx. a basis set for correlated wave functions,” *The Journal of chemical physics*, vol. 72, no. 1, pp. 650–654, 1980.
- [239] A. Szabo and N. S. Ostlund, *Modern quantum chemistry: introduction to advanced electronic structure theory*. Courier Corporation, 2012.
- [240] T. H. Dunning Jr, “Gaussian basis sets for use in correlated molecular calculations. i. the atoms boron through neon and hydrogen,” *The Journal of chemical physics*, vol. 90, no. 2, pp. 1007–1023, 1989.
- [241] R. Hoffmann, “How Chemistry and Physics Meet in the Solid State,” *Angewandte Chemie International Edition in English*, vol. 26, no. 9, pp. 846–878, 1987.

- [242] M. Marsman, “VASP : Basics (DFT , PW , PAW , ...),” *University of Vienna*.
- [243] P. E. Blöchl, “Projector augmented-wave method,” *Physical Review B*, vol. 50, no. 24, pp. 17953–17979, 1994.
- [244] J. W. Frankenfeld, W. F. Taylor, and D. W. Brinkman, “Storage stability of synfuels from oil shale. 1. general features of sediment formation in model fuel systems,” *Industrial and Engineering Chemistry Product Research and Development*, vol. 22, no. 4, pp. 608–614, 1983.
- [245] C. G. Kabana, S. Botha, C. Schmucker, C. Woolard, and B. Beaver, “Oxidative stability of middle distillate fuels. Part 1: Exploring the soluble macromolecular oxidatively reactive species (SMORS) mechanism with jet fuels,” *Energy and Fuels*, vol. 25, no. 11, pp. 5145–5157, 2011.
- [246] M. J. Frisch, G. W. Trucks, H. B. Schlegel, G. E. Scuseria, M. A. Robb, J. R. Cheeseman, G. Scalmani, V. Barone, B. Mennucci, G. A. Petersson, H. Nakatsuji, M. Caricato, X. Li, H. P. Hratchian, A. F. Izmaylov, J. Bloino, G. Zheng, J. L. Sonnenberg, M. Hada, M. Ehara, K. Toyota, R. Fukuda, J. Hasegawa, M. Ishida, T. Nakajima, Y. Honda, O. Kitao, H. Nakai, T. Vreven, J. A. Montgomery, Jr., J. E. Peralta, F. Ogliaro, M. Bearpark, J. J. Heyd, E. Brothers, K. N. Kudin, V. N. Staroverov, R. Kobayashi, J. Normand, K. Raghavachari, A. Rendell, J. C. Burant, S. S. Iyengar, J. Tomasi, M. Cossi, N. Rega, J. M. Millam, M. Klene, J. E. Knox, J. B. Cross, V. Bakken, C. Adamo, J. Jaramillo, R. Gomperts, R. E. Stratmann, O. Yazyev, A. J. Austin, R. Cammi, C. Pomelli, J. W. Ochterski, R. L. Martin, K. Morokuma, V. G. Zakrzewski, G. A. Voth, P. Salvador, J. J. Dannenberg, S. Dapprich, A. D. Daniels, Ö. Farkas, J. B. Foresman, J. V. Ortiz, J. Cioslowski, and D. J. Fox, “Gaussian 09 Revision E.01,” 2009. Gaussian Inc. Wallingford CT 2009.
- [247] S. Grimme, S. Ehrlich, and L. Goerigk, “Effect of the damping function in dispersion corrected density functional theory,” *Journal of computational chemistry*, vol. 32, no. 7, pp. 1456–1465, 2011.
- [248] S. Miertuš, E. Scrocco, and J. Tomasi, “Electrostatic interaction of a solute with a continuum. a direct utilizaion of ab initio molecular potentials for the prevision of solvent effects,” *Chemical Physics*, vol. 55, no. 1, pp. 117–129, 1981.

- [249] S. Grimme, “Supramolecular binding thermodynamics by dispersion-corrected density functional theory,” *Chemistry—A European Journal*, vol. 18, no. 32, pp. 9955–9964, 2012.
- [250] R. F. Ribeiro, A. V. Marenich, C. J. Cramer, and D. G. Truhlar, “Use of solution-phase vibrational frequencies in continuum models for the free energy of solvation,” *The Journal of Physical Chemistry B*, vol. 115, no. 49, pp. 14556–14562, 2011.
- [251] R. Paton, “Goodvibes,” 2016.
- [252] C. Riplinger and F. Neese, “An efficient and near linear scaling pair natural orbital based local coupled cluster method,” *The Journal of chemical physics*, vol. 138, no. 3, p. 034106, 2013.
- [253] C. Riplinger, B. Sandhoefer, A. Hansen, and F. Neese, “Natural triple excitations in local coupled cluster calculations with pair natural orbitals,” *The Journal of chemical physics*, vol. 139, no. 13, p. 134101, 2013.
- [254] C. Riplinger, P. Pinski, U. Becker, E. F. Valeev, and F. Neese, “Sparse maps—a systematic infrastructure for reduced-scaling electronic structure methods. ii. linear scaling domain based pair natural orbital coupled cluster theory,” *The Journal of chemical physics*, vol. 144, no. 2, p. 024109, 2016.
- [255] M. Saitow, U. Becker, C. Riplinger, E. F. Valeev, and F. Neese, “A new near-linear scaling, efficient and accurate, open-shell domain-based local pair natural orbital coupled cluster singles and doubles theory,” *The Journal of chemical physics*, vol. 146, no. 16, p. 164105, 2017.
- [256] Y. Guo, C. Riplinger, U. Becker, D. G. Liakos, Y. Minenkov, L. Cavallo, and F. Neese, “Communication: An improved linear scaling perturbative triples correction for the domain based local pair-natural orbital based singles and doubles coupled cluster method [dlpno-ccsd (t)],” *The Journal of chemical physics*, vol. 148, no. 1, p. 011101, 2018.
- [257] F. Neese, F. Wennmohs, U. Becker, and C. Riplinger, “The ORCA quantum chemistry program package,” *Journal of Chemical Physics*, vol. 152, no. 22, 2020.

- [258] D. Min and J. Boff, "Chemistry and reaction of singlet oxygen in foods," *Comprehensive reviews in food science and food safety*, vol. 1, no. 2, pp. 58–72, 2002.
- [259] B. Dellinger, S. Lomnicki, L. Khachatryan, Z. Maskos, R. W. Hall, J. Adoukpe, C. McFerrin, and H. Truong, "Formation and stabilization of persistent free radicals," *Proceedings of the Combustion Institute*, vol. 31 I, no. 1, pp. 521–528, 2007.
- [260] H. Shadnia and J. S. Wright, "Understanding the toxicity of phenols: Using quantitative structure-activity relationship and enthalpy changes to discriminate between possible mechanisms," *Chemical Research in Toxicology*, vol. 21, no. 6, pp. 1197–1204, 2008.
- [261] M. Michalík, P. Poliak, V. Lukeš, and E. Klein, "From phenols to quinones: Thermodynamics of radical scavenging activity of para-substituted phenols," *Phytochemistry*, vol. 166, no. July, p. 112077, 2019.
- [262] G. A. Russell, "Deuterium-isotope effects in the autoxidation of aralkyl hydrocarbons. mechanism of the interaction of peroxy radicals¹," *Journal of the American Chemical Society*, vol. 79, no. 14, pp. 3871–3877, 1957.
- [263] R. Lee, G. Gryn'Ova, K. U. Ingold, and M. L. Coote, "Why are: Sec -alkylperoxyl bimolecular self-reactions orders of magnitude faster than the analogous reactions of tert -alkylperoxyls? the unanticipated role of CH hydrogen bond donation," *Physical Chemistry Chemical Physics*, vol. 18, no. 34, pp. 23673–23679, 2016.
- [264] K. Adamic, J. A. Howard, and K. U. Ingold, "Absolute rate constants for hydrocarbon autoxidation. XVI. Reactions of peroxy radicals at low temperatures," *Canadian Journal of Chemistry*, vol. 47, no. 20, pp. 3803–3808, 1969.
- [265] A. R. Smith, S. Di Muzio, F. Ramondo, and G. Meloni, "Peroxy self-reaction leading to the formation of furfural," *Physical Chemistry Chemical Physics*, vol. 21, no. 20, pp. 10228–10237, 2019.
- [266] J. Howard and J. Bennett, "The self-reaction of sec-alkylperoxy radicals: a kinetic electron spin resonance study," *Canadian Journal of Chemistry*, vol. 50, no. 14, pp. 2374–2377, 1972.

- [267] G. Mendenhall and E. Quinga, "Deuterium isotope cage effects in the dismutation of alkoxy radicals. significance for the mode of alkylperoxy termination," *International journal of chemical kinetics*, vol. 17, no. 11, pp. 1187–1190, 1985.
- [268] E. Quinga and G. Mendenhall, "Chemiluminescence from hyponitrite esters. excited triplet states from dismutation of geminate alkoxy radical pairs," *Journal of the American Chemical Society*, vol. 105, no. 21, pp. 6520–6521, 1983.
- [269] J. Helberg and D. A. Pratt, "Autoxidation vs. antioxidants-the fight for forever," *Chemical Society Reviews*, vol. 50, no. 13, pp. 7343–7358, 2021.
- [270] R. E. Gawley, "A proposal for (slight) modification of the hughes-ingold mechanistic descriptors for substitution reactions," *Tetrahedron letters*, vol. 40, no. 23, pp. 4297–4300, 1999.
- [271] S. L. Matlow and G. W. Wheland, "Orientation in Aromatic Substitution: A Theoretical Study of the Competition between Groups," *Journal of the American Chemical Society*, vol. 77, no. 13, pp. 3653–3655, 1955.
- [272] Hongchang, "Sulfonation mechanism of benzene with SO₃ in sulfuric acid or oleum or aprotic solvent: Obeying the transition state theory via a trimolecular electrophilic substitution clarified by density functional theory calculation," *Computational and Theoretical Chemistry*, vol. 1112, pp. 111–122, 2017.
- [273] T. Stuyver, D. Danovich, F. De Proft, and S. Shaik, "Electrophilic Aromatic Substitution Reactions: Mechanistic Landscape, Electrostatic and Electric-Field Control of Reaction Rates, and Mechanistic Crossovers," *Journal of the American Chemical Society*, vol. 141, no. 24, pp. 9719–9730, 2019.
- [274] M. C. Pirrung, L. Deng, Z. Li, and K. Park, "Synthesis of 2, 5-dihydroxy-3-(indol-3-yl) benzoquinones by acid-catalyzed condensation of indoles with 2, 5-dichlorobenzoquinone," *The Journal of Organic Chemistry*, vol. 67, no. 24, pp. 8374–8388, 2002.
- [275] M. G. Corradini, C. Costanini, G. Protà, and T. Schultz, "Acid-catalyzed reactions of indoles with 1, 4-quinones.," *ChemInform*, vol. 20, no. 33, 1989.
- [276] S. Baena-Zambrana, S. L. Repetto, C. P. Lawson, and J. K. Lam, "Behaviour of water in jet fuel - A literature review," *Progress in Aerospace Sciences*, vol. 60, pp. 35–44, 2013.

- [277] M. Gurry and F. Aldabbagh, “A new era for homolytic aromatic substitution: Replacing Bu₃SnH with efficient light-induced chain reactions,” *Organic and Biomolecular Chemistry*, vol. 14, no. 16, pp. 3849–3862, 2016.
- [278] W. R. Bowman and J. M. Storey, “Synthesis using aromatic homolytic substitution—recent advances,” *Chemical Society Reviews*, vol. 36, no. 11, pp. 1803–1822, 2007.
- [279] S. Liu, F. Zhao, X. Chen, G. J. Deng, and H. Huang, “Aerobic oxidative functionalization of indoles,” *Advanced Synthesis and Catalysis*, vol. 362, no. 18, pp. 3795–3823, 2020.
- [280] M. Nonella, “A Generalized Resonance Model for Substituted 1,4-Benzoquinones,” *Journal of Physical Chemistry A*, vol. 103, no. 35, pp. 7069–7075, 1999.
- [281] J. S. Yadav, B. V. Reddy, and T. Swamy, “InBr₃-Catalyzed Conjugate Addition of Indoles to p-Quinones: An Efficient Synthesis of 3-Indolylquinones,” *Synthesis*, vol. 44, no. 1, pp. 106–110, 2004.
- [282] J. Stejskal, P. Bober, M. Trchová, J. Horský, Z. Walterová, S. K. Filippov, T. Plachý, and M. Mrlík, “Oxidation of pyrrole with: P -benzoquinone to semiconducting products and their application in electrorheology,” *New Journal of Chemistry*, vol. 42, no. 12, pp. 10167–10176, 2018.
- [283] F. Takahashi, K. Nogi, and H. Yorimitsu, “Catalytic inter- and intramolecular coupling of aryl sulfones,” *Phosphorus, Sulfur and Silicon and the Related Elements*, vol. 194, no. 7, pp. 742–745, 2019.
- [284] B. D. Boss and R. N. Hazlett, “Oxidation of hydrocarbons in the liquid phase: n-dodecane in a borosilicate glass chamber at 200 °C,” *Canadian Journal of Chemistry*, vol. 47, pp. 4176–4182, 1969.
- [285] D. Naegeli, M. Sirman, C. Moses, and R. Hill, “Kinetics of deposit precursors in jet fuels: Structure of jet fuels v,” *Preprints-American Chemical Society. Division of Petroleum Chemistry*, vol. 43, no. 3, pp. 394–400, 1998.
- [286] T. Edwards and L. Q. Maurice, “Surrogate mixtures to represent complex aviation and rocket fuels,” *Journal of Propulsion and Power*, vol. 17, no. 2, pp. 461–466, 2001.

- [287] S. Eser, R. Venkataraman, and O. Altin, "Deposition of carbonaceous solids on different substrates from thermal stressing of JP-8 and jet A fuels," *Industrial and Engineering Chemistry Research*, vol. 45, no. 26, pp. 8946–8955, 2006.
- [288] J. Bacha, J. Freel, A. Gibbs, L. Gibbs, G. Hemighaus, K. Hoekman, J. Horn, M. Ingham, L. Jossens, D. Kohler, D. Lesnini, J. Mcgeehan, M. Nikanjam, E. Olsen, R. Organ, B. Scott, M. Sztenderowicz, A. Tiedemann, C. Walker, J. Lind, J. Jones, D. Scott, and J. Mills, "Diesel Fuels Technical Review," tech. rep., 2007.
- [289] R. Dinkov, G. Hristov, D. Stratiev, and V. Boynova Aldayri, "Effect of commercially available antioxidants over biodiesel/diesel blends stability," *Fuel*, vol. 88, pp. 732–737, apr 2009.
- [290] C. M. Hansen, *Hansen solubility parameters: a user's handbook*. CRC press, 2007.
- [291] Abbott S, Yamamoto H, "Hspip software," 2015.
- [292] O. Altin and S. Eser, "Carbon deposit formation from thermal stressing of petroleum fuels," *ACS Division of Fuel Chemistry, Preprints*, vol. 49, no. 2, pp. 764–766, 2004.
- [293] K. T. Reddy, N. P. Cernansky, and R. S. Cohen, "Degradation mechanisms of n-Dodecane with sulfur and nitrogen dopants during thermal stressing," *Journal of Propulsion and Power*, vol. 5, no. 1, pp. 6–13, 1989.
- [294] R. D. Offenbauer, J. A. Brennan, and R. C. Miller, "Sediment Formation in Catalytically Cracked Distillate Fuel Oils," *Industrial and Engineering Chemistry*, vol. 49, no. 8, pp. 1265–1266, 1957.
- [295] R. Plate and H. C. Ottenheijm, "Synthesis of 2-(alkylthio) indoles," *Tetrahedron*, vol. 42, no. 16, pp. 4511–4516, 1986.
- [296] R. J. Spears, C. McMahon, and V. Chudasama, "Cysteine protecting groups: Applications in peptide and protein science," *Chemical Society Reviews*, vol. 50, no. 19, pp. 11098–11155, 2021.
- [297] G. W. Mushrush, R. V. Honeychuck, W. M. Stalick, J. E. Slone, E. J. Beal, and D. R. Hardy, "The reaction of 3-methyl indole with para-ethylbenzene

- sulfonic acid: Fuel incompatibility reactions,” *Fuel Science and Technology International*, vol. 13, no. 6, pp. 793–805, 1995.
- [298] H. Jiang and A. Studer, “Intermolecular radical carboamination of alkenes,” *Chemical Society Reviews*, vol. 49, no. 6, pp. 1790–1811, 2020.
- [299] B. Wessling, “Conductive polymers as organic nanometals,” in *Handbook of nanostructured materials and nanotechnology*, pp. 501–575, Elsevier, 2000.
- [300] P. D. MacLean, E. E. Chapman, S. L. Dobrowolski, A. Thompson, and L. R. C. Barclay, “Pyrroles as antioxidants: Solvent effects and the nature of the attacking radical on antioxidant activities and mechanisms of pyrroles, dipyrinones, and bile pigments,” *Journal of Organic Chemistry*, vol. 73, no. 17, pp. 6623–6635, 2008.
- [301] K. Namsheer and C. S. Rout, “Conducting polymers: a comprehensive review on recent advances in synthesis, properties and applications,” *RSC Advances*, vol. 11, no. 10, pp. 5659–5697, 2021.
- [302] Y. Luo, X. Yue, P. Wei, A. Zhou, X. Kong, and S. Alimzhanova, “A state-of-the-art review of quinoline degradation and technical bottlenecks,” *Science of the Total Environment*, vol. 747, p. 141136, 2020.
- [303] Z. Zhang, X. Yue, Y. Duan, and Z. Rao, “A study on the mechanism of oxidized quinoline removal from acid solutions based on persulfate-iron systems,” *RSC Advances*, vol. 10, no. 21, pp. 12504–12510, 2020.
- [304] A. R. Katritzky, C. A. Ramsden, J. A. Joule, and V. V. Zhdankin, “Reactivity of Six-membered Rings,” *Handbook of Heterocyclic Chemistry*, pp. 242–382, 2010.
- [305] J. D. Mosley, A. M. Ricks, P. V. Schleyer, J. I. Wu, and M. A. Duncan, “IR spectroscopy of α - And β -protonated pyrrole via argon complex photodissociation,” *Journal of Physical Chemistry A*, vol. 116, no. 39, pp. 9689–9695, 2012.
- [306] J. K. Howard, K. J. Rihak, A. C. Bissember, and J. A. Smith, “The Oxidation of Pyrrole,” *Chemistry - An Asian Journal*, vol. 11, no. 2, pp. 155–167, 2016.

- [307] B. Ariche and A. Rahmouni, "Theoretical study on the acidities of pyrrole, indole, carbazole and their hydrocarbon analogues in dmsO," *Canadian Journal of Chemistry*, vol. 96, no. 12, pp. 1001–1009, 2018.
- [308] M. M. Gacek and J. C. Berg, "The role of acid-base effects on particle charging in apolar media," *Advances in Colloid and Interface Science*, vol. 220, pp. 108–123, 2015.
- [309] A. D1655, "Standard specification for aviation turbine fuels," *Annual Book of Standards*, 2010.
- [310] S. Zabarnick and D. K. Phelps, "Density functional theory calculations of the energetics and kinetics of jet fuel autoxidation reactions," *Energy & fuels*, vol. 20, no. 2, pp. 488–497, 2006.
- [311] C. M. Parks, E. Alborzi, S. G. Blakey, A. J. Meijer, and M. Pourkashanian, "Density functional theory calculations on copper-mediated peroxide decomposition reactions: Implications for jet fuel autoxidation," *Energy & Fuels*, vol. 34, no. 6, pp. 7439–7447, 2020.
- [312] C. Gattinoni, J. P. Ewen, and D. Dini, "Adsorption of surfactants on α -Fe₂O₃ (0001): a density functional theory study," *The Journal of Physical Chemistry C*, vol. 122, no. 36, pp. 20817–20826, 2018.
- [313] K. O. Sarfo, P. Murkute, O. B. Isgor, Y. Zhang, J. Tucker, and L. Árnadóttir, "Density functional theory study of the initial stages of Cl-induced degradation of α -Cr₂O₃ passive film," *Journal of The Electrochemical Society*, vol. 167, no. 12, p. 121508, 2020.
- [314] M.-F. Ng, D. J. Blackwood, H. Jin, and T. L. Tan, "Dft study of oxygen reduction reaction on chromia and hematite: Insights into corrosion inhibition," *The Journal of Physical Chemistry C*, vol. 124, no. 25, pp. 13799–13808, 2020.
- [315] C. Cantarelli, B. Darenne, M. A. Fortunato, T. de Bruin, and D. Costa, "Dft screening of adsorption of biodiesel molecules on aluminium and stainless steel surfaces," *Results in Surfaces and Interfaces*, p. 100050, 2022.
- [316] R. N. Hazlett, *Thermal oxidation stability of aviation turbine fuels*, vol. 1. Astm International, 1991.

- [317] G. w. Mushrush, “Fuel instability 1: Organo-sulfur hydroperoxide reactions,” *Fuel science & technology international*, vol. 10, no. 9, pp. 1523–1560, 1992.
- [318] P. M. Rawson, R. L. Webster, D. Evans, and S. Abanteriba, “Contribution of sulfur compounds to deposit formation in jet fuels at 140° c using a quartz crystal microbalance technique,” *Fuel*, vol. 231, pp. 1–7, 2018.
- [319] D. W. Naegeli, “The role of sulfur in the thermal stability of jet fuel,” in *Turbo Expo: Power for Land, Sea, and Air*, vol. 78590, p. V002T02A053, American Society of Mechanical Engineers, 1999.
- [320] B. Beaver, L. Gao, C. Burgess-Clifford, and M. Sobkowiak, “On the mechanisms of formation of thermal oxidative deposits in jet fuels. are unified mechanisms possible for both storage and thermal oxidative deposit formation for middle distillate fuels?,” *Energy & fuels*, vol. 19, no. 4, pp. 1574–1579, 2005.
- [321] J. Ervin, S. Heneghan, C. Martel, and T. Williams, “Surface effects on deposits from jet fuels,” in *Turbo Expo: Power for Land, Sea, and Air*, vol. 78804, p. V003T06A017, American Society of Mechanical Engineers, 1995.
- [322] R. Venkataraman and S. Eser, “Characterisation of solid deposits from the thermal-oxidative degradation of jet fuel,” *International Journal of Oil, Gas and Coal Technology*, vol. 1, no. 1-2, pp. 126–137, 2008.
- [323] A. Raman, R. Quiñones, L. Barriger, R. Eastman, A. Parsi, and E. S. Gawalt, “Understanding organic film behavior on alloy and metal oxides,” *Langmuir*, vol. 26, no. 3, pp. 1747–1754, 2010.
- [324] A. R. Mohan and S. Eser, “Analysis of carbonaceous solid deposits from thermal oxidative stressing of Jet-A fuel on iron- and nickel-based alloy surfaces,” *Industrial and Engineering Chemistry Research*, vol. 49, no. 6, pp. 2722–2730, 2010.
- [325] O. Altin and S. Eser, “Characterization of carbon deposits from jet fuel on Inconel 600 and Inconel X surfaces,” *Industrial and Engineering Chemistry Research*, vol. 39, no. 3, pp. 642–645, 2000.
- [326] S. Boichenko, O. Vovk, and A. Iakovlieva, “Overview of innovative technologies for aviation fuels production,” 2013.

- [327] A. Rohrbach, J. Hafner, and G. Kresse, “Ab initio study of the (0001) surfaces of hematite and chromia: Influence of strong electronic correlations,” *Physical Review B - Condensed Matter and Materials Physics*, vol. 70, no. 12, pp. 1–17, 2004.
- [328] R. Ovcharenko, E. Voloshina, and J. Sauer, “Water adsorption and O-defect formation on Fe₂O₃(0001) surfaces,” *Physical Chemistry Chemical Physics*, vol. 18, no. 36, pp. 25560–25568, 2016.
- [329] X. G. Wang and J. R. Smith, “Surface phase diagram for Cr₂O₃(0001): Ab initio density functional study,” *Physical Review B - Condensed Matter and Materials Physics*, vol. 68, no. 20, pp. 3–6, 2003.
- [330] A. Hill, F. Jiao, P. Bruce, A. Harrison, W. Kockelmann, and C. Ritter, “Neutron diffraction study of mesoporous and bulk hematite, α -Fe₂O₃,” *Chemistry of Materials*, vol. 20, no. 15, pp. 4891–4899, 2008.
- [331] N. Golosova, D. Kozlenko, S. Kichanov, E. Lukin, H.-P. Liermann, K. Glazyrin, and B. Savenko, “Structural and magnetic properties of Cr₂O₃ at high pressure,” *Journal of Alloys and Compounds*, vol. 722, pp. 593–598, 2017.
- [332] A. Jain, G. Hautier, C. J. Moore, S. P. Ong, C. C. Fischer, T. Mueller, K. A. Persson, and G. Ceder, “A high-throughput infrastructure for density functional theory calculations,” *Computational Materials Science*, vol. 50, no. 8, pp. 2295–2310, 2011.
- [333] L. Kamrani Moghaddam, S. Ramezani Paschevari, M. A. Zaimy, A. Abdalaian, and A. Jebali, “The inhibition of epidermal growth factor receptor signaling by hexagonal selenium nanoparticles modified by siRNA,” *Cancer Gene Therapy*, vol. 23, no. 9, pp. 321–325, 2016.
- [334] G. Kresse and J. Hafner, “Ab initio molecular dynamics for liquid metals,” *Physical review B*, vol. 47, no. 1, p. 558, 1993.
- [335] G. Kresse and J. Furthmüller, “Efficiency of ab-initio total energy calculations for metals and semiconductors using a plane-wave basis set,” *Computational materials science*, vol. 6, no. 1, pp. 15–50, 1996.

- [336] G. Kresse and J. Furthmüller, “Efficient iterative schemes for ab initio total-energy calculations using a plane-wave basis set,” *Phys. Rev. B*, vol. 54, pp. 11169–11186, Oct 1996.
- [337] G. Román-Pérez and J. M. Soler, “Efficient implementation of a van der waals density functional: Application to double-wall carbon nanotubes,” *Phys. Rev. Lett.*, vol. 103, p. 096102, Aug 2009.
- [338] D. Kopač, D. L. Jurković, B. Likozar, and M. Huš, “First-principles-based multiscale modelling of nonoxidative butane dehydrogenation on Cr_2O_3 (0001),” *ACS catalysis*, vol. 10, no. 24, pp. 14732–14746, 2020.
- [339] A. Raman and E. S. Gawalt, “Self-assembled monolayers of alkanolic acids on the native oxide surface of ss316l by solution deposition,” *Langmuir*, vol. 23, no. 5, pp. 2284–2288, 2007.
- [340] A. J. Therrien, A. J. Hensley, R. T. Hannagan, A. C. Schilling, M. D. Marcinkowski, A. M. Larson, J.-S. McEwen, and E. C. H. Sykes, “Surface-templated assembly of molecular methanol on the thin film ’29’ Cu (111) surface oxide,” *The Journal of Physical Chemistry C*, vol. 123, no. 5, pp. 2911–2921, 2019.
- [341] C. J. Murphy, J. Carrasco, T. J. Lawton, M. L. Liriano, A. E. Baber, E. A. Lewis, A. Michaelides, and E. C. H. Sykes, “Structure and energetics of hydrogen-bonded networks of methanol on close packed transition metal surfaces,” *The Journal of chemical physics*, vol. 141, no. 1, p. 014701, 2014.
- [342] C. Vericat, M. E. Vela, G. Corthey, E. Pensa, E. Cortés, M. H. Fonticelli, F. Ibanez, G. Benitez, P. Carro, and R. C. Salvarezza, “Self-assembled monolayers of thiolates on metals: a review article on sulfur-metal chemistry and surface structures,” *Rsc Advances*, vol. 4, no. 53, pp. 27730–27754, 2014.
- [343] J. Noh, H. S. Kato, M. Kawai, and M. Hara, “Surface and adsorption structures of dialkyl sulfide self-assembled monolayers on Au (111),” *The Journal of Physical Chemistry B*, vol. 106, no. 51, pp. 13268–13272, 2002.
- [344] G. Kresse and D. Joubert, “From ultrasoft pseudopotentials to the projector augmented-wave method,” *Physical review b*, vol. 59, no. 3, p. 1758, 1999.
- [345] P. E. Blöchl, “Projector augmented-wave method,” *Physical review B*, vol. 50, no. 24, p. 17953, 1994.

- [346] W. Tang, E. Sanville, and G. Henkelman, “A grid-based bader analysis algorithm without lattice bias,” *Journal of Physics: Condensed Matter*, vol. 21, no. 8, p. 084204, 2009.
- [347] E. Sanville, S. D. Kenny, R. Smith, and G. Henkelman, “Improved grid-based algorithm for bader charge allocation,” *Journal of computational chemistry*, vol. 28, no. 5, pp. 899–908, 2007.
- [348] G. Henkelman, A. Arnaldsson, and H. Jónsson, “A fast and robust algorithm for bader decomposition of charge density,” *Computational Materials Science*, vol. 36, no. 3, pp. 354–360, 2006.
- [349] M. Yu and D. R. Trinkle, “Accurate and efficient algorithm for bader charge integration,” *The Journal of chemical physics*, vol. 134, no. 6, p. 064111, 2011.
- [350] A. P. Bartók and J. R. Yates, “Regularized scan functional,” *The Journal of chemical physics*, vol. 150, no. 16, p. 161101, 2019.
- [351] H. Evans, D. Hilton, and R. Holm, “Chromium-depleted zones and the oxidation process in stainless steels,” *Oxidation of metals*, vol. 10, no. 3, pp. 149–161, 1976.
- [352] J. Sun, T. Stirner, and A. Matthews, “Structure and surface energy of low-index surfaces of stoichiometric α -al₂o₃ and α -cr₂o₃,” *Surface and Coatings Technology*, vol. 201, no. 7, pp. 4205–4208, 2006.
- [353] X.-G. Wang, W. Weiss, S. K. Shaikhutdinov, M. Ritter, M. Petersen, F. Wagner, R. Schlögl, and M. Scheffler, “The hematite (α -fe₂o₃)(0001) surface: evidence for domains of distinct chemistry,” *Physical Review Letters*, vol. 81, no. 5, p. 1038, 1998.
- [354] L. M. Balster, S. Zabarnick, R. C. Striebich, L. M. Shafer, and Z. J. West, “Analysis of polar species in jet fuel and determination of their role in autoxidative deposit formation,” *Energy & fuels*, vol. 20, no. 6, pp. 2564–2571, 2006.
- [355] E. Alborzi, S. Blakey, H. Ghadbeigi, and C. Pinna, “Prediction of growth of jet fuel autoxidative deposits at inner surface of a replicated jet engine burner feed arm,” *Fuel*, vol. 214, pp. 528–537, feb 2018.

- [356] O. Mamun, K. T. Winther, J. R. Boes, and T. Bligaard, “High-throughput calculations of catalytic properties of bimetallic alloy surfaces,” *Scientific Data*, vol. 6, no. 1, pp. 1–9, 2019.
- [357] M. Grzybowski, K. Skonieczny, H. Butenschön, and D. T. Gryko, “Comparison of oxidative aromatic coupling and the scholl reaction,” *Angewandte Chemie - International Edition*, vol. 52, no. 38, pp. 9900–9930, 2013.
- [358] P. D. McDonald and G. A. Hamilton, *Mechanisms of Phenolic Oxidative Coupling Reactions*, vol. 5. Academic Press, INC., 1973.
- [359] C.-L. Sun and Z.-J. Shi, “Transition-metal-free coupling reactions,” *Chemical Reviews*, vol. 114, no. 18, pp. 9219–9280, 2014. PMID: 25184859.
- [360] M. Monge-Palacios, E. Grajales-González, G. Kukkadapu, and S. M. Sarathy, “Kinetics of the benzyl + HO₂ and benzoyl + OH barrierless association reactions: fate of the benzyl hydroperoxide adduct under combustion and atmospheric conditions,” *Physical Chemistry Chemical Physics*, vol. 22, no. 16, pp. 9029–9039, 2020.
- [361] F. Minisci, “Recent aspects of homolytic aromatic substitutions.,” *Topics in current chemistry*, vol. 62, pp. 1–48, 1976.
- [362] D. P. Curran and A. I. Keller, “Radical additions of aryl iodides to arenes are facilitated by oxidative rearomatization with dioxygen,” *Journal of the American Chemical Society*, vol. 128, no. 42, pp. 13706–13707, 2006.
- [363] O. Altin and S. Eser, “Carbon deposition from thermal stressing of petroleum fuels,” *ACS National Meeting Book of Abstracts*, vol. 228, no. 1, 2004.
- [364] S. Jain and M. P. Sharma, “Review of different test methods for the evaluation of stability of biodiesel,” *Renewable and Sustainable Energy Reviews*, vol. 14, no. 7, pp. 1937–1947, 2010.
- [365] S. Zabarnick, “Chemical kinetic modeling of jet fuel autoxidation and antioxidant chemistry,” *Industrial Engineering Chemistry Research*, vol. 32, pp. 1012–1017, jun 1993.
- [366] D. Wang, A. Violi, D. H. Kim, and J. A. Mullholland, “Formation of naphthalene, indene, and benzene from cyclopentadiene pyrolysis: A DFT study,” *Journal of Physical Chemistry A*, vol. 110, no. 14, pp. 4719–4725, 2006.

- [367] J. Vercammen, M. Bocus, S. Neale, A. Bugaev, P. Tomkins, J. Hajek, S. Van Minnebruggen, A. Soldatov, A. Krajnc, G. Mali, V. Van Speybroeck, and D. E. De Vos, “Shape-selective C–H activation of aromatics to biaryllic compounds using molecular palladium in zeolites,” *Nature Catalysis*, vol. 3, no. 12, pp. 1002–1009, 2020.
- [368] P. J. Steel, “Aromatic biheterocycles: Syntheses, structures, and properties,” *Advances in heterocyclic chemistry*, vol. 67, pp. 2–118, 1997.
- [369] G. Zotti, S. Zecchin, G. Schiavon, R. Seraglia, A. Berlin, and A. Canavesi, “Structure of Polyindoles from Anodic Coupling of Indoles: An Electrochemical Approach,” *Chemistry of Materials*, vol. 6, no. 10, pp. 1742–1748, 1994.
- [370] S. Zabarnick, P. Zelesnik, and R. R. Grinstead, “Jet fuel deposition and oxidation: dilution, materials, oxygen, and temperature effects,” in *Turbo Expo: Power for Land, Sea, and Air*, vol. 78804, p. V003T06A006, American Society of Mechanical Engineers, 1995.
- [371] K. Yang, C. Oses, and S. Curtarolo, “Modeling off-stoichiometry materials with a high-throughput ab-initio approach,” *Chemistry of Materials*, vol. 28, no. 18, pp. 6484–6492, 2016.
- [372] P. L. Bhoorasingh and R. H. West, “Transition state geometry prediction using molecular group contributions,” *Physical Chemistry Chemical Physics*, vol. 17, no. 48, pp. 32173–32182, 2015.
- [373] J. S. Ervin, S. P. Heneghan, C. R. Martel, and T. F. Williams, “Surface effects on deposits from jet fuels,” *Proceedings of the ASME Turbo Expo*, vol. 3, 1995.
- [374] J. Calbo, J. C. Sancho-García, E. Ortí, and J. Aragó, “DLPNO-CCSD(T) scaled methods for the accurate treatment of large supramolecular complexes,” *Journal of Computational Chemistry*, vol. 38, no. 21, pp. 1869–1878, 2017.
- [375] K. Qian, K. E. Edwards, J. H. Diehl, and L. A. Green, “Fundamentals and Applications of Electrospray Ionization Mass Spectrometry for Petroleum Characterization,” 2004.
- [376] C. J. Boushey, A. M. Coulston, C. L. Rock, and E. Monsen, *Nutrition in the Prevention and Treatment of Disease*. Elsevier, 2001.

- [377] V. N. Burd, R. Bantleon, and K. H. Van Pee, "Oxidation of indole and indole derivatives catalyzed by nonheme chloroperoxidases," *Applied Biochemistry and Microbiology*, vol. 37, no. 3, pp. 248–250, 2001.
- [378] "Pubchem."
- [379] E. Tervola, K. N. Truong, J. S. Ward, A. Priimagi, and K. Rissanen, "Fluorescence enhancement of quinolines by protonation," *RSC Advances*, vol. 10, no. 49, pp. 29385–29393, 2020.
- [380] M. C. Sicilia, A. Ni no, and C. Muñoz-Caro, "Mechanism of pyridine protonation in water clusters of increasing size," *Journal of Physical Chemistry A*, vol. 109, no. 37, pp. 8341–8347, 2005.
- [381] R. L. Hinman and E. B. Whipple, "The Protonation of Indoles: Position of Protonation," *Journal of the American Chemical Society*, vol. 84, no. 13, pp. 2534–2539, 1962.
- [382] H. Chen, L. Hakka, R. Hinman, A. Kresge, and E. Whipple, "Basic strength of carbazole. estimate of the nitrogen basicity of pyrrole and indole," *Journal of the American Chemical Society*, vol. 93, no. 20, pp. 5102–5107, 1971.

Chapter 10

Appendix

10.1 Investigations into the SMORS Mechanism

10.1.1 Thermochemical and Kinetic Data

Species	ΔS (kcal molK ⁻¹)	ΔH (kcal mol ⁻¹)	ΔG (kcal mol ⁻¹)
0	0	0	0
PC1	-1.73E-02	-8.63	2.25
TS1	-2.33E-03	8.94	10.40
I1	1.97E-02	0.093	-12.26
PC2	-1.54E-02	-1.42	8.27
TS2	-1.09E-03	12.11	12.80
P1	-8.97E-04	-6.80	-6.24
Quinone Production	-	-	-
P1	0	0	0
PC3	-1.80E-02	-3.92	7.35
TS3	-5.38E-03	2.05	5.43
I2	-1.02E-03	-5.95	-5.31
a-pathway	-	-	-

TS4a	-3.75E-04	34.67	34.91
P2a	3.91E-02	-104.39	-128.92
b-pathway	-	-	-
TS4b	2.06E-04	25.40	25.27
I3b	2.86E-03	-82.52	-84.31
TS5b	8.35E-04	44.79	44.26
P2b	3.48E-02	-57.38	-79.23
c-pathway	-	-	-
TS4c	-5.64E-04	10.52	10.87
P2c	3.95E-02	-108.21	-133.00
d-pathway	-	-	-
I3d	8.39E-03	2.00	-3.27
TS5d	-2.25E-02	4.72	18.84
P2d	2.05E-02	-92.22	-105.08
Other Phenol Oxidation Pathways	-	-	-
a-pathway	-	-	-
P1	0	0	0
PC4a	-1.80E-02	-3.92	8.03
TS6a	-3.60E-03	50.48	51.43
P4	3.90E-02	-38.06	-62.53
b-pathway	-	-	-
PC4b	-2.00E-02	-4.51	8.03
TS6b	-1.51E-03	50.48	51.43
P3	1.27E-02	-68.44	-76.42

SMORS Proposed	-	-	-
0	0	0	0
PC4b	-1.62E-02	-2.61	7.59
TS6b	-4.92E-03	166.97	170.06
P3	-2.05E-03	-116.35	-115.06
SMORS Acid	-	-	-
0	0	0	0
PC5	-2.18E-03	-23.95	-10.26
TS7	-7.95E-04	6.33	6.83
I5	1.31E-04	-8.93	-9.02
TS8	-1.03E-03	6.45	7.10
I6	1.04E-03	-12.42	-13.07
SMORS	1.23E-03	-77.36	-78.13
SMORS HAS pathway	-	-	-
Free-Radical Indole	-	-	-
0	0	0	0
PC6a	-2.05E-03	-7.79	5.08
TS9a	3.99E-04	19.23	19.04
I7a	2.12E-02	6.34	-6.99
PC7a	-1.87E-02	-8.32	3.40
TS10a	-6.34E-04	3.07	3.47
I8a	-1.11E-03	-43.05	-42.35
TS11a	-3.43E-04	47.42	47.64
Free-Radical Quinone	-	-	-

0	0	0	0
PC6b	-1.69E-02	-4.01	6.58
TS9b	-2.03E-03	11.23	12.50
I7b	2.13E-02	3.28	-10.08
PC7b	-1.94E-02	-7.13	5.07
TS10b	-1.26E-03	2.23	3.02
I8b	-2.31E-03	-31.86	-30.41
TS11b	-1.46E-03	1.85	2.76
I9	1.52E-03	-31.22	-32.18
PC8	-2.40E-02	-10.10	4.98
T12	-2.52E-02	12.11	27.92
SMORS	2.49E-02	11.58	-4.04

Table 10.1: Calculated thermochemical and kinetic relative values at the B3LYP-D3//cc-pvTZ *n*-Dodecane PCM level of theory with the exception of the **SMORS Proposed** section which was calculated at the B3LYP-D3//cc-pvDZ *n*-Dodecane PCM level of theory. Enthalpy values are corrected with GoodVibes at 298K.

10.1.2 Intrinsic Reaction Coordinate Calculations

10.1.2.1 TS4c

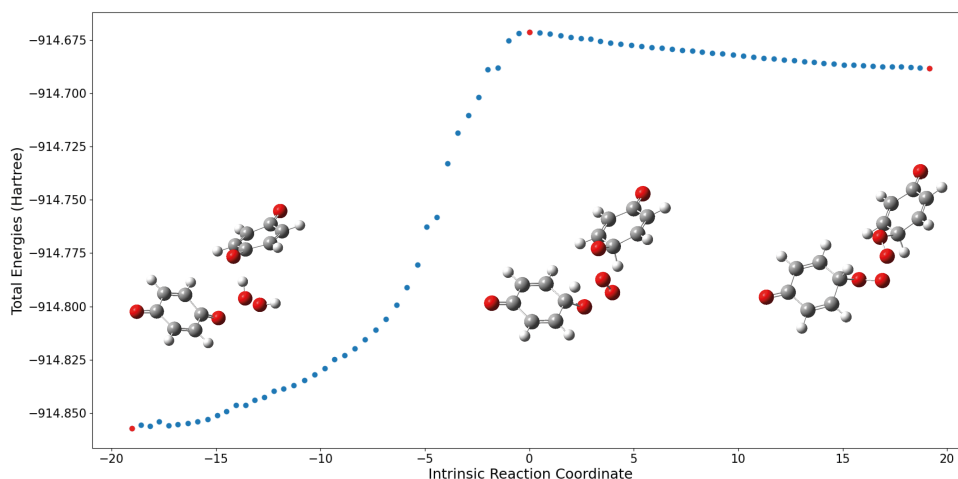


Figure 10.1: TS4c IRC plot. Using the local quadratic approximation for the predictor step

10.1.3 DLNO-CCSD(T) Electronic Energy Corrected Gibbs Energy for Phenol Oxidation

The DLPNO calculations presented in Figure 10.2 show the same overall reactive trend for the production of quinones as the B3LYP-D3//cc-pvTZ level of theory (Figure 4.2). Interestingly, the largest divergence in energies between the pure DFT method and DLPNO-CCSD(T) are found with the separated structures **PC3** and **I3d**. With respect to **PC3**, the addition of the DPNO-CCSD(T) energy correction predicted the B3LYP-D3//cc-pvTZ calculated pre-collision complex to be greater energy than **TS3**. This implies a lower energy pre-collision likely exists or **TS3** proceeds without a pre-collision complex. Likewise, the DPNO-CCSD(T) energy correction led to **TS5d** to be in lower energy than the separated complex **I3d**. Calculation of **TS5** from separated species **ISd2** led to a positive barrier. Differences in these long-range calculations between the B3LYP/cc-pvTZ levels of theory likely arise from the MP2 treatment of weakly correlated long-range electron pairs in the DLPNO method.[374]

The results for the DLPNO-CCSD(T) corrected non-quinone phenol oxidation pathways are presented in Figure 10.3. Once again, the same reactive trend is observed, validating our pure DFT method.

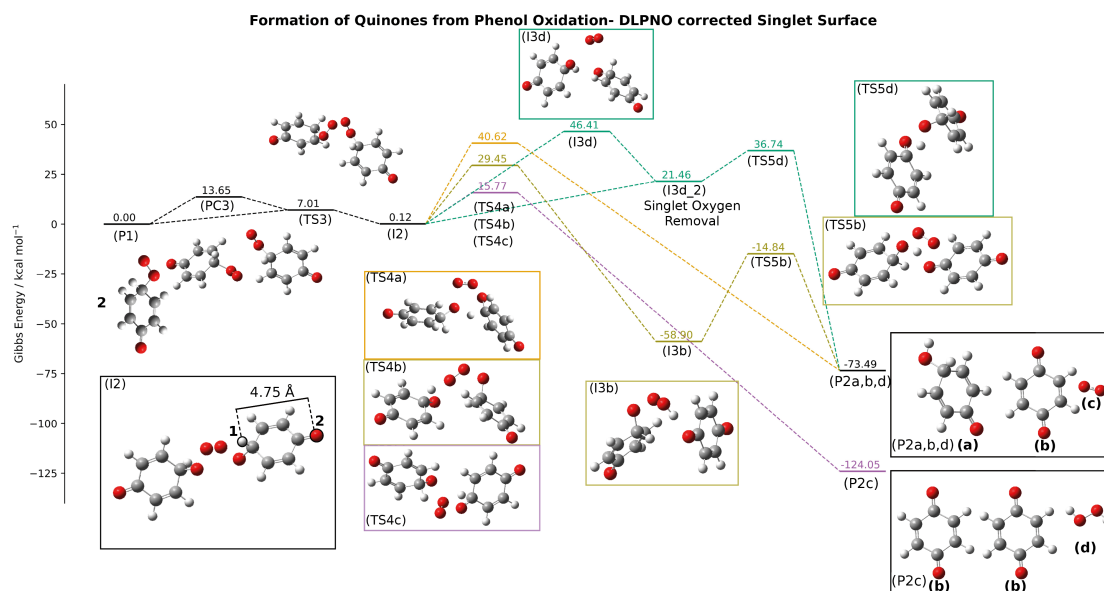


Figure 10.2: Quinone producing pathways on the singlet surface, where electronic energies are corrected by single point DLPNO-CCSD(T)//def2-TZVP calculations which are added to the B3LYP-D3//cc-pvTZ enthalpic and entropic corrections.

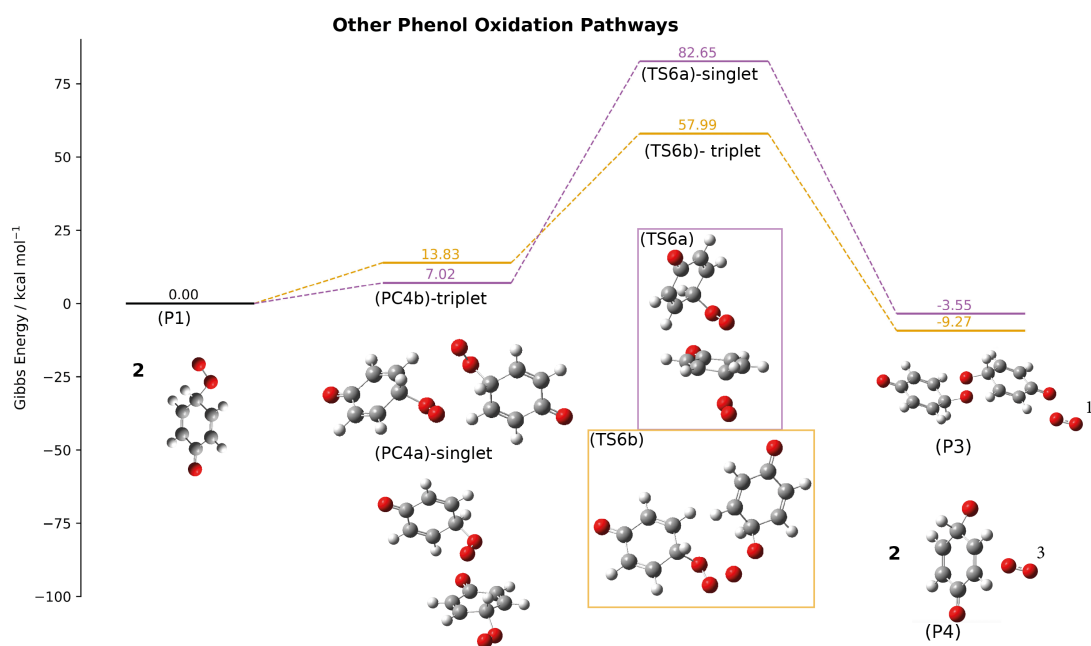


Figure 10.3: Non-quinone phenol oxidation pathways, where electronic energies are corrected by single point DLPNO-CCSD(T)//def2-TZVP calculations which are added to the B3LYP-D3//cc-pvTZ enthalpic and entropic corrections.

10.1.3.1 Pseudo-Detailed Mechanism

A pseudo-detailed mechanism was constructed to explore the production of tetroxide species competing with other autoxidation and AH reaction pathways. The oxygen concentration was kept fixed at 1.8 mmol L^{-1} , representing an open system. The RH concentration was kept at 4.4 mol L^{-1} .^[24] The concentration of AH was varied between 0.1 , 0.01 , and 0.001 mol L^{-1} . The pseudo-detailed mechanism is presented in Table 10.2 and is a combination of autoxidation mechanism presented in reference [76] and our calculated DFT values for AH. The mechanism was run for a 24 h time period at 140°C . The pseudo-detailed mechanism was integrated over time in MATLAB using an in-house code the ode45 solver.

Reaction Step	A	E_a
$\text{RH} \longrightarrow \text{R}\cdot + \text{H}\cdot$	$5.40\text{E}+13$	61.5

$O_2 + RH \longrightarrow RO_2H$	4.90E+06	-8.63
$R\cdot + O_2 \longrightarrow RO_2\cdot$	1.35E+06	0
$RO_2\cdot + RH \longrightarrow RO_2H + R\cdot$	4.75E+10	14.45
$R\cdot + R\cdot \longrightarrow R_2$	2.58E+11	0
$RO_2H \longrightarrow RO\cdot + HO\cdot$	5.00E+13	33
$RO_2H + RO_2H \longrightarrow RO\cdot + RO_2\cdot + H_2O$	1.00E+10	24.1
$HO\cdot + RH \longrightarrow H_2O + R\cdot$	2.50E+09	5.1
$RO\cdot \longrightarrow Rprime + Carbonyl$	2.80E+12	9
$RO\cdot + RH \longrightarrow ROH + R\cdot$	1.80E+09	5.3
$Rprime + RH \longrightarrow alkene + R\cdot$	1.10E+09	10.1
$RO_2\cdot \longrightarrow R\cdot + O_2$	1.00E+16	18.9
$RO_2\cdot + RO\cdot \longrightarrow RO_2H + Carbonyl$	1.10E+09	10.5
$RO_2\cdot + RO_2\cdot \longrightarrow RO\cdot + RO\cdot + O_2$	9.60E+10	0
$RO\cdot + RO\cdot \longrightarrow Carbonyl + ROH + O_2$	1.10E+09	17.5
$AH + RO_2\cdot \longrightarrow RO_2H + A\cdot$	2.67E+12	8.94
$RO\cdot + RO\cdot \longrightarrow ROOR$	2.70E+09	0
$A\cdot + RH \longrightarrow AH + R\cdot$	1.72E+12	21.10
$AH + R\cdot \longrightarrow A\cdot + RH$	8.61E+12	8.24
$AH + RO\cdot \longrightarrow A\cdot + ROH$	3.78E+12	0.295
$A\cdot + A\cdot \longrightarrow Insoluble$	3.00E+09	0
$AH + A\cdot \longrightarrow AHA(.)$	1.82E+12	20.05
$AHA(.) + RO_2H \longrightarrow Insoluble + RO\cdot + H_2O$	4.30E+08	7.87
$A\cdot + ROH \longrightarrow AH + RO\cdot$	2.36E+12	15.94
$A\cdot + ROOH \longrightarrow AH + ROO\cdot$	4.99E+12	8.49

$A \cdot + O_2 \longrightarrow \text{KetoPeroxy}$	8.94E+09	12.11
$\text{KetoPeroxy} + \text{KetoPeroxy} \longrightarrow \text{Tetroxide}$	3.00E+09	0

Table 10.2: Psuedo-Detailed Mechanism for tetroxide production, where AH values are calculated at the B3LYP-D3//cc-pVTZ level of theory. Here AH represents a phenolic species. The RH reaction parameters are found in refernce [76] and are calibrated for *n*-dodecane. For bimolecular reactions, the units of the pre-exponential factor A are $\text{L mol}^{-1} \text{s}^{-1}$ for bimolecular reactions and s^{-1} for unimolecular reactions. The units of E_a are kcal mol^{-1} .

The change in ROH and Tetroxide concentration over time is presented in Figure 10.4, and the concentration of all the species at the end of the run is presented in Table 10.3. It is clear that although the concentration of tetroxide is low, it competes directly with the autoxidation of *n*-dodecane. In fact, lower concentrations of phenol lead to higher concentrations of tetroxide, potentially due to higher concentrations of phenol suppressing chain carriers.

10.1.4 Flask Test

A surrogate fuel was built using 0.1 mol L^{-1} indole (Sigma Aldrich, >99%) and phenol (ACROS Organics, >99%) added to *n*-dodecane (ACROS Organics, >99%). The flask was heated to 140°C under 1 bar molecular oxygen for 24 h. The deposit and the stressed solution were dissolved in 5 mL of trisolvent, a mixture of 1:1:1 methanol (SLS, $\geq 99.8\%$), toluene (SLS, $\geq 99.5\%$) and acetone (SLS, >99%). The trisolvent mixture was analyzed in negative LCMS mode because the expected SMORS species contain acidic phenolic -OH groups.

For LCMS an Agilent Technologies 6530 Accurate Mass LC-MS QToF instrument was used. The samples were directly injected into the a Agilent Zorbax Extend-C18 $2.1 \text{ mm} \times 50 \text{ mm}$, $1.8 \mu\text{m}$ column. The mobile phase was run at a 20 : 1 ratio of 70 : 30 acetonitrile:water containing 0.1% formic acid to water for the first 10 min. For the next two minutes the ratio was switched to 1 : 20 70 : 30 acetonitrile:water containing 0.1% formic acid. Then for the remaining 3 min the final solvent mixture was 20 : 1 ratio of 70 : 30 acetonitrile:water containing 0.1% formic acid to water. The mass spectrometer on the LCMS was operated at 350°C with a pressure of 45 psig. Data was collected over a 50-3000 m/z range, with a 4000 V capillary

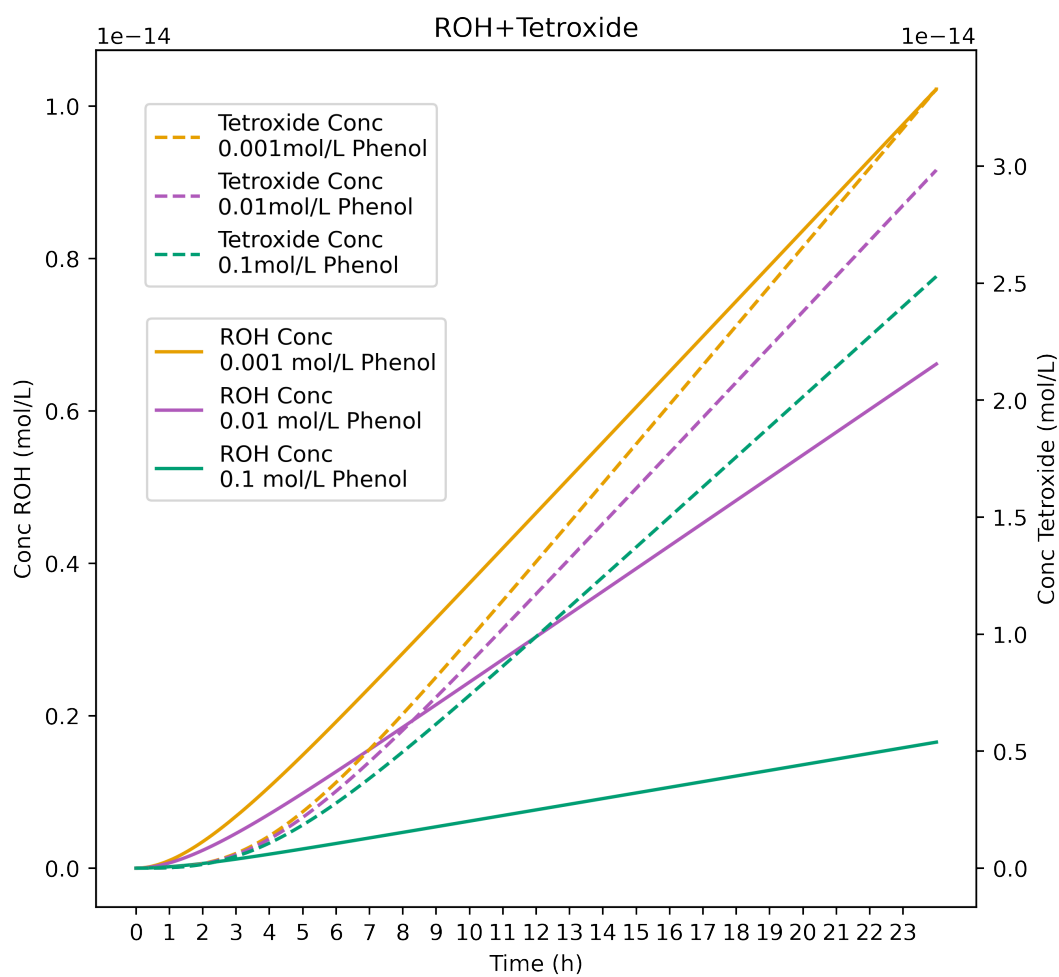


Figure 10.4: Comparison of ROH and Tetroxide concentration formed from the keto peroxy self-reaction produced from the mechanism presented in Table 10.2

Species	Phenol Concentration		
	0.1mol/L	0.01mol/L	0.001mol/L
R.	1.83E-26	1.84E-25	1.88E-24
O2	1.80E-03	1.80E-03	1.80E-03
RO2.	4.15E-27	1.66E-25	2.42E-24
RH	4.40E+00	4.40E+00	4.40E+00
RO2H	1.20E-16	4.83E-16	7.64E-16
R2	7.43E-36	7.40E-34	7.65E-32
RO.	7.78E-32	3.13E-30	4.84E-29
OH.	9.35E-28	3.77E-27	5.96E-27
ROH	1.65E-15	6.62E-15	1.02E-14
Rprime	1.72E-28	6.92E-27	1.07E-25
Carbonyl	3.02E-19	1.21E-17	1.86E-16
H2O	1.65E-15	6.63E-15	1.04E-14
alkene	3.02E-19	1.21E-17	1.86E-16
AH	1.00E-01	1.00E-02	1.00E-03
A.	2.06E-22	2.42E-22	2.70E-22
H.	5.83E-14	5.83E-14	5.83E-14
HOO.	1.29E-17	1.29E-17	1.29E-17
ROOR	1.27E-48	2.03E-45	4.81E-43
AHA	7.90E-17	9.19E-18	1.02E-18
Insoluble	1.21E-23	5.61E-24	9.71E-25
KetoPeroxy	1.09E-14	1.18E-14	1.25E-14
Tetroxide	2.53E-14	2.98E-14	3.33E-14

Table 10.3: Species concentration after running the mechanism presented in Table 10.2 for a 24 h time period at 140 °C

voltage, fragmenter voltage of 125 V. A Duel ESI ion source allowed for real-time mass accuracy calibration, allowing for probably chemical formulas of the ions to be elucidated. All the solutions were analyzed in negative mode.

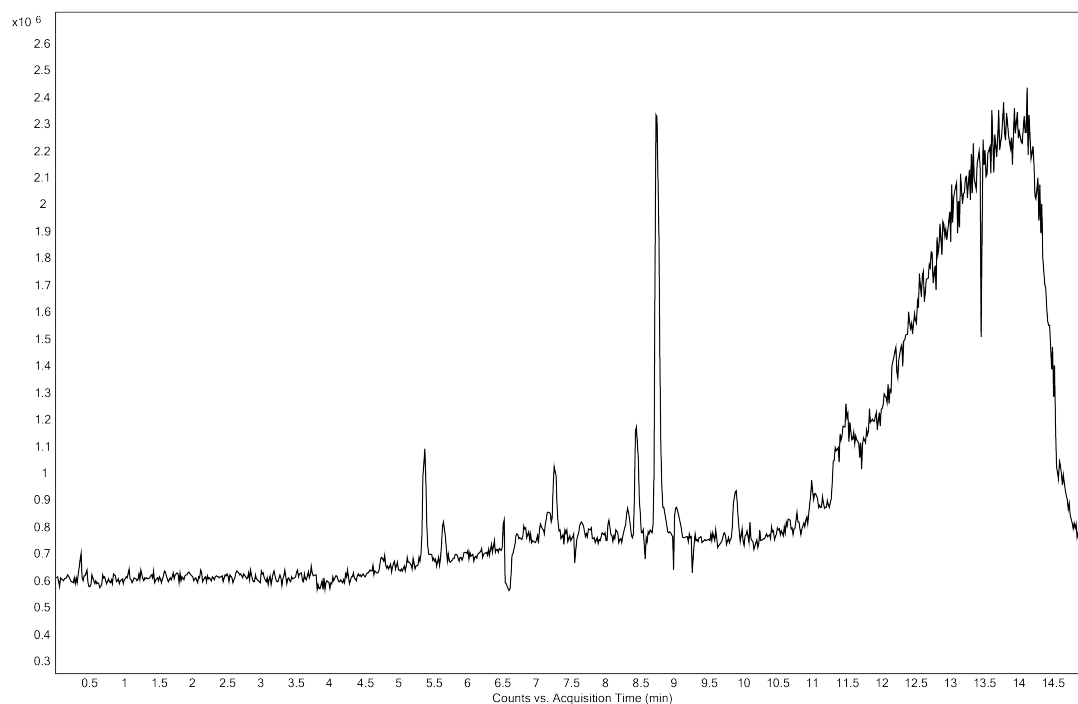
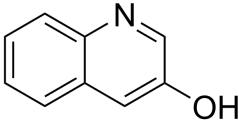
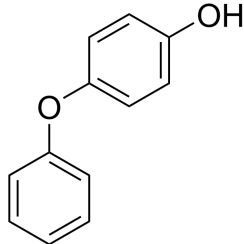
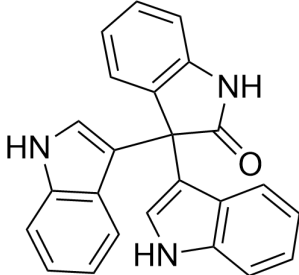
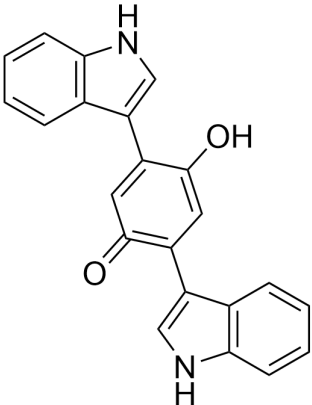
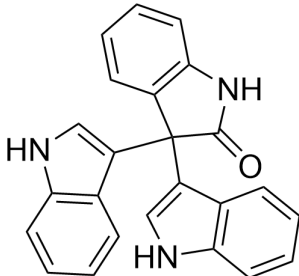


Figure 10.5: Chromatogram of (-)LCMS indole + phenol in *n*-dodecane deposit/solution solvent.

Acquisition Time (min)	Mass Measured [M-H] ⁻	Elemental Formula	Deviation from Actual Mass (ppm)	Possible Structures
0.390	Background	-	-	
5.382	164.0354	C ₈ H ₇ NO ₃	-0.65	

5.664	144.0452	C_9H_7NO	2.29	
6.543	226.9754	No Formula	-	
7.273	185.0609	$C_{12}H_{10}O_2$	-0.49	
8.069	362.1318	$C_{24}H_{17}N_3O$	-5.55	
8.318	339.1154	$C_{22}H_{16}N_2O_2$	-4.31	
8.451	362.1319	$C_{24}H_{17}N_3O$	-5.08	

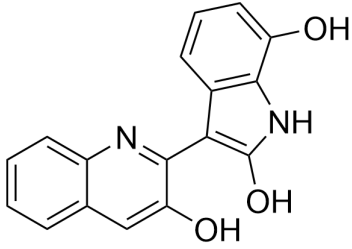
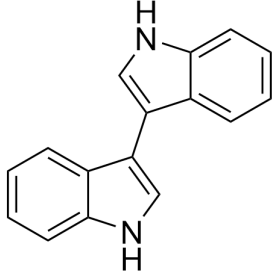
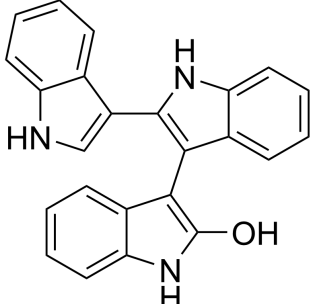
8.749	293.0954	$C_{17}H_{14}N_2O_3$	-3.18	
9.031	231.0930	$C_{16}H_{12}N_2$	-1.18	
9.031	317.1191	$C_{21}H_{18}O_3$	-2.54	?
9.894	380.1418	$C_{24}H_{19}N_3O_2$	-1.23	

Table 10.4: Compounds detected by (-)LCMS in the 0.1 mol L^{-1} indole + phenol in *n*-dodecane deposit/solution solvent. Entries assigned ? could not be identified with confidence.

A second surrogate using the above method but with the addition of 0.1 mol L^{-1} dodecanethiol (Oakwood Chemicals, >98%)

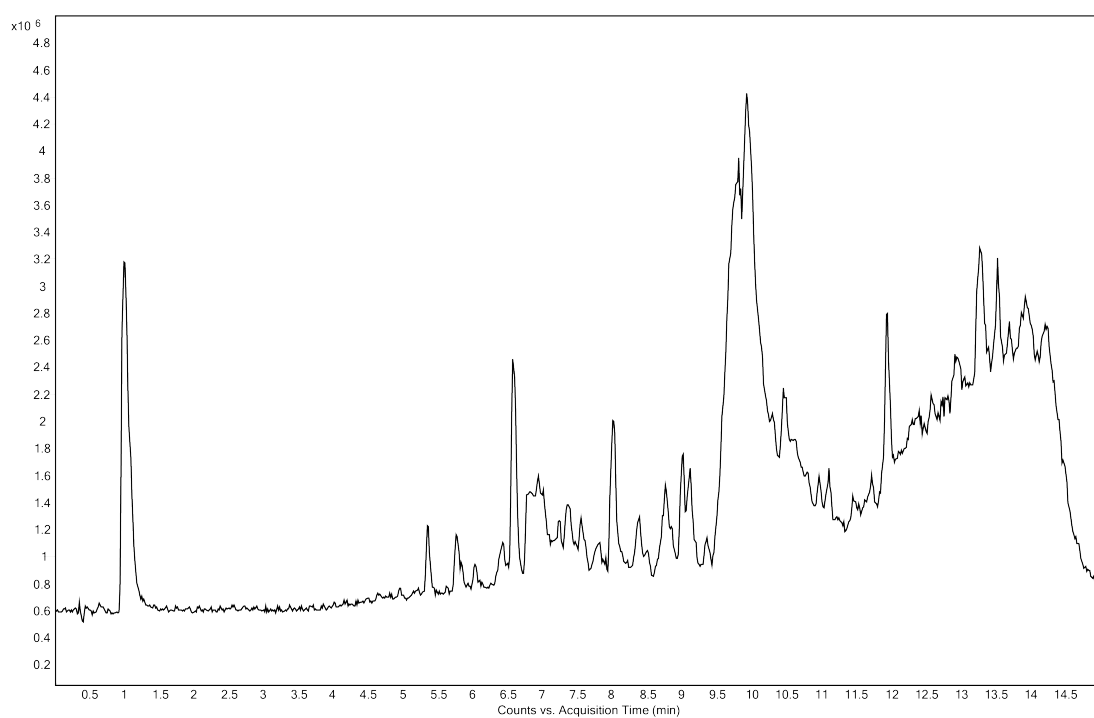
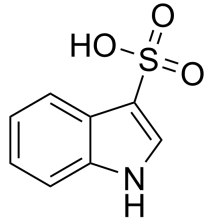
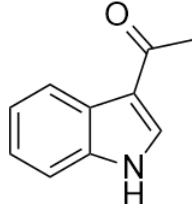
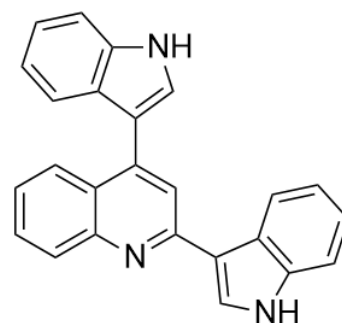
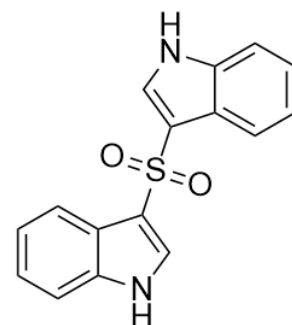


Figure 10.6: Chromatogram of (-)-LCMS indole + phenol + dodecanethiol in *n*-dodecane deposit/solution solvent.

Acquisition Time (min)	Mass Measured [M-H] ⁻	Elemental Formula	Deviation from Actual Mass (ppm)	Possible Structures
0.986	196.0079	C ₈ H ₇ NO ₃ S	-2.01	
5.381	164.0332	No Formula	-	-
5.845	158.0609	C ₁₀ H ₉ NO	2.04	

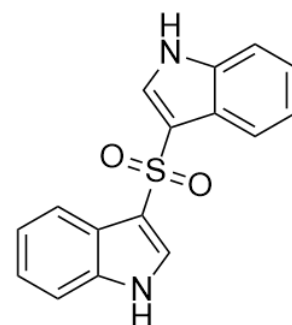
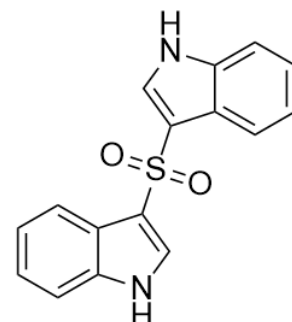
6.028	389.1168	$C_{19}H_{22}N_2O_5S$	1.81
6.442	279.0598	$C_{16}H_{12}N_2OS$	-0.13
6.591	358.1364	$C_{25}H_{17}N_3$	-3.40
6.790	358.1142	$C_{16}H_{25}NO_4S$	3.21
6.790	472.0936	$C_{28}H_{15}N_3O_5$	1.45
6.940	295.0550	$C_{16}H_{12}N_2O_2S$	-1.08
7.023	295.0550	$C_{16}H_{12}N_2O_2S$	-0.98
7.255	604.2110	$C_{40}H_{31}NO_5$	1.97
7.255	705.2417	$C_{52}H_{34}O_3$	2.19
7.387	475.1579	$C_{32}H_{20}N_4O$	-2.66

?



?

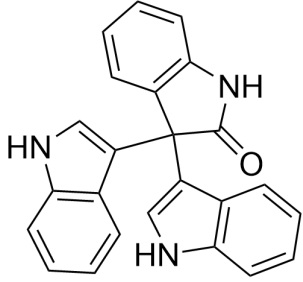
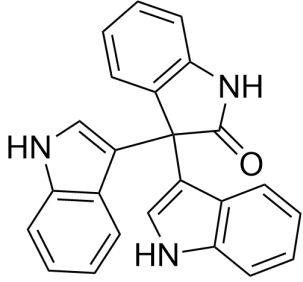
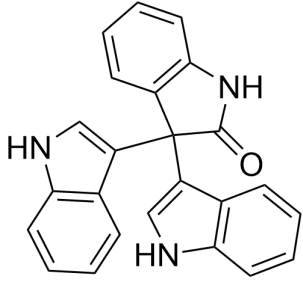
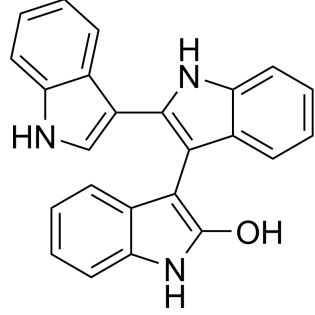
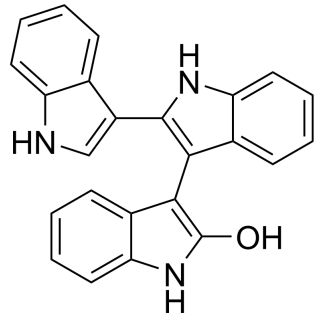
?



?

?

Oxidized Indole Tetramer

7.553	576.2197	$C_{40}H_{27}N_5$	-0.84	Indole Pentamer
8.018	362.1311	$C_{24}H_{17}N_3O$	-2.89	
8.399	362.1306	$C_{24}H_{17}N_3O$	-1.49	
8.781	362.1305	$C_{24}H_{17}N_3O$	-1.10	
9.029	231.0930	$C_{16}H_{12}N_2$	-1.23	
9.129	477.1734	$C_{24}H_{19}N_3O_2$	-1.23	

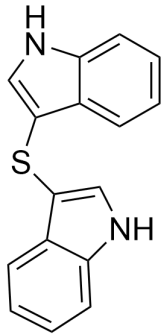
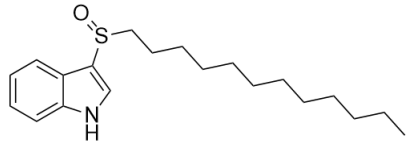
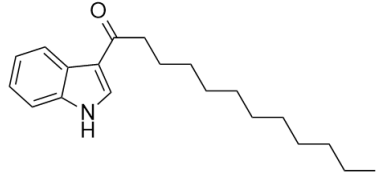
9.378	263.0646	$C_{16}H_{12}N_2S$	0.73	
9.809	249.1541	$C_{12}H_{26}SO_3$	-3.84	Dodecane Sulfonic Acid
9.942	249.1534	$C_{12}H_{26}SO_3$	-1.35	Dodecane Sulfonic Acid
10.456	249.1534	$C_{12}H_{26}SO_3$	-1.35	Dodecane Sulfonic Acid
10.456	601.1880	$C_{37}H_{30}O_8$	-1.37	?
10.970	314.2125	$C_{20}H_{29}NO_2$	-0.01	Indole + Dodecane Ester
10.970	428.2055	$C_{19}H_{31}N_3O$	0.73	Indole + Undecane Ester
10.970	512.2704	$C_{35}H_{35}N_3O$	0.90	?
10.970	629.2638	$C_{34}H_{37}N_5O$	-2.47	?
11.030	332.2057	$C_{20}H_{31}NOS$	-0.86	
11.948	298.2185	$C_{20}H_{29}NO$	-2.30	
13.292	624.2850	$C_{40}H_{39}N_3O_4$	3.16	? (too many hydrogens for SMORS)
11.03	332.2057	$C_{44}H_{42}N_4O_2$	-0.86	? (too many hydrogens for SMORS)

Table 10.5: Compounds detected by (-)LCMS in the 0.1 mol L⁻¹ indole + phenol + dodecanethiol in *n*-dodecane deposit/solution solvent. Entries assigned ? could not be identified with confidence.

10.2 The Interaction of Nitrogen Heteroatomics with Sulfur

10.2.1 Hansen Solubility Sphere and Table of Sphere Calibration Data

In Hansen solubility theory, three Hansen solubility parameters (HSPs) are assigned to each molecule: δD for dispersion, δP for polarity, and δH for hydrogen bonding. As a consequence, each solvent exists in a 3-dimensional space of HSPs. The HSP distance between two molecules in the 3d HSP space is given by:

$$Ra^2 = 4(\delta D_1 - \delta D_2)^2 + (\delta P_1 - \delta P_2)^2 + (\delta H_1 + \delta H_2)^2 \quad (10.1)$$

Where R_a is the Hansen distance.

The HSP parameters for the test solvents were either obtained from the HSPIP dataset or calculated using the software. The HSPIP software requires a series of test solvents/solutes, tested for their solubility in the *n*-dodecane. A score 0 is assigned to insoluble solvents and a score of 1 is assigned to soluble solvents. In each case, 0.1 mol L^{-1} of each test compound was added to 5 mL of *n*-dodecane. Resulting from the series of tests is a 'sphere' in 3d HSP space, whose dimensions are determined by the solubility of the sphere. The radius of sphere R_0 is then used to assess the solubility of a proposed solvent, where R_a of the test molecule is used in the following equation:

$$RED = R_a/R_0. \quad (10.2)$$

Where RED stands for Relative Energy Difference. A $RED > 1$ implies the molecule is likely insoluble in your main solvent (*n*-dodecane in this case), whereas a $RED < 1$ implies the molecule is soluble. Our calculated sphere was composed of 13 lab grade compounds known for their presence in fuel, and gave a fit of 1 according to HSPIP software. The results for these tests are presented in Table 10.6 in the appendix. Here it is important to acknowledge that the solubility of the deposit precursors in pure *n*-dodecane this study will likely be different to a conventional fuel due to the presence of aromatic compounds and minor components. Nevertheless, these parameters are useful to understand insoluble formation our surrogate fuel, and to improve the HSP method for future studies.

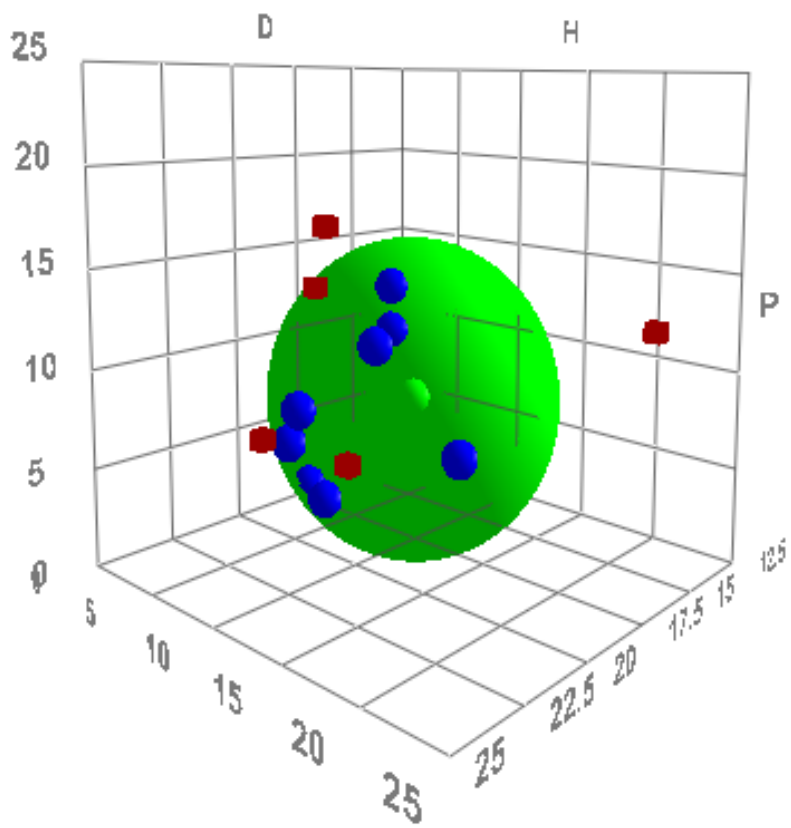


Figure 10.7: HSPIP Sphere

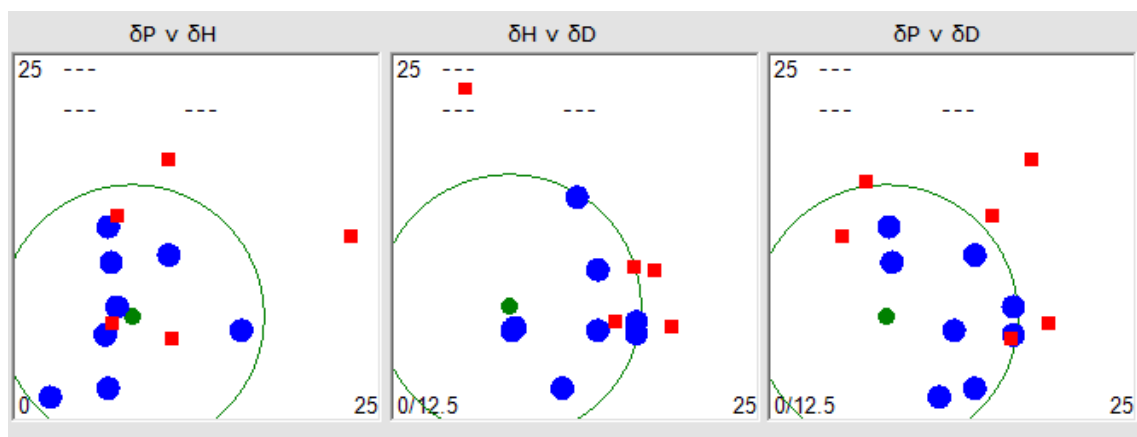


Figure 10.8: HSPIP Sphere parameter fits

Table 10.6: Hansen Solubility test solvents and their Associated HSPs. The sphere gave a fit of 1.000

Solvent	Database/Calculated HSP	δD	δP	δH	Score	RED
Indigo	Calculated	21.10	17.4	10.0	0	1.639
Carbazole	Database	21.7	6.4	6.2	0	1.243
p-Benzoquinone	Database	19.8	13.7	6.5	0	1.121
Water	Database	15.5	16.0	42.3	0	4.042
2-Naphthol	Database	20.4	5.4	10.2	0	1.000
Methanol	Database	14.7	12.3	22.3	0	1.800
Di- <i>n</i> -Butyl Sulfoxide	Database	16.4	10.5	6.1	1	0.443
Naphthalene	Database	19.2	2.0	5.9	1	0.884
Pyrrole	Database	19.2	11.0	10.0	1	0.863
Dipropyl Sulfone	Database	16.3	12.9	5.9	1	0.705
Toluene	Database	18.0	1.4	2.0	1	0.961
Indole	Database	20.5	7.5	6.5	1	0.973
Phenol	Database	18.5	5.9	14.9	1	0.979
Quinoline	Database	20.5	5.6	5.7	1	0.995

10.2.2 Analysis of Clean Solutions

All solutions were analyzed in the trisolvent matrix apart from the clean indole solution.

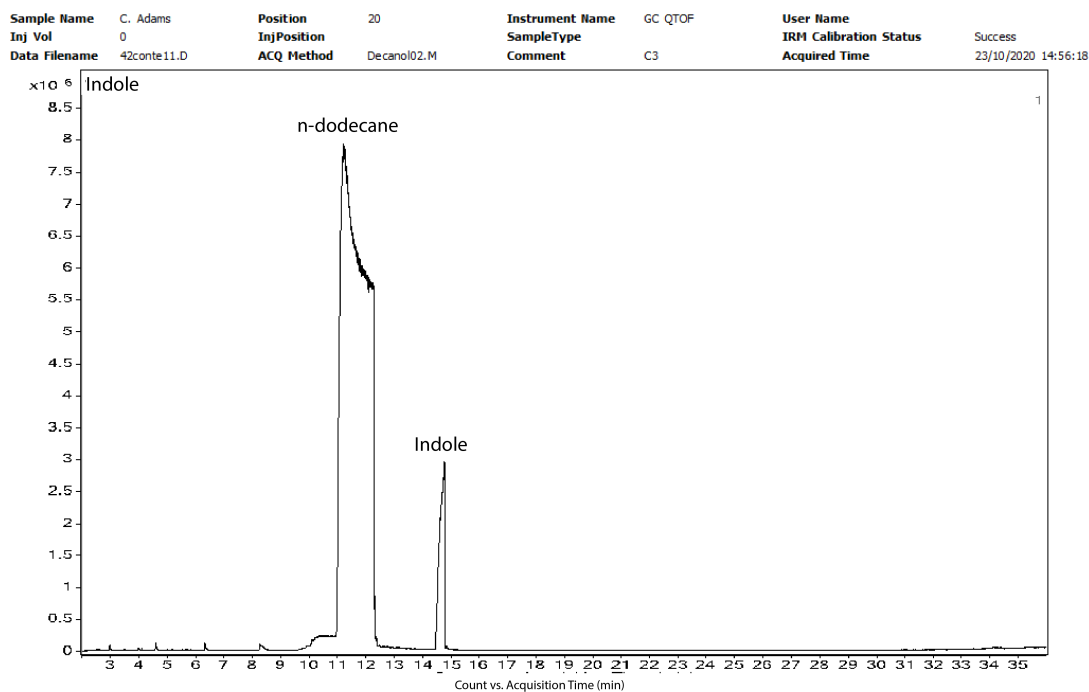


Figure 10.9: Clean Indole GCMS analysis

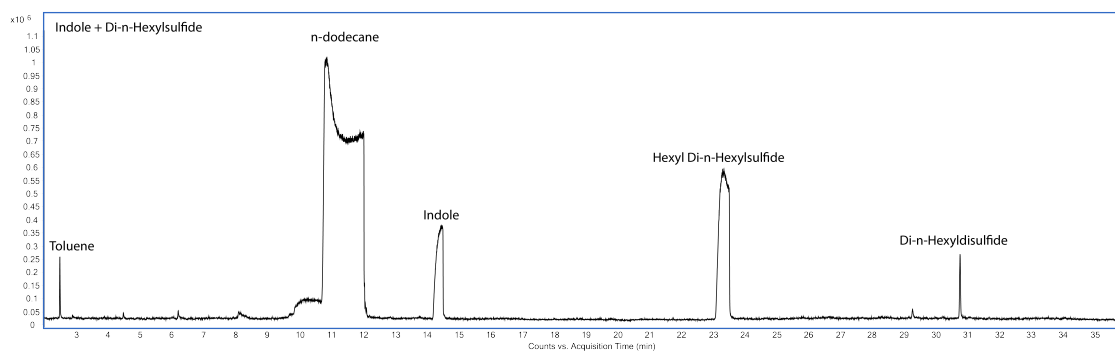


Figure 10.10: Clean Indole + Hexyl-*n*-Sulfide GCMS analysis

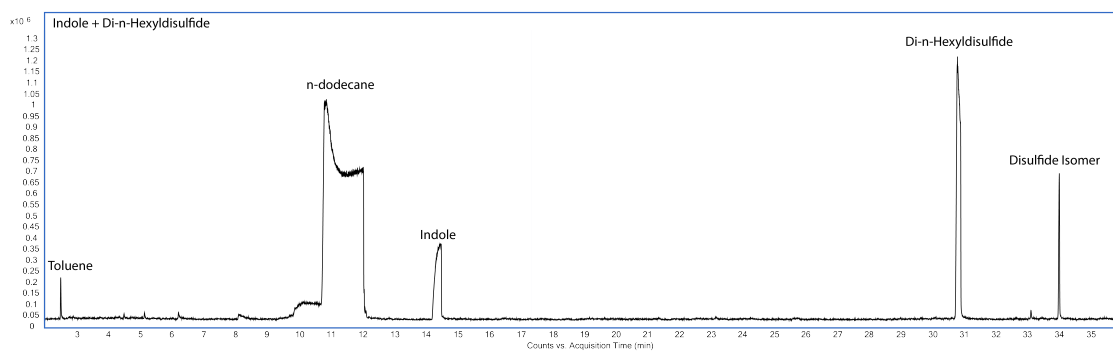


Figure 10.11: Clean Indole Hexyl-*n*-Disulfide GCMS analysis

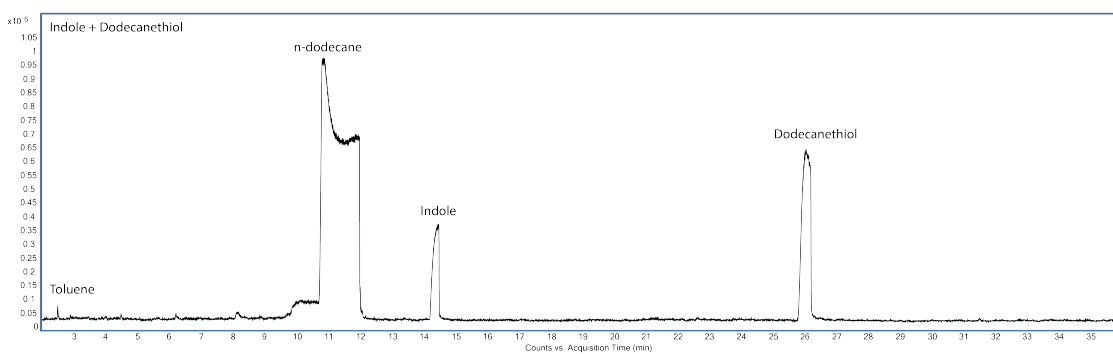


Figure 10.12: Clean Indole Dodecanethiol GCMS analysis

10.2.3 GCMS Analysis of Stressed *n*-Dodecane

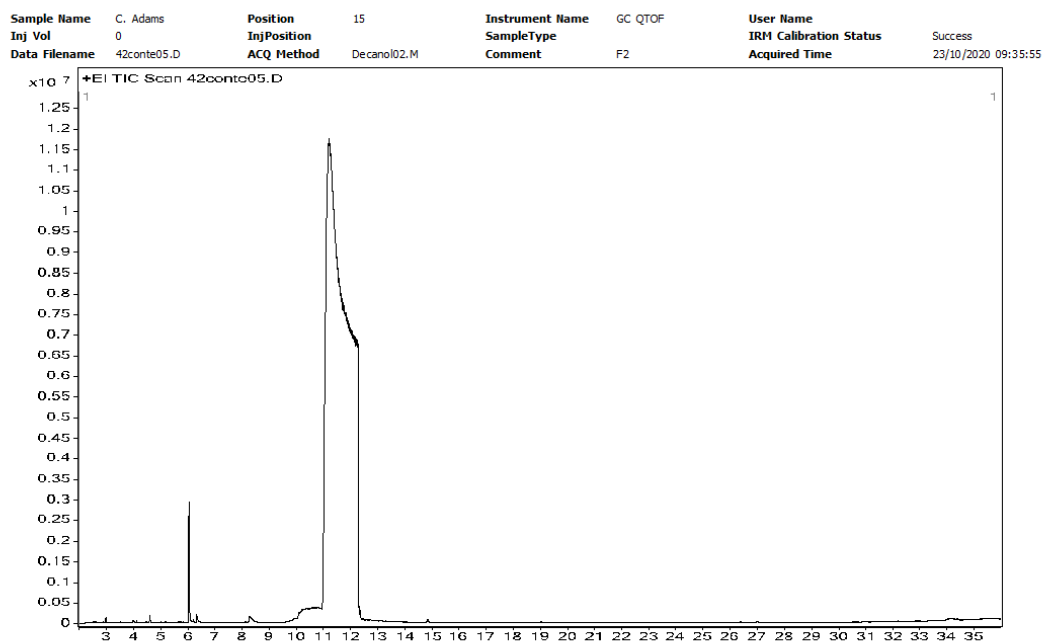


Figure 10.13: Clean *n*-dodecane GC chromatogram

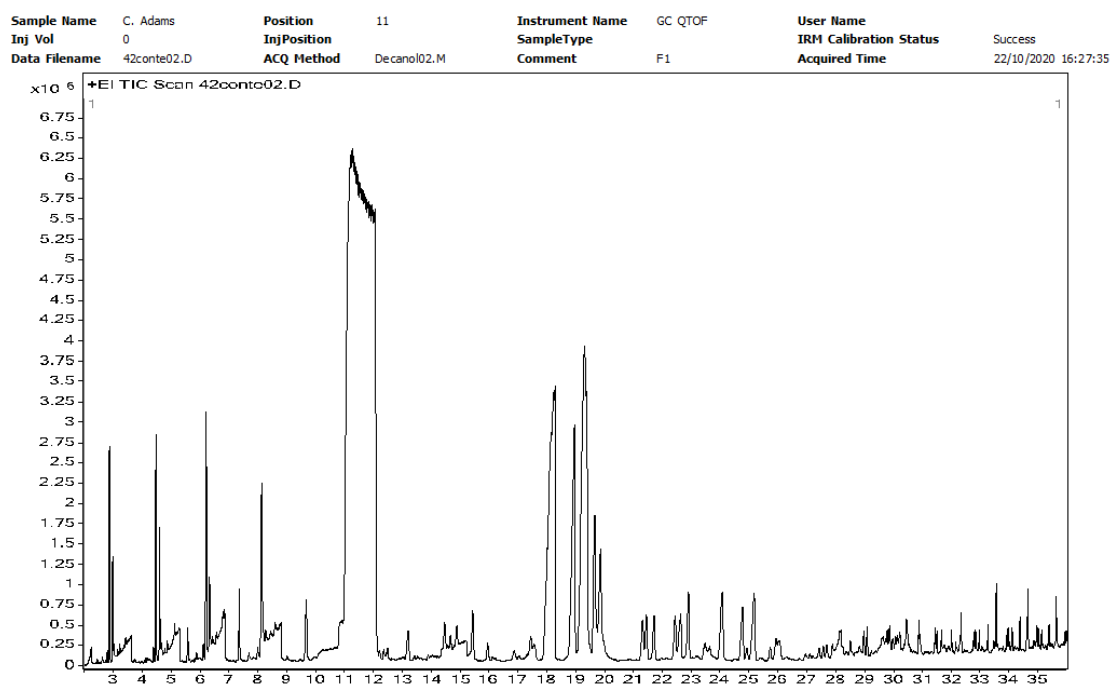


Figure 10.14: Stressed *n*-dodecane GC-MS chromatogram run 1

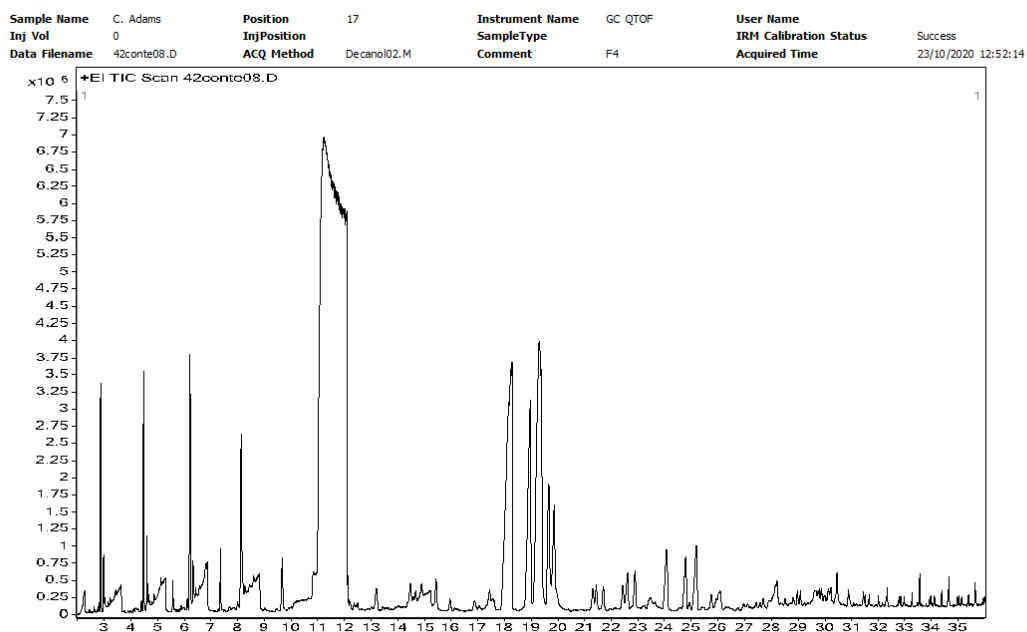


Figure 10.15: Stressed *n*-dodecane GC-MS chromatogram run 2

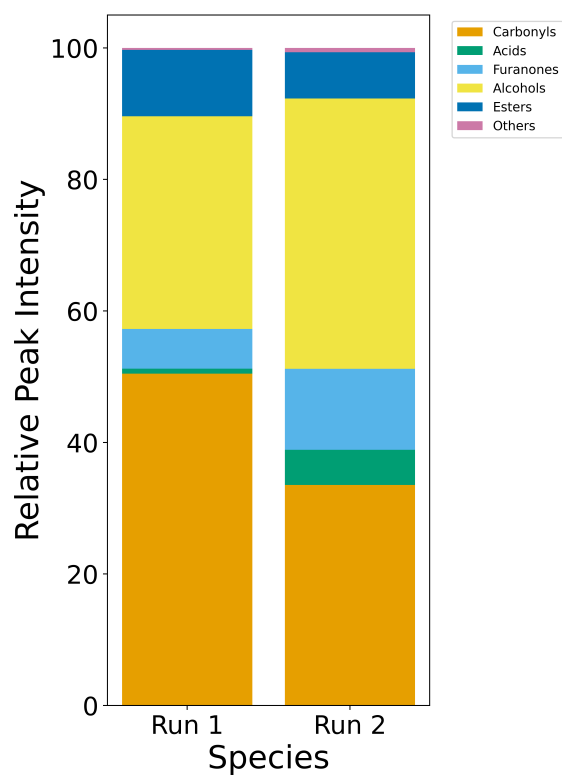


Figure 10.16: GC relative peak intensities of oxygenated species detected by MS in *n*-dodecane stressed for 24 h at 140 °C

10.2.4 Sediment Masses and Appearance of Flasks from Indole Runs



Figure 10.17: Visual comparison of the indole, indole+hexyl sulfide, indole+hexyl disulfide and indole+dodecanethiol flasks

Mixture	Deposit Mass (g)
Indole	0.0064
Indole + Di- <i>n</i> -Hexyl Sulfide	0.0292
Indole + Di- <i>n</i> -Hexyl Disulfide	0.0132
Indole + 1-Dodecanethiol	0.0962

Table 10.7: Deposit masses generated after 24 h thermal stressing at 140 °C in 1 bar oxygen

10.2.5 Indole Analysis

The results of the 8h indole thermal stressing experiment will be discussed in this section, supported by the direct analysis of deposit by LCMS and GCMS analysis of the methanol extract of the stressed solution. After 8hrs of thermal stressing the indole flask produced a yellow hazy color, with minimal visible deposits. Gravimetric analysis of these deposits are presented in Table 10.7. More peaks were observed in (+)LCMS (Figure 10.18) than negative-ion mode (Figure 10.20) since the basic nitrogen is more amenable to protonation forming the $[M+H]^+$. [375] The deposit that was dissolved in *n*-dodecane analyzed in positive mode presented in Figure 10.18. A majority of peaks (**a**, **b**, **d**, **e**, **f**, **g**) are associated with indole oxidative coupling. Selected putative structures for the compounds detected in positive ion mode are presented in Figure 10.19. Some of the oxidative coupling products contained oxidized indole groups (**1** and **3**), however indole oligomers were also formed without the involvement of oxidized indoles (**2**, $C_{24}H_{15}N_3$). Oxindole was predicted to be more likely be detected in positive ion mode as a carbonyl group is more weakly basic than alcohol groups, therefore more amenable to protonation. The oxidative coupling products involve the formation of indoline moieties within the deposit structure (**2**), which are expected to occur from coupling reactions between indoles. The relative size of the LCMS peaks indicate the majority of deposits is formed from **1** and **2**. Interestingly, no indole dimers were observed in the deposits, only trimers and larger oligomers, which could imply that dimers still remain in solution. Nonetheless, Hansen solubility analysis of a proposed indole dimer gives a RED value of 1.13, suggesting that the dimer would be insoluble in *n*-dodecane, which implies that dimers formed here are quickly consumed to form larger oligomers.

In addition to indole coupling products, the compound $C_{14}H_{17}NO_5$ was observed whose structure could not be assigned with confidence. In order to elucidate the ion we can turn to the GCMS analysis performed. GCMS chromatograms of the LLE concentrated thermally stressed solution (Figure 10.22) indicates the presence of indole-esters. Indole esters could form from acids formed from the autoxidation of *n*-dodecane reacting with the basic nitrogen on the indole, possibly forming the $C_{14}H_{17}NO_5$ detected. The GCMS chromatogram also indicates the presence of products of *n*-dodecane oxidation as different ketones. Compared to the pure *n*-dodecane stressed GCMS chromatogram (in Figure 10.13, 10.14 and 10.15), the presence of

other *n*-dodecane autoxidation products was markedly reduced implying indole is acting as an antioxidant here. By contrast, Zabarnick *et al.* found that indole added to a surrogate solvent at a lower 100 mg L^{-1} concentration had a little effect on the headspace oxygen content, suggesting indole had neither pro- or antioxidant properties. Ion suppression can be ruled out as a reason for the reduced detection of *n*-dodecane products because *n*-dodecane autoxidation products retain for different times to the heteroatoms used (see chromatograms in section 10.2.3). [376] Unfortunately, the GCMS chromatogram was unable to identify any more information about the indole coupling products other than the indole ester peak detected from the concentrated stressed solution. Presumably, the low-volatility/low-concentration of the coupling products meant that further information about the deposit pre-cursors could not be found.

Looking at the (-)LCMS chromatogram, there is evidence of indole oxidative coupling products and an oxidized indole species (Table 10.9). The compound identified at peak **a** in the negative chromatogram with the formula $\text{C}_8\text{H}_7\text{NO}_3$ could be a number of oxidized species containing acidic functional groups. Several possible structures of the $\text{C}_8\text{H}_7\text{NO}_3$ compound are presented in Figure 10.21 as **5a**, **5b**, and **5c**. The peaks observed for (-)LCMS are more likely to contain acidic functional groups like $-\text{OH}$ and $-\text{COOH}$ groups due to the greater tendency to form $[\text{M}-\text{H}]^-$ ions. The formation of indole acids via ring opening reactions has been documented previously [377] and has been suggested to occur in fuel.[64] The ions $\text{C}_{24}\text{H}_{13}\text{N}_3\text{O}$ (**4**) and $\text{C}_{24}\text{H}_{17}\text{N}_3\text{O}$ are evidence of indole trimers, also detected in positive ion mode. The ion $\text{C}_{28}\text{H}_{15}\text{N}_3\text{O}$ has excess carbons to be conclusively assigned to an indole trimer, and too few hydrogens to arise from the reaction with an *n*-dodecane fragment. Results from the Pubchem online chemical database indicate the possibility of several aromatic structures, potential arising from the rearomatization of indole ring-opening products.[378]

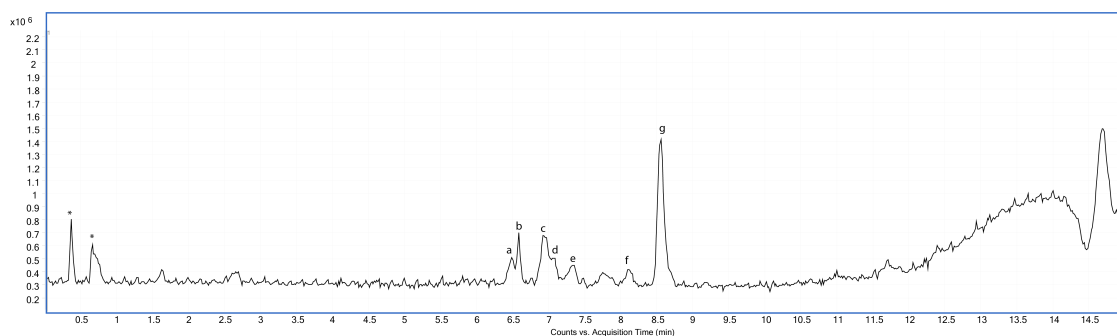


Figure 10.18: (+)LCMS chromatogram for indole 0.1 mol l^{-1} deposit dissolved in trisolvent, background ions highlighted in with a *, all other species detected labelled with roman characters presented in Table 10.8.

Peak Label	Chemical Formula	Mass Measured $[M+H]^+$	Deviation from Actual Mass [ppm]
a	$C_{24}H_{15}N_3O$	362.1305	-5.08
b	$C_{24}H_{17}N_3O$	364.1453	-2.06
c	$C_{14}H_{17}NO_5$	280.1172	-1.07
d	$C_{24}H_{13}N_3O$	360.1142	-2.93
e	$C_{32}H_{26}N_4$	467.2236	-0.90
f	$C_{24}H_{15}N_3$	346.1351	-3.51
g	$C_{24}H_{17}N_3O$	364.1457	-3.38
g	$C_{48}H_{34}N_6O_2$	749.2648 ¹	-1.15

Table 10.8: Peaks associated with (+)LCMS in figure 10.8. Selected possible structures for **b,e** and **g**. Sample(s) labelled with 1 were found as $[M+Na]^+$ adducts

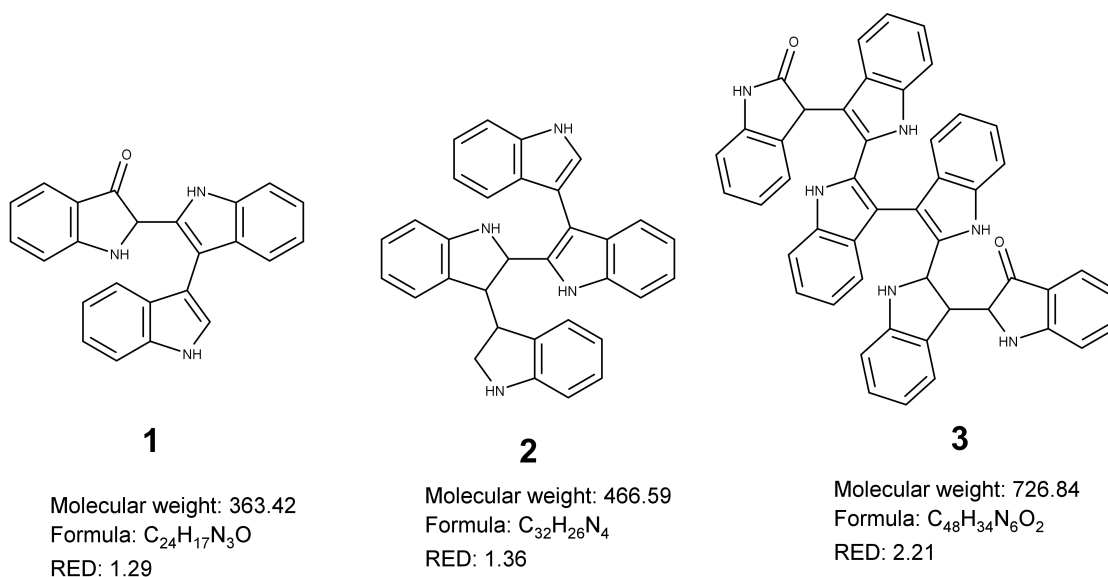


Figure 10.19: Selective putative structures found in (+)LCMS from the 8h indole run from table 10.8. The RED based on calculated HSP are presented for each structure.

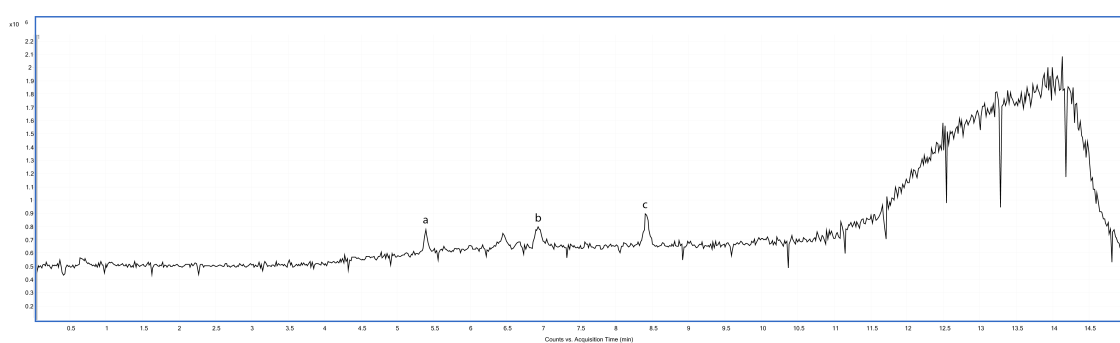


Figure 10.20: (-)LCMS chromatogram for indole 0.1 mol l⁻¹ deposit dissolved in trisolvent, background ions highlighted in with a *, all other species detected labelled with roman characters presented in table

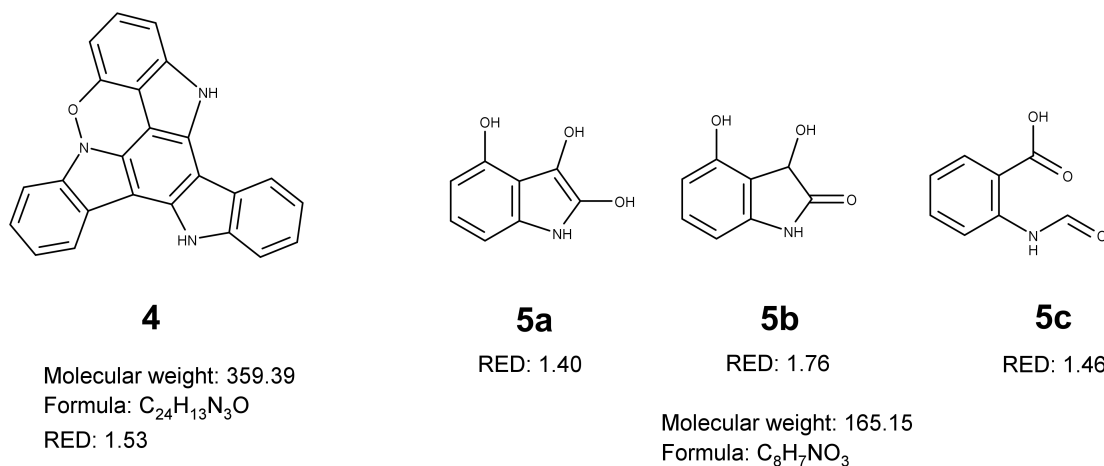


Figure 10.21: Selective putative structures analyzed found in (-)LCMS from the 8h indole run from table 5.1. The RED based on calculated HSP are presented for each structure.

Peak Label	Chemical Formula	Mass Measured $[M-H]^-$	Deviation from Actual Mass [ppm]
a	$C_8H_7NO_3$	164.0349	+2.52
b	$C_{24}H_{13}N_3O$	358.0990	-2.67
b	$C_{28}H_{15}N_3O$	472.0918	+4.81
c	$C_{24}H_{17}N_3O$	362.1306	-1.51

Table 10.9: Peaks associated with figure 10.18. Selected possible structures found in peaks **a** and **b** are presented in 10.21

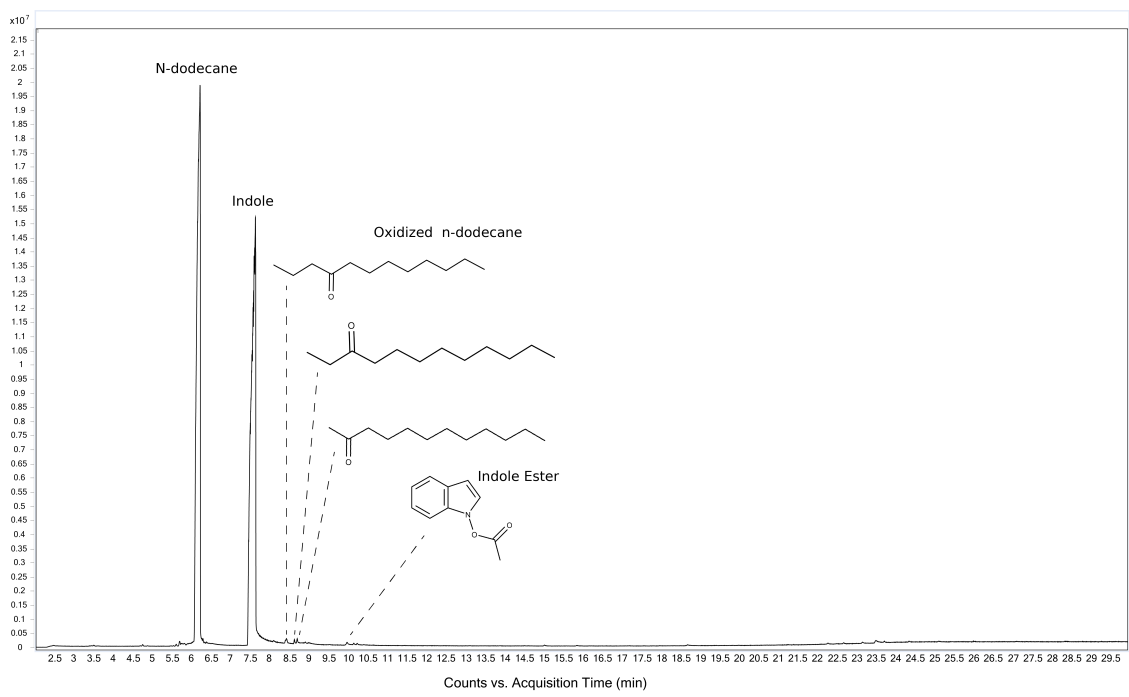


Figure 10.22: LLE enhanced GCMS chromatogram from the 8h indole 0.1mol L⁻¹ solution analysis. The peaks present are labeled with their associated structures detected by mass spectroscopy.

10.2.6 GCMS Chromatograms of Liquid-Liquid Extract from the Stress Heteroatom Solutions

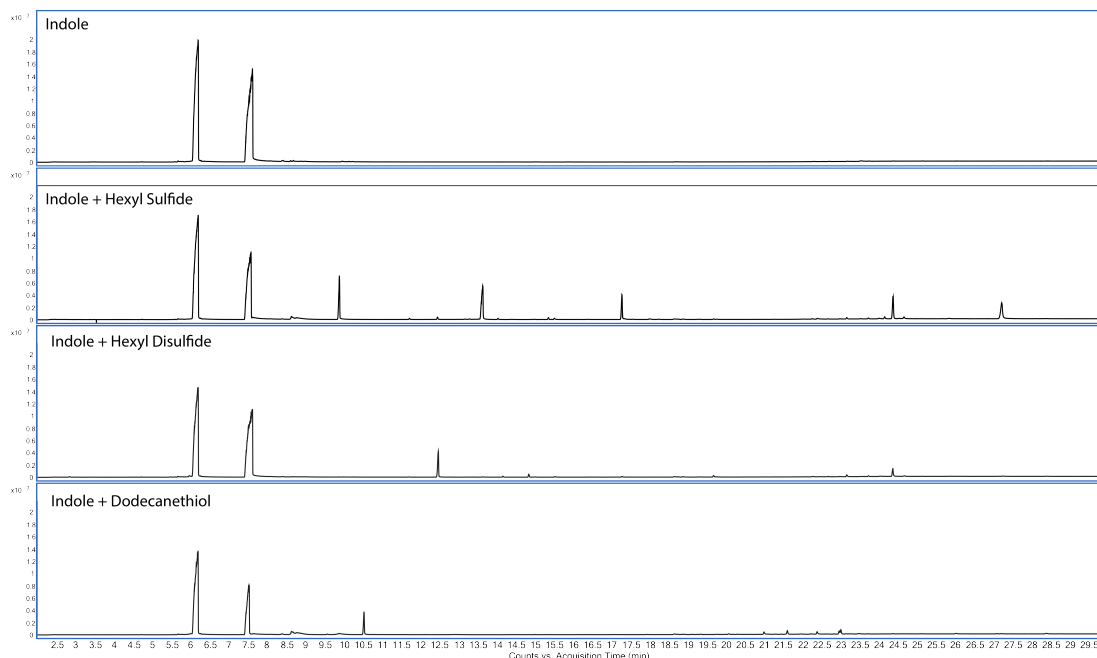
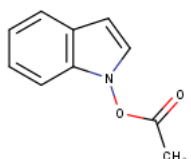
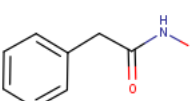


Figure 10.23: GCMS analysis of the solution from the LLE concentration enhanced Indole and Sulfur + Indole test

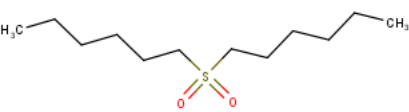
The structures corresponding to the labelled peaks are presented below. The match factor is calculated from the similarity between the unknown spectrum and NIST library's known spectrums. The reverse-match factor is similar to the match factor, except that peaks not present in the NIST library are ignored.

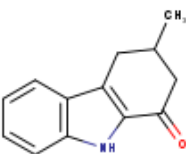
Table 10.10: Ions observed in Hexyl Sulfide GCMS chromatogram Figure 10.24

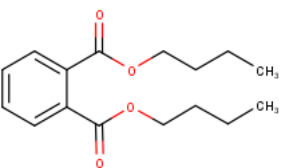
Peak (retention time in min) Detected Compound (Match Factor + Reverse Match Factor with the NIST database)

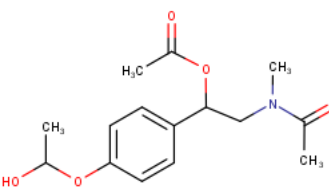
a (8.1)	 <chem>CN(C)C(=O)O[C@@H]1C=CC=C2C=CC=CC12</chem> (744, 784)
b (11.7)	 <chem>CN(O)C(=O)Cc1ccccc1</chem> (574, 666)

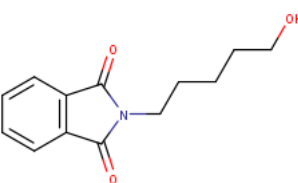
c (12.5)  (832, 836)

d (14.0)  (778, 804)

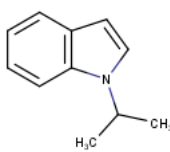
e (14.9)  (521, 696)

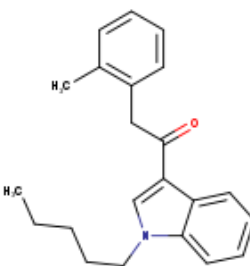
f (15.0)  (793, 915)

g (17.3)  (614, 616)

h (17.4)  (478, 588)

i (18.0)  (654, 810)

j (18.1)  (421, 756)

k (18.8)  (738, 753)

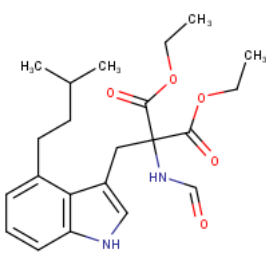
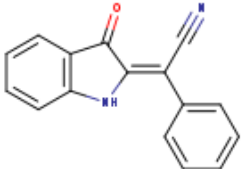
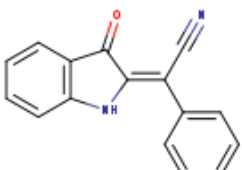
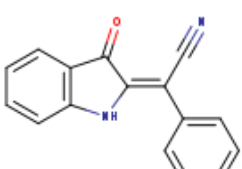
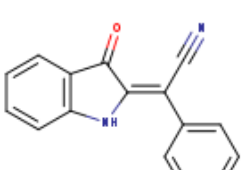
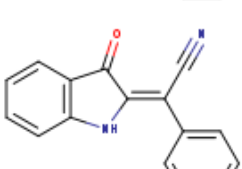
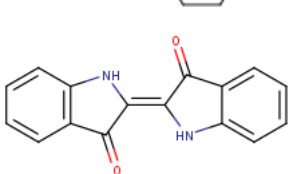
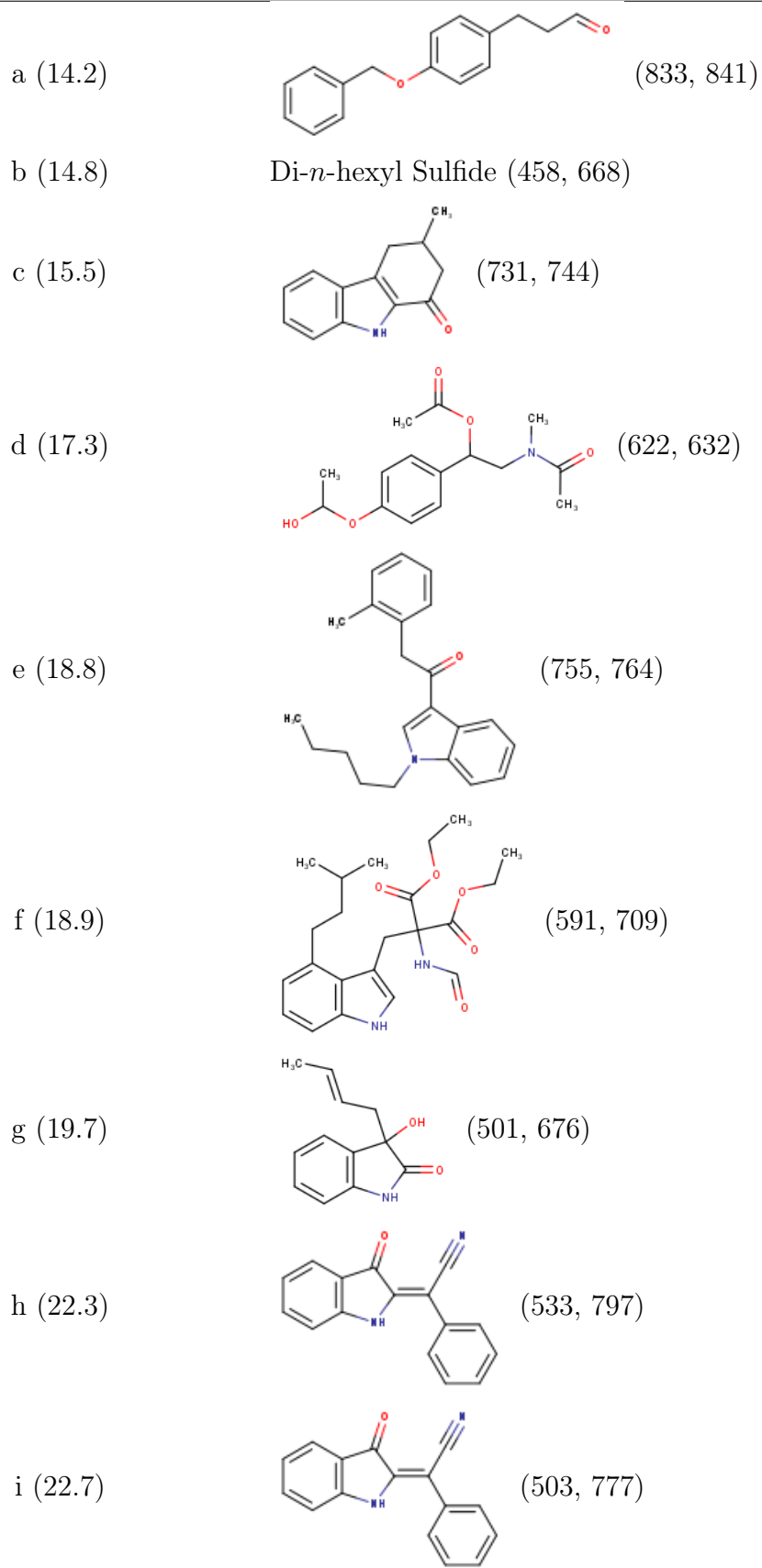
l (18.9)		(568, 599)
m (22.3)		(568, 776)
n (23.2)		(505, 757)
o (23.7)		(590, 769)
p (24.2)		(623, 766)
q (24.4)		(635, 765)
r (27.2)		(467, 532)

Table 10.11: Ions observed in Di-*n*-hexyl-Disulfide GCMS chromatogram Figure 10.25

Peak (retention time in min) Detected Compound (Match Factor + Reverse Match Factor with the NIST database)



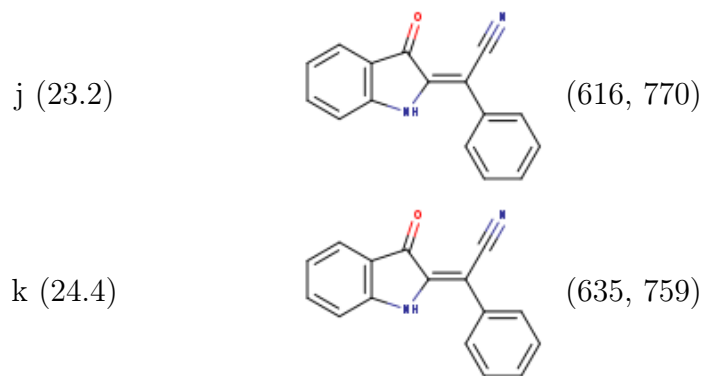
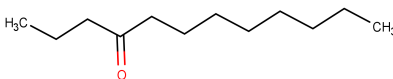
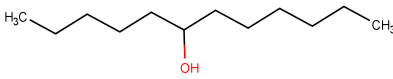
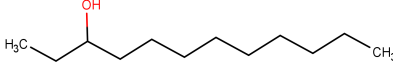
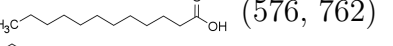
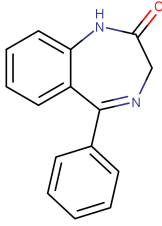
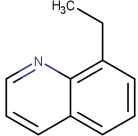
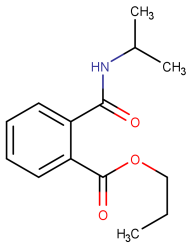
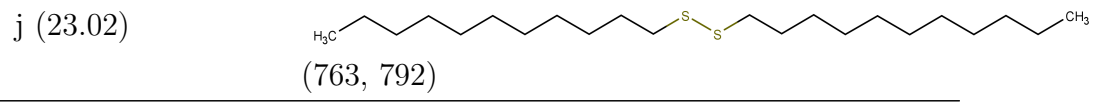
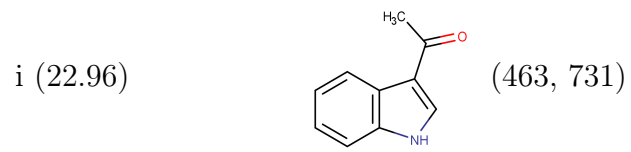


Table 10.12: Ions observed in Dodecanethiol GCMS chromatogram Figure 10.26

Peak (retention time in min)	Detected Compound (Match Factor + Reverse Match Factor with the NIST database)
a (8.41)	 (569, 696)
b (8.64)	 (746, 813)
c (8.77)	 (739, 795)
d (9.58)	 (576, 762)
e (9.88)	 (637, 895)
f (20.04)	 (621, 673)
g (20.97)	 (492, 761)
h (21.59)	



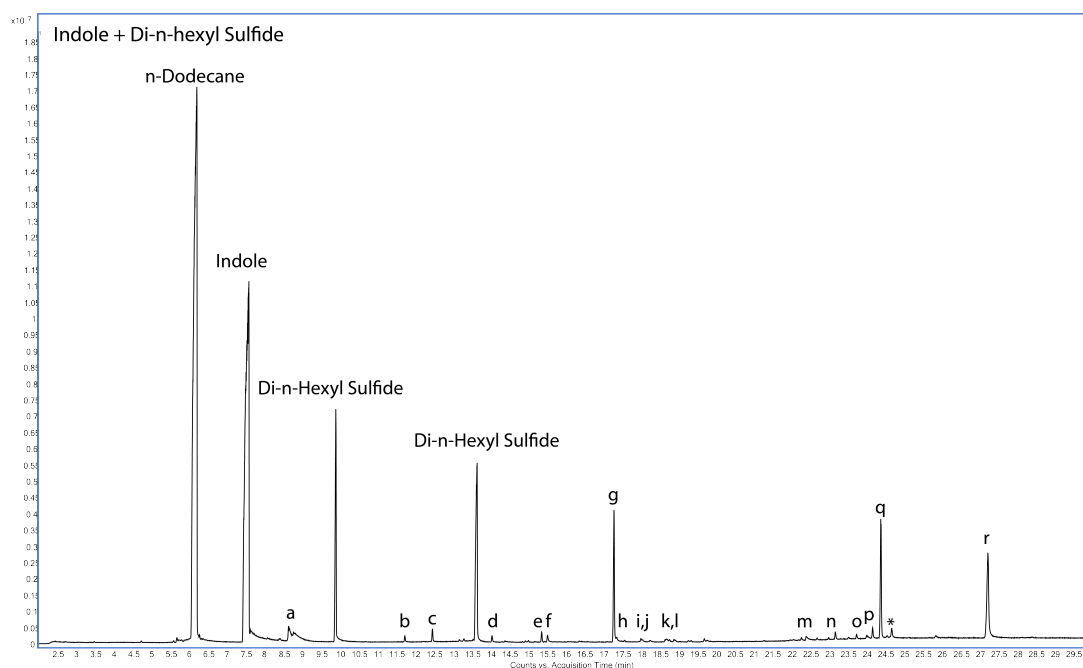


Figure 10.24: GCMS analysis of the solution from the LLE concentration enhanced Indole and Di-*n*-hexylsulfide 8 h test. The major peaks are labelled on the figure, the minor peaks are labelled with roman characters, and are detailed in Table 10.10. The * peak could not be assigned with confidence.

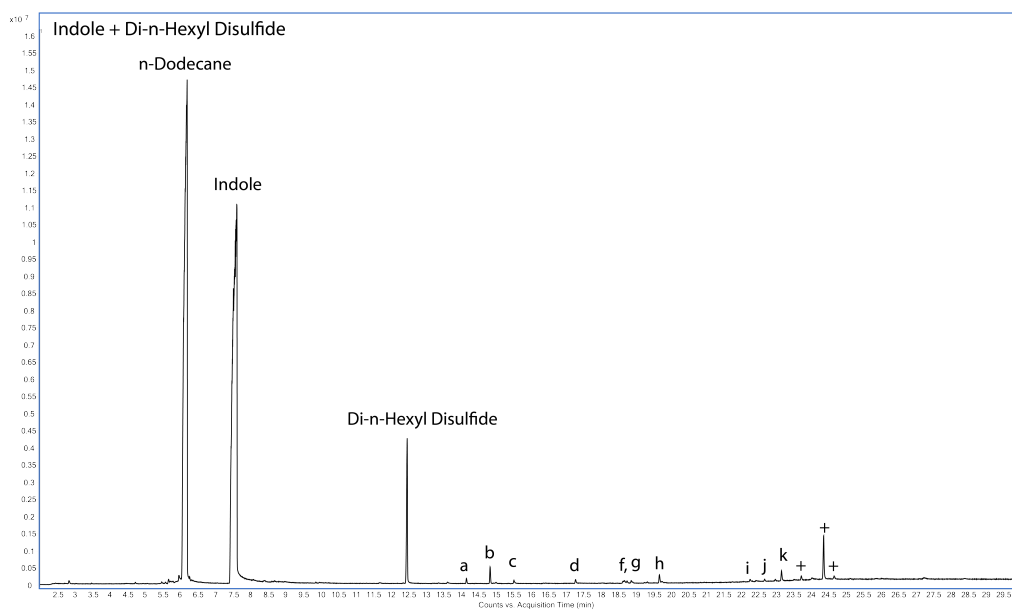


Figure 10.25: GCMS analysis of the solution from the LLE concentration enhanced Indole and Di-*n*-hexyldisulfide 8 h test. The major peaks are labelled on the figure, the minor peaks are labelled with roman characters, and are detailed in Table 10.11. The + peaks are column bleed species.

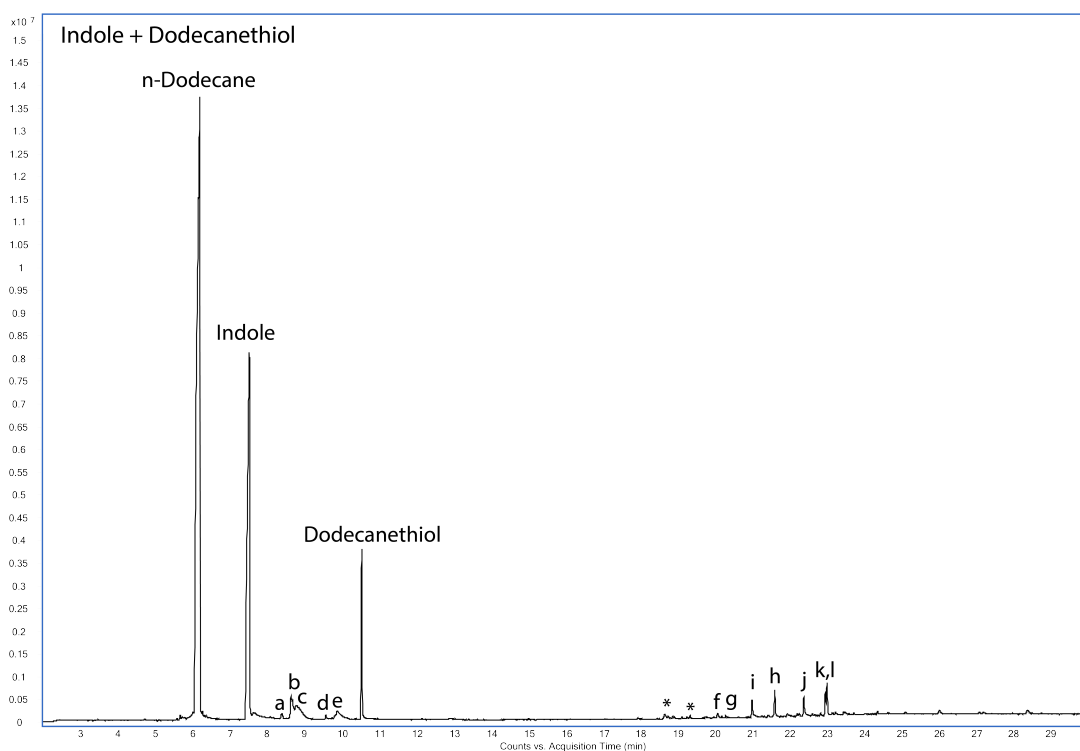


Figure 10.26: GCMS analysis of the solution from the LLE concentration enhanced Indole and Dodecanethiol 8 h test. The major peaks are labelled on the figure, the minor peaks are labelled with roman characters, and are detailed in Table 10.12. The * peak could not be assigned with confidence.

10.2.7 LCMS areas associated with Each Species Class

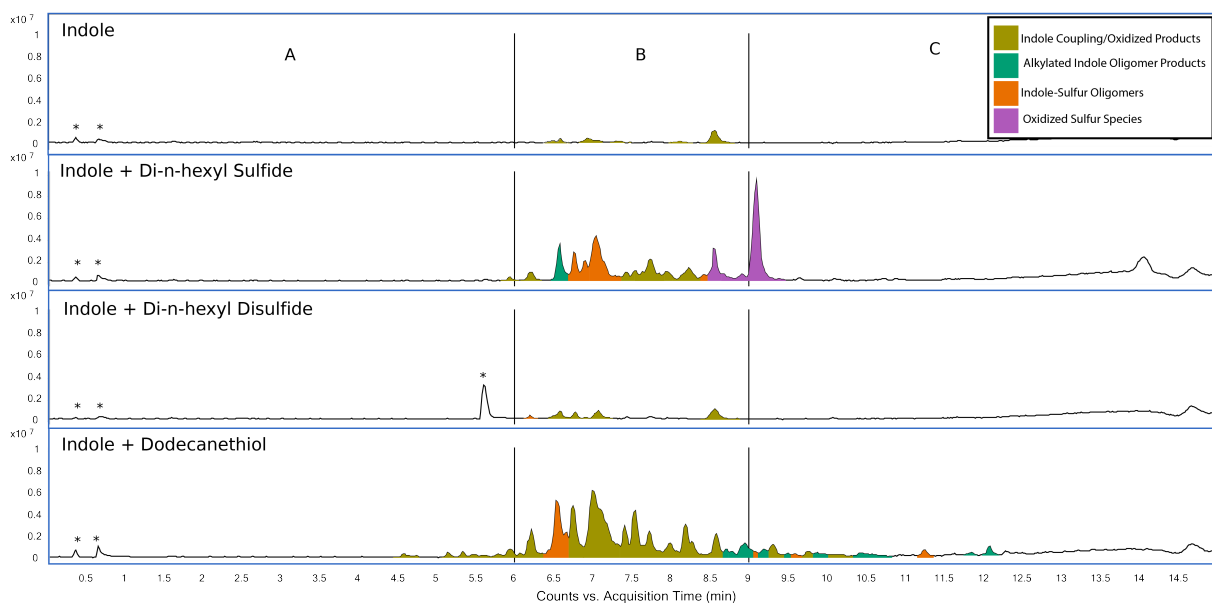


Figure 10.27: (+)LCMS chromatograms of the deposit from the Indole and Sulfur + Indole surrogates. The compounds labelled * are found as 'background ions'.

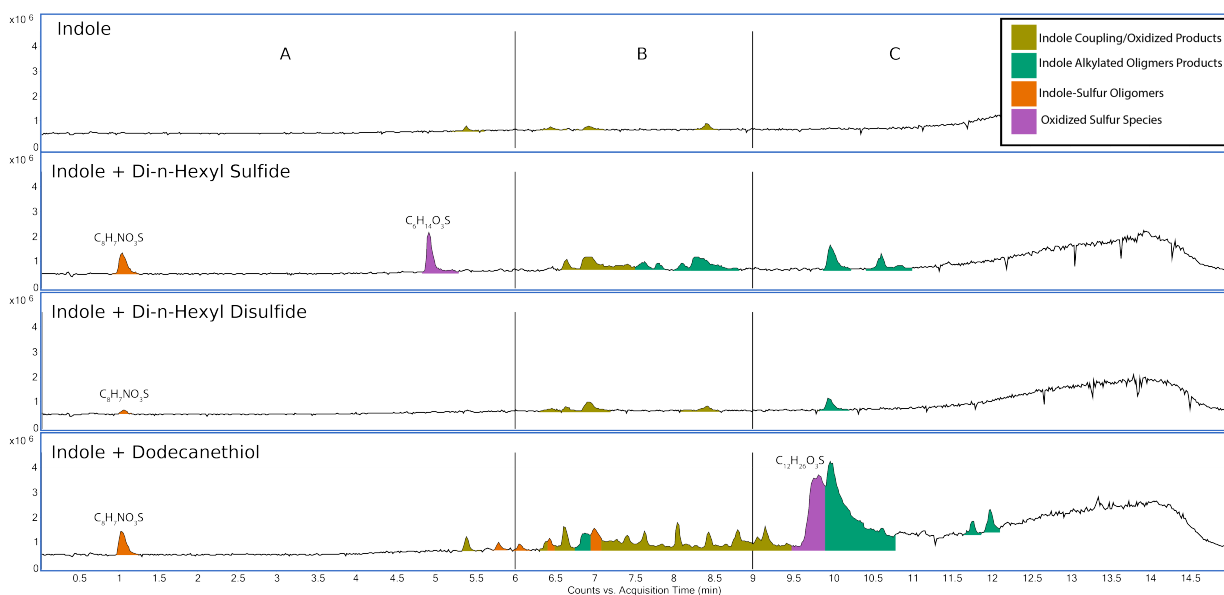


Figure 10.28: (-)LCMS chromatograms of the deposit from the of Indole and Sulfur + Indole surrogates.

10.2.8 Compounds Detected in LCMS Chromatograms

For the compounds detected here, the compound associated with the molecular ion is presented as a chemical formula. The mass of the molecular ion is presented, with the deviation from the actual mass in ppm. The deviation is calculated as follows: 1) the probable formula is identified using the MassHunter software 2) the actual molecular weight (Mw) of the compound is identified from the Mw of the molecular ion peak (e.g. for and $[M-H]^-$, the Mw would be the Mw of the molecular ion + the Mw of a proton) 3) the difference between the Mw of the probable formula and the actual Mw of the compound found is presented as ppm. For example, for the peak 219.0918 detected with $[M+H]^+$ actual Mw is 218.08396 (219.0918-1.00784), which is assigned the probable formula of $C_{15}H_{10}N_2$ with 218.0844 has a difference of 0.0075 from the actual Mw, which is reported as a deviation of -0.75 ppm.

10.2.8.1 Indole+Sulfur

Region	Sample											
	Indole			Indole + RSR			Indole + RSSR			Indole + RSH		
	Formula	[M+H] ⁺	ppm	Formula	[M+H] ⁺	ppm	Formula	[M+H] ⁺	ppm	Formula	[M+H] ⁺	ppm
A (0-6min)	-	-	-	C ₁₅ H ₁₀ N ₂	219.0918	-0.75	-	-	-	C ₇ H ₅ NO	120.0445	-1.08
	-	-	-	C ₄₀ H ₂₅ N ₅ O	592.2130	0.46	-	-	-	C ₇ H ₇ NO ₂	138.0553	-2.6
	-	-	-	-	-	-	-	-	-	C ₁₆ H ₁₄ N ₂ O ₂	267.1135	-1.95
	-	-	-	-	-	-	-	-	-	C ₁₅ H ₁₀ N ₂	219.0920	-1.49
	-	-	-	-	-	-	-	-	-	C ₁₅ H ₁₀ N ₂	219.0920	-1.49
	-	-	-	-	-	-	-	-	-	C ₁₅ H ₁₀ N ₂	219.0920	-1.23
	-	-	-	-	-	-	-	-	-	C ₁₅ H ₁₀ N ₂	219.0920	-1.23
	-	-	-	-	-	-	-	-	-	C ₁₆ H ₁₀ N ₂	247.0866	-0.65
	-	-	-	-	-	-	-	-	-	C ₃₉ H ₂₃ N ₅ O	578.1984	-1.33
	-	-	-	-	-	-	-	-	-	C ₁₅ H ₁₂ N ₂	221.1084	-4.58
B (6-9min)	C ₂₄ H ₁₅ N ₃ O	362.1305	-5.08	C ₁₆ H ₁₄ N ₂	235.1239	-3.62	C ₂₄ H ₂₅ N ₃ O ₂ S	420.1728	2.74	C ₁₉ H ₁₂ N ₂ O	578.1984	-1.33
	C ₂₄ H ₁₇ N ₃ O	364.1453	-2.06	C ₂₅ H ₁₅ N ₃	390.1247	-2.52	C ₂₄ H ₁₅ N ₃ O	362.1302	-3.33	C ₂₅ H ₁₅ N ₃ O ₂	390.1255	-4.03
	C ₁₄ H ₁₇ NO ₅	280.1172	-1.07	C ₂₁ H ₁₈ N ₂ O ₄	362.1316*	3.65	C ₂₅ H ₁₇ N ₃	360.1509	-1.76	C ₁₆ H ₁₄ N ₂	235.1233	-1.20
	C ₂₄ H ₁₃ N ₃ O	360.1142	-2.93	C ₂₀ H ₂₃ N ₃ S	350.1518*	2.32	C ₂₄ H ₁₃ N ₃ O	360.1150	-4.96	C ₂₁ H ₁₉ N ₃ OS	362.1312	1.66
	C ₃₂ H ₂₆ N ₄	467.2236	-0.9	C ₁₆ H ₁₄ N ₂	235.1239	-3.62	C ₄₈ H ₃₀ N ₆ O	707.2561	-1.13	C ₂₀ H ₂₁ N ₃ S	336.1525	1.49
	C ₂₄ H ₁₅ N ₃	346.1351	-3.51	C ₁₇ H ₂₄ N ₂ O ₂	327.1513*	2.32	C ₁₆ H ₁₀ N ₂ O	247.0871	-1.79	C ₂₁ H ₁₉ N ₃ OS	362.1310	2.66
	C ₂₄ H ₁₇ N ₃ O	364.1457	-3.38	C ₂₁ H ₁₇ N ₃ OS	360.1158	0.70	C ₄₀ H ₂₇ N ₅	578.2357	-2.70	C ₃₂ H ₁₈ N ₄ O ₂	491.1522	-3.68
	C ₂₄ H ₁₇ N ₃ O	364.1457	-3.38	C ₂₄ H ₂₃ N ₃ OS	402.1619	3.85	C ₂₄ H ₁₇ N ₃ O	364.1459	-3.79	C ₂₁ H ₁₉ N ₃ OS	362.1312	1.66
	C ₄₈ H ₃₄ N ₆ O ₂	749.2648*	-1.15	C ₃₀ H ₂₅ N ₃	428.2127	-1.66	C ₄₈ H ₃₆ N ₆ O ₂	749.2656	-2.32	C ₂₃ H ₁₇ N ₃	336.1506	-2.76
	-	-	-	C ₄₈ H ₃₀ N ₆ O	707.2551	0.98	-	-	-	C ₂₄ H ₁₅ N ₃ O	362.1297	-2.89
	-	-	-	C ₃₃ H ₂₀ N ₄	473.1777	-2.97	-	-	-	C ₃₂ H ₁₈ N ₄ O ₂	491.1507	-0.63
	-	-	-	C ₃₂ H ₂₀ N ₄ O	477.1722	-3.12	-	-	-	C ₂₅ H ₁₇ N ₃	360.1521	-2.04
	-	-	-	C ₄₀ H ₂₅ N ₅	576.2196	-2.19	-	-	-	C ₂₄ H ₂₁ N ₃ O	368.1768	-2.35
	-	-	-	C ₂₉ H ₂₃ N ₃	414.1985*	-4.29	-	-	-	C ₂₁ H ₁₇ N ₃ OS	360.1158	-0.47
	-	-	-	C ₃₅ H ₃₄ N ₄ OS	559.2519	1.71	-	-	-	C ₂₇ H ₁₆ N ₃ O	402.1604	-0.28
	-	-	-	C ₄₀ H ₂₇ N ₅	578.2367	-4.12	-	-	-	C ₄₀ H ₂₅ N ₅ O ₃	624.2051	-2.84
	-	-	-	C ₃₅ H ₃₄ N ₄ S	543.2571	1.28	-	-	-	C ₃₇ H ₂₇ N ₅ OS	295.6044†	-0.70
	-	-	-	C ₃₀ H ₂₃ N ₃ O	442.1932	-3.63	-	-	-	C ₄₁ H ₃₄ N ₆ O ₆	354.1335	2.46
	-	-	-	C ₃₂ H ₂₂ N ₄	463.1935	-3.42	-	-	-	C ₄₈ H ₃₀ N ₆ O	707.2563	-1.05
	-	-	-	C ₃₃ H ₂₀ N ₄	473.1773	-2.39	-	-	-	C ₃₂ H ₂₀ N ₄ O	477.01735	-4.86
	-	-	-	C ₁₆ H ₁₄ N ₂	235.1237	-2.78	-	-	-	C ₄₀ H ₂₇ N ₅	578.2363	-3.87
	-	-	-	C ₃₅ H ₃₂ N ₄ O	557.2360	1.62	-	-	-	C ₃₂ H ₂₂ N ₄	463.1935	-3.34
	-	-	-	C ₂₇ H ₂₇ N ₃ OS	442.1936	2.34	-	-	-	C ₁₆ H ₁₄ N ₂	235.1234	-1.25
	-	-	-	C ₁₂ H ₂₆ OS	219.1792	-4.17	-	-	-	C ₁₆ H ₁₀ N ₂ O	247.0871	-1.86
	-	-	-	C ₁₄ H ₂₄ OS	241.1609	5.03	-	-	-	C ₅₀ H ₃₂ N ₆ O ₂	749.2640	2.91
	-	-	-	C ₂₆ H ₅₀ O ₂ S	459.3327	0.66	-	-	-	C ₃₃ H ₂₂ N ₄ O ₂	507.1830	-2.32
	-	-	-	C ₅₀ H ₄₇ N ₇ O	918.3592	-0.55	-	-	-	C ₂₄ H ₁₇ N ₃ O	364.1458	-3.19
	-	-	-	-	-	-	-	-	-	C ₁₄ H ₁₉ NO	218.1541	-0.61
	-	-	-	-	-	-	-	-	-	C ₅₀ H ₃₂ N ₆ O ₂	749.2646	2.36
	-	-	-	-	-	-	-	-	-	C ₂₈ H ₃₀ N ₂ O	411.24508	-4.09
	-	-	-	-	-	-	-	-	-	C ₂₈ H ₃₂ N ₂	397.26548	-3.19
	-	-	-	-	-	-	-	-	-	C ₂₄ H ₁₇ N ₃ O	364.1458	-3.19
	-	-	-	-	-	-	-	-	-	C ₁₆ H ₁₀ N ₂ O ₂	263.08258	-3.53
	-	-	-	-	-	-	-	-	-	C ₄₄ H ₄₀ N ₄	625.3349	-3.28
-	-	-	-	-	-	-	-	-	C ₂₄ H ₁₇ N ₃ O	364.1448	-0.78	
-	-	-	-	-	-	-	-	-	C ₂₄ H ₁₉ N ₃ O	366.1606	-0.96	
C (9-15min)	-	-	-	C ₁₂ H ₂₆ OS	219.1787	-4.17	-	-	-	C ₃₆ H ₃₇ N ₃	512.3073	-1.90
	-	-	-	C ₂₂ H ₂₀ N ₂ O ₂	329.1651	-0.51	-	-	-	C ₃₃ H ₃₉ N ₃ OS	526.2876	0.64
	-	-	-	-	-	-	-	-	-	C ₅₂ H ₄₃ N ₅ O ₂	770.34926	-0.31
	-	-	-	-	-	-	-	-	-	C ₁₆ H ₁₂ N ₂	233.10866	-5.2
	-	-	-	-	-	-	-	-	-	C ₂₄ H ₁₇ N ₃ O	364.1452	-1.69
	-	-	-	-	-	-	-	-	-	C ₃₃ H ₃₉ N ₃ OS	526.2876	0.64
	-	-	-	-	-	-	-	-	-	C ₃₅ H ₃₅ N ₃	498.2919	-2.53
	-	-	-	-	-	-	-	-	-	C ₄₁ H ₄₄ N ₄ OS	641.32896	1.80
	-	-	-	-	-	-	-	-	-	C ₃₆ H ₃₅ N ₃ O	526.2858	0.85
	-	-	-	-	-	-	-	-	-	C ₂₄ H ₁₇ N ₃	348.1506	-2.88
	-	-	-	-	-	-	-	-	-	C ₃₆ H ₃₇ N ₃ O	528.3013	-0.36
	-	-	-	-	-	-	-	-	-	C ₄₄ H ₄₀ N ₄ O	641.2373	0.24
	-	-	-	-	-	-	-	-	-	C ₂₄ H ₁₅ N ₃	346.1337	0.79
	-	-	-	-	-	-	-	-	-	C ₃₆ H ₃₇ N ₃	512.3073	-2.63
	-	-	-	-	-	-	-	-	-	C ₂₀ H ₃₁ NOS	334.2216	-4.73
-	-	-	-	-	-	-	-	-	C ₃₆ H ₃₅ N ₃ O	526.2870	-2.99	
-	-	-	-	-	-	-	-	-	C ₂₀ H ₂₉ NO	300.2338	-4.70	

Table 10.13: Compounds detected by (+)LCMS detected in the indole(+sulfur) deposit in Figure 10.27 presented order of elution time of the analysis of deposits produced by the surrogates after 8 h 140 °C. *=[M+Na]⁺, †=[M+2H]⁺.

Region	Sample											
	Indole			Indole + RSR			Indole + RSSR			Indole + RSH		
	Formula	[M-H] ⁻	ppm	Formula	[M-H] ⁻	ppm	Formula	[M-H] ⁻	ppm	Formula	[M-H] ⁻	ppm
A (0-6min)	C ₈ H ₇ NO ₃	164.0349	2.66	C ₈ H ₇ NO ₃ S	196.00768	-0.99	C ₈ H ₇ NO ₃ S	196.0071	2.18	C ₈ H ₇ NO ₃ S	196.0078	-1.98
	-	-	-	C ₆ H ₁₄ O ₃ S	164.0594	-1.25	-	-	-	C ₈ H ₇ NO ₃	164.03528	0.86
	-	-	-	-	-	-	-	-	-	C ₂₃ H ₁₂ N ₂ S	347.0659	-0.07
B (6-9min)	C ₂₆ H ₁₈ O ₂	361.1223	2.51	C ₂₅ H ₁₇ N ₃	358.1357	-1.62	C ₂₅ H ₁₇ N ₃	358.1354	-0.89	C ₁₉ H ₁₂ N ₂ O	578.1984	-1.33
	C ₂₄ H ₁₃ N ₃ O	358.0990	-2.67	C ₂₄ H ₁₃ N ₃ O	358.0996	-2.67	C ₂₄ H ₁₃ N ₃ O	358.0993	-2.74	C ₂₄ H ₁₇ N ₃ O	362.1306	-1.62
	C ₂₈ H ₁₅ N ₃ O ₅	472.0918	4.81	C ₂₈ H ₁₅ N ₃ O ₅	472.0920	4.09	C ₂₈ H ₁₅ N ₃ O ₅	472.0918	4.51	C ₁₆ H ₁₂ N ₂ OS	279.0599	-0.41
	C ₂₄ H ₁₇ N ₃ O	362.1306	-1.51	C ₃₂ H ₂₀ N ₄ O	475.1578	-2.70	C ₂₄ H ₁₇ N ₃ O	362.1302	-0.89	C ₂₅ H ₁₇ N ₃	358.1356	-1.30
	-	-	-	C ₃₈ H ₃₀ N ₄ O	557.2357	-1.52	-	-	-	C ₂₄ H ₁₃ N ₃ O	358.0998	-3.23
	-	-	-	C ₃₀ H ₂₃ N ₃ O	440.1722	-0.66	-	-	-	C ₁₆ H ₁₂ N ₂ O ₂ S	295.0548	-0.18
	-	-	-	C ₂₉ H ₂₃ N ₃	412.1827	-1.63	-	-	-	C ₂₄ H ₁₃ N ₃ O	358.0993	-1.85
	-	-	-	C ₄₂ H ₃₀ N ₄ O ₅	669.2125	2.93	-	-	-	C ₂₄ H ₁₃ N ₃ O	358.0987	-0.68
	-	-	-	C ₃₀ H ₂₃ N ₃ O	440.1778	-1.94	-	-	-	C ₃₂ H ₂₀ N ₄ O	475.1576	-2.01
	-	-	-	C ₃₄ H ₂₅ N ₃ O	554.1712	1.80	-	-	-	C ₃₂ H ₂₀ N ₄ O	475.1576	-2.01
	-	-	-	C ₂₈ H ₁₇ N ₃ O ₄	458.1139	2.06	-	-	-	C ₁₆ H ₁₂ N ₂ O ₃	279.0779	-0.86
	-	-	-	C ₃₈ H ₃₀ N ₄ O ₂	573.2316	-3.14	-	-	-	C ₂₄ H ₁₇ N ₃ O	362.1311	-2.85
	-	-	-	-	-	-	-	-	-	C ₂₄ H ₁₇ N ₃ O	362.1306	-1.79
-	-	-	-	-	-	-	-	-	C ₂₄ H ₁₇ N ₃ O	362.1309	-3.54	
C (9-15min)	-	-	-	C ₂₈ H ₁₇ N ₃ O ₄	458.1139	-4.17	C ₂₈ H ₁₇ N ₃ O ₄	458.1135	2.72	C ₁₆ H ₁₂ N ₂	231.0930	-0.62
	-	-	-	C ₃₈ H ₃₀ N ₄ O ₂	573.2316	-3.14	-	-	-	C ₃₂ H ₂₂ N ₄ O	477.1729	-1.48
	-	-	-	-	-	-	-	-	-	C ₁₂ H ₂₆ O ₃ S	249.1539	-2.88
	-	-	-	-	-	-	-	-	-	C ₂₈ H ₁₇ N ₃ O ₄	458.1137	2.34
	-	-	-	-	-	-	-	-	-	C ₃₉ H ₃₇ N ₃ O ₅	626.2641	-0.67
	-	-	-	-	-	-	-	-	-	C ₂₀ N ₂₉ NO	298.2182	-1.46

Table 10.14: Compounds detected by (-)LCMS in the indole(+sulfur) deposit in Figure 10.28 presented order of elution time of after 8 h 140 °C

10.2.8.2 Nitrogen+Sulfur Runs

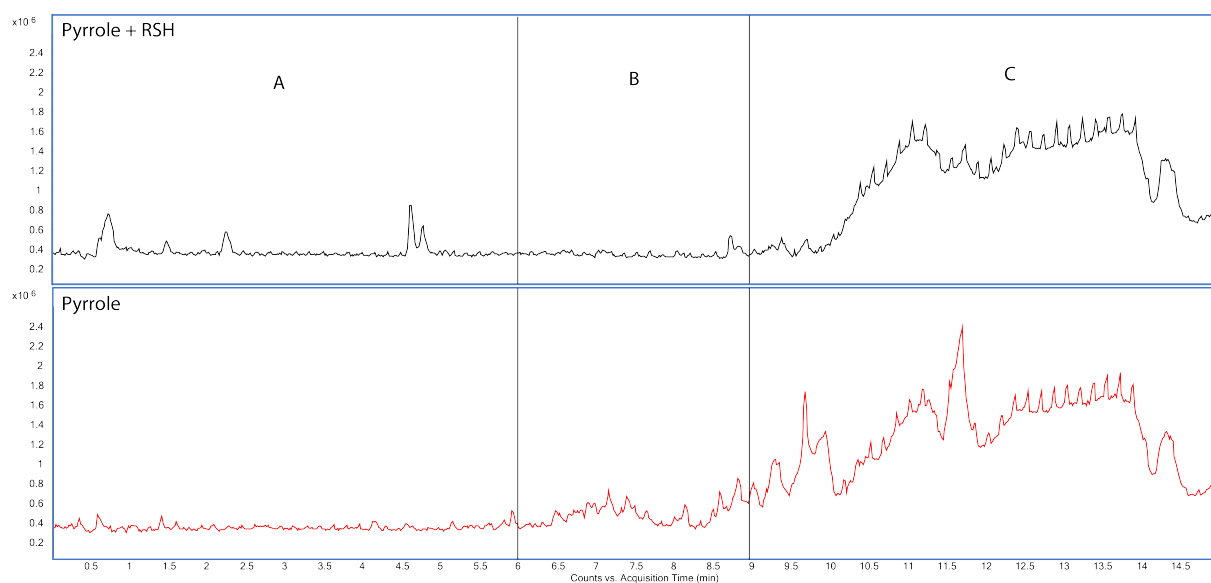


Figure 10.29: LCMS(+) chromatograms of the dissolved Pyrrole and Pyrrole + Dodecanethiol deposit

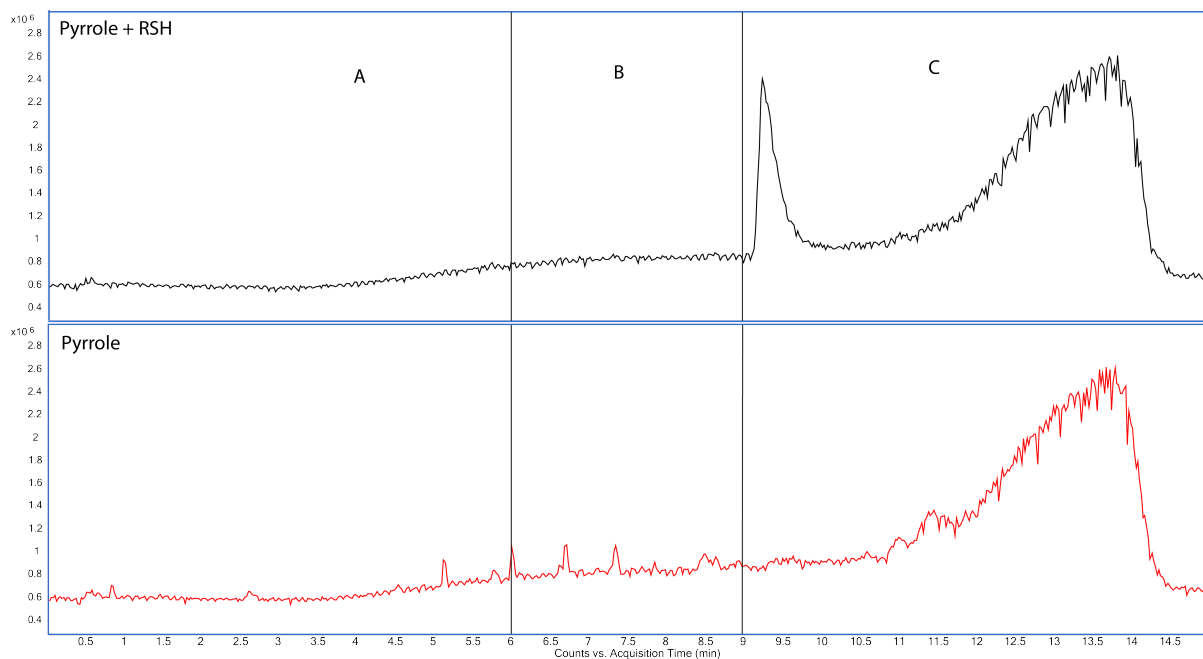


Figure 10.30: LCMS(-) chromatograms of the dissolved Pyrrole and Pyrrole + Dodecanethiol deposit

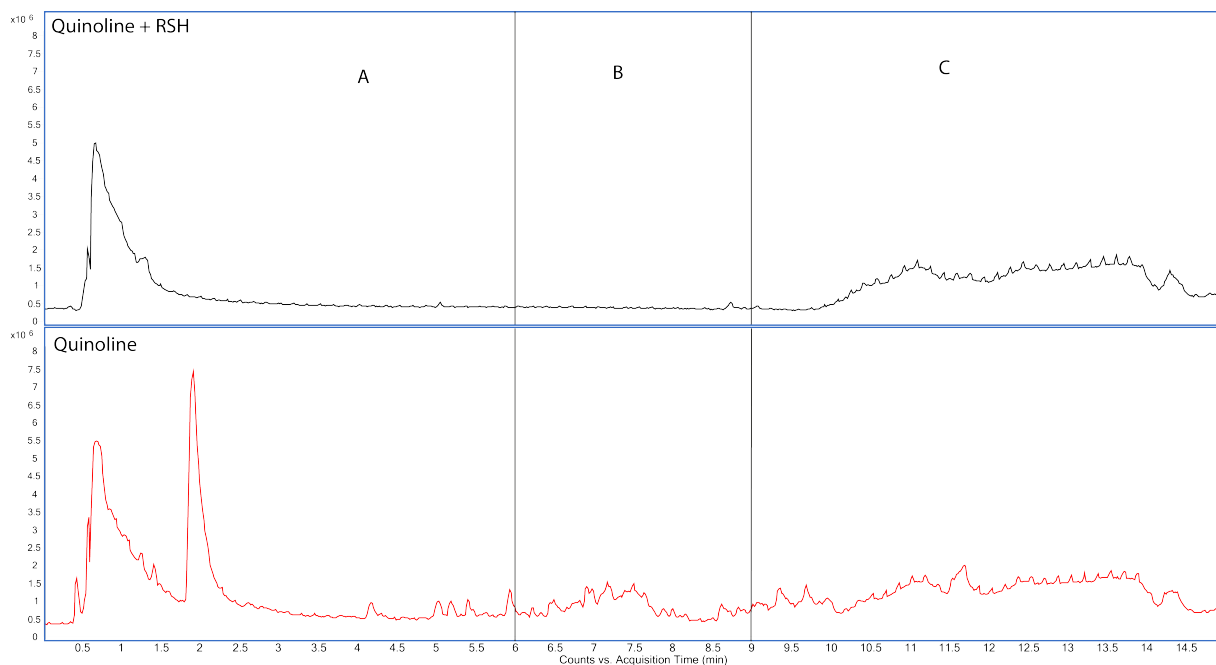


Figure 10.31: LCMS(+) chromatograms of the dissolved Quinoline and Quinoline + Dodecanethiol deposit

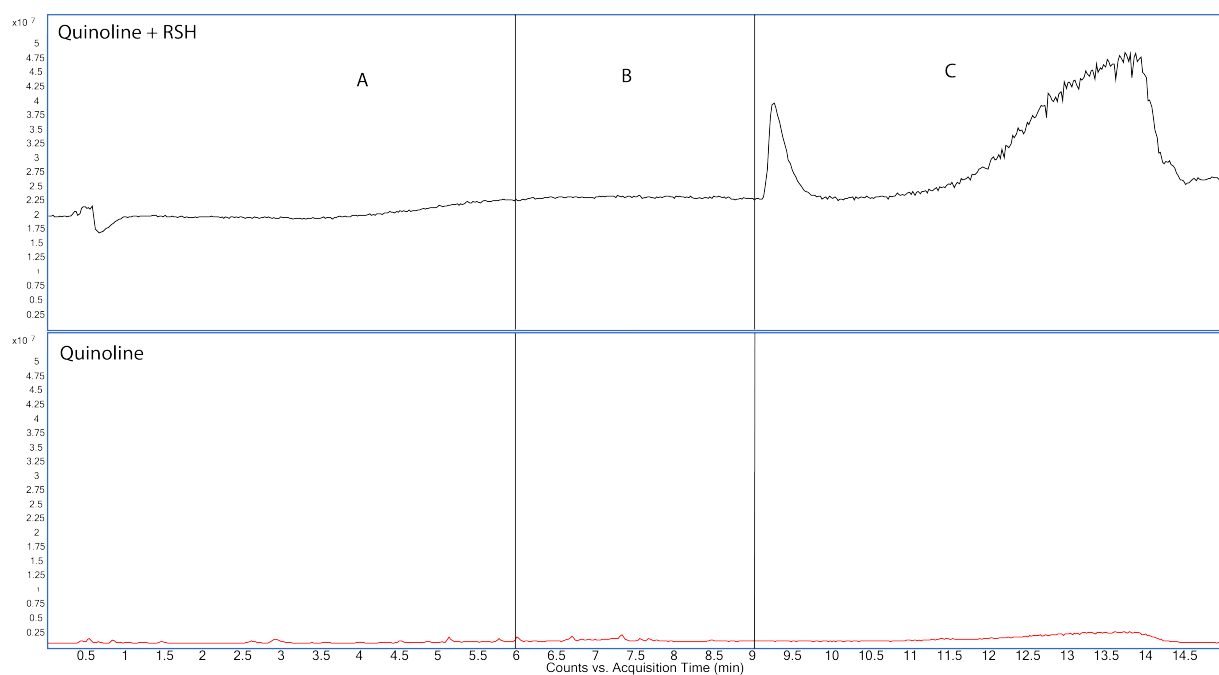


Figure 10.32: LCMS(-) chromatograms of the dissolved Quinoline and Quinoline + Dodecanethiol deposit

10.3 Appearance of Pyrrole and Quinoline Flasks

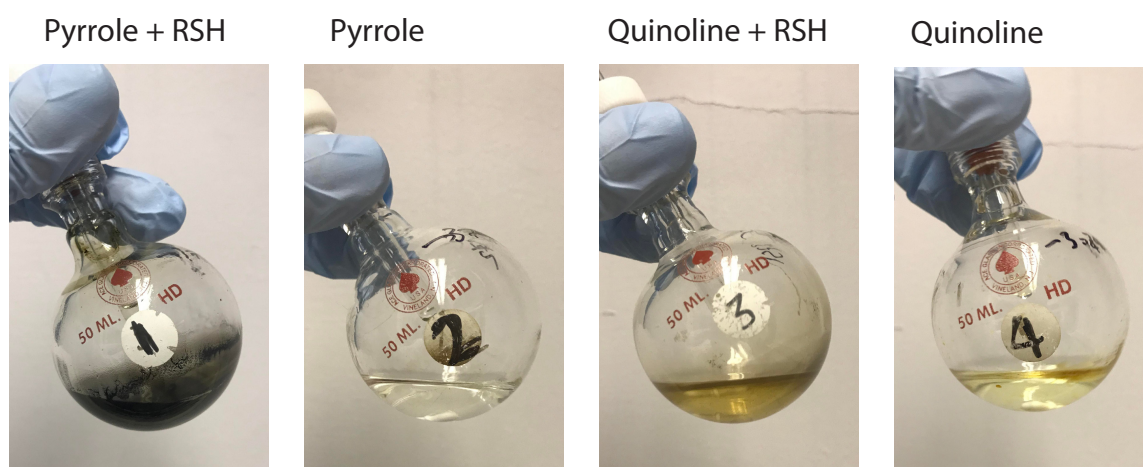


Figure 10.33: Visual comparison of the Pyrrole + Dodecanethiol, Pyrrole, Quinoline + Dodecanethiol, and Quinoline flasks

Region	Sample											
	Pyrrole			Pyrrole + RSH			Quinolene			Quinolene RSH		
	Formula	[M+H] ⁺	ppm	Formula	[M+H] ⁺	ppm	Formula	[M+H] ⁺	ppm	Formula	[M+H] ⁺	ppm
A	-	-	-	C ₈ H ₁₀ N ₂ O	173.0692	-4.13	C ₉ H ₇ N	130.0658	-4.74	C ₉ H ₇ N	130.09572	-3.92
(0-6min)	-	-	-	C ₁₆ H ₂₀ N ₄ O*	323.1485	-2.29	C ₉ H ₇ NO	146.0608	-4.74	-	-	-
	-	-	-	C ₁₃ H ₁₁ N ₃	210.1027	-1.97	C ₁₆ H ₁₉ NO	242.1550	-3.99	-	-	-
	-	-	-	C ₁₃ H ₁₁ N ₃	210.1031	-2.48	C ₁₆ H ₁₉ NO	242.1539	-1.99	-	-	-
	-	-	-	-	-	-	C ₈ H ₁₄ O ₃	181.0836	0.32	-	-	-
	-	-	-	-	-	-	C ₁₇ H ₂₁ NO	256.1697	3.73	-	-	-
	-	-	-	-	-	-	C ₁₂ H ₂₄ O ₇ *	303.1417	-0.63	-	-	-
B	-	-	-	C ₂₂ H ₂₄ N ₆ O ₄	437.1940	-1.56	C ₁₂ H ₂₂ O ₄	253.1415	-1.46	C ₂₅ H ₂₆ N ₄ O	437.1950	-0.06
(6-9min)	-	-	-	C ₂₅ H ₂₀ N ₆ O ₃	453.1665	1.35	C ₁₈ H ₂₃ NO	270.1858	2.47	C ₂₈ H ₂₂ N ₄ O	453.1628	0.7
	-	-	-	-	-	-	C ₁₂ H ₂₂ O ₄	253.1423	-4.87	-	-	-
	-	-	-	-	-	-	C ₁₂ H ₂₄ O ₄	271.1524	-3.11	-	-	-
	-	-	-	-	-	-	C ₁₉ H ₂₅ NO	284.2019	-0.93	-	-	-
	-	-	-	-	-	-	C ₁₂ H ₂₂ O ₄	253.1424	-5.39	-	-	-
	-	-	-	-	-	-	C ₁₂ H ₂₄ O ₅ *	271.1529	-4.59	-	-	-
	-	-	-	-	-	-	C ₁₂ H ₂₄ O ₅ *	271.1529	-4.92	-	-	-
	-	-	-	-	-	-	C ₁₂ H ₂₆ O ₆	289.1624	-0.62	-	-	-
	-	-	-	-	-	-	C ₂₄ H ₃₀ O ₆ *	437.1948	-0.20	-	-	-
C	C ₁₂ H ₂₂ O ₂	199.1697	-1.96	-	-	-	C ₁₂ H ₂₂ O	183.1744	-0.20	-	-	-
(9-15min)	C ₁₂ H ₂₄ O ₃	239.1629	-4.77	-	-	-	C ₁₂ H ₂₂ O ₂ *	199.1623	0.10	-	-	-
	-	-	-	-	-	-	C ₁₂ H ₂₂ O ₂ *	221.1515	0.82	-	-	-
	-	-	-	-	-	-	C ₁₂ H ₂₄ O ₃ *	239.1614	2.09	-	-	-
	-	-	-	-	-	-	C ₁₂ H ₂₆ O ₄ *	257.1728	-1.37	-	-	-
	-	-	-	-	-	-	C ₁₂ H ₂₄ O	185.1903	-1.57	-	-	-

Table 10.15: Compounds detected by (+)LCMS in the dissolved deposits chromatograms in Figure 10.29 and Figure 10.31 after 8 h 140 °C. Compounds superscripted with * parent ions were detected as Na adducts.

Region	Sample											
	Pyrrole			Pyrrole + RSH			Quinoline			Quinoline RSH		
	Formula	[M-H] ⁻	ppm	Formula	[M-H] ⁻	ppm	Formula	[M-H] ⁻	ppm	Formula	[M-H] ⁻	ppm
A (0-6min)	-	-	-	-	-	-	C ₄ H ₆ O ₄	117.0194	-0.34	-	-	-
	-	-	-	-	-	-	C ₅ H ₈ O ₃	115.0398	2.57	-	-	-
	-	-	-	-	-	-	C ₈ H ₇ NO ₃	164.0358	-2.72	-	-	-
	-	-	-	-	-	-	C ₆ H ₁₀ O ₃	129.0558	-0.17	-	-	-
	-	-	-	-	-	-	C ₆ H ₁₂ O ₃	131.0715	-0.86	-	-	-
	-	-	-	-	-	-	C ₇ H ₁₂ O ₃	143.0718	-3.10	-	-	-
	-	-	-	-	-	-	C ₇ H ₁₄ O ₃	145.0878	-5.01	-	-	-
	-	-	-	-	-	-	C ₈ H ₁₄ O ₃	157.0876	-3.08	-	-	-
B (6-9min)	-	-	-	-	-	-	C ₈ H ₁₆ O ₃	159.1033	-3.44	-	-	-
	-	-	-	-	-	-	C ₉ H ₁₈ O ₃	173.1192	-4.60	-	-	-
	-	-	-	-	-	-	C ₁₀ H ₂₀ O ₃	187.1347	-3.51	-	-	-
C (9-15min)	C ₁₂ H ₂₂ O ₂	199.1697	-1.96	C ₁₂ H ₂₆ O ₃ S	249.1539	-3.64	-	-	-	C ₁₂ H ₂₆ O ₃ S	249.1539	-3.63
	C ₁₂ H ₂₄ O ₃	239.1629	-4.77	-	-	-	-	-	-	-	-	-

Table 10.16: Compounds detected by (-)LCMS in the dissolved deposits chromatograms in Figure 10.30 and Figure 10.32 after 8 h 140 °C

10.4 Sulfonation Barriers of Various Common Fuel Nitrogen Heterocycles

In this section we present the calculated barriers for the sulfonation of various nitrogen heterocycles. A recent study has highlighted that sulfonation of benzene in apolar solvents occurs more rapidly as a trimolecular electrophilic substitution involving two SO₃ reacting, but as the SO₃ will be a limiting reagent in this reaction, the barriers to the bimolecular reaction will be presented too.[272]

Fuel <i>n</i> - Heteroatom	Reaction with Two SO ₃ (kcal mol ⁻¹)	Reaction with One SO ₃ (kcal mol ⁻¹)
Indole	3.49	28.49
Pyrrole	3.75	28.58
Pyridine	27.70	44.54
Quinoline	31.75	48.75

Table 10.17: Coupling reactions between 6-membered and 5-membered nitrogen heteroatoms at the DFT/B3LYP-D3/cc-pVTZ level of theory

10.4.1 Electrostatic Potential of Various Nitrogen Heterocycles

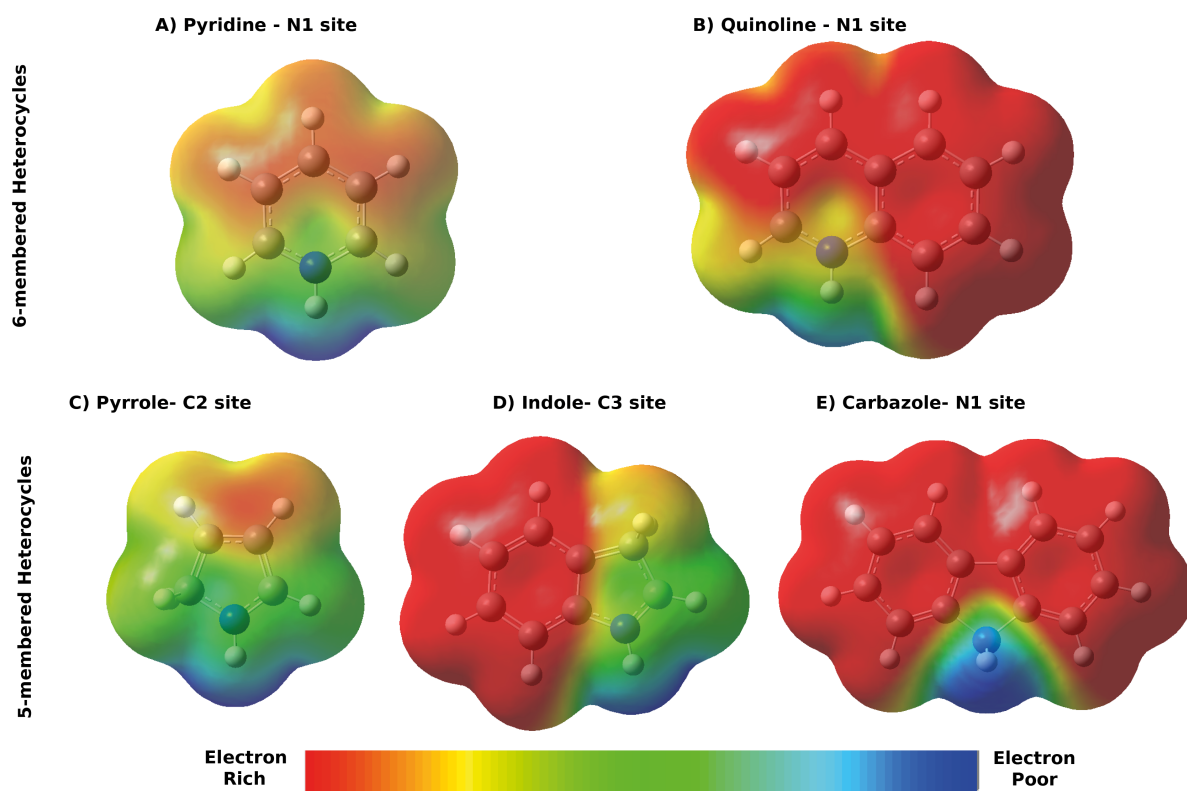


Figure 10.34: Electrostatic potential (ESP) onto total electron density of common protonated nitrogen heterocycles calculated at the DFT/B3LYP-D3/cc-pVTZ level of theory. The most favored protonation site is selected based on previous literature.[379, 305, 380, 381, 382] Areas in red show electron excess, whereas areas in blue show electron deficiency.

10.5 Understanding the Wall Deposition Mechanism

10.5.1 Relaxed Surface Terminations

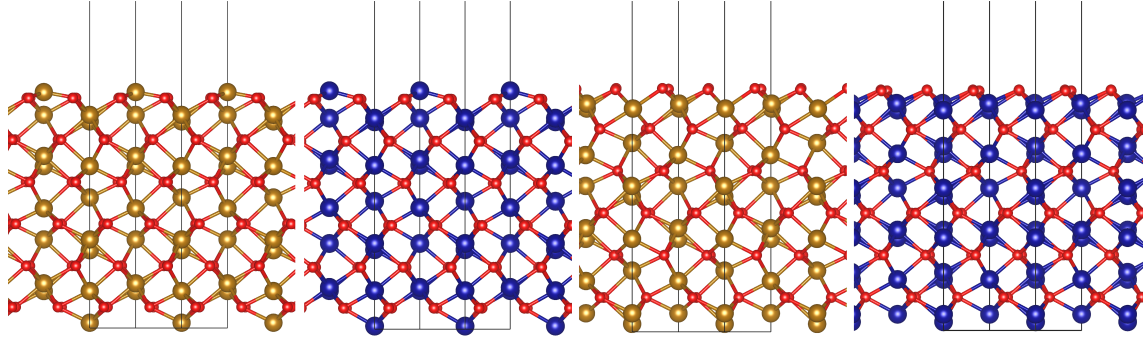


Figure 10.35: Relaxed metal-terminated Fe_2O_3 (brown atoms), metal-terminated Cr_2O_3 (blue atoms), oxygen-terminated Fe_2O_3 and oxygen-terminated Cr_2O_3 from left to right

10.5.2 Adsorption Energies

	Fe ₂ O ₃		Cr ₂ O ₃	
	Metal top-site	Oxygen top-site	Metal top-site	Oxygen top-site
RSR	-1.25 (+0.10)	-0.92 (-0.16)	-0.56 (+0.01)	-0.15 (+0.15)
RS(O)2OH	-1.12 (-0.42)	-2.26	-0.97 (-0.48)	-2.43
RS(O)3OH	-1.10 (-0.62)	-2.37	-1.00 (-0.66)	-2.51
RSH	-1.05 (-0.17)	-0.92 (-0.15)	-0.63 (-0.13)	-0.59 (-0.18)
RCOOH	-0.54 (-0.19)	-1.86	-0.55 (-0.21)	-1.58
ROH	-0.67 (-0.13)	-1.18 (-0.20)	-0.52 (-0.18)	-0.94 (-0.19)
RC(O)H	-1.02 (-0.10)	-1.02 (-0.13)	-0.70 (-0.19)	-0.85 (-0.22)
RH-parallel	-0.51 (-0.11)	-0.46 (-0.12)	-0.41 (-0.13)	-0.41 (-0.12)
RH-perpendicular	-0.42 (-0.12)	-0.37 (-0.11)	-0.35 (-0.12)	-0.35 (-0.12)

Table 10.18: Calculated adsorption energies all in eV on the metal-terminated oxides, values in (brackets) are the contribution of lateral VdW interactions to the total adsorption energy in cases of physisorption.

	Fe ₂ O ₃		Cr ₂ O ₃	
	Metal top-site	Oxygen top-site	Metal top-site	Oxygen top-site
RSR	-1.35 (+0.16)	-1.03 (+0.16)	-0.23 (+0.18)	-1.22 (-0.16)
RS(O)2OH	-1.45 (-0.24)	-2.00	-0.45 (-0.51)	-1.48 (-0.30)
RS(O)3OH	-0.89 (-0.45)	-1.30	-0.66 (-0.68)	-1.03 (-0.07)
RSH	-1.14 (-0.18)	-0.34	-0.69 (-0.18)	-1.20 (-0.16)
RCOOH	-0.18 (-0.15)	-0.72 (+0.06)	-0.23 (-0.22)	-0.58 (-0.08)
ROH	-0.77 (-0.18)	-0.81 (-0.16)	-0.47 (-0.18)	-0.72 (-0.16)
RC(O)H	-0.65 (-0.19)	-0.23 (-0.13)	-0.55 (-0.24)	-1.10 (-0.23)
RH-parallel	-0.43 (-0.13)	-0.61 (-0.13)	-0.39 (-0.12)	-0.41 (-0.13)
RH-perpendicular	-0.36 (-0.12)	-0.53 (-0.12)	-0.35 (-0.12)	-0.35 (-0.12)

Table 10.19: Calculated adsorption energies all in eV on the oxygen-terminated oxides, values in (brackets) are the contribution of lateral VdW interactions to the total adsorption energy in cases of physisorption.

10.5.3 Alkane Adsorption Charge Density Difference Plots

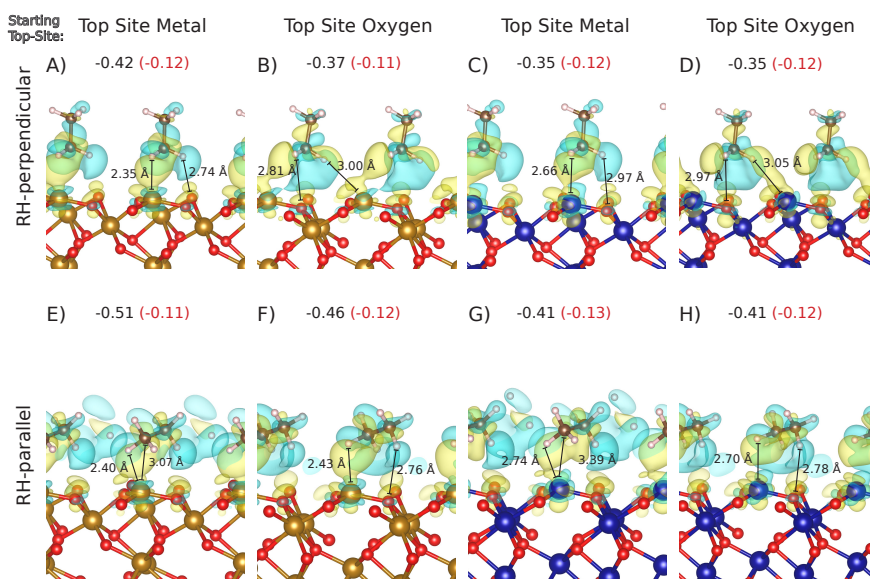


Figure 10.36: Charge density difference plots showing ethane ethane adsorbed onto transition metal-terminated Cr_2O_3 (blue atoms) and Fe_2O_3 (brown atoms). Yellow represents areas of charge accumulation, blue indicates areas of charge depletion. The adsorption energies are shown alongside each structure, along with the lateral VdW contributions to adsorption in red.

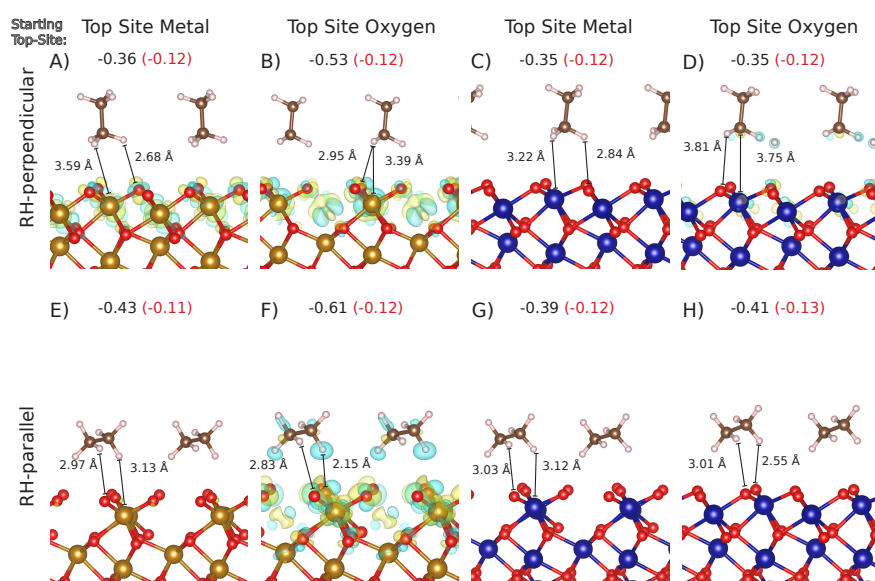


Figure 10.37: Charge density difference plots showing ethane ethane adsorbed onto transition oxygen-terminated Cr_2O_3 (blue atoms) and Fe_2O_3 (brown atoms). Yellow represents areas of charge accumulation, blue indicates areas of charge depletion. The adsorption energies are shown alongside each structure, along with the lateral VdW contributions to adsorption in red.

10.5.4 Effect of Tail Length

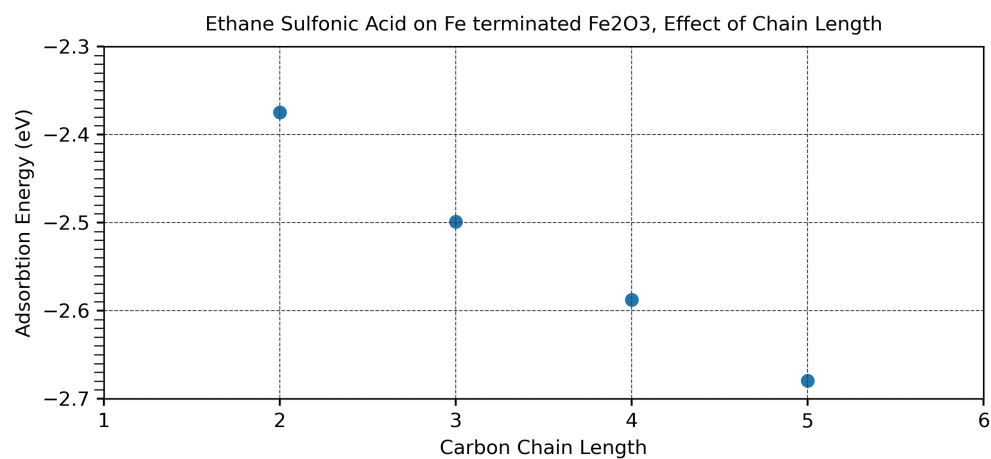


Figure 10.38: Effect of tail length on the adsorption energy of sulfonic acid adsorbed onto metal terminated Fe₂O₃

10.5.5 Detailed Geometries Surface Structures

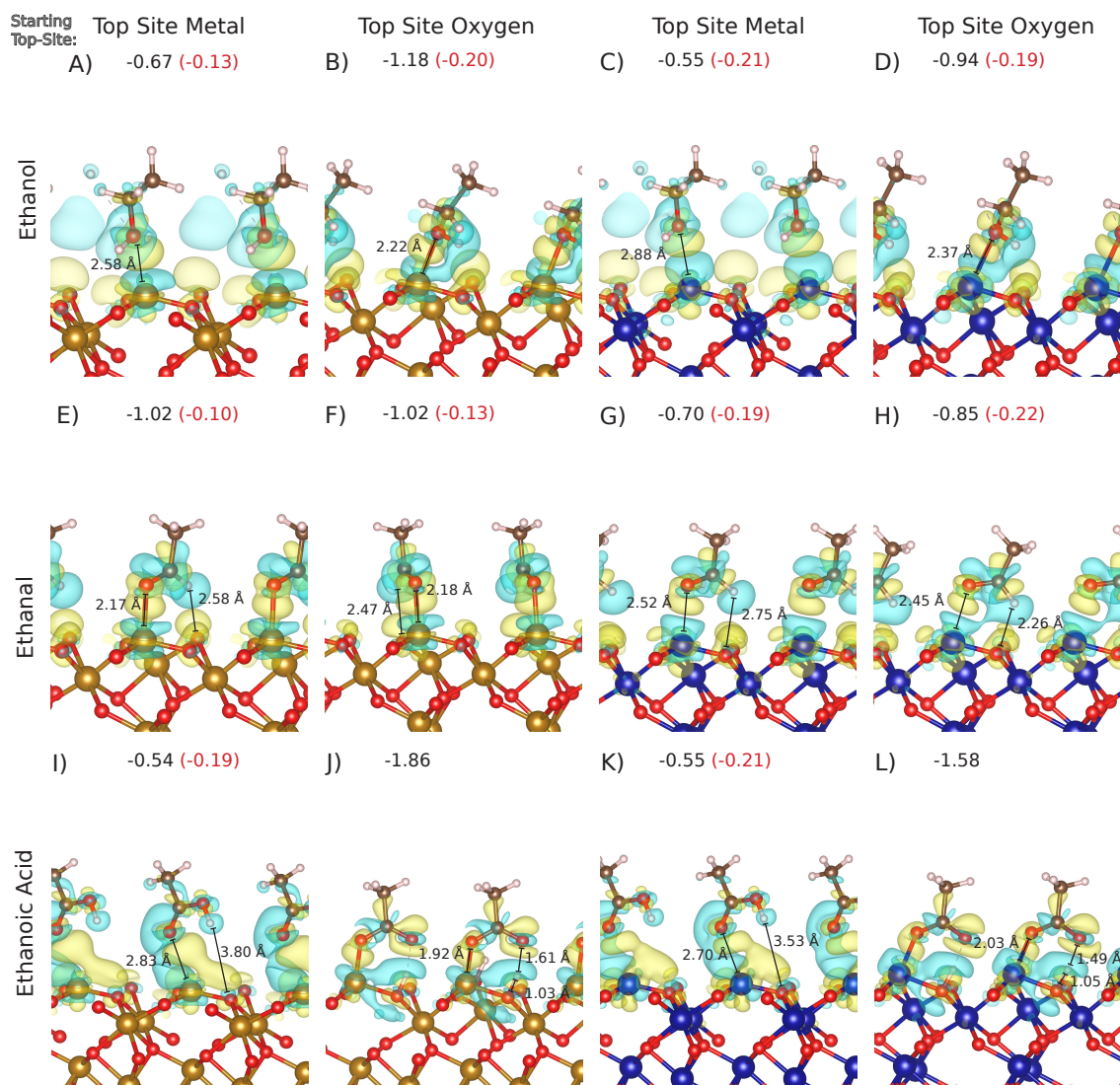


Figure 10.39: Charge density difference plots showing oxygenated species adsorbed onto transition metal-terminated Cr_2O_3 (blue atoms) and Fe_2O_3 (brown atoms). Yellow represents areas of charge accumulation, blue indicates areas of charge depletion. The adsorption energies are shown alongside each structure, along with the lateral VdW contributions to adsorption in red.

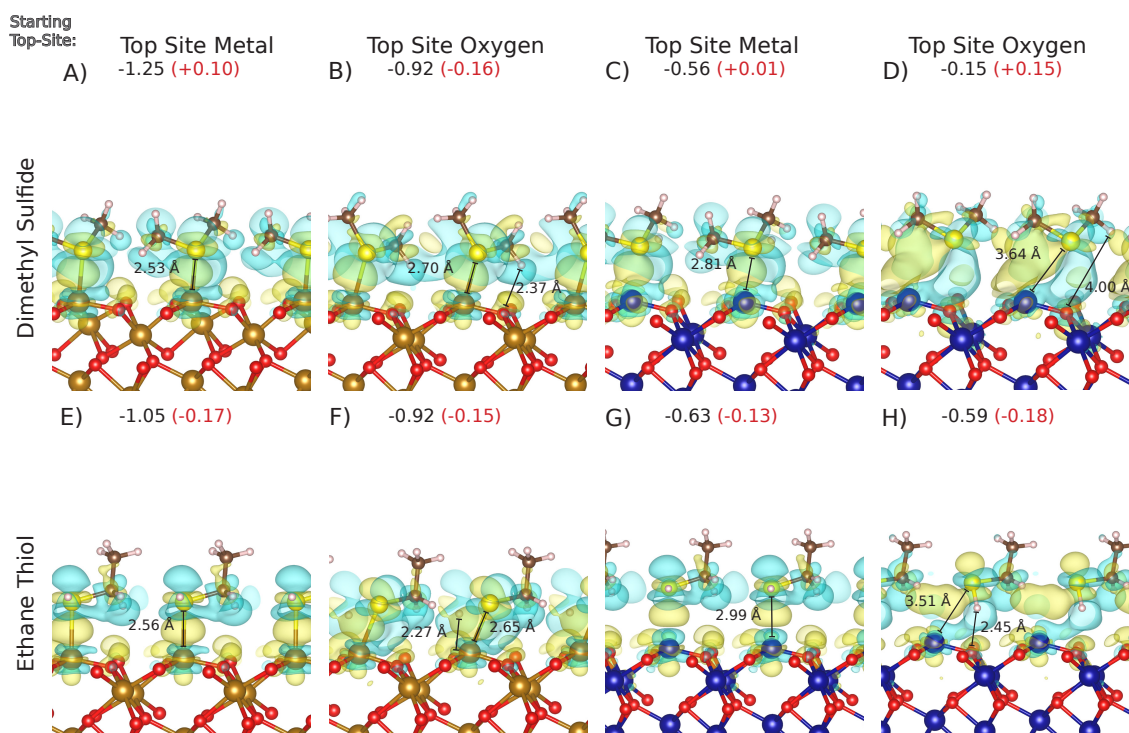


Figure 10.41: Charge density difference plots showing dimethyl sulfide and ethane thiol adsorbed onto transition metal-terminated Cr_2O_3 (blue atoms) and Fe_2O_3 (brown atoms). Yellow represents areas of charge accumulation, blue indicates areas of charge depletion. The adsorption energies are shown alongside each structure, along with the lateral VdW contributions to adsorption in red.

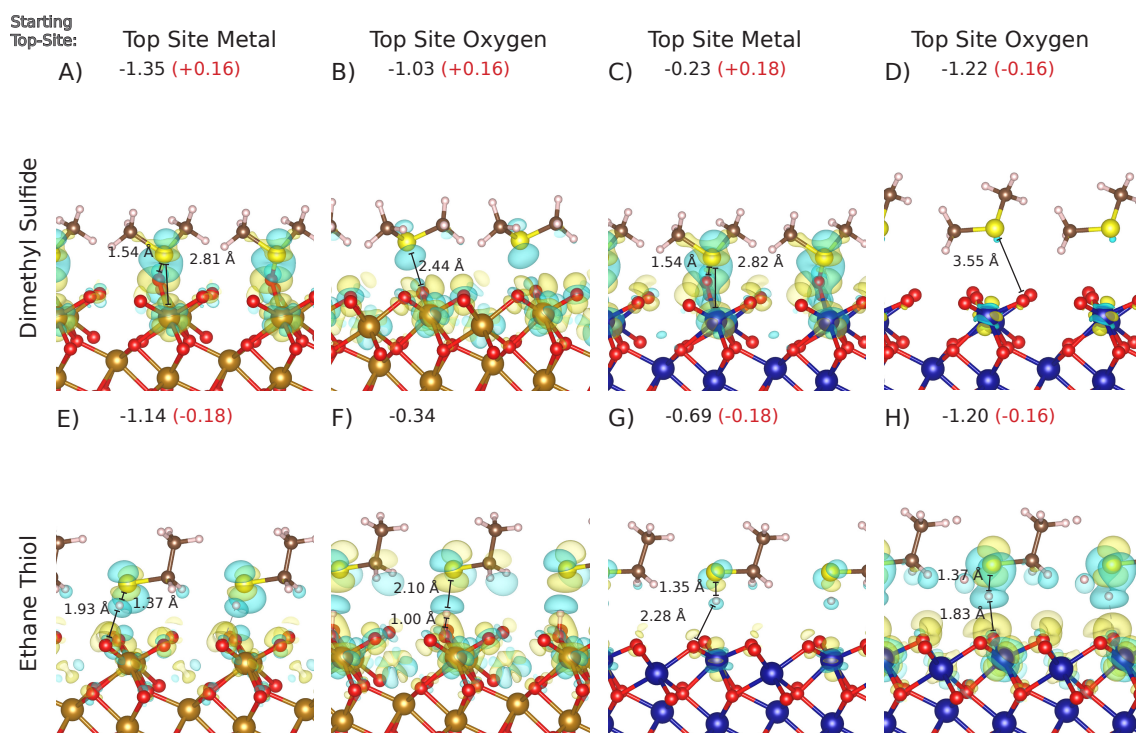


Figure 10.42: Charge density difference plots showing dimethyl sulfide and ethane thiol adsorbed onto transition oxygen-terminated Cr_2O_3 (blue atoms) and Fe_2O_3 (brown atoms). Yellow represents areas of charge accumulation, blue indicates areas of charge depletion. The adsorption energies are shown alongside each structure, along with the lateral VdW contributions to adsorption in red.

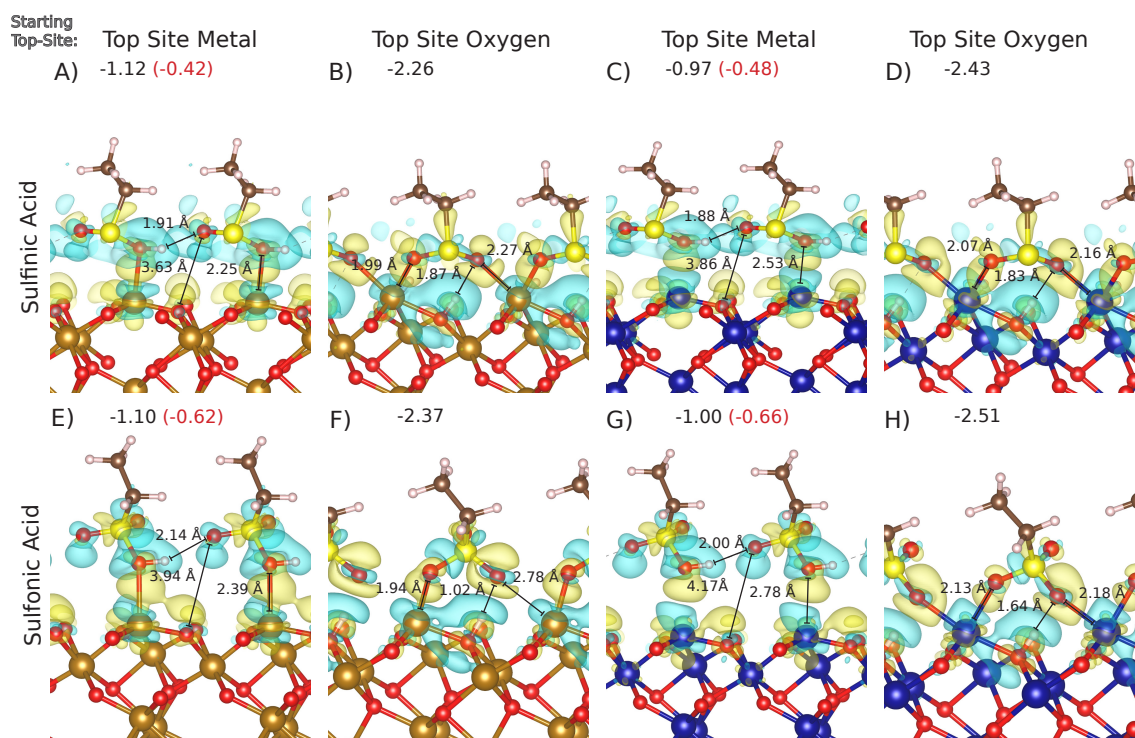


Figure 10.43: Charge density difference plots showing ethane sulfur acids adsorbed onto transition metal-terminated Cr_2O_3 (blue atoms) and Fe_2O_3 (brown atoms). Yellow represents areas of charge accumulation, blue indicates areas of charge depletion. The adsorption energies are shown alongside each structure, along with the lateral VdW contributions to adsorption in red.

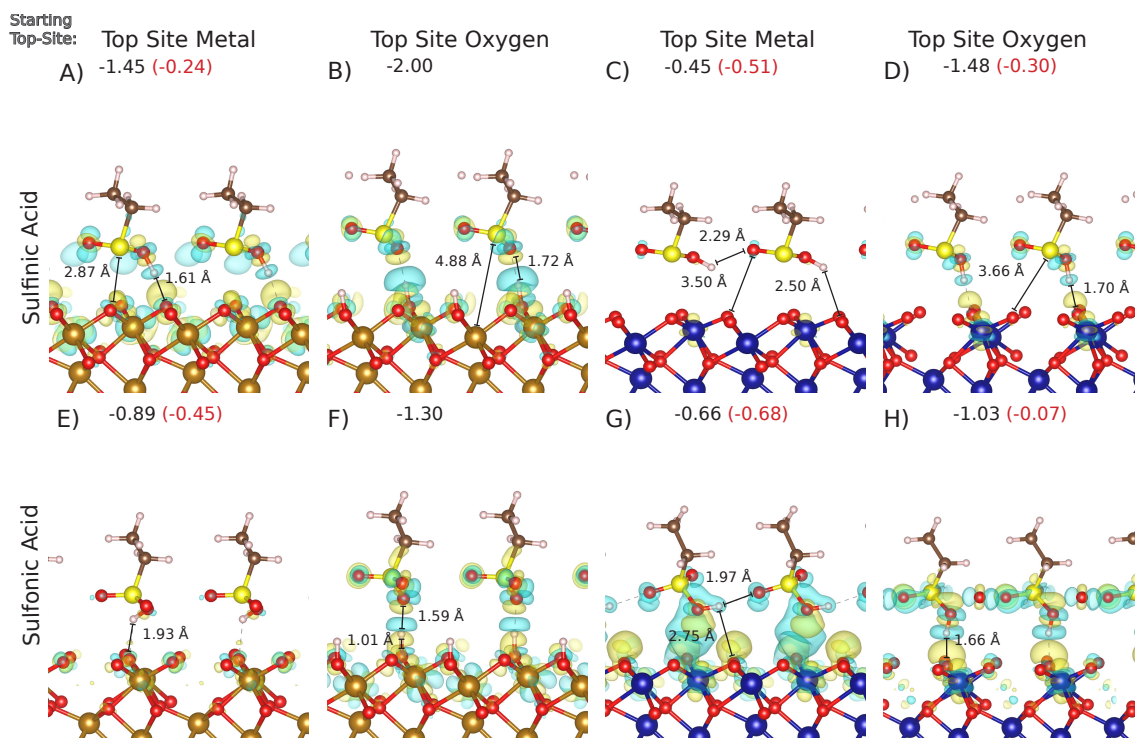


Figure 10.44: Charge density difference plots showing ethane sulfur acids adsorbed onto transition oxygen-terminated Cr_2O_3 (blue atoms) and Fe_2O_3 (brown atoms). Yellow represents areas of charge accumulation, blue indicates areas of charge depletion. The adsorption energies are shown alongside each structure, along with the lateral VdW contributions to adsorption in red.

10.6 DFT Calculated Routes to Jet Fuel Deposits

10.6.1 IRC Calculation of the Re-aromatization

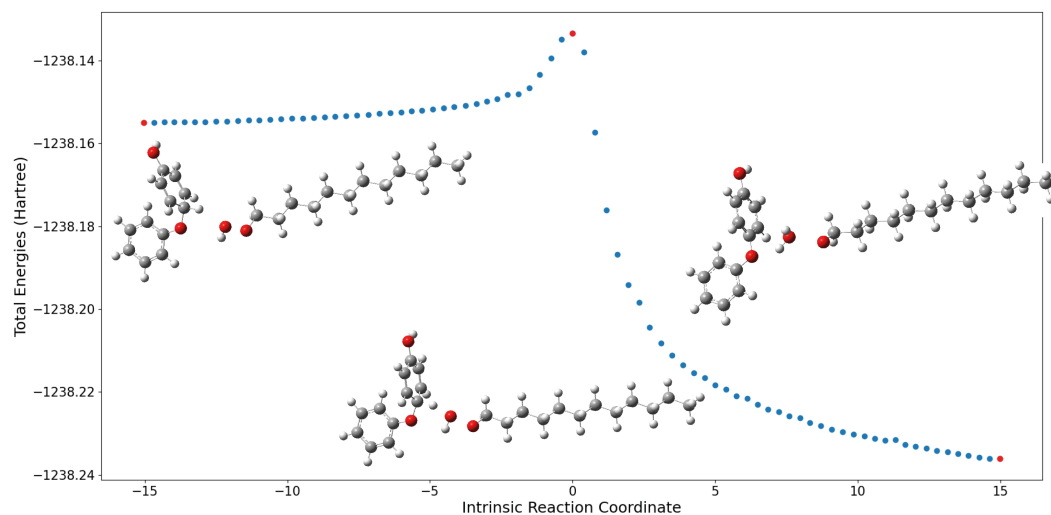


Figure 10.45: IRC calculation showing the transition state of the ROOH re-aromatization of the phenol σ -intermediate. In this case, R refers to a dodecane moiety. The transition state yields a phenol dimer, an RO \cdot and H₂O.

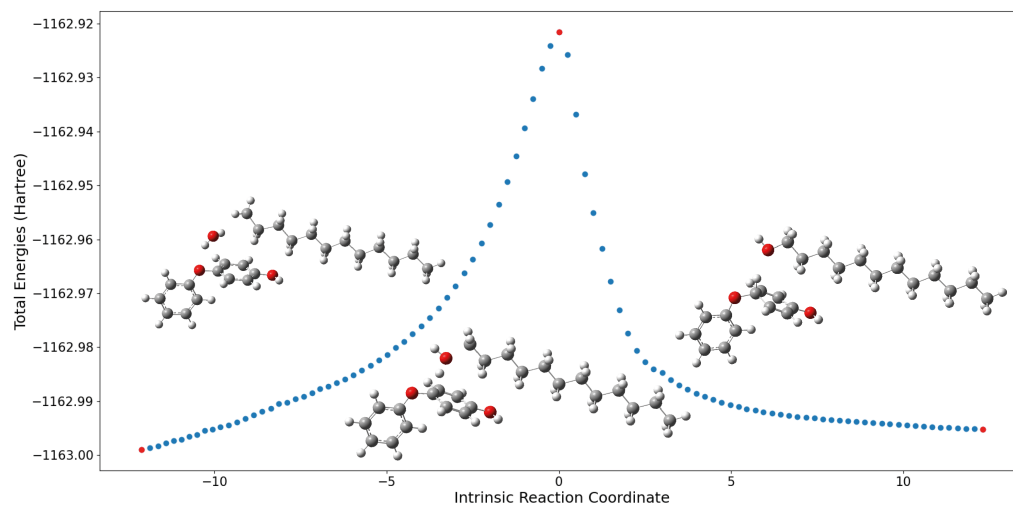


Figure 10.46: IRC calculation showing the transition state of the ROH re-aromatization of the phenol σ -intermediate. In this case, R refers to a dodecane moiety. The transition state yields a phenol dimer, an R \cdot and H₂O.

10.6.2 Thermochemical and Kinetic Parameters Calculated for Each Step

Table 10.20: All kinetic data calculated at the B3LYP-D3//cc-pVTZ level of theory for the reaction mechanisms added to the BAS scheme. For bimolecular reactions, the units of the pre-exponential factor A are $\text{L mol}^{-1} \text{s}^{-1}$ for bimolecular reactions and s^{-1} for unimolecular reactions. The units of E_a are kcal mol^{-1} .

Reaction Number	Reaction	Indole		Pyrrole		Toluene		Phenol		Quinoline		Naphthalene	
		A	E_a	A	E_a	A	E_a	A	E_a	A	E_a	A	E_a
16	AH + ROO· \longrightarrow A· + ROOH	2.57E+12	10.87	1.56E+13	18.23	7.41E+12	29.09	2.67E+12	8.94	1.3581E+13	25.13	7.80E+12	23.39
25	A· + RH \longrightarrow R·	9.80E+08	20.62	2.67E+12	20.86	7.14E+12	7.08	1.72E+12	21.10	8.6083E+12	12.34	7.64E+12	8.50
26	AH + R· \longrightarrow RH	1.76E+12	10.95	2.09E+12	16.53	3.94E+12	19.29	8.61E+12	8.24	4.5206E+12	17.62	5.50E+12	20.98
27	AH + RO· \longrightarrow ROH	6.69E+12	2.97	2.22E+12	5.68	3.59E+12	11.14	3.78E+12	0.29	9.7775E+12	10.33	1.02E+13	14.76
28	A· + A· \longrightarrow Insoluble	3.00E+09	0.00	3.00E+09	0.00	3.00E+09	0.00	3.00E+09	0.00	3.00E+09	0.00	.00E+09	0.00
29	AH + A· \longrightarrow AHA·	2.42E+12	16.67	2.7758E+08	6.29	1.02E+13	5.31	1.82E+12	20.05	4.57E+12	8.49	5.30E+12	6.62
30	AHA· + RO ₂ H \longrightarrow Insoluble + RO· + H ₂ O	5.84E+08	5.50	9.28E+08	0.077	3.75E+08	7.55	4.30E+08	7.86	2.30E+08	7.45	4.78E+08	11.65
31	A· + ROH \longrightarrow RO·	7.04E+12	12.60	3.38E+12	12.97	6.81E+12	2.62	2.36E+12	15.94	8.60E+12	5.79	6.85E+12	4.19
32	A· + ROOH \longrightarrow AH + ROO·	5.09E+12	5.97	6.24E+12	7.09	2.30E+12	0.00	4.99E+12	8.49	8.60E+12	1.35	7.70E+12	0.48

10.6.3 Comparison of Different Sites for Pyrrole and Indole

10.6.3.1 Pyrrole

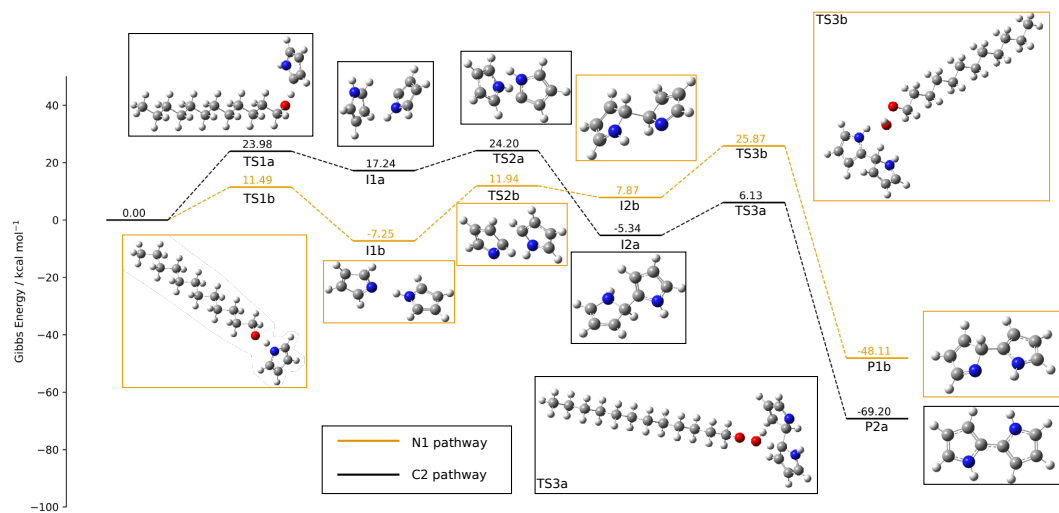


Figure 10.47: Potential energy surface for the pyrrole coupling at the C2 position, comparing H-abstraction at the N1 or C2 position

10.6.3.2 Indole

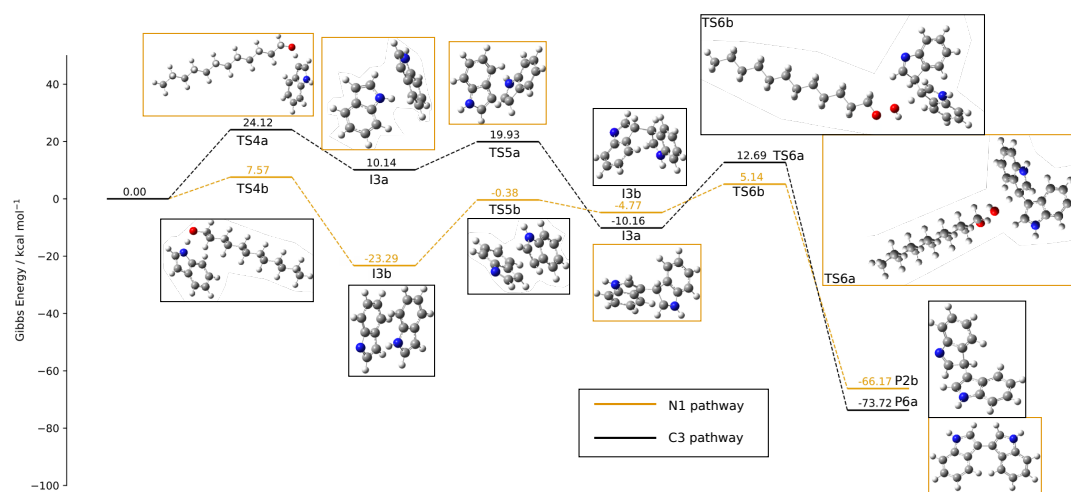


Figure 10.48: Potential energy surface for the indole coupling at the C3 position, comparing H-abstraction at the N1 or C3 position

10.6.4 HAS Reaction Between Propanal Doublet and Various N-heterocycles

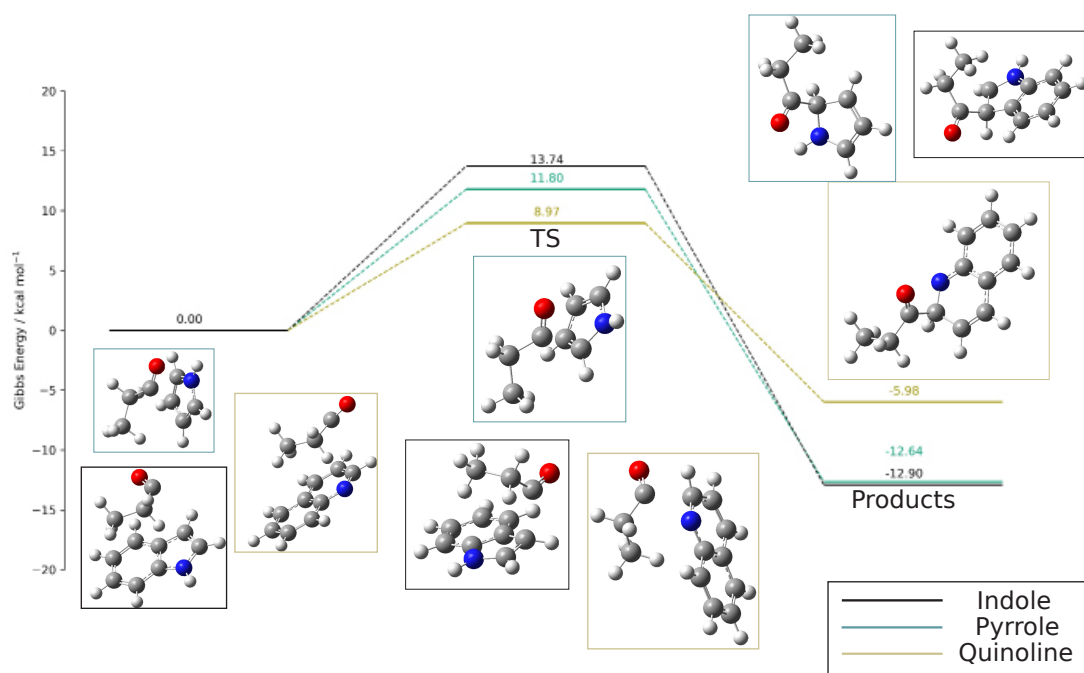


Figure 10.49: Propanal doublet HAS attack step pathway calculated at the B3LYP-D3//cc-pVTZ level. The barriers heights are in the order from largest to smallest; indole > pyrrole > quinoline, which is also reflected in the $A \cdot + AH$ barrier heights.

10.6.5 Effect of Temperature on Each Mechanism

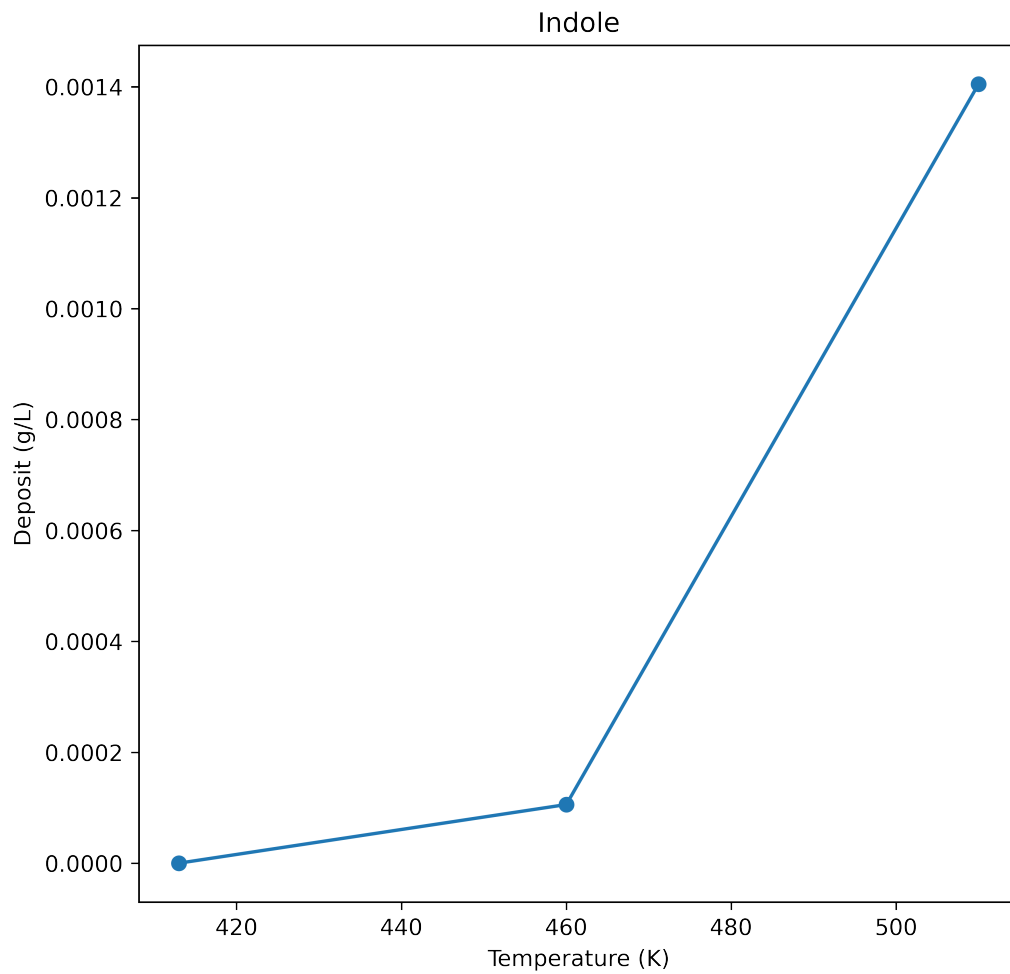


Figure 10.50: Effect of temperature on the concentration of deposits for the indole pseudo-detailed mechanism

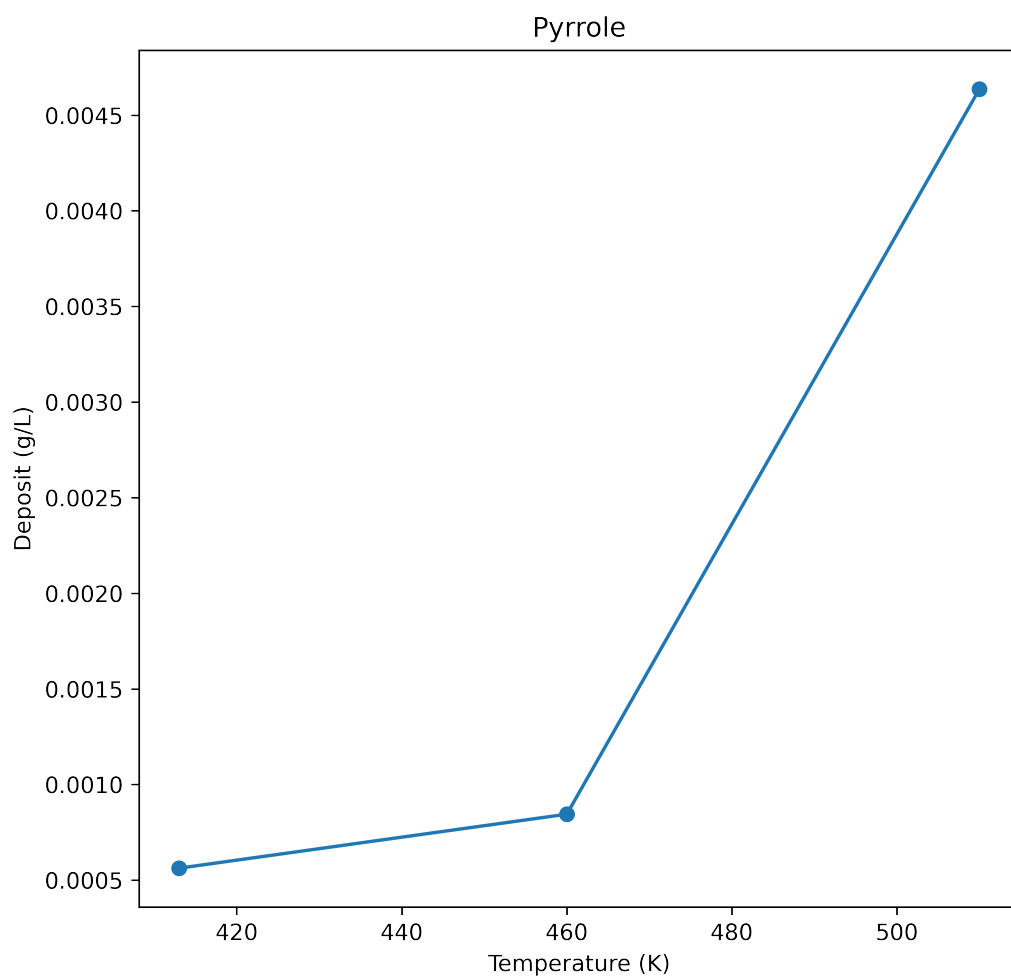


Figure 10.51: Effect of temperature on the concentration of the deposits for the pyrrole pseudo-detailed mechanism

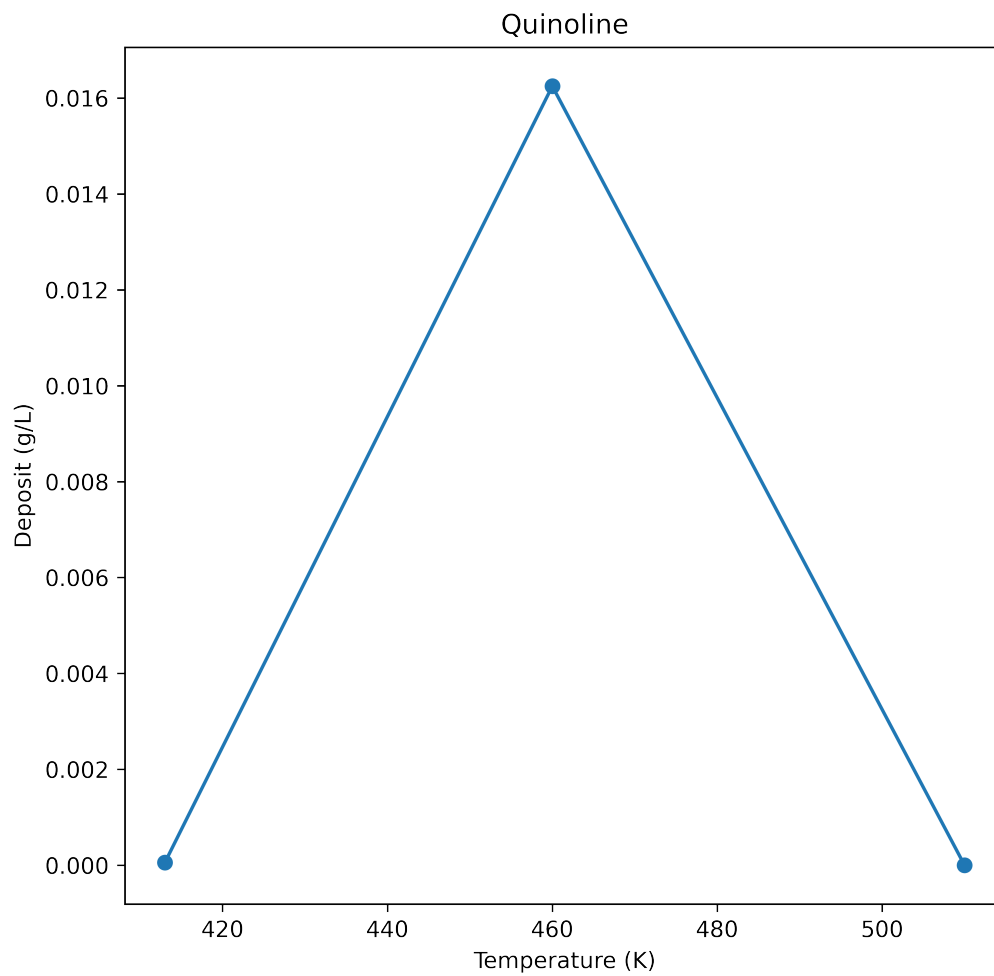


Figure 10.52: Effect of temperature on the concentration of deposits for the quinoline pseudo-detailed mechanism

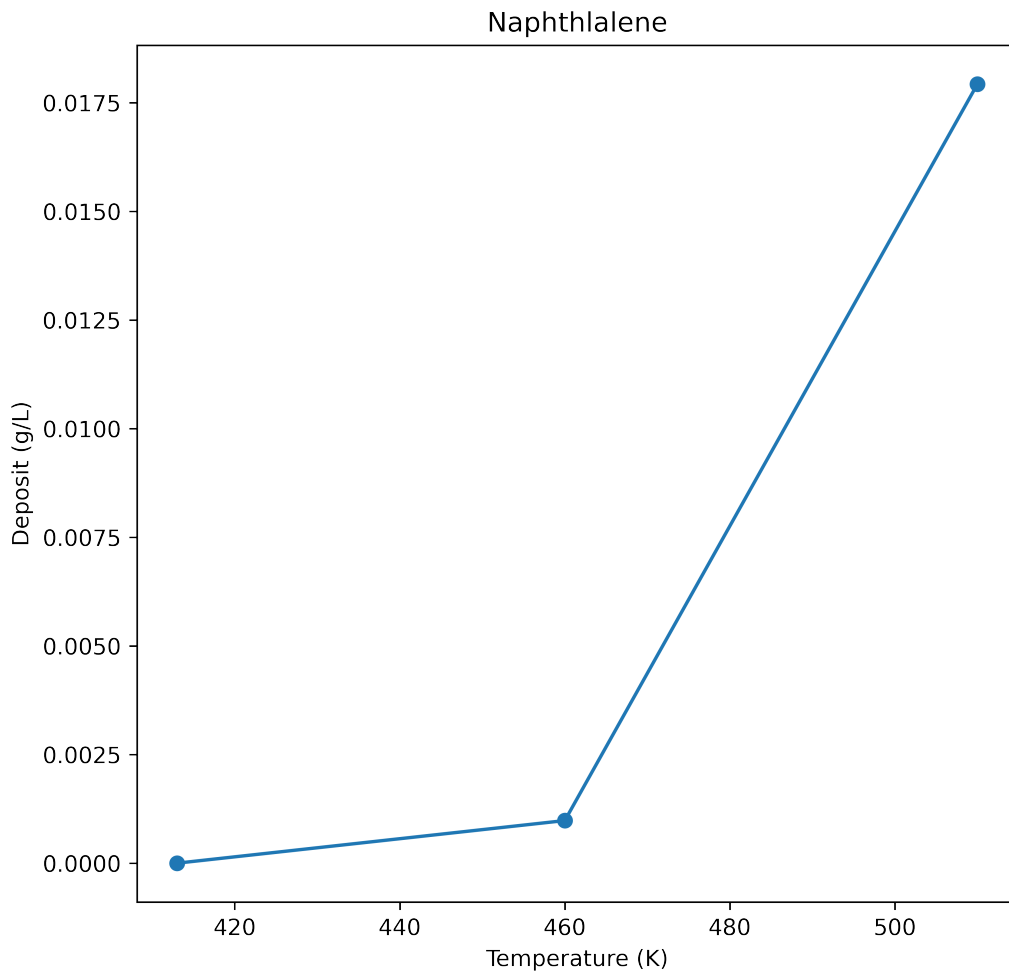


Figure 10.53: Effect of temperature on the concentration of deposits for the naphthlalene pseudo-detailed mechanism

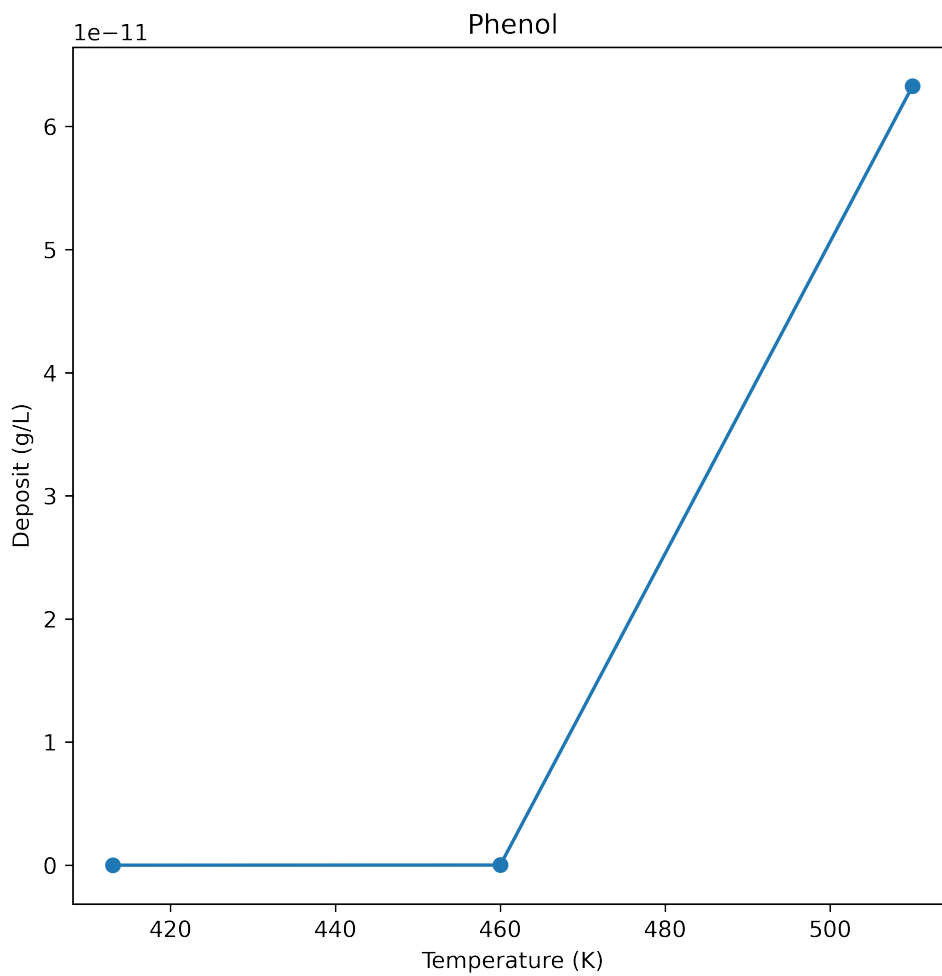


Figure 10.54: Effect of temperature on the concentration of deposits for the phenol pseudo-detailed mechanism

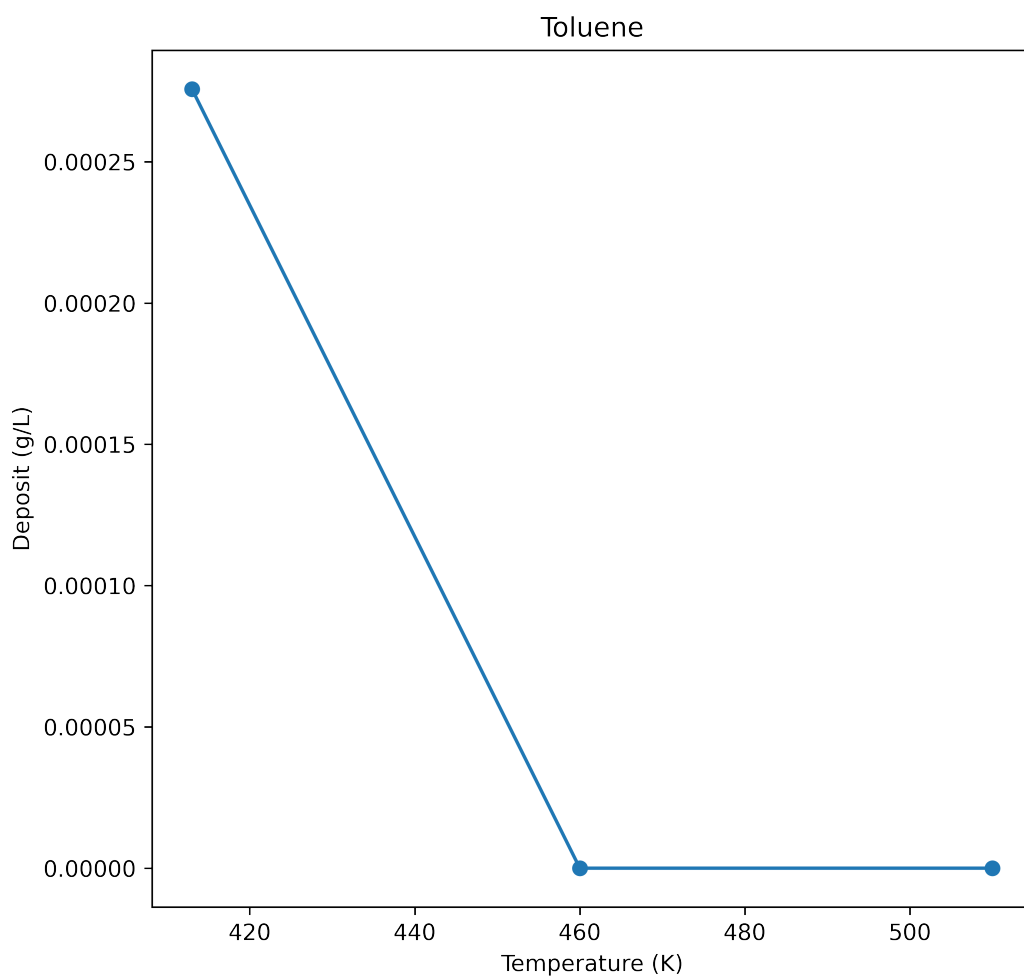


Figure 10.55: Effect of temperature on the concentration of deposits for the toluene pseudo-detailed mechanism